frontiers | Research Topics

Additive manufacturing for polymers

Edited by
Jianlei Wang, Jingjun Wu, Jia-Tao Miao and Tuck-Whye Wong

Published in
Frontiers in Materials

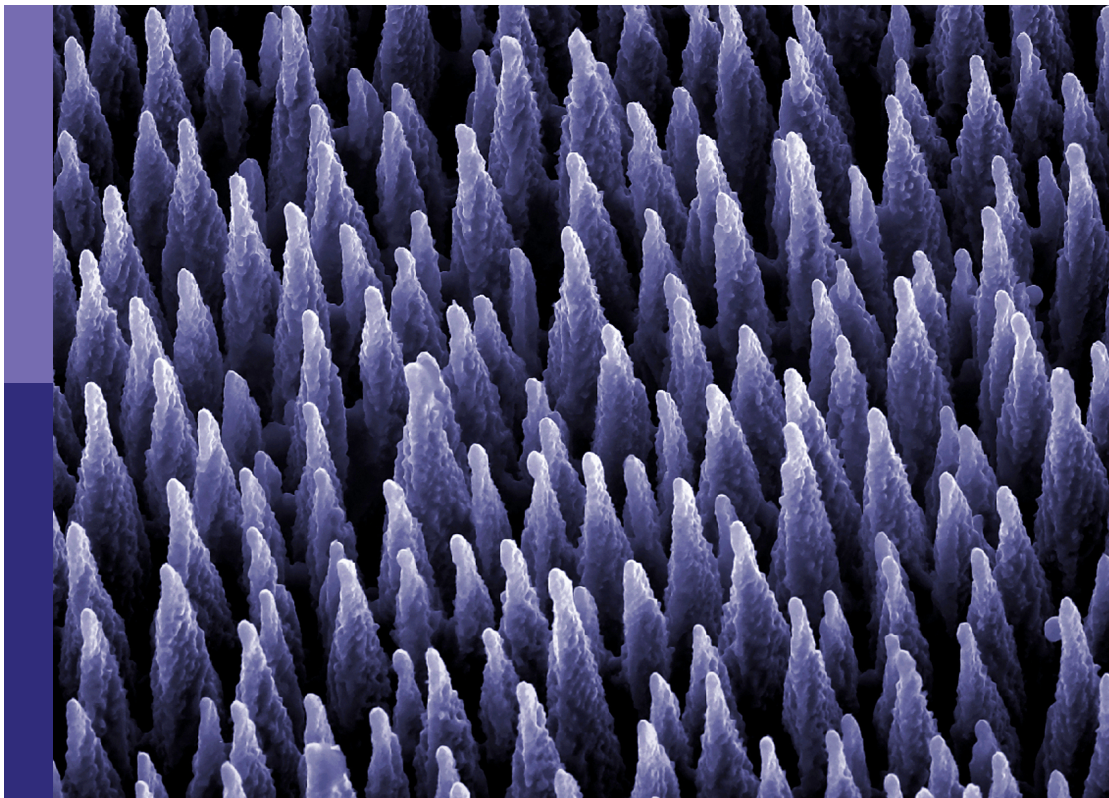

ISSN 1664-8714
ISBN 978-2-8325-2833-4
DOI 10.3389/978-2-8325-2833-4

About Frontiers

Frontiers is more than just an open access publisher of scholarly articles: it is a pioneering approach to the world of academia, radically improving the way scholarly research is managed. The grand vision of Frontiers is a world where all people have an equal opportunity to seek, share and generate knowledge. Frontiers provides immediate and permanent online open access to all its publications, but this alone is not enough to realize our grand goals.

Frontiers journal series

The Frontiers journal series is a multi-tier and interdisciplinary set of open-access, online journals, promising a paradigm shift from the current review, selection and dissemination processes in academic publishing. All Frontiers journals are driven by researchers for researchers; therefore, they constitute a service to the scholarly community. At the same time, the *Frontiers journal series* operates on a revolutionary invention, the tiered publishing system, initially addressing specific communities of scholars, and gradually climbing up to broader public understanding, thus serving the interests of the lay society, too.

Dedication to quality

Each Frontiers article is a landmark of the highest quality, thanks to genuinely collaborative interactions between authors and review editors, who include some of the world's best academicians. Research must be certified by peers before entering a stream of knowledge that may eventually reach the public - and shape society; therefore, Frontiers only applies the most rigorous and unbiased reviews. Frontiers revolutionizes research publishing by freely delivering the most outstanding research, evaluated with no bias from both the academic and social point of view. By applying the most advanced information technologies, Frontiers is catapulting scholarly publishing into a new generation.

What are Frontiers Research Topics?

Frontiers Research Topics are very popular trademarks of the *Frontiers journals series*: they are collections of at least ten articles, all centered on a particular subject. With their unique mix of varied contributions from Original Research to Review Articles, Frontiers Research Topics unify the most influential researchers, the latest key findings and historical advances in a hot research area.

Find out more on how to host your own Frontiers Research Topic or contribute to one as an author by contacting the Frontiers editorial office: frontiersin.org/about/contact

Additive manufacturing for polymers

Topic editors

Jianlei Wang — Chinese Academy of Sciences (CAS), China
Jingjun Wu — Zhejiang University, China
Jia-Tao Miao — Jiangnan University, China
Tuck-Whye Wong — University of Technology Malaysia, Malaysia

Citation

Wang, J., Wu, J., Miao, J.-T., Wong, T.-W., eds. (2023). *Additive manufacturing for polymers*. Lausanne: Frontiers Media SA. doi: 10.3389/978-2-8325-2833-4

Table of contents

frontiers | Frontiers in Materials

TYPE Editorial
PUBLISHED 13 June 2023
DOI 10.3389/fmats.2023.1230323

OPEN ACCESS

EDITED AND REVIEWED BY
Robert Li,
City University of Hong Kong, Hong Kong SAR, China

*CORRESPONDENCE
Jianlei Wang,
jlwang@fjirsm.ac.cn

RECEIVED 28 May 2023
ACCEPTED 01 June 2023
PUBLISHED 13 June 2023

CITATION
Zhou X and Wang J (2023), Editorial: Additive manufacturing for polymers. *Front. Mater.* 10:1230323. doi: 10.3389/fmats.2023.1230323

Editorial: Additive manufacturing for polymers

Xuan Zhou[1,2,3] and Jianlei Wang[1,2]*

[1]Key Laboratory of Design and Assembly of Functional Nanostructures, Fujian Provincial Key Laboratory of Nanomaterials, Fujian Institute of Research on the Structure of Matter, Chinese Academy of Sciences, Fuzhou, China, [2]CAS Haixi Industrial Technology Innovation Center, Ningbo, China, [3]University of Chinese Academy of Sciences, Beijing, China

KEYWORDS

3D printing, additive manufacturing, polymers, process, applications, modelling

Editorial on the Research Topic
Additive manufacturing for polymers

Additive manufacturing (AM), also known as 3D printing, is a kind of technology that manufactures solid parts based on a 3D model (CAD model) with a layer-by-layer accumulation of materials; this allows AM to make flexible and customized designs of product structures and to quickly and accurately transform design ideas into prototypes or even parts to shorten the time-to-market and reduce costs, with irreplaceable advantages in the manufacturing of complex structural characteristics and the delicate design of component structures. However, there are still many limitations in the development of polymer 3D printing, such as the restricted available materials, and the mechanical strength of the products still needs to be higher than those produced by traditional methods. Hence, to further expand the application area of AM and break the development bottleneck, developing new high-performance AM materials and optimizing the AM printing process (including improving resolution, precision, scale, and speed) are highly required.

This Research Topic aimed to capture the recent developments of advancing new technologies, processes, methods, materials, systems, and applications in AM of polymers, expecting to widen the knowledge in this area and promote research and application. The Research Topic has currently collected nine papers, including six original research articles and three reviews.

The six original research papers mainly focus on the development of new materials. Liang et al. successfully prepared Sn-doped β-tricalcium phosphate (Sn@TCP) scaffolds by direct inject writing 3D printing and high-temperature sintering. The osteogenesis of the prepared Sn@TCP was correlated with the concentration of doped Sn. Moreover, the Sn@TCP scaffolds exhibited satisfactory biocompatibility and demonstrated better compressive and osteogenic abilities than pure TCP scaffolds, showing the potential of 3D-printed tin-doped β-TCP scaffolds for tissue engineering.

Li et al. grew microporous Mo_2N single crystals and polycrystalline Mo_2N from nonporous MoO_3 single crystals. Mo_2N had a much higher N_2 reduction reaction rate than MoO_3 single crystals. In addition, the porous Mo_2N single crystals exhibited better catalytic efficiency and long-term stability than polycrystalline Mo_2N. This investigation suggested a new approach for developing and designing molybdenum-based porous single crystals as electrocatalysts for ammonia synthesis.

Li et al. prepared poly (N-isopropyl acrylamide) gels by 3D printing and *in situ* polymerized polyaniline on poly (N-isopropyl acrylamide) substrate using phytic acid to

constitute an interpenetrating network. The composite hydrogels had excellent tensile properties, high electrical conductivity, and sensitive thermal response sensitivity, which could be used in stimulus-response electronics, flexible electronics, and artificial intelligence wearable devices.

Liu et al. developed two different lattice-oriented porous single crystalline-like TiO_2 by a lattice reconstruction strategy of solid-solid phase transformation. Next, Ti^{3+} was introduced into the lattice to obtain a series of Ti_nO_{2n-1} monomers with a Magneli phase. Porous single crystalline-like Ti_nO_{2n-1} had an enhanced exciton lifetime, exhibited significant visible light absorption, and could be used as an electrode to provide strong photocurrents, opening up new avenues for the design of novel photovoltaic materials and the tuning of surface photoreactivity.

Lee et al. evaluated the mechanical strength of 3D-printed agate-based composites. They demonstrated that the arrangement and thickness of the reinforcement layers were vital factors affecting the physical properties of 3D-printed composites.

Belei et al. analyzed the effect of printed Laser-Powder Bed Fusion surface roughness and Fused Filament Fabrication parameters on the strength of Ti-6Al-4V/PA-CF joints produced by this process combination using a three-point bending test method. The data analysis indicated that the printing speed was the main parameter affecting the joint strength, followed by the inclination angle, with the coating height exhibiting only a minor effect.

The three reviews primarily summarized the AM of functional polymer composites with enhanced mechanical, electrical, biological, optical, and other properties. Sun et al. reviewed the respective manufacturing mechanisms and applications of AM and foaming. They summarized several methods for generating cellular structures through AM: 1) cellular scaffolds; 2) composite printing foam; 3) post-foaming of printed solid scaffolds; and 4) *in situ* foam 3D printing. Finally, the Research Topic and development trends of the 3D printing foams were analyzed.

Li et al. described the principle of vat polymerization technology and reviewed the current development of vat polymerization technology for manufacturing nanocomposites. Next, they analyzed the challenges faced by the 3D printing of nanocomposites based on vat polymerization and pointed out that the development bottleneck should be broken by further reducing the production cost of nanofillers and improving the compatibility of nanofillers with the resin matrix.

Miao et al. reviewed the tribological properties of carbon nanotubes (CNTs)-modified polymer composites. They analyzed the lubrication mechanism of polymers and the factors that influence the tribological properties of CNTs/polymer composites. In addition, the limitations of CNTs in improving the tribological properties of polymers were summarized, providing a reference for the preparation of high-performance polymers.

In conclusion, this Research Topic presented insightful and innovative reports focusing on the polymer AM technique, promoting the development of this field. We sincerely thank all authors and reviewers for contributing to this Research Topic.

Author contributions

XZ: writing—original draft preparation. JW: writing—review and editing. All authors contributed to the article and approved the submitted version.

Funding

This work is supported by Ningbo Public Welfare Science and Technology Planning Project (Grant No. 2022S099), the Regional Development Project of Fujian (Grant No. 2022H4020), the STS Project of Putian-CAS (Grant No. 2020HJST009), the Major Project of Science and Technology in Fuzhou (Grant No. 2021-ZD-281), and the Fuzhou Foreign Scientific and Technological Cooperation Projects (Grant No. 2022-Y-008).

Acknowledgments

We thank the authors participating in this Research Topic for their excellent articles and reviewers for their valuable comments.

Conflict of interest

The authors declare that the research was conducted in the absence of any commercial or financial relationships that could be construed as a potential conflict of interest.

Publisher's note

frontiers | Frontiers in Materials

TYPE Original Research
PUBLISHED 09 September 2022
DOI 10.3389/fmats.2022.1016820

OPEN ACCESS

EDITED BY
Jianlei Wang,
Chinese Academy of Sciences (CAS), China

REVIEWED BY
Xu Zhang,
Jiangnan University, China
Hongli Mao,
Nanjing Tech University, China
Yu Wang,
Changchun Institute of Applied Chemistry (CAS), China

*CORRESPONDENCE
Chen Zhang,
zc_jlu@hotmail.com

SPECIALTY SECTION
This article was submitted to Polymeric and Composite Materials, a section of the journal Frontiers in Materials

RECEIVED 11 August 2022
ACCEPTED 23 August 2022
PUBLISHED 09 September 2022

CITATION
Liang H, Fu G, Liu J, Tang Y, Wang Y, Chen S, Zhang Y and Zhang C (2022), A 3D-printed Sn-doped calcium phosphate scaffold for bone tissue engineering.
Front. Mater. 9:1016820.
doi: 10.3389/fmats.2022.1016820

A 3D-printed Sn-doped calcium phosphate scaffold for bone tissue engineering

Hong Liang[1], Gaosheng Fu[2], Jinrui Liu[1], Yueting Tang[1], Yujue Wang[1], Shan Chen[1], Yanjie Zhang[1] and Chen Zhang[1,2]*

[1]School of Materials and Chemistry Engeering, School of Geography and Oceanography, Minjiang University, Fuzhou, China, [2]Industrial Design Institute, Minjiang University, Fuzhou, China

Recent developments in 3D printing technology have been applied in the field of tissue engineering to fabricate customized bone repair scaffolds. β-tricalcium phosphate (β-TCP) is a bioceramic material with excellent potential as a scaffold foundation. Doping metallic ions with β-TCP will significantly enhance the mechanical property and bone regeneration performance compared with pure β-TCP specimens. In this study, we proposed a protocol for the fabrication of a Sn-doped β-TCP (Sn@TCP) scaffold using 3D printing technology, and the effect of Sn-doping on the physicochemical properties of the material and its *in vitro* bioactivity were investigated. Polyethylene glycol and polyvinyl alcohol were used as binder to construct Sn@TCP scaffolds which have good biocompability and can break down into H_2O and CO_2 after scaffolds sintering. The appearance of the scaffold constructed by 3D printing technology closely matched the computer design. The incorporation of Sn into β-TCP improved the compressive strength of the scaffold. Moreover, the Sn@TCP scaffold retained the inherently good biocompatibility of β-TCP and exhibited better osteoinduction capability than pure β-TCP scaffolds. Notably, the osteoinduction ability of Sn@TCP scaffolds were dependent on the Sn content. In conclusion, the 3D printing of Sn@TCP scaffolds with enhanced mechanical properties and osteoblast-inducing activity show great promise as scaffold materials in bone tissue engineering applications.

KEYWORDS

β-tcp, Sn-doping, 3D printing, mechanical properties, osteogenic induction

Introduction

In many instances, patients can develop bone defects due to injury, congenital diseases, and tumors. In these cases, bone substitutes are needed to fill and repair the defects (Grado et al., 2018). In the 1980s, calcium phosphate cements (CPCs) emerged as the first bone substitute materials. Since then, CPCs have been employed as injectable biomaterials in synthetic bone substitutes because of their excellent osteocompatibility with the apatite mineral component of human bone and ease of use (Petre et al., 2019). In addition, β-TCP has shown to be a bioresorbable ceramic

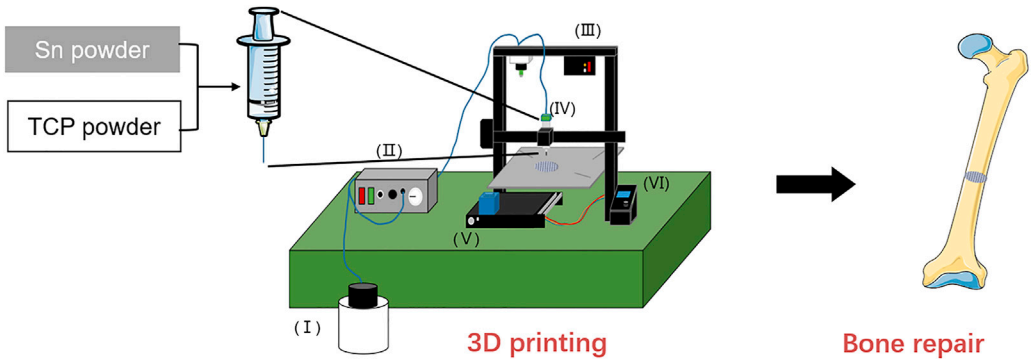

FIGURE 1
Schematic illustration of the preparation for Sn doping TCP scaffolds. Structure composition of 3D printer, I: Compressor, II: controller of compressor, III: pressure alarm, IV: printhead, V: *z*-axis screw, VI: controller of printing.

for bone tissue regeneration. For decades, β-TCP has been investigated as a potential scaffolding material for bone tissue engineering due to its biocompatibility, controlled bioactivity, and resorption/solubilization stability. Furthermore, it is physicochemically and structurally similar to natural bone (Vollmer et al., 2015; Kang et al., 2020).

In recent studies, doping of β-TCP with metallic ions, such as titanium (Ti), zinc (Zn) and magnesium (Mg) with β-TCP, showed

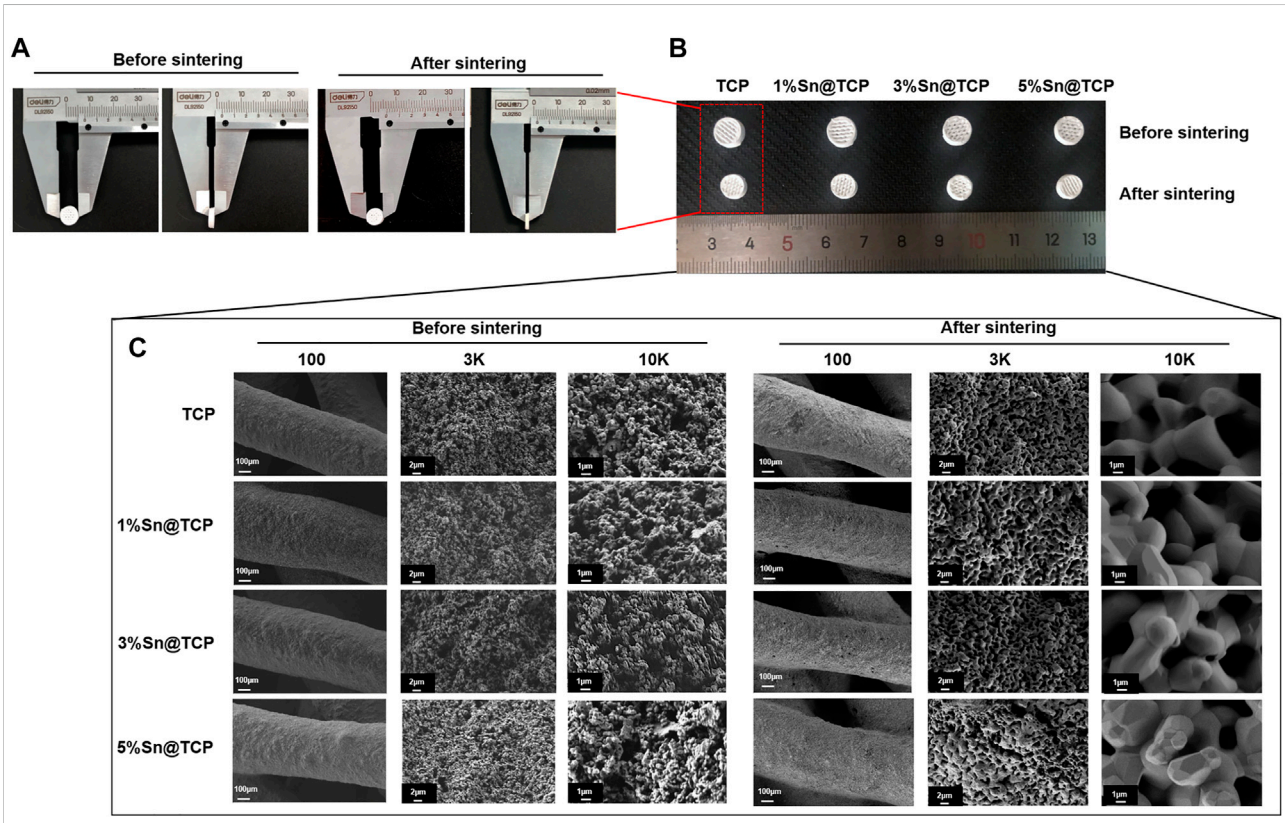

FIGURE 2
Morphology and structure of β-TCP (TCP) and Sn@TCP scaffolds. **(A–B)** The diameter and height of scaffolds before and after sintering. **(C)** SEM morphology of TCP, 1%Sn@TCP, 3%Sn@TCP and 5%Sn@TCP before and after sintering (Magnification from 100 to 10K, bar = 100 μm, 2μm, and 1 μm).

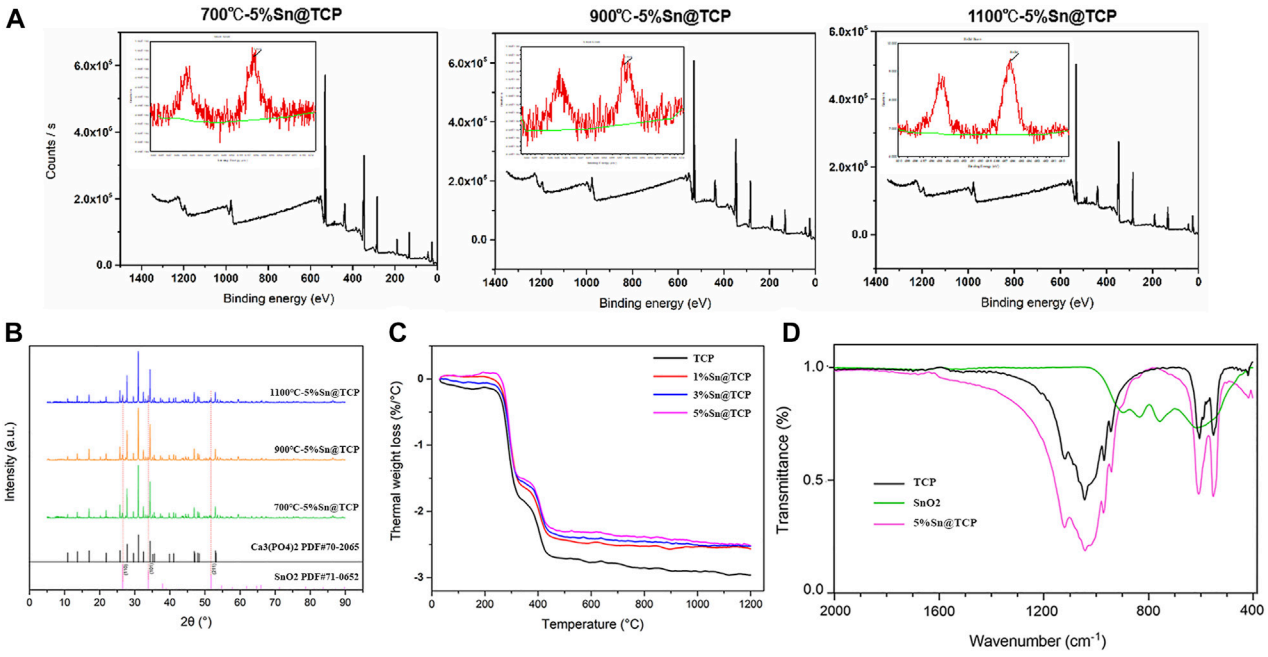

FIGURE 3
Characterization of TCP powders with different Sn doping. **(A)** XPS spectra of 5%Sn@TCP with different sintering temperature (700°C, 900°C and 1,100°C). **(B)** XRD pattern of 5%Sn@TCP with different sintering temperature (700°C, 900°C and 1,100°C). **(C)** TG-DSC curves of TCP powders with different Sn doping after 1,100°C sintering. **(D)** FT-IR spectra of TCP, SnO_2 and 5%Sn@TCP powders.

significantly better bone regeneration than pure β-TCP specimens (Samanta et al., 2019). The incorporation of Mn into β-TCP improved the physicochemical properties and bilineage bioactivities (Deng et al., 2017). Tin (Sn) is one of the most essential trace elements in the human body and is shown to promote tissue growth (Nagy et al., 2000; Tao and Zhang, 2003; Lynch and Duckworth, 2020). Sn-based alloys, such as Mg-Sn alloys, Ti-Nb-Sn alloy, and Mg-Sn alloys combined with biphasic calcium phosphate ceramic (HA+β-TCP). These Sn-based alloys exhibit strength, creep resistance, and biocompatibility. They have been widely employed in biomedical applications involving different parts of the human body, including bone tissue implants and dental implants (Kubasek et al., 2013; Shuai et al., 2016; Wang et al., 2015). Therefore, Sn-doped β-TCP scaffolds may improve the compressive strength of bone and promote osteogenesis. However, to our knowledge, few studies on Sn-doped β-TCP scaffolds for bone tissue engineering have been reported.

Since bone defects can vary in appearance, the appearance of the scaffolds must closely match to effectively fill the defect. The porous structure of the scaffold provides space for cell growth and blood vessel formation. It also contributes to osteogenic differentiation. Therefore, the size and pore structure of the scaffold must be compatible with the bone defect repair *in vivo*. 3D printing technology can customize scaffolds with individual size and pore structure based on computer designs (Mishra et al., 2021; Ye et al., 2021; Zhang et al., 2021). The goal of this research was to fabricate a 3D-printed Sn-doped β-TCP scaffold for bone tissue applications. Moreover, we investigated the effects of Sn content on the physicochemical properties and bioactivity of the scaffold *in vitro*.

Materials and methods

Materials and reagents

β-TCP powder was purchased from Kunshan Chinese Technology New Materials Co., LTD. Sn powder was purchased from Aladdin® (Shanghai, China). The Sn-doping β-TCP scaffolds used for this work were the TCP, 1%Sn@TCP, 3%Sn@TCP and 5%Sn@TCP with nominal composition of 0 wt% Sn, 1 wt% Sn, 3 wt% Sn, and 5 wt% Sn. Tissue-Tek® OCT compound agent as a binder was purchased from Sakura Finetek United States (CA, United States). The 3D printer was assembled by ourselves, and the illustration as shown in Figure 1.

Cells

Human Umbilical Vein Endothelial Cells (HUVECs) were purchased from Cell Bank (Chinese Academy of Sciences, Shanghai, China) and cultured in endothelial cell medium (ECM, ScienCell, CA, United States). Rat bone marrow-derived

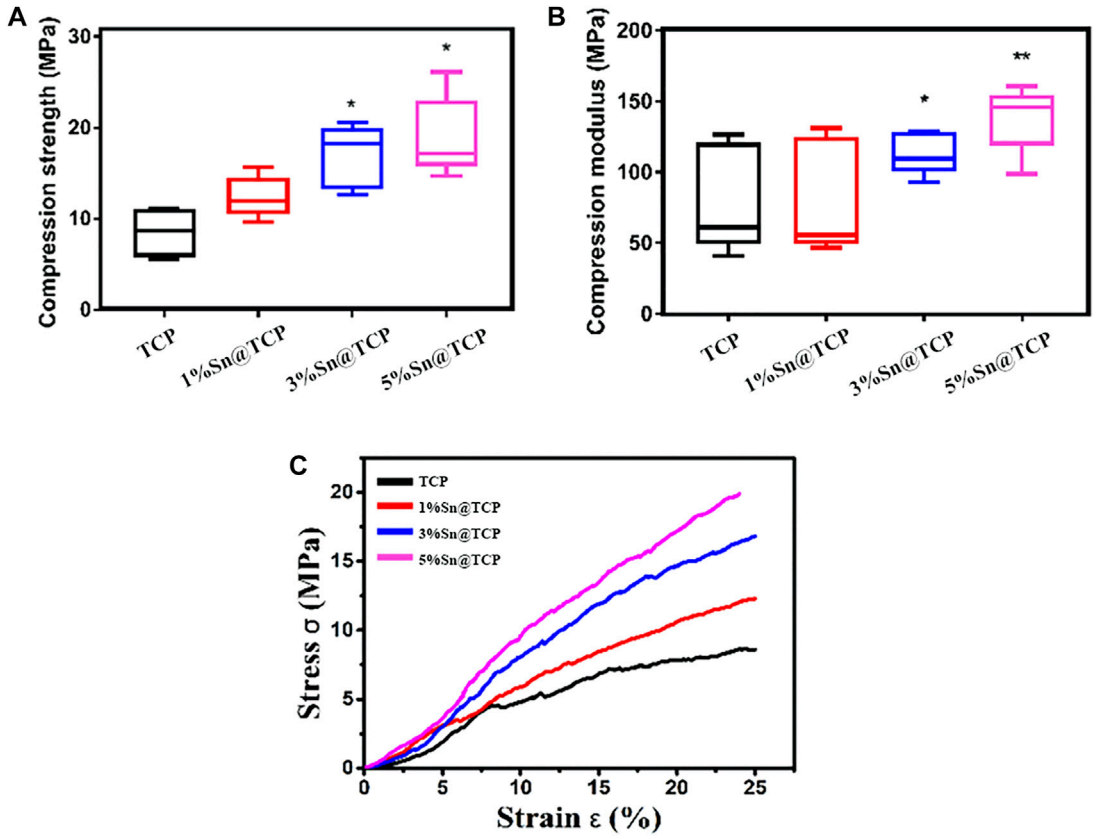

FIGURE 4
Mechanical Property of TCP scaffolds with different Sn doping. **(A)** The compression strength of TCP scaffolds with different Sn doping. **(B)** The compression modulus of TCP scaffolds with different Sn doping. **(C)** Strain-stress curve of TCP scaffolds with different Sn doping. Five scaffolds for each group (n = 5). Significance (*$p < 0.05$, **$p < 0.01$)

mesenchymal stem cell (BMSC) Isolation and Culture. 4-week-old SD rats weighing 200 ± 10 g were sacrificed by cervical dislocation and soaked in 75% ethanol for 30min. The skin, muscle and other soft tissues were obtuse separated from the tibia and femur on a super clean work table, and the tibia and femur were separated and rinsed repeatedly with PBS solution for use for several times. Sterile surgical instruments were cut off the epiphysisof long diaphysis, and only the diaphysis was preserved. DMEM low-glucose medium was extracted with a 23 G sterile syringe to slowly wash the bone marrow cavity, which showed that the contents of the bone marrow cavity oozed together with the medium. A centrifuge tube was placed at the bottom to collect the cell suspension, centrifuged at 1,000 r/min for 5 min, and the supernatant was discarded.

Design and fabricate of Sn incorporated β-TCP scaffold

Solidworks software (2014 version) was used to design the scaffold for printing. The 3D scaffold was designed as a cylindrical shape with a base area diameter of 8 mm and a height of 2 mm Simplify3D software was used to set the print parameters (printing speed: 4 mm/s, filling rate: 40%). A total of 3 g β-TCP or β-TCP@Sn (1, 3, 5% Sn doped in β-TCP) and 3 g binder were mixed for 10 min to prepare the paste for printing. The scaffolds were printed by a 3D printer assembled by ourselves. After the scaffolds were printed, there were dried in the air for 48 h and then placed inside the muffle furnace for sintering (heating rate: 10°C/min, heating temperature and time: 700°C, 900°C or 1,100°C for 3 h).

Characterization of 3D printed scaffolds

Scanning electron microscope (SEM, Sigma 300, Zeiss, Germany) was used to examine the morphology of 3D printed scaffolds. X-Ray diffraction (XRD) patterns were recorded using a D8 ADVANCE system (BRUKER, Germany) operating at 40 kV and 30 mA using a CU Kα1 radiation ($\lambda = 1.54$ Å). The XRD patterns were obtained over the range of 2θ from 5° to 90° with an angular step interval of 0.0334°. The oxidation level of Sn in Sn-doped TCP

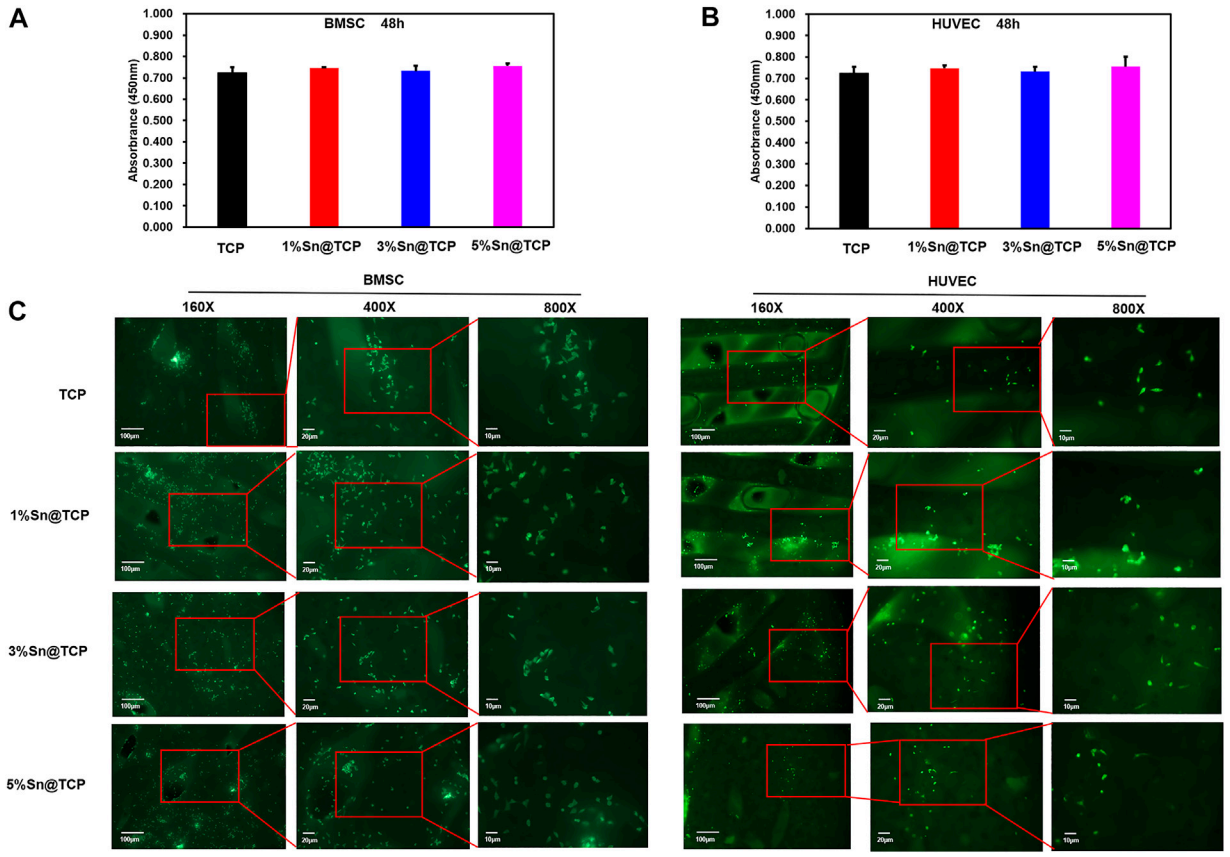

FIGURE 5
Cell growth on Sn@TCP scaffolds. **(A)** The viability of BMSC cells growth on scaffolds for 48 h. **(B)** The viability of HUVEC cells growth on scaffolds for 48 h. **(C)** The fluorescence staining of BMSC and HUVEC cells growth on scaffolds for 48 h (Magnification from ×160 to 800X, bar = 100 μm, 20μm, and 10 μm).

scaffold was determined by XPS (Thermo ESCALAB 250XI, Thermo Fisher, MA, United States). The thermal properties of the samples were studied by Thermogravimetric and differential scanning calorimetry (TG-DSC) (NETZSCH STA 449F3, Germany).

Mechanical properties

To evaluate the mechanical properties of Sn-doped, universal testing machine (Zwick/Roell Z020, Germany) was employed to measure compression strength, compression yield stress, compression modulus and stress-stain curve. The parameters are as following: test mode: compress; compression rate: 0.2 mm/min, parallel experiment: 5 times/group.

2.6 Cell proliferation on scaffolds

Cell experiments were performed by using rat BMSC primary cells and human HUVEC cell line. Each scaffold was sterilized with a autoclave followed by seeding 1×10^4 BMSC or HUVEC cells on each scaffold in a humidified incubator at 37°C and 5% CO_2. After 1–7 days in culture, WST-8 solution (10% v/v in medium) (CCK-8, Dojindo, Japan) was added to each well. After 2 h of incubation, 100 μL of each well was removed to a new 96-well plate. The absorbance value at 450 nm was measured on a multifunction microplate scanner (Tecan Infinite M200). For cell attachment, the BMSCs and HUVECs on the surface of different 3D scaffolds were visualized by Calcein-AM (Dojindo). The cell/scaffolds samples were observed under a fluorescence microscope (DMIL, LEICA, Germany).

Osteogenesis differentiation

For differentiation, ALP assay was carried out to evaluate osteogenesis ability of the BMSCs. Briefly, BMSC cells were seeded with 1×10^4 cells/well in a 24-well cell culture plate containing different scaffolds for 7 and 14 days. Then the cells were washed three times with PBS and fixed with 4%

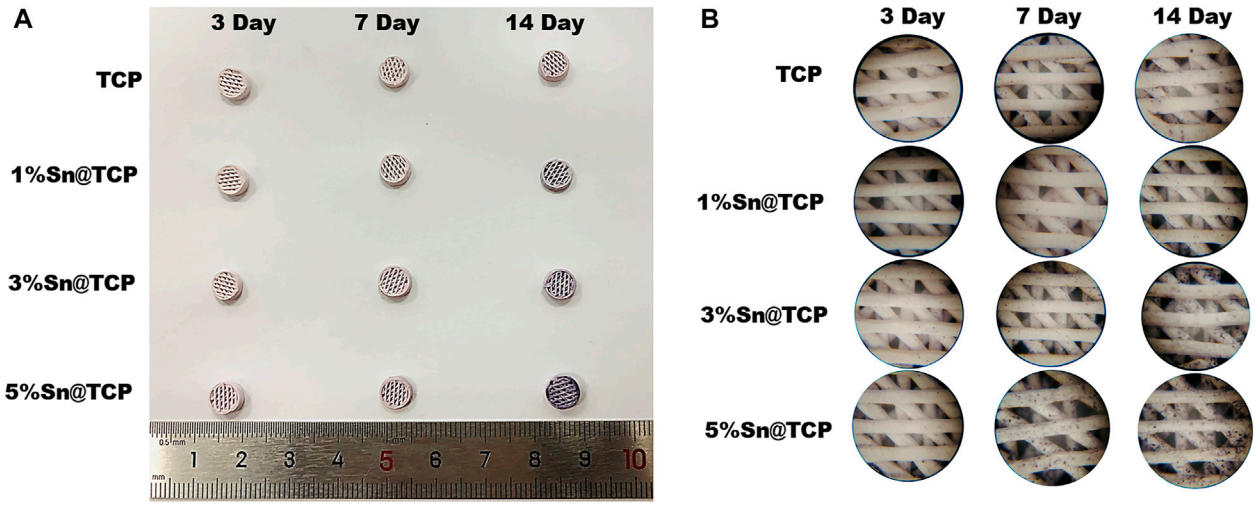

FIGURE 6
Osteoblast inducing activity of Sn@TCP scaffolds during 14 days **(A)** The photographs of ALP staining of Sn@TCP scaffolds in 3 days, 7 days and 14 days **(B)** The magnified photographs of ALP staining of Sn@TCP scaffolds in 3 days, 7 days and 14 days (Magnification 4 X).

paraformaldehyde for 15 min. The cells were rinsed gently in deionized water for 1 min. The cells were stained by alkaline-dye mixture at room temperature for 30 min and rinsed thoroughly in deionized water for 5 min. Finally, the cells on the scaffold were observed using a stereoscopic microscope (SMZ800N, Nikon, Japan).

Statistical analysis

The data were analyzed using Origin 8.0 and are presented as the mean ± standard deviation. For analysis of multiple groups, the statistic difference was evaluated by variance analysis (ANOVA one-way, Origin 8.0). A p-value of <0.05 was statistically significant.

Results and discussion

Morphology and structure of scaffolds

The Sn-doped β-TCP scaffolds were prepared by direct inject writing (DIW) 3D printing, and the fabrication process is shown in Figure 1. The β-TCP and Sn were mixed into binder agent (a water mixture of polyethylene glycol and polyvinyl alcohol, PEG + PVA) to form PEG + PVA/Sn-doped β-TCP composite material. After 3D printing and sintering, the Sn-doped β-TCP (Sn@TCP) scaffolds were constructed. The diameter and height of scaffolds and SEM images are shown in Figure 2. In Figures 2A,B, the diameter and thickness of scaffolds before sintering were 8.02 and 2.24 mm, while the diameter and thickness of scaffolds after sintering was 6.52 and 1.58 mm, respectively. The shrinkage in diameter and thickness was 18.7 and 29.5%, respectively. The appearance of the scaffolds was in accordance with the computer design.

In Figure 2C, the SEM images reveal sufficient pores in the samples after sintering, which can promote bone tissue growth. In addition, the Sn-doped materials with Sn doping display the surface of displayed angular structures on the surface. With the increase in Sn content, the angular structures of the material surface became more obvious. At a 45° angle to each filament layer, the pores were regular rhombus-shaped.

Physicochemical characterization

According to the XPS spectrum, the oxidation level of Sn in Sn@TCP was +4. The XPS spectra of 5%Sn@TCP with different sintering temperature (700°C, 900°C, and 1,100°C) indicate the same optimal sintering temperature, and an increase in the Sn3d peak after sintering at 1,100°C was observed (Figure 3A). The phase composition was verified by the Joint Committee on Powder Diffraction Standards reference patterns of β-TCP and SnO_2 (PDF No. 70–2065 and PDF No. 71–0652). The specific peaks of SnO_2 are shown in the red dotted trace in Figure 3B. As shown in Figure 3B, the peak of 5%Sn@TCP (sintering at 1,100°C) at 2θ degree around 52° increased significantly, compared with 900 and 700°C. The result indicates the optimal temperature for sintering was 1,100°C, and this is consistent with previous reports. TG-DSC analysis displayed the same trend of four groups (TCP, 1%Sn@TCP, 3%Sn@TCP,

and 5%Sn@TCP), while the weight loss percentage of TCP was the highest, compared with Sn@TCP (Figure 3C). This may result from increased oxidation of Sn during sintering. The FT-IR spectra of TCP showed a strong PO_4^{3-} peak between 1,061 and 1,024 $cm^{-}1$, corresponding to the anti-symmetric P-O stretching mode that is present in both TCP and 5Sn@TCP. The second PO_4^{3-} peak between 550 and 600 cm^{-1} corresponded to the O-P-O bending mode (Singh et al., 2016). A small peak between 800 and 900 cm^{-1} was attributed to O-Sn-O bending (Figure 3D). The mechanical properties of TCP scaffolds with different Sn contents were tested. The compression strength of 3%Sn@TCP and 5%Sn@TCP increased significantly, compared with pure TCP, as shown in Figure 4A. In addition, the compression modulus and strain-stress curve of 5%Sn@TCP enhanced significantly, compared with TCP, 1%Sn@TCP, and 3%Sn@TCP (Figures 4B,C).

Biocompatibility and osteoinduction evaluation

The cytotoxicity of TCP, 1%Sn@TCP, 3%Sn@TCP, and 5% Sn@TCP scaffolds was evaluated by examining both viability and morphologies of BMSC and HUVEC cells over 48 h. Figures 5A,B showed the cell viability of BMSC and HUVEC cells cultured in scaffolds for 48 h, compared with the negative control (TCP scaffold group). The cells cultured in 1%Sn@TCP, 3%Sn@TCP, and 5%Sn@TCP scaffolds had comparable cell viability to the negative control. This phenomenon is consistent with the reported biocompatibility of Sn-containing biomaterials. Calcein-AM staining was used to indicate the living cells and reflect the morphologies of BMSC and HUVEC cells on different scaffolds after 48 h. From Figure 5C, the number of cells stained with Calcein-AM was almost same in all of the four groups, and the cell morphology remained intact. Our results showed the Sn-doped β-TCP scaffolds exhibited good biocompatibility that was comparable to β-TCP scaffolds.

The upregulation of ALP activity indicates early mineralization of osteogenic differentiation in BMSC (Deng et al., 2017). Therefore, we chose ALP staining to evaluate the Osteogenesis differentiation activity of scaffolds. No significant difference in the level of ALP secretion was observed for β-TCP scaffolds over time. On day 14, a small number of cells secreted ALP. In contrast, Sn-doped β-TCP scaffolds showed an evident purple color, and the ALP staining of the scaffolds was dependent on the Sn content and culture duration (Figure 6).

Conclusion

In this study, we have fabricated Sn-doped TCP scaffolds successfully by DIW 3D printing and high-temperature sintering. The TCP scaffolds were doped with different ratios (0 wt% Sn, 1 wt% Sn, 3 wt% Sn, and 5 wt%) Sn and used the polyethylene glycol and polyvinyl alcohol as binder. Compared with pure TCP scaffolds, the Sn@TCP scaffolds exhibited higher mechanical properties and osteoinduction capability, presenting a Sn concentration dependent manner. Besides, the Sn@TCP scaffolds possessed good biocompatibility. Therefore, the Sn-doped TCP scaffolds satisfy the requirements for bone regeneration and represent a viable strategy for bone defect repair.

Data availability statement

The raw data supporting the conclusions of this article will be made available by the authors, without undue reservation.

Ethics statement

The animal study was reviewed and approved by Institutional Animal Care and Use Committee of Minjiang University (Approval ID: 20200821-02R).

Author contributions

HL: Conceptualization, Methodology, Writing—Original Draft, Funding acquisition. GF Methodology, Funding acquisition. JL: Investigation, Formal analysis. YT: Validation, Formal analysis. YW: Investigation, Validation. SC: Lab Resources, Funding acquisition. YZ: Lab Resources. CZ: Conceptualization, Writing—Review; Editing, Supervision, Project administration, Funding acquisition.

Funding

This work was supported by National Natural Science Foundation of China (Grant. No. 21904054, 81801849), the Natural Science Foundation of Fujian Province, China (Grant. No. 2020J05176, 2020J01865, 2022J05240), the Fujian Province Science and Technology plan, China (Grant. No. 2020Y4018), the Fund of Fujian Innovation Center of Additive Manufacturing, China (Grant. No. ZCZZ202-15).

Conflict of interest

The authors declare that the research was conducted in the absence of any commercial or financial relationships that could be construed as a potential conflict of interest.

Publisher's note

References

Deng, C. J., Yao, Q., Feng, C., Li, J., Wang, L., Cheng, G., et al. (2017). Retracted: 3D printing of bilineage constructive biomaterials for bone and cartilage regeneration. *Adv. Funct. Mat.* 27 (36), 1703117. doi:10.1002/adfm.201703117

Grado, F. D. G., Laetitia, K., Ysia, I. G., Quentin, W., Anne-Marie, M., Nadia, B. J., et al. (2018). Bone substitutes: a review of their characteristics, clinical use, and perspectives for large bone defects management. *J. Tissue Eng.* 9, 204173141877681. doi:10.1177/2041731418776819

Kang, H. J., Makkar, P., Padalhin, A. R., Lee, G. H., and Lee, B. T. (2020). Comparative study on biodegradation and biocompatibility of multichannel calcium phosphate based bone substitutes. *Mater. Sci. Eng. C* 110, 110694. doi:10.1016/j.msec.2020.110694

Kubasek, J., Vojtěcha, D., Lipov, J., and Ruml, T. (2013). Structure, mechanical properties, corrosion behavior and cytotoxicity of biodegradable Mg-X (X=Sn, Ga, In) alloys. *Mater. Sci. Eng. C* 33 (4), 2421–2432. doi:10.1016/j.msec.2013.02.005

Lynch, R. J. M., and Duckworth, R. M. (2020). Chapter 4: Microelements: Part I: Zn, Sn, Cu, Fe and I. *Monogr. Oral Sci.* 28, 32–47. doi:10.1159/000499007

Mishra, P. K., Senthil, P., Adarsh, S., and Anoop, M. S. (2021). An investigation to study the combined effect of different infill pattern and infill density on the impact strength of 3D printed polylactic acid parts. *Compos. Commun.* 24, 100605. doi:10.1016/j.coco.2020.100605

Nagy, L., Szorcsik, A., and Kovacs, K. (2000). Tin compounds in pharmacy and nutrition. *Acta Pharm. hung.* 70 (2), 53–71.

Petre, D. G., Nadar, R., Tu, Y., Paknahad, A., and Leeuwenburgh, S. C. G. (2019). Thermoresponsive brushes facilitate effective reinforcement of calcium phosphate cements. *ACS Appl. Mat. Interfaces* 11 (30), 26690–26703. doi:10.1021/acsami.9b08311

Samanta, S. K., Devi, K. B., Das, P., Mukherjee, P., Chanda, A., Roy, M., et al. (2019). Metallic ion doped tri-calcium phosphate ceramics: Effect of dynamic loading on *in vivo* bone regeneration. *J. Mech. Behav. Biomed. Mat.* 96, 227–235. doi:10.1016/j.jmbbm.2019.04.051

Shuai, C., Zhou, Y. Z., Lin, X., Yang, Y. W., Gao, C., Shuai, X., et al. (2016). Preparation and characterization of laser-melted mg-sn-zn alloys for biomedical application. *J. Mat. Sci. Mat. Med.* 28 (1), 13. doi:10.1007/s10856-016-5825-z

Singh, S. S., Roy, A., Lee, B., Banerjee, I., and Kumta, P. N. (2016). Synthesis, characterization, and *in-vitro* cytocompatibility of amorphous β-tri-calcium magnesium phosphate ceramics. *Mater. Sci. Eng. C* 67, 636–645. doi:10.1016/j.msec.2016.04.076

Tao, L., and Zhang, X. Li. (2003). Trace element tin and health. *Guangdong Trace Elem. Sci.* 10 (11), 7–12.

Vollmer, N., King, K. B., and Ayers, R. (2015). Biologic potential of calcium phosphate biopowders produced via decomposition combustion synthesis. *Ceram. Int.* 41 (6), 7735–7744. doi:10.1016/j.ceramint.2015.02.105

Wang, X., Li, J. T., Xie, M. Y., Qu, L. J., Zhang, P., and Li, X. L. (2015). Structure, mechanical property and corrosion behaviors of (HA + β-TCP)/Mg–5Sn composite with interpenetrating networks. *Mater. Sci. Eng. C* 56, 386–392. doi:10.1016/j.msec.2015.06.047

Ye, G. Y., Bi, H. J., Li, Z. L., and Hu, Y. C. (2021). Compression performances and failure modes of 3D printed pyramidal lattice truss composite structures. *Compos. Commun.* 24, 100615. doi:10.1016/j.coco.2020.100615

Zhang, X., Wang, J. L., and Liu, T. X. (2021). 3D printing of polycaprolactone-based composites with diversely tunable mechanical gradients via multi-material fused deposition modeling. *Compos. Commun.* 23, 100600. doi:10.1016/j.coco.2020.100600

frontiers | Frontiers in Materials

TYPE Review
PUBLISHED 28 November 2022
DOI 10.3389/fmats.2022.1083931

OPEN ACCESS

EDITED BY
Jingjun Wu,
Zhejiang University, China

REVIEWED BY
Xu Zhang,
Jiangnan University, China
Mingfeng Chen,
Fujian Normal University, China
Nidhin Divakaran,
Central Institute of Plastics Engineering and Technology, India

*CORRESPONDENCE
Lixin Wu,
lxwu@fjirsm.ac.cn

SPECIALTY SECTION
This article was submitted to Polymeric and Composite Materials, a section of the journal Frontiers in Materials

RECEIVED 29 October 2022
ACCEPTED 14 November 2022
PUBLISHED 28 November 2022

CITATION
Sun B and Wu L (2022), Research progress of 3D printing combined with thermoplastic foaming.
Front. Mater. 9:1083931.
doi: 10.3389/fmats.2022.1083931

Research progress of 3D printing combined with thermoplastic foaming

Bin Sun[1,2,3] and Lixin Wu[1,2]*

[1]Key Laboratory of Design and Assembly of Functional Nanostructures, Fujian Provincial Key Laboratory of Nanomaterials, Fujian Institute of Research on the Structure of Matter, Chinese Academy of Sciences, Fuzhou, China, [2]CAS Haixi Industrial Technology Innovation Center, Ningbo, China, [3]University of Chinese Academy of Sciences, Beijing, China

Thermoplastic foam additive manufacturing is a brand-new industry that perfectly combines the advantages of polymer foaming with AM. The 3D printing industry currently suffers from limited available materials and monolithic part manufacturing, and 3D printed foam offers a new way of thinking to address these challenges. Designing multifunctional components with additive manufacturing gives designers great flexibility, while foaming reduces the weight of materials and costs. The combination of the two allows for the creation of lightweight structural and functional items with differentiated physical properties. This one-of-a-kind and innovative approach can be achieved in the printed section. 3D printing foam, on the other hand, is still in its infancy. This review examines the respective functions and applications of additive manufacturing and foaming, and then attempts to summarize four commonly used 3D printing methods at this stage:1) cellular scaffolds; 2) composite printing foam; 3) post-foaming of printed solid scaffolds; 4) *in-situ* foam 3D printing. Among these methods, *in-situ* foam 3D printing is the technique that properly merges the foaming and fused filament fabrication processes. Although in the early stages of research and not yet fully established, this foam 3D printing technique seems to be the trend to replace other foaming processes.

KEYWORDS

3D printing, thermoplastics, foaming, reviews, microcellular foams

1 Introduction

In today's increasingly energy-constrained world, polymer foam products are attracting widespread attention for their material-saving and low-cost qualities, as well as their good mechanical and thermal stability, low thermal conductivity and excellent dielectric properties (Di Maio and Kiran, 2018). The design concept of thermoplastic foaming perfectly fits the human pursuit of high-performance materials by improving the mechanical properties of materials while decreasing material density. Nevertheless, each high-performance thermoplastic foam has a relatively single function, and the addition of micro- and nano-nucleating agents is an effective technique to improve the foam structure and give it better mechanical properties. With the development of high-end fields such as

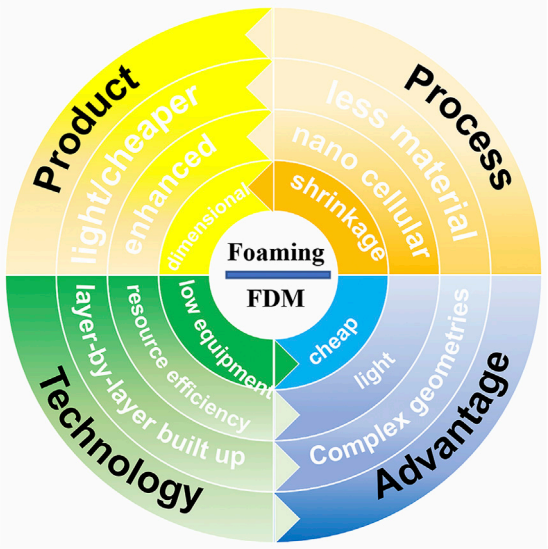

FIGURE 1
The huge advantages of the combination of additive manufacturing and foaming are expected to make it an epoch-making manufacturing process.

building materials, automotive, aerospace and military industry, thermoplastic polymer foam materials and products are also facing new challenges (Ling et al., 2013; Costeux, 2014; Forest et al., 2015). The accuracy and performance of the foam produced by traditional foam molding technology can no longer meet the increasingly stringent requirements. The foam produced by the microcellular foam molding process has smaller pore sizes than the original defects or microscopic cracks in conventional foam. These micro-pores can blunt the cracks in the original material and improve the mechanical properties of the material by increasing the strength of the plastic.

Additive manufacturing is an emerging manufacturing technology that uses digital models (Shmueli et al., 2019; Narupai and Nelson, 2020) as a basis to create solid objects from materials in a layer-by-layer build-up (Nadgorny and Ameli, 2018). Because additive manufacturing does not require the process planning of subtractive manufacturing, it largely simplifies the process of producing complex parts. This has overturned the traditional manufacturing concepts and models, and has had a profound impact on the transformation of traditional manufacturing into modern manufacturing.

The current microcellular foaming methods generally include batch foaming method, rapid temperature rise method, rapid pressure reduction method, continuous extrusion foaming method, injection molding foaming method, etc. Here, we propose that additive manufacturing technology can also be used as a novel microcellular foam molding process. Combined with seemingly unrelated concepts of thermoplastic foaming and additive manufacturing, it enables the development of unique engineered materials with a variety of geometric shapes and specific physical properties. Figure 1 depicts the respective advantages of additive manufacturing and foaming. It is believed that 3D printing foaming technology will become an advanced technology with broad application prospects. This review will focus on these two topics (Attaran, 2017).

2 Additive manufacturing and foaming are two relatively independent technologies

2.1 Additive manufacturing

2.1.1 3D printing methods

Often referred to as 3D printing, additive manufacturing (AM) was initially created in the 1980s to address the extremely specific demands of model creation and rapid prototyping (RP). Since then, it has evolved into a versatile technological platform for rapid prototyping and computer-assisted design (CAD) (Hofmann, 2014). A variety of techniques that quickly and easily convert virtual solid model data into physical model are what constitute additive manufacturing (Rashid, 2019). Without the requirement for molds or machining, which are typical of traditional forming and subtractive manufacturing, it allows custom components to be made from metals (Yang et al., 2022), ceramics (Felzmann et al., 2012; Franchin et al., 2022) and polymers. Polymer-based additive manufacturing can be roughly classified into four categories, each of which has its own technology. Among them, polymers are undoubtedly the most frequently used additive manufacturing material category. Table 1 summarizes the advantages and disadvantages of AM classification methods for polymers. The first additive manufacturing technique is photopolymerization, in which a liquid photopolymer in a vat is selectively cured by photoactivated polymerization (Kaiser and Chalfin, 2017). Stereolithography (SLA) (Credi et al., 2016; Palaganas et al., 2017; Voet et al., 2018), digital light processing (DLP) (Ligon-Auer et al., 2016; Zhu et al., 2017, 2018), continuous liquid interface production (CLIP) (Tumbleston et al., 2015; Janusziewicz et al., 2016) and multiphoton polymerization (MPP) (Nikolić and Stevanović, 2006) etc., All fall into this category. In stereolithography, the light source may be either a laser or a projector in digital processing of the light (Borrello et al., 2018). The second technique is called powder bed fusion technology (PFT), where the polymer is delivered towards the print bed as a powder layer and then portions of the powder bed are thermally fused. Selective laser sintering (SLS) also belongs to this technology, as defined in the standard text of ASTM F2792-12 (Kaiser and Chalfin, 2017).The technique can be applied in cores or molds for manufacturing facilities made of various metal alloys as well as organic materials like sand. The powder bed used

TABLE 1 Multiple AM processes for polymers, with benefits and drawbacks.

Multiple processes	Typical and largest build volume	Typical materials	Advantages	Disadvantages
Vat photopolymerization	50–100 μm	acrylates/epoxides	excellent surface quality and precision	limited mechanical properties
SLA				
CLIP exposure from bottom	75 μm	acrylates	high build speed	limited mechanical properties
	25–100 μm	acrylates/epoxides	low initial vat volume	
multiphoton lithography	0.1–5 μm	acrylates	very high resolution	low build speed; limited materials
Powder Bed Fusion	50–100 μm	PA12; PEEK	greatest mechanical characteristics; least anisotropy	rough surfaces; unusable unsintered powder
Material and Binder Jetting polyjet	25 μm	acrylates	quick; allows multi-material	need for low viscosity ink
Aerosol jet printing	10 μm	conductive inks/ dielectrics	high resolution; low temp process	need for low viscosity ink
3D printing (binder jetting)	100 μm	starch, PLA, ceramics	quick; allows multi-material	low resolution; limited materials; high anisotropy
Laminated Object Manufacturing	200–300 μm	PVC, paper	compact desktop 3D printer	limited materials; low resolution; high anisotropy
Material Extrusion	100–150 μm	ABS, PLA, PC, HIPS	inexpensive machines and materials	low mechanical strength; rough surfaces
Fused Deposition Modeling				
3D dispensing	100μm-1 cm	thermoplastics, composites	broad range of materials	rough surfaces; narrow viscosity process window

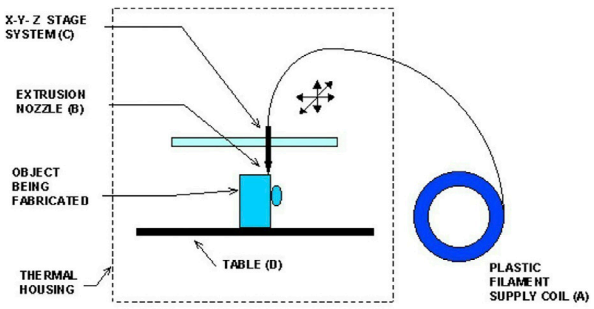

FIGURE 2
The popular FFF procedure uses an X-Y-Z-mobile extrusion head to apply thermoplastic lines. Copyright 2014, American Chemical Society.

in the majority of SLS applications is made of thermoplastic polymers, especially different types of polyamide like PA11 and PA12 (Hofmann, 2014). The third technique is called material jetting, in which UV crosslinking is employed to selectively deposit viscous droplets of photopolymers (Udroiu et al., 2019). Material extrusion is the final significant additive manufacturing technique (Schirmeister et al., 2019). This technique is based on the original fused filament manufacturing (FFF) process and relies on a simple design using thermoplastic materials that appear to be essentially industry standard. (Li et al., 2020). The idea of melting a "typical" plastic product and extruding it *via* a narrow, heated nozzle seems to be quite straightforward as shown in the schematic of Figure 2 (Hofmann, 2014). This allows the extruded melt to deposit in the X-Y control motion of the anterior layer of the manufactured element (Rashid, 2019).

Additive manufacturing technology plays an important role in meeting the needs of individual production, overcoming many of the long-standing limitations of traditional processes. However, the technology still has certain shortcomings. For example, models printed with ABS or PET have rough details and poor fineness (Fu et al., 2021). Multiple material substitution combinations are required to produce fine print details. In addition, the SLS powder sintering process requires additional curing of the printed object; otherwise, it tends to cause liquid absorption and staining of the porous surface Wang et al. (2020b). Due to the limitations of material properties, additive manufacturing is still unable to accurately replace real products and remains more at the stage of simulating products. On the other hand, additive manufacturing is not very efficient. For the 3D printers commonly used in the market, a three-dimensional plastic model the size of a puck requires 28 h (Stansbury and Idacavage, 2016) of continuous machine work. The development of lightweight thermoplastic polymer foams enables researchers to quickly print small-scale parts before expanding them. An innovative and creative manufacturing process is created by the successful combination of polymer foaming with additive manufacturing, and thermoplastic polymer foam can be produced by SLA (Wirth et al., 2020), FFF and direct ink

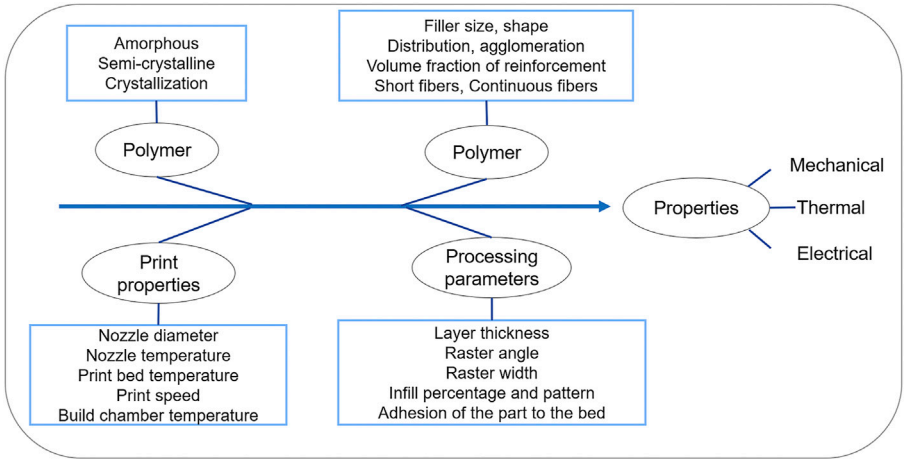

FIGURE 3
Several factors that influence the characteristics of FFF printed items.

writing (Chen et al. (2018a), 2019), etc. Of these combined foaming processes, the SLA process is available for fewer materials because it requires a higher cure rate. In addition, SLA relies on the combination of cured polymers with soluble components for post-processing to form honeycomb structures (Wirth et al., 2020). In contrast, the FFF process is well suited to thermoplastic foams due to its low system cost, wide material selection, and improved toughness. The FFF technologies will be highlighted in this review.

2.1.2 Introduction and application of fused filament manufacturing

Since Scott Crump created fused deposition modeling (FDM) and received a patent for it in 1989, the term "fused filament fabrication" (FFF) is widely used as a replacement (Schmitt et al., 2017). A fusion of thermoplastic material is extruded from the nozzle by heating and then the material is selectively printed on the platform according to the predetermined trajectory of the model slice (Zhang et al., 2020). The raw material, which is targeted at the inside of the hot-end, is bought on reels of filament with a 1.75 or 3 mm diameter (Eltorai et al., 2015). For amorphous or semi-crystalline polymers, the extruder is heated to a polymer-appropriate process temperature, which is either above the glass or melting temperature for semi-crystalline polymers (Nadiyapara and Pande, 2017). For a successful construction procedure, the CAD geometry parameters for a particular filament, build speed, processing temperature, and polymer melt rheology must all be carefully balanced (Pérez et al., 2018). The various elements that affect the performance of FFF printers are graphically represented in Figure 3. On the other hand, there are many challenges in implementing the FFF process to achieve thermoplastic foaming. Since it is printed in one piece, the structure used for support may also be embedded inside the model during the printing process and cannot be removed. At the same time, human manipulation can lead to warping, deformation, etc. Hwang et al. effectively solves the deformation problem due to the thermal expansion of the material by embedding metal particles into the polymer (Hwang et al., 2015). In addition to the control of deformation problems, Kokkinis et al. developed a magnetically assisted 3D printing platform in terms of workpiece anisotropy (Kokkinis et al., 2015). They achieved particle orientation control by adding magnetized aluminum platelets to a polymer matrix. Owing to the arrangement of anisotropic particles, the target performance of the workpiece in a specific direction was improved (Liu et al., 2022). Another problem with the FFF process is that the printed part contains a certain amount of porosity that can adversely affect the final mechanical properties (Kakumanu and Srinivas Sundarram, 2018). Even though the technology can achieve high precision in theory, it is still very difficult to manufacture in practice.

Because it can print objects made of various material types and then alter the print substance, FFF has the obvious benefit of allowing for more users control over device manufacturing for experimental applications (Weng et al., 2016). FFF is used as a tool for bioengineering tissue, with components ranging from bones or teeth to blood vessels or organ scaffolding. FFF is being used in a multitude of ways in the building industry (Zhang et al., 2021). In contrast to complicated geometries, FFF provides design freedom that aids in the optimization of design models that enable higher functional integration and lower material waste. Biomimetic actuators, such as worm-like and flower-like actuators, are examples of intricate magnetic actuators with complex topologies. FFF has been successfully applied to these actuators (Qi et al., 2020). In conclusion, additive manufacturing is becoming increasingly prevalent outside of

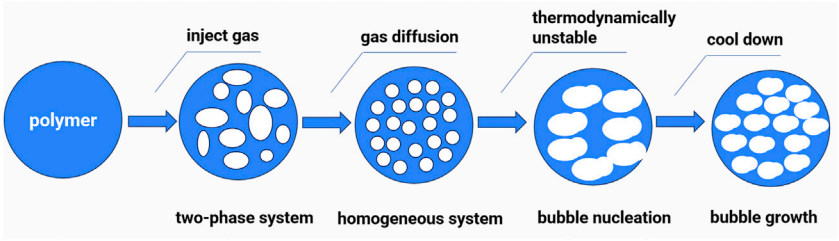

FIGURE 4
Polymer molding foaming process.

specialized industries and is currently used in a variety of fields, including lightweight engineering, energy technology, pharmaceuticals and even food production. It performs significantly more than just its conventional role in rapid prototyping, rapid tooling, and concept modeling (Gross et al., 2014).

2.2 Foaming

2.2.1 Foaming and foaming mechanism in polymers

The concept of polymer foams was originally proposed in the hope of introducing a large number of voids into the polymer matrix that were smaller than the defects already existed in the polymer. Therefore, the rigidity of the product can be improved while the quality of the product is reduced, and other properties such as strength are not significantly affected. Polymer foam materials, as compared to non-foamed materials, have certain good qualities like high impact strength, extended fatigue life, high toughness (Zhai et al., 2022), strong thermal stability (Wicklein et al., 2015; Hu et al., 2019), low thermal conductivity (Ji et al., 2013) and dielectric constant (Wu et al., 2013), etc. Polymeric foams can be generated using a variety of techniques, including physical blowing agents (PBA) (Sauceau et al., 2011; Zhai et al., 2022) and chemical blowing agents (CBA) (Sadik et al., 2018). Thermally expandable microspheres (TEMs) (Diani and Gall, 2006; Peng et al., 2013; Zhang et al., 2019) have received increasing attention as a type of PBA. The polymer foam molding process generally includes three basic stages: the formation stage of the polymer/gas homogeneous system; the nucleation stage of the bubbles; and the growth and shaping stage of the cells, as shown in Figure 4. At first, the gas diffuses and disperses into the polymer under specific conditions, and after a certain time it reaches thermodynamic equilibrium to form a homogeneous system; changing the temperature or pressure causes the gas solubility in the homogeneous system to drop quickly, resulting in a supersaturated state. Numerous microscopic bubbles are generated in the system as it tends to revert to a low-energy steady state. The system's pressure differential between the inner and outer the bubbles increases as the system's gas solubility is further reduced, which causes the bubbles to grow and expand. Afterward, the system is cooled and shaped to take on the final cell shape and structure.

2.2.2 Polymer foam technology

In order to manufacture polymer foam materials, the foam molding process can be separated into batch autoclave foaming (Yeh et al., 2017), continuous extrusion foaming (Lee et al., 2008; Sauceau et al., 2011), and injection molding foaming (Ameli et al., 2014; Villamil Jiménez et al., 2020), depending on the degree of continuous operation. Table 2 lists the various foaming techniques in alphabetical order. Batch autoclave foaming is typically performed in a high-pressure reactor, which provides the sample being foamed with a specific high temperature and high pressure airtight environment, allowing gases like CO_2 and N_2 to gradually diffuse and dissolve into the polymer matrix. Cell nucleation develops and finally takes shape as the thermodynamic conditions change. Anson Wong (Wong et al., 2011) and colleagues examined the foaming behavior of semi-crystalline polymers and discovered that samples using the Wessling method, including HDPE, PP, and PET, showed varying degrees of crystallization. They discovered that the dissolution slope reduced as crystallinity increased. This indicates that the amorphous area of the polymer is the sole place where adsorption takes place. Due to the semi-continuous foaming process, the diffusion of the gas in the polymer matrix can take place at a much higher rate and efficiency (Yu et al., 2015). Kuma et al. (Kumar et al., 2000) proposed a method for producing solid-phase PET foamed sheets using a semi-continuous method in response to the drawbacks of discontinuous methods for producing polymeric micro-foam materials. After the gas had been saturated, the separator layer was removed with a heating device and then foamed. The last foaming technology is continuous foaming, which is currently the most popular polymer foaming technology (Rizvi et al., 2018; Li et al., 2021; Gunasekaran et al., 2022a). Supercritical CO_2 can significantly reduce the time required for polymers to reach

TABLE 2 The properties of different foaming techniques.

Techniques	Foaming technology	Phase of polymer while foaming	Melt strength of polymer	Cell morphology	Expansion	Notes
Batch process	bead foaming	high-elastic phase	high; hard segment improves melt strength	uniform and closed cell structure	high	beads made of elastomers not crosslinked
	compression molding foaming		improves melt strength		high	elastomer plates or sheets
	carbon dioxide autoclaves foaming		high			N_2 is another option of PBA; rubbers or elastomers must be crosslinked
Semi-continuous process	injection molding foaming (Mucell process)	melt phase	low	presence of open-cells	low	extension of the chain is required to increase foamability
	injection molding foaming (core-back process)	melt state high-elastic phase	relatively high	uniform with open-cells present	high	extension of the chain is required to increase foam expansion ratio
Continuous process	extrusion foaming	melt phase	low	poor cell morphology with open-cells present	low	extension of the chain is required to increase foamability
	extrusion foaming with underwater granulator	melt phase	low	uniform with open-cells present	high	extension of the chain is required to increase foam expansion ratio

saturation, allowing for the production of microporous polymers in an industrial environment (Yeh et al., 2017; Hu et al., 2021). Therefore, it is imperative to provide a continuous preparation technology for micro-foamed materials based on established plastic processing techniques like extrusion (Nofar, 2016; Rizvi et al., 2018) and injection molding (Jahani et al., 2014, 2015; Contreras et al., 2020).

3 Approaches to generating cellular structures through additive manufacturing

When solids are converted into cellular materials, their single-valued qualities are enlarged (Ashby, 2006). Properties include stiffness, strength, thermal conductivity and diffusivity, electrical resistivity, (Wang et al. 2(2020a); Nofar et al., 2022) all of which have numerous potential applications in the areas of personal thermal management (Hu et al., 2020; Zhou and Hsieh, 2020), IR stealth (Ahn et al., 2019), superhydrophobic surfaces (Wu et al., 2020), and sensors (Hu et al., 2020). Performance is significantly influenced by density and honeycomb structure in addition to the polymer matrix. Compared to conventional production techniques, additive manufacturing offers unprecedented flexibility in achieving controlled structure, geometric characteristics, feature, and complexity (Kim and Oh, 2008). Conventional foams have a random distribution of porosity throughout, inspired by the topology of natural honeycomb structures. Structures found in bone and wood, for example, where the solids and voids are organized in accordance with the load-bearing requirements (Jiang et al., 2020). First, it should be noted that additive manufacturing utilizes two distinct forms of porosity. When building the structure layer by layer, there are still certain voids without polymer deposition even when the filler content is set to 100% (Nofar et al., 2022). However, porosity can also be used to create certain honeycomb structures. The porosity parameter generated in this manner is controversial and even considered as a drawback in studies. Specific pore types can carry out specialized tasks like sound and thermal insulation. Regular porous scaffolds, such as cellular structures Chen et al. (2018b), truss-based lattices (Rehme, 2010), octahedron and rhombicuboctahedron structures (Liu et al., 2017), and surface based lattices like gyroid or diamond structures (Maskery et al., 2018) are the main focus of additive manufacturing research. To date, the following methods have been documented for generating cellular structures by additive manufacturing (FFF printing technology): 1) cellular scaffolds; 2) composite printing foam; 3) post-foaming of printed solid scaffolds; 4) *in-situ* foam 3D printing. Of course, there are many challenges in implementing thermoplastic foams using the FFF process. Pre-foaming must use foamed filament as the raw material for additive manufacturing, limiting the range of honeycomb mesh structures that can be obtained and also risking loss of structure during the printing process (Kuang et al., 2017). Complex post-processing stages, high pressure-reducing device requirements,

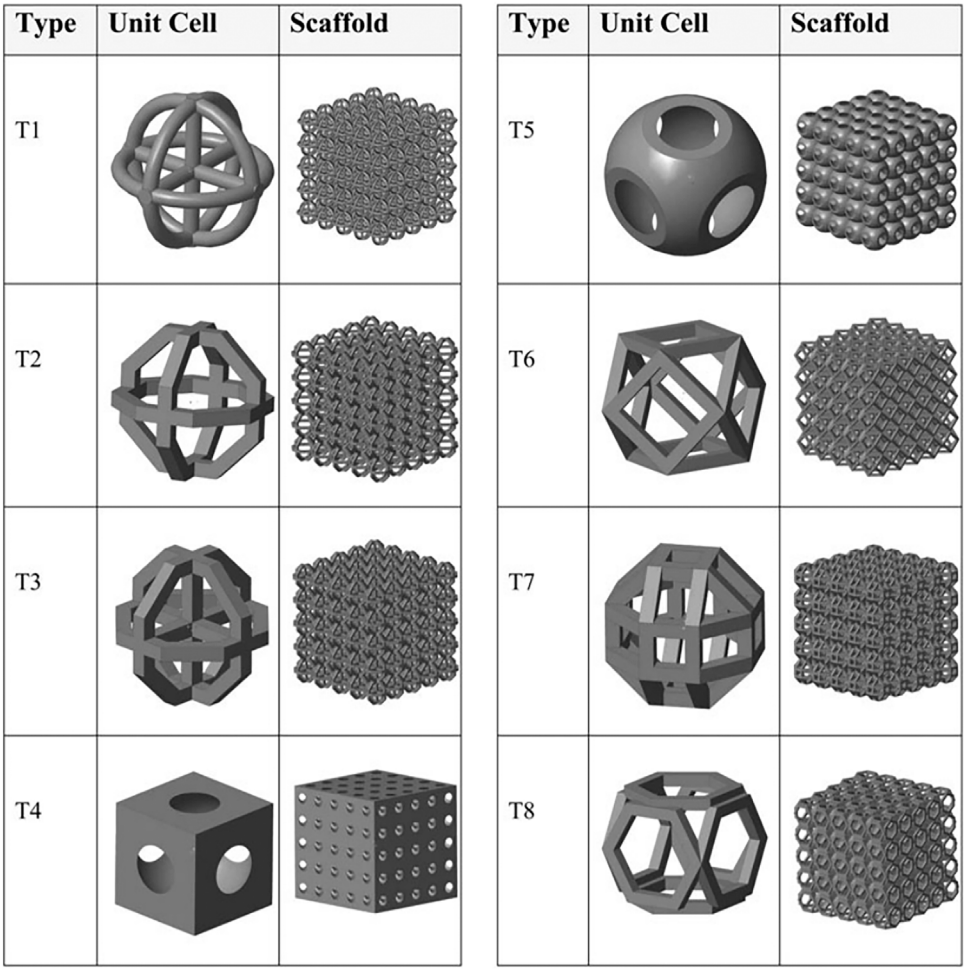

FIGURE 5
Models of all (eight) types of unit cells and scaffolds. Copyright 2016, Mary Ann Liebert. Inc.

and limited expansion may be problems for post-foaming methods, which retouch the item after printing (Zhai et al., 2022). *In-situ* foaming, on the other hand, is the most recent approach that matches the foaming and fused filament fabrication processes flawlessly. However, obtaining an uniform and stable polymer or gas solution *via* the foaming agent during the material extrusion process is difficult. The approach may result in inhomogeneous cell nucleation, poor vesicle density, uneven cell structure, and other problems. Below, we detail the particular material molding process.

3.1 Cellular scaffolds

Cellular scaffolds designed by conventional manufacturing methods (Yang et al., 2001) have a single type of pore unit, and most of them can only make coarse adjustments to individual parameters such as porosity and pore size (Jia et al., 2020; Jiang et al., 2020). The internal microscopic honeycomb structure of the forming scaffold is random, and the pores are not completely connected, which cannot meet the actual needs. FFF printing technology applied to cellular scaffolds assembly can not only precisely control the spatial structure distribution of the scaffold, but also effectively control the functional gradient of the scaffold material, thus enabling the engineering of scaffold manufacturing. On the other hand, the construction of honeycomb structures by layer-by-layer printing is different from the traditional foaming process. In terms of mechanical qualities and accessible active surfaces, hierarchical cellular scaffolds perform better than their non-hierarchical counterparts. This is due to hierarchical cellular scaffolds are highly heterogeneous at mesoscale in geometry and porosity distribution, with coupling effect among cells (Wang et al., 2018; Yin et al., 2023).The FFF method may produce a variety of

random and ordered geometries. The resulting scaffold topology can then be used to modify the unit cell units, as shown in Figure 5, to alter the overall quality of the completed project (Habib et al., 2016). In this instance, the specified geometry, unit cell components, and their structures can be used to modify the mechanical characteristics of this structured cellular structure (Pajunen et al., 2019). By employing additive manufacturing, two-dimensional (2D) and three-dimensional (3D) architectures of composite have been created to investigate the impact of unit cell connection and geometry on mechanical properties. Sirui Bi et al. synthesized brittle foams with regulated morphological properties and conducted an array of tests to gauge the compressive response and strength of 3D printed foams (Bi et al., 2020).

Highly porous scaffold materials are required for tissue engineering (TE)with the aim of accommodating and directing proliferation, regeneration, and development of cells in three dimensions (Habib et al., 2016). Polymeric materials have shown strong competitiveness in cellular scaffolds, such as polyethylene glycol (PEG) (Liang et al., 2022), poly (L-lactic acid) (PLLA) (Kuang et al., 2017), polyglycolic acid (PGA) (Yang et al., 2001), polycaprolactone (PCL) and their copolymers (Cho et al., 2019). Porous scaffolds prepared from these synthetic polymers have biocompatible, high porosity and interconnected pores that allow for the accommodation of large numbers of cells in these pores (Melchels et al., 2010). FFF printing technology is used to create personalized TE scaffold materials and can even carry cells for *in situ* cell printing on tissue defect sites. Insoles for the treatment of diabetes also benefit from an optimized porous structure. The design with a variable gradient modulus enhances the contact stress between the foot and the insole to avoid ulceration. (Ma et al., 2019). However, a significant barrier to the therapeutic use of 3D printed cellular structures is the realization of tissue heterogeneity through the controlled distribution of various cell and biomaterial types at the micro- and macro-scales (Fang et al., 2022). All in all, it could be stated that the main objective of 3D printed cellular structures is novel functional integration, which can be precisely accomplished by regulating the important characteristics of unit cells (Nofar et al., 2022).

3.2 Composite printing foam

3D printing of polymer composites addresses these issues by combining the polymer matrix and nanomaterial reinforcements to generate a society with more valuable structural and functional features than either of the constituents could achieve on their own (Thomas et al., 2019).These reinforcements are usually denser and can be incorporated directly into the polymer matrix to form porous structures (Patil et al., 2019; Bharath et al., 2020; Bonthu et al., 2020).The development of polymer matrix composites, which have great mechanical performance and outstanding functionality, is made feasible by adding

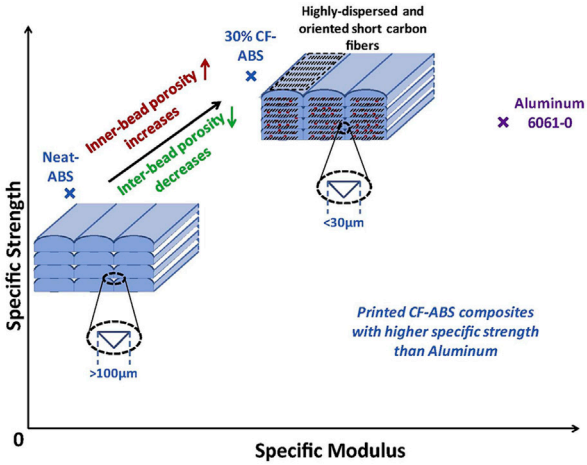

FIGURE 6
Schematic diagram of 3D-printed fiber-reinforced composite by Fused Filament Fabrication. Copyright 2014, Elsevier.

reinforcements to polymers in the form of fibers, particles or nanomaterials (Wang et al., 2017). Porosity and fiber orientation of composites have a considerable impact on the properties of final composite products (Patil et al., 2019). The short fiber (0.2–0.4 mm) reinforced acrylonitrile–butadiene–styrene composite made by FFF printing composite foam is depicted in Figure 6 (Tekinalp et al., 2014). Printed composite foams had relatively higher porosity than composites made by traditional compression molding (CE), but their tensile strength and modulus were comparable. The purpose of this research is to develop a compression molding-based manufacturing technique for glass micro-balloon/high density polyethylene (GMB/HDPE) syntactic foams (Jayavardhan et al., 2017) while examining their mechanical characteristics in order to establish correlations between structures and features. They claimed that the entrapped hollow spheres were retained in the produced filaments as well as in the 3D printed samples (Jayavardhan et al., 2017; Bonthu et al., 2020).As the Figure 7 shows, particle fracture increases with increasing GMB content due to increased particle-to-particle interaction during processing and a higher breakdown of GMB is seen in the syntactic foam developed at a higher screw speed. M. Doddamani et al. generated three distinct volume fractions of GMB particles with varying wall thicknesses 20%, 40%, and 60% (particle density variations) (Doddamani, 2019). When compared to HDPE matrix resin, storage modulus, loss modulus, and damping are seen to increase with particle wall thickness and volume fraction. When these composite foams are combined, they often allow for the tailoring of properties in two dimensions (i.e., wall thickness and volume fraction modification), providing versatility in creating materials for a wide variety of purposes.

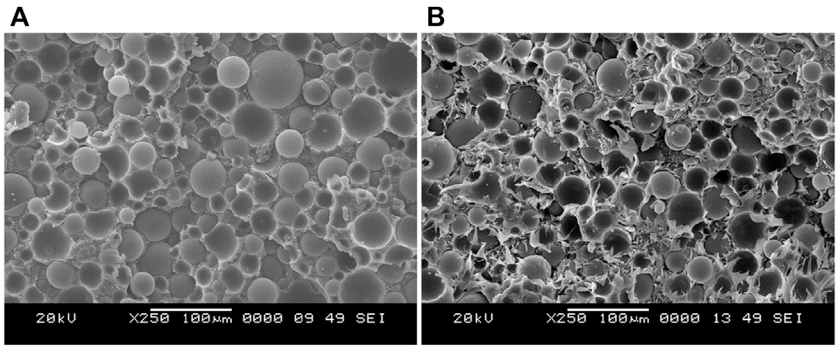

FIGURE 7
SEM image of H200-60 syntactic foam that has been formed and frozen and was taken at the same magnifications for **(A)** 10 and **(B)** 40 rpm screw rotation Copyright 2017, Elsevier.

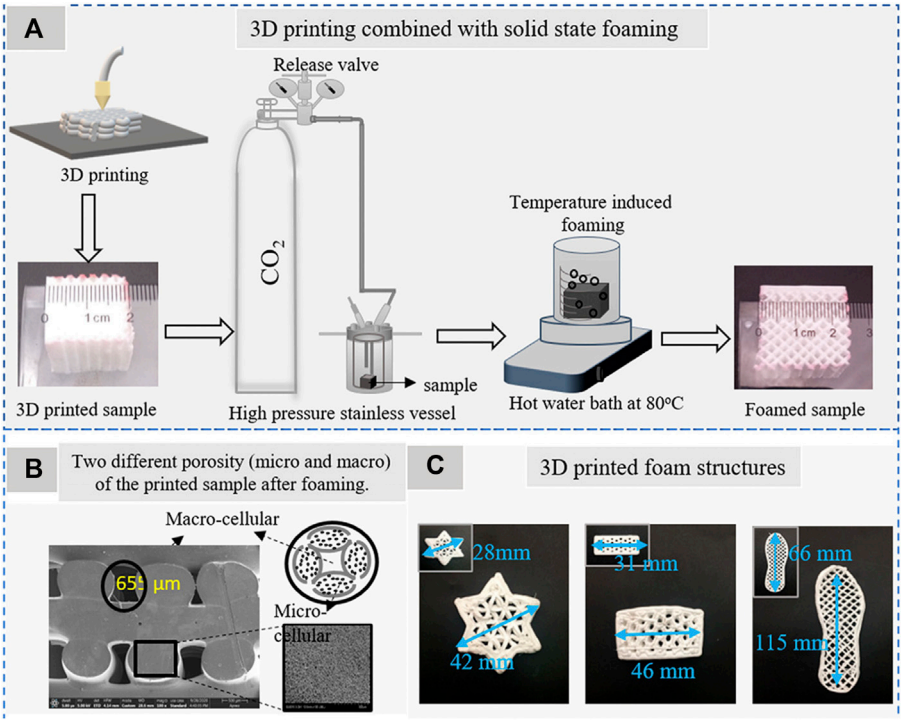

FIGURE 8
(A) Schematic presentation of the 3D printing combined CO_2 solid-state foaming process. **(B)** Two different porosities of the printed sample. **(C)** 3D printed foamed sample with different structures. Copyright 2022, American Chemical Society.

3.3 Post-foaming of printed solid scaffolds

FFF printing technology in combination with gas foaming technology was used to construct a recently created solid scaffold with a precise microstructure of about 10 µm (Zhou et al., 2016). The sample is first 3D printed using FFF in this process, and then a porous structure is created in the sample using the gas foaming technique. By trimming and cutting stages in the post-processing of the foam, this method of printing cellular foam with post-foaming in conjunction with additive manufacturing plays an important role in decreasing the traditional supercritical gas foaming phase and minimizing material waste. Figure 8 shows the rapid CO_2 foaming process of 3D printed thermoplastic polyurethane elastomer developed by our research group

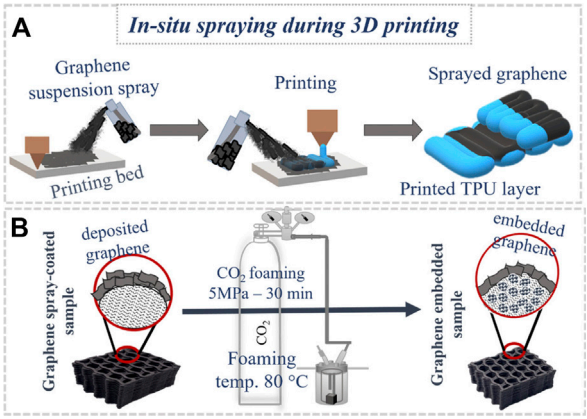

FIGURE 9
(A) Fabrication process of the in situ spray-coated 3D printed sensor. **(B)** Graphene embedding and microporous generation. Copyright 2022, American Chemical Society.

(Gunasekaran et al., 2022a). In this work, the foaming behavior of printed TPU elastomers with three different hardness values was examined. The resulting foam samples can be used for high-end applications, such as shoe bottoms, which conventional foaming cannot provide (Gunasekaran et al., 2022a). Additionally, compared to their un-foamed counterparts, microcellular TPU honeycombs showed greater elasticity and better elastic recovery (Hu et al., 2021). The foam produced through the post-foaming route also differs from prefabricated structures in terms of its properties. For example, the foaming technique produces a low mass density and high sensitivity sensor in addition to creating a conductive network on the surface and interface of the printing system. Figure 9 (Gunasekaran et al., 2022b) depicts the conductive TPU foam's assembly procedure. Our research has shown that adding graphene sensors directly to the surface of TPU has a limited impact, and that foaming creates a microporous structure that helps embed graphene and create a conductive network.

3.4 *In-Situ* foam 3D printing

In-situ foam 3D printing is the technique that properly merges the foaming and fused filament fabrication processes. Despite in the early stages of study and not yet fully established, this foam 3D printing technique appears to be the most successful way to produce foamed printed structures (Nofar et al., 2022). There are now two proven techniques for *in-situ* foam 3D printing, with the key distinction being whether a single-phase polymer or a gaseous solution is reached before cell nucleation and growth (Kalia et al., 2022). Unexpanded filaments containing blowing agents, either physical or chemical blowing agents, are prepared in the first technique. Thermally expandable microspheres (TEMs) can be used to 3D print *in-situ* foam without the need for extra gas impregnation (Cai et al., 2021). TEM has also been found to provide a more homogeneous porous structure in conventional foam operations like as extrusion and injection molding when compared to alternative foaming techniques (Peng et al., 2013; Kmetty and Litauszki, 2020). This method may be able to address the aforementioned difficulties without the need for any extra preprocessing, postprocessing, or specialized 3D printing equipment (Contreras et al., 2020). In a recent study, Andersson et al. (2021) looked into the mechanical strength, micromorphology of *in situ* foam 3D printed using PLA and TEM-ethylene vinyl acetate masterbatch. However, the reported foams had substantial differences in densities, brittleness, and rough surfaces, which can be related to the formulation of the material as well as the lack of homogeneous TEM dispersion (Andersson et al., 2021). They also showed nonuniform cellular architecture.

In addition, the second *in-situ* foaming method involves foaming the extruded filament by means of an external CO_2 gas. The filament exits the nozzle during printing, and foam expands as a result of changes in the thermodynamics. As shown in Figure 10, Li et al. (2020) reported using polyetherimide and polylactic acid (PLA) filaments to manufacture hierarchical porous portions that were impregnated with CO_2 gas. Zhang et al. (2022) offered a simple solution by combining 3D FFF printing with supercritical microcellular foaming to address the primary obstacle for tissue-engineering scaffolds with hierarchical topologies. As seen Figure 11 (Zhang et al., 2022), the flexibility of additive manufacturing design results in pores are larger than microns due to layer stacking, whereas microcellular structures result in pores smaller than microns due to foaming. *In-situ* foam 3D printing requires an additional stage of gas impregnation before printing and the gas-saturated filaments commence to release gas as soon as they are removed from the high-pressure chamber, which is one of its biggest advantages. As a result, the first barrier is generating a homogeneous polymer matrix from a physical blowing agent, and the second barrier is handling and printing filaments that have been impregnated with gas.

To avoid the issues of low melt strength, poor foam expansion ratio, low cell density, and uneven shape of big cells caused by the use of gaseous or chemical blowing agents, special printer systems or pretreatment processes need to be developed. (Damanpack et al., 2021). As shown in Figure 12, PLA was employed as the feedstock material along with a polyethylene carrier, two weight percent triethyl citrate (TEC) plasticizer, and zero to five weight percent acrylonitrile-based TEM (Kalia et al., 2022). An improved extrusion procedure was used to create the unexpanded filaments, and then a commercially available printer was used to 3D print foam in place (Kalia et al., 2022). The degree of foam densities and TEM content was connected with the microstructure, cellular morphology, density, thermal and mechanical properties of the printed foams.

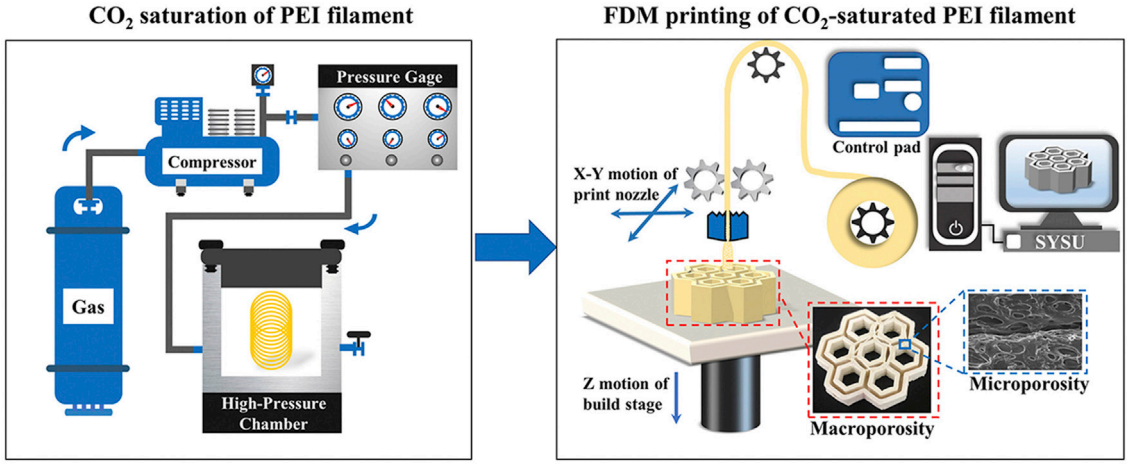

FIGURE 10
Diagram of the CO2-saturated PEI filament's FFF printing process. Copyright 2020, Elsevier.

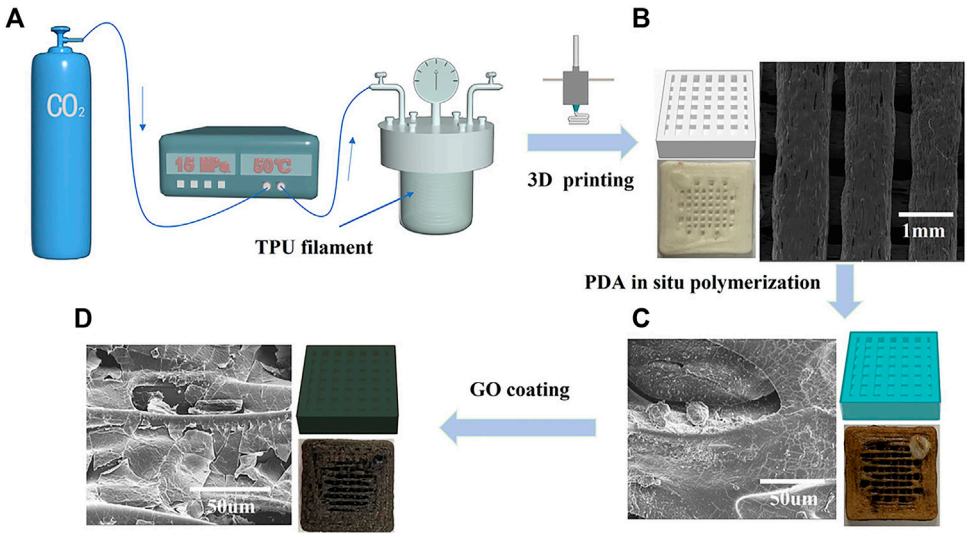

FIGURE 11
Schematic illustration of the fabrication for FFF printed TPU scaffold with microcellular foaming and surface coating with graphene oxide. Copyright 2022, Wiley-VCH.

4 Summary and trends in 3D printing foams

Overall, the combination of additive printing with polymer foam opens up new possibilities for the production of lightweight goods with complex structures and hierarchical features. Depending on the shape of the created foamed part, we can also classify the first two processes as pre-foaming, the third as post-foaming, and the final as *in-situ* foaming. Pre-foaming must use foamed filament as the raw material for additive manufacturing, limiting the range of honeycomb mesh structures that can be obtained and also risking loss of structure during the printing process. Complex post-processing stages, high pressure-reducing device requirements, and limited expansion may be problems for post-foaming methods, which retouch the parts after printing. On the other hand, *in-situ* foaming is the latest approach that matches perfectly with foaming and FFF process. However, obtaining a homogeneous and stable polymer/gas solution *via* the foaming agent during the material extrusion process is difficult. The

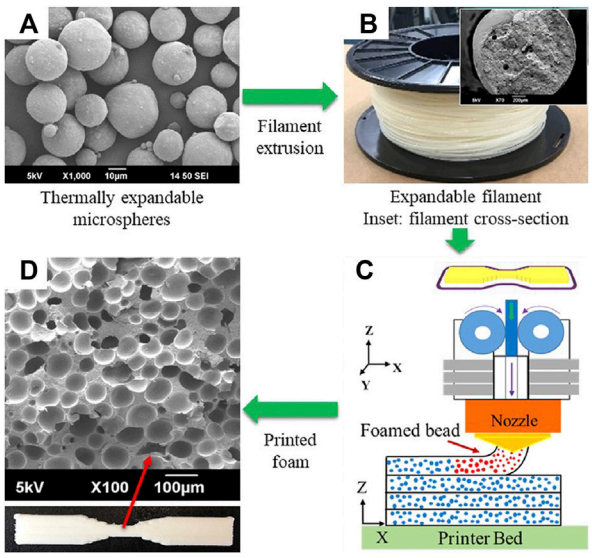

FIGURE 12
Overview of the in situ foam 3D-printing process: **(A)** TEM particles as blowing agents, **(B)** extruded expandable filament with an inset SEM micrograph showing its cross-sectional view, **(C)** part design and schematic of the in situ foam printing process, and **(D)** example of the printed tensile sample with a SEM micrograph showing the microcellular morphology in the Y-Z plane. Copyright 2022, American Chemical Society.

approach may result in inhomogeneous cell nucleation, poor vesicle density, uneven cell structure, and other problems.

The problems that arise in the use of gas or chemical blowing agents can be avoided by developing special printer systems or pretreatment processes. However, the current 3D printing foaming still has many shortcomings and defects, and the future direction of development may focus on the development of filament-free method by free-form technology. Establishing parallel strategies for thermoplastic printing and foaming to overcome the limitations of thermoplastic material selection, uncertainties caused by inhomogeneous dissolution of foaming agents. This method eliminates the manufacturing process of filaments and injects the foaming agent directly into the extruder barrel, thus achieving the integration of extrusion foaming and foaming injection molding.

Author contributions

LW: Funding acquisition, conceptualization, reviewing, project administration. BS: Methodology, literature search and sorting, writing.

Funding

This work is supported by Ningbo public welfare science and technology planning project (Grant No: 2022S099), the STS Project of Fujian-CAS (Grant Nos: 2021T3039, 2021T3047, 2021T3018, 2022T3009, 2022T3019, 2022T3045, 2022T3064), the regional development project of Fujian (Grant No: 2022H4020),the STS Project of Putian-CAS (Grant No: 2020HJST009) and the Major Project of Science and Technology in Fuzhou (Grant No: 2021-ZD-281), the project of Fujian Market Supervision Administration (Grant No: FJMS2021023).

Conflict of interest

The authors declare that the research was conducted in the absence of any commercial or financial relationships that could be construed as a potential conflict of interest.

Publisher's note

All claims expressed in this article are solely those of the authors and do not necessarily represent those of their affiliated organizations, or those of the publisher, the editors and the reviewers. Any product that may be evaluated in this article, or claim that may be made by its manufacturer, is not guaranteed or endorsed by the publisher.

References

Ahn, J., Lim, T., Yeo, C. S., Hong, T., Jeong, S. M., Park, S. Y., et al. (2019). Infrared invisibility cloak based on polyurethane-tin oxide composite microtubes. *ACS Appl. Mat. Interfaces* 11, 14296–14304. doi:10.1021/acsami.8b22535

Ameli, A., Jahani, D., Nofar, M., Jung, P. U., and Park, C. B. (2014). Development of high void fraction polylactide composite foams using injection molding: Mechanical and thermal insulation properties. *Compos. Sci. Technol.* 90, 88–95. doi:10.1016/j.compscitech.2013.10.019

Andersson, H., Örtegren, J., Zhang, R., Grauers, M., and Olin, H. (2021). Variable low-density polylactic acid and microsphere composite material for additive manufacturing. *Addit. Manuf.* 40, 101925. doi:10.1016/j.addma.2021.101925

Ashby, M. F. (2006). The properties of foams and lattices. *Phil. Trans. R. Soc. A* 364, 15–30. doi:10.1098/rsta.2005.1678

Attaran, M. (2017). The rise of 3-D printing: The advantages of additive manufacturing over traditional manufacturing. *Bus. Horiz.* 60, 677–688. doi:10.1016/j.bushor.2017.05.011

Bharath, H. S., Sawardekar, A., Waddar, S., Jeyaraj, P., and Doddamani, M. (2020). Mechanical behavior of 3D printed syntactic foam composites. *Compos. Struct.* 254, 112832. doi:10.1016/j.compstruct.2020.112832

Bi, S., Chen, E., and Gaitanaros, S. (2020). Additive manufacturing and characterization of brittle foams. *Mech. Mat.* 145, 103368. doi:10.1016/j.mechmat.2020.103368

Bonthu, D., Bharath, H. S., Gururaja, S., Prabhakar, P., and Doddamani, M. (2020). 3D printing of syntactic foam cored sandwich composite. *Compos. Part C. Open Access* 3, 100068. doi:10.1016/j.jcomc.2020.100068

Borrello, J., Nasser, P., Iatridis, J. C., and Costa, K. D. (2018). 3D printing a mechanically-tunable acrylate resin on a commercial DLP-SLA printer. *Addit. Manuf.* 23, 374–380. doi:10.1016/j.addma.2018.08.019

Cai, J. H., Huang, M. L., Chen, X. D., and Wang, M. (2021). Thermo-expandable microspheres strengthened polydimethylsiloxane foam with unique softening behavior and high-efficient energy absorption. *Appl. Surf. Sci.* 540, 148364. doi:10.1016/j.apsusc.2020.148364

Chen, Q., Cao, P. F., and Advincula, R. C. (2018a). Mechanically robust, ultraelastic hierarchical foam with tunable properties via 3D printing. *Adv. Funct. Mat.* 28, 1800631–1800639. doi:10.1002/adfm.201800631

Chen, Q., Zhao, J., Ren, J., Rong, L., Cao, P. F., and Advincula, R. C. (2019). 3D printed multifunctional, hyperelastic silicone rubber foam. *Adv. Funct. Mat.* 29, 1900469–9. doi:10.1002/adfm.201900469

Chen, Y., Li, T., Jia, Z., Scarpa, F., Yao, C. W., and Wang, L. (2018b). 3D printed hierarchical honeycombs with shape integrity under large compressive deformations. *Mat. Des.* 137, 226–234. doi:10.1016/j.matdes.2017.10.028

Cho, Y. S., Choi, S., Lee, S. H., Kim, K. K., and Cho, Y. S. (2019). Assessments of polycaprolactone/hydroxyapatite composite scaffold with enhanced biomimetic mineralization by exposure to hydroxyapatite via a 3D-printing system and alkaline erosion. *Eur. Polym. J.* 113, 340–348. doi:10.1016/j.eurpolymj.2019.02.006

Contreras, V., Maturana, F. J., Poveda, J., Núñez, K. C., Merino, J. C., and Pastor, J. M. (2020). Optimization of injection parameters to obtain selected properties on foamed PP with hollow glass microspheres and thermally expandable microspheres using Taguchi method. *J. Cell. Plast.* 54, 313–327. doi:10.1177/0021955X20943097

Costeux, S. (2014). CO 2 -blown nanocellular foams. *J. Appl. Polym. Sci.* 131. doi:10.1002/app.41293

Credi, C., Fiorese, A., Tironi, M., Bernasconi, R., Magagnin, L., Levi, M., et al. (2016). 3D printing of cantilever-type microstructures by stereolithography of ferromagnetic photopolymers. *ACS Appl. Mat. Interfaces* 8, 26332–26342. doi:10.1021/acsami.6b08880

Damanpack, A. R., Sousa, A., and Bodaghi, M. (2021). Porous plas with controllable density by fdm 3d printing and chemical foaming agent. *Micromachines* 12, 866–868. doi:10.3390/mi12080866

Di Maio, E., and Kiran, E. (2018). Foaming of polymers with supercritical fluids and perspectives on the current knowledge gaps and challenges. *J. Supercrit. Fluids* 134, 157–166. doi:10.1016/j.supflu.2017.11.013

Diani, J., and Gall, K. (2006). Finite strain 3D thermoviscoelastic constitutive model. *Society* 46, 1–10. doi:10.1002/pen.20497

Doddamani, M. (2019). Influence of microballoon wall thickness on dynamic mechanical analysis of closed cell foams. *Mat. Res. Express* 6, 125348. doi:10.1088/2053-1591/ab62f4

Eltorai, A. E. M., Nguyen, E., and Daniels, A. H. (2015). Three-dimensional printing in orthopedic surgery. *Orthopedics* 38, 684–687. doi:10.3928/01477447-20151016-05

Fang, Y., Guo, Y., Liu, T., Xu, R., Mao, S., Mo, X., et al. (2022). Advances in 3D bioprinting. *Chin. J. Mech. Eng. Addit. Manuf. Front.* 1, 100011. doi:10.1016/j.cjmeam.2022.100011

Felzmann, B. R., Gruber, S., Mitteramskogler, G., Tesavibul, P., Boccaccini, A. R., Liska, R., et al. (2012). Lithography-based additive manufacturing of cellular ceramic structures. *Adv. Eng. Mat.* 14, 1052–1058. doi:10.1002/adem.201200010

Forest, C., Chaumont, P., Cassagnau, P., Swoboda, B., and Sonntag, P. (2015). Polymer nano-foams for insulating applications prepared from CO2 foaming. *Prog. Polym. Sci.* 41, 122–145. doi:10.1016/j.progpolymsci.2014.07.001

Franchin, G., Elsayed, H., Botti, R., Huang, K., Schmidt, J., Giometti, G., et al. (2022). Additive manufacturing of ceramics from liquid feedstocks. *Chin. J. Mech. Eng. Addit. Manuf. Front.* 1, 100012. doi:10.1016/j.cjmeam.2022.100012

Fu, Y., Downey, A., Yuan, L., Pratt, A., and Balogun, Y. (2021). *In situ* monitoring for fused filament fabrication process: A review. *Addit. Manuf.* 38, 101749. doi:10.1016/j.addma.2020.101749

Gross, B. C., Erkal, J. L., Lockwood, S. Y., Chen, C., and Spence, D. M. (2014). Evaluation of 3D printing and its potential impact on biotechnology and the chemical sciences. *Anal. Chem.* 86, 3240–3253. doi:10.1021/ac403397r

Gunasekaran, H. B., Ponnan, S., Thirunavukkarasu, N., Laroui, A., Wu, L., and Wang, J. (2022a). Rapid carbon dioxide foaming of 3D printed thermoplastic polyurethane elastomers. *ACS Appl. Polym. Mat.* 4, 1497–1511. doi:10.1021/acsapm.1c01846

Gunasekaran, H. B., Ponnan, S., Zheng, Y., Laroui, A., Wang, H., Wu, L., et al. (2022b). Facile fabrication of highly sensitive thermoplastic polyurethane sensors with surface- and interface-impregnated 3D conductive networks. *ACS Appl. Mat. Interfaces* 14, 22615–22625. doi:10.1021/acsami.2c03351

Habib, F. N., Nikzad, M., Masood, S. H., and Saifullah, A. B. M. (2016). Design and development of scaffolds for tissue engineering using three-dimensional printing for bio-based applications. *3D Print. Addit. Manuf.* 3, 119–127. doi:10.1089/3dp.2015.0014

Hofmann, M. (2014). 3D printing gets a boost and opportunities with polymer materials. *ACS Macro Lett.* 3, 382–386. doi:10.1021/mz4006556

Hu, B., Li, M., Jiang, J., and Zhai, W. (2021). Development of microcellular thermoplastic polyurethane honeycombs with tailored elasticity and energy absorption via CO2 foaming. *Int. J. Mech. Sci.* 197, 106324. doi:10.1016/j.ijmecsci.2021.106324

Hu, F., Wu, S., and Sun, Y. (2019). Hollow-structured materials for thermal insulation. *Adv. Mat.* 31, 1801001–1801017. doi:10.1002/adma.201801001

Hu, X., Tian, M., Xu, T., Sun, X., Sun, B., Sun, C., et al. (2020). Multiscale disordered porous fibers for self-sensing and self-cooling integrated smart sportswear. *ACS Nano* 14, 559–567. doi:10.1021/acsnano.9b06899

Hwang, S., Reyes, E. I., Moon, K. sik, Rumpf, R. C., and Kim, N. S. (2015). Thermo-mechanical characterization of metal/polymer composite filaments and printing parameter study for fused deposition modeling in the 3D printing process. *J. Electron. Mat.* 44, 771–777. doi:10.1007/s11664-014-3425-6

Jahani, D., Ameli, A., Jung, P. U., Barzegari, M. R., Park, C. B., and Naguib, H. (2014). Open-cell cavity-integrated injection-molded acoustic polypropylene foams. *Mat. Des.* 53, 20–28. doi:10.1016/j.matdes.2013.06.063

Jahani, D., Ameli, A., Saniei, M., Ding, W., Park, C. B., and Naguib, H. E. (2015). Characterization of the structure, acoustic property, thermal conductivity, and mechanical property of highly expanded open-cell polycarbonate foams. *Macromol. Mat. Eng.* 300, 48–56. doi:10.1002/mame.201400125

Janusziewicz, R., Tumbleston, J. R., Quintanilla, A. L., Mecham, S. J., and DeSimone, J. M. (2016). Layerless fabrication with continuous liquid interface production. *Proc. Natl. Acad. Sci. U. S. A.* 113, 11703–11708. doi:10.1073/pnas.1605271113

Jayavardhan, M. L., Kumar, B. R. B., Doddamani, M., Singh, A. K., Zeltmann, S. E., and Gupta, N. (2017). Development of glass microballoon/HDPE syntactic foams by compression molding. *Compos. Part B Eng.* 130, 119–131. doi:10.1016/j.compositesb.2017.07.037

Ji, J., Zhang, L. L., Ji, H., Li, Y., Zhao, X., Bai, X., et al. (2013). Nanoporous Ni(OH) 2 thin film on 3D ultrathin-graphite foam for asymmetric supercapacitor. *ACS Nano* 7, 6237–6243. doi:10.1021/nn4021955

Jia, H., Lei, H., Wang, P., Meng, J., Li, C., Zhou, H., et al. (2020). An experimental and numerical investigation ofcompressive response ofdesigned Schwarz Primitive triply periodic minimal surface with non-uniform shell thickness. *Extreme Mech. Lett.* 37, 100671. doi:10.1016/j.eml.2020.100671

Jiang, H., Ziegler, H., Zhang, Z., Meng, H., Chronopoulos, D., and Chen, Y. (2020). Mechanical properties of 3D printed architected polymer foams under large deformation. *Mat. Des.* 194, 108946. doi:10.1016/j.matdes.2020.108946

Kaiser, D. L., and Chalfin, K. (2017). Standards from ASTM international technical committee E56 on nanotechnology. *Metrol. Stand. Nanotechnol.* 229, 269–278. doi:10.1002/9783527800308.ch15

Kakumanu, V., and Srinivas Sundarram, S. (2018). Dual pore network polymer foams for biomedical applications via combined solid state foaming and additive manufacturing. *Mat. Lett.* 213, 366–369. doi:10.1016/j.matlet.2017.11.027

Kalia, K., Francoeur, B., Amirkhizi, A., and Ameli, A. (2022). *In situ* foam 3D printing of microcellular structures using material extrusion additive manufacturing. *ACS Appl. Mat. Interfaces* 14, 22454–22465. doi:10.1021/acsami.2c03014

Kim, G. D., and Oh, Y. T. (2008). A benchmark study on rapid prototyping processes and machines: Quantitative comparisons of mechanical properties, accuracy, roughness, speed, and material cost. *Proc. Institution Mech. Eng. Part B J. Eng. Manuf.* 222, 201–215. doi:10.1243/09544054JEM724

Kmetty, Á., and Litauszki, K. (2020). Development of poly (lactide acid) foams with thermally expandable microspheres. *Polym. (Basel)* 12, 463. doi:10.3390/polym12020463

Kokkinis, D., Schaffner, M., and Studart, A. R. (2015). Multimaterial magnetically assisted 3D printing of composite materials. *Nat. Commun.* 6, 8643. doi:10.1038/ncomms9643

Kuang, T., Chen, F., Chang, L., Zhao, Y., Fu, D., Gong, X., et al. (2017). Facile preparation of open-cellular porous poly (L-lactic acid) scaffold by supercritical carbon dioxide foaming for potential tissue engineering applications. *Chem. Eng. J.* 307, 1017–1025. doi:10.1016/j.cej.2016.09.023

Kumar, V., Juntunen, R. P., and Barlow, C. (2000). Impact strength of high relative density solid state carbon dioxide blown crystallizable poly(ethylene terephthalate) microcellular foams. *Cell. Polym.* 19, 25–37.

Lee, S. T., Kareko, L., and Jun, J. (2008). Study of thermoplastic PLA foam extrusion. *J. Cell. Plast.* 44, 293–305. doi:10.1177/0021955X08088859

Li, B., Zhao, G., Wang, G., Zhang, L., Gong, J., and Shi, Z. (2021). Biodegradable PLA/PBS open-cell foam fabricated by supercritical CO2 foaming for selective oil-adsorption. *Sep. Purif. Technol.* 257, 117949. doi:10.1016/j.seppur.2020.117949

Li, M., Jiang, J., Hu, B., and Zhai, W. (2020). Fused deposition modeling of hierarchical porous polyetherimide assisted by an *in-situ* CO2 foaming technology. *Compos. Sci. Technol.* 200, 108454. doi:10.1016/j.compscitech.2020.108454

Liang, H., Fu, G., Liu, J., Tang, Y., Wang, Y., Chen, S., et al. (2022). A 3D-printed Sn-doped calcium phosphate scaffold for bone tissue engineering. *Front. Mat.* 9, 1–8. doi:10.3389/fmats.2022.1016820

Ligon-Auer, S. C., Schwentenwein, M., Gorsche, C., Stampfl, J., and Liska, R. (2016). Toughening of photo-curable polymer networks: A review. *Polym. Chem.* 7, 257–286. doi:10.1039/c5py01631b

Ling, J., Zhai, W., Feng, W., Shen, B., Zhang, J., and Zheng, W. G. (2013). Facile preparation of lightweight microcellular polyetherimide/graphene composite foams for electromagnetic interference shielding. *ACS Appl. Mat. Interfaces* 5, 2677–2684. doi:10.1021/am303289m

Liu, L., Kamm, P., García-Moreno, F., Banhart, J., and Pasini, D. (2017). Elastic and failure response of imperfect three-dimensional metallic lattices: The role of geometric defects induced by selective laser melting Lu. *J. Mech. Phys. Solids* 107, 160–184. doi:10.1016/j.jmps.2017.07.003

Liu, W. C., Chou, V. H. Y., Behera, R. P., and Le Ferrand, H. (2022). Magnetically assisted drop-on-demand 3D printing of microstructured multimaterial composites. *Nat. Commun.* 13, 5015. doi:10.1038/s41467-022-32792-1

Ma, Z., Lin, J., Xu, X., Ma, Z., Tang, L., Sun, C., et al. (2019). Design and 3D printing of adjustable modulus porous structures for customized diabetic foot insoles. *Int. J. Lightweight Mater. Manuf.* 2, 57–63. doi:10.1016/j.ijlmm.2018.10.003

Maskery, I., Aremu, A. O., Parry, L., Wildman, R. D., Tuck, C. J., and Ashcroft, I. A. (2018). Effective design and simulation of surface-based lattice structures featuring volume fraction and cell type grading. *Mat. Des.* 155, 220–232. doi:10.1016/j.matdes.2018.05.058

Melchels, F. P. W., Bertoldi, K., Gabbrielli, R., Velders, A. H., Feijen, J., and Grijpma, D. W. (2010). Mathematically defined tissue engineering scaffold architectures prepared by stereolithography. *Biomaterials* 31, 6909–6916. doi:10.1016/j.biomaterials.2010.05.068

Nadgorny, M., and Ameli, A. (2018). Functional polymers and nanocomposites for 3D printing of smart structures and devices. *ACS Appl. Mat. Interfaces* 10, 17489–17507. doi:10.1021/acsami.8b01786

Nadiyapara, H. H., and Pande, S. (2017). A review of variable slicing in fused deposition modeling. *J. Inst. Eng. India. Ser. C* 98, 387–393. doi:10.1007/s40032-016-0272-7

Narupai, B., and Nelson, A. (2020). 100th anniversary of macromolecular science viewpoint: Macromolecular materials for additive manufacturing. *ACS Macro Lett.* 9, 627–638. doi:10.1021/acsmacrolett.0c00200

Nikolić, S., and Stevanović, G. (2006). Neurocysticercosis--pathogenesis and clinical aspects. *Srp. Arh. Celok. Lek.* 134, 246–250. doi:10.1117/1.JBO.17.10

Nofar, M. (2016). Effects of nano-/micro-sized additives and the corresponding induced crystallinity on the extrusion foaming behavior of PLA using supercritical CO2. *Mat. Des.* 101, 24–34. doi:10.1016/j.matdes.2016.03.147

Nofar, M., Utz, J., Geis, N., Altstädt, V., and Ruckdäschel, H. (2022). Foam 3D printing of thermoplastics: A symbiosis of additive manufacturing and foaming technology. *Adv. Sci. (Weinh).* 9, 2105701–2105718. doi:10.1002/advs.202105701

Pajunen, K., Johanns, P., Pal, R. K., Rimoli, J. J., and Daraio, C. (2019). Design and impact response of 3D-printable tensegrity-inspired structures. *Mat. Des.* 182, 107966. doi:10.1016/j.matdes.2019.107966

Palaganas, N. B., Mangadlao, J. D., De Leon, A. C. C., Palaganas, J. O., Pangilinan, K. D., Lee, Y. J., et al. (2017). 3D printing of photocurable cellulose nanocrystal composite for fabrication of complex architectures via stereolithography. *ACS Appl. Mat. Interfaces* 9, 34314–34324. doi:10.1021/acsami.7b09223

Patil, B., Kumar, B. R. B., Bontha, S., Krishna, V., Powar, S., Kumar, V. H., et al. (2019). Eco-friendly lightweight fi lament synthesis and mechanical characterization of additively manufactured closed cell foams. *Compos. Sci. Technol.* 183, 107816. doi:10.1016/j.compscitech.2019.107816

Peng, J., Srithep, Y., Wang, J., Yu, E., Turng, L. S., and Peng, X. F. (2013). Comparisons of microcellular polylactic acid parts injection molded with supercritical nitrogen and expandable thermoplastic microspheres: Surface roughness, tensile properties, and morphology. *J. Cell. Plast.* 49, 33–45. doi:10.1177/0021955X12450208

Pérez, M., Medina-Sánchez, G., García-Collado, A., Gupta, M., and Carou, D. (2018). Surface quality enhancement of fused deposition modeling (FDM) printed samples based on the selection of critical printing parameters. *Mater. (Basel)* 11, 1382. doi:10.3390/ma11081382

Qi, S., Guo, H., Fu, J., Xie, Y., Zhu, M., and Yu, M. (2020). 3D printed shape-programmable magneto-active soft matter for biomimetic applications. *Compos. Sci. Technol.* 188, 107973. doi:10.1016/j.compscitech.2019.107973

Rashid, A. (2019). *Additive manufacturing technologies*. Editor S. Chatti and T. Tolio (Springer, Berlin, Heidelberg: CIRP Encyclopedia of Production Engineering). doi:10.1007/978-3-642-35950-7_16866-1

Rehme, O. (2010). Cellular design for laser freeform fabrication. Available at: https://cuvillier.de/uploads/preview/public_file/1820/9783869552736.pdf.

Rizvi, A., Tabatabaei, A., Vahedi, P., Mahmood, S. H., and Park, C. B. (2018). Non-crosslinked thermoplastic reticulated polymer foams from crystallization-induced structural heterogeneities. *Polymer* 135, 185–192. doi:10.1016/j.polymer.2017.12.006

Sadik, T., Pillon, C., Carrot, C., and Reglero Ruiz, J. A. (2018). Dsc studies on the decomposition of chemical blowing agents based on citric acid and sodium bicarbonate. *Thermochim. Acta* 659, 74–81. doi:10.1016/j.tca.2017.11.007

Sauceau, M., Fages, J., Common, A., Nikitine, C., and Rodier, E. (2011). New challenges in polymer foaming: A review of extrusion processes assisted by supercritical carbon dioxide. *Prog. Polym. Sci.* 36, 749–766. doi:10.1016/j.progpolymsci.2010.12.004

Schirmeister, C. G., Hees, T., Licht, E. H., and Mülhaupt, R. (2019). 3D printing of high density polyethylene by fused filament fabrication. *Addit. Manuf.* 28, 152–159. doi:10.1016/j.addma.2019.05.003

Schmitt, B. M., Zirbes, C. F., Bonin, C., Lohmann, D., Lencina, D. C., and Da Costa Sabino Netto, A. (2017). A comparative study of cartesian and delta 3d printers on producing PLA parts. *Mat. Res.* 20, 883–886. doi:10.1590/1980-5373-mr-2016-1039

Shmueli, Y., Jiang, J., Zhou, Y., Xue, Y., Chang, C. C., Yuan, G., et al. (2019). Simultaneous *in situ* X-ray scattering and infrared imaging of polymer extrusion in additive manufacturing. *ACS Appl. Polym. Mat.* 1, 1559–1567. doi:10.1021/acsapm.9b00328

Stansbury, J. W., and Idacavage, M. J. (2016). 3D printing with polymers: Challenges among expanding options and opportunities. *Dent. Mat.* 32, 54–64. doi:10.1016/j.dental.2015.09.018

Tekinalp, H. L., Kunc, V., Velez-garcia, G. M., Duty, C. E., Love, L. J., Naskar, A. K., et al. (2014). Highly oriented carbon fiber – polymer composites via additive manufacturing. *Compos. Sci. Technol.* 105, 144–150. doi:10.1016/j.compscitech.2014.10.009

Thomas, S., Joseph, K., and S, M. (2019). *Related titles* in-situ *synthesis of polymer nanocomposites characterization techniques for polymer nanocomposites handbook of biopolymer-based materials modeling and prediction of polymer nanocomposite properties multilayer thin films handbook of biodegra*.

Tumbleston, J. R., Shirvanyants, D., Ermoshkin, N., Janusziewicz, R., Johnson, A. R., Kelly, D., et al. (2015). Continuous liquid interface production of 3D objects. *Sci.* 347, 1349–1352. doi:10.1126/science.aaa2397

Udroiu, R., Braga, I. C., and Nedelcu, A. (2019). Evaluating the quality surface performance of additive manufacturing systems: Methodology and a material jetting case study. *Mater. (Basel)* 12, 995. doi:10.3390/ma12060995

Villamil Jiménez, J. A., Le Moigne, N., Bénézet, J. C., Sauceau, M., Sescousse, R., and Fages, J. (2020). Foaming of PLA composites by supercritical fluid-assisted processes: A review. *Molecules* 25, 3408. doi:10.3390/molecules25153408

Voet, V. S. D., Strating, T., Schnelting, G. H. M., Dijkstra, P., Tietema, M., Xu, J., et al. (2018). Biobased acrylate photocurable resin formulation for stereolithography 3D printing. *ACS Omega* 3, 1403–1408. doi:10.1021/acsomega.7b01648

Wang, J., Mubarak, S., Dhamodharan, D., Divakaran, N., Wu, L., and Zhang, X. (2020a). Fabrication of thermoplastic functionally gradient composite parts with anisotropic thermal conductive properties based on multicomponent fused deposition modeling 3D printing. *Compos. Commun.* 19, 142–146. doi:10.1016/j.coco.2020.03.012

Wang, S., Zheng, Z., Zhu, C., Ding, Y., and Yu, J. (2018). Crushing and densification of rapid prototyping polylactide foam: Meso-structural effect and a statistical constitutive model. *Mech. Mat.* 127, 65–76. doi:10.1016/j.mechmat.2018.09.003

Wang, X., Jiang, M., Zhou, Z., Gou, J., and Hui, D. (2017). 3D printing of polymer matrix composites : A review and prospective. *Compos. Part B Eng.* 110, 442–458. doi:10.1016/j.compositesb.2016.11.034

Wang, Y., Tan, Q., Pu, F., Boone, D., and Zhang, M. (2020b). A review of the application of additive manufacturing in prosthetic and orthotic clinics from a biomechanical perspective. *Engineering* 6, 1258–1266. doi:10.1016/j.eng.2020.07.019

Weng, Z., Wang, J., Senthil, T., and Wu, L. (2016). Mechanical and thermal properties of ABS/montmorillonite nanocomposites for fused deposition modeling 3D printing. *Mat. Des.* 102, 276–283. doi:10.1016/j.matdes.2016.04.045

Wicklein, B., Kocjan, A., Salazar-Alvarez, G., Carosio, F., Camino, G., Antonietti, M., et al. (2015). Thermally insulating and fire-retardant lightweight anisotropic foams based on nanocellulose and graphene oxide. *Nat. Nanotechnol.* 10, 277–283. doi:10.1038/nnano.2014.248

Wirth, D. M., Jaquez, A., Gandarilla, S., Hochberg, J. D., Church, D. C., and Pokorski, J. K. (2020). Highly expandable foam for lithographic 3D printing. *ACS Appl. Mat. Interfaces* 12, 19033–19043. doi:10.1021/acsami.0c02683

Wong, A., Chu, R. K. M., Leung, S. N., Park, C. B., and Zong, J. H. (2011). A batch foaming visualization system with extensional stress-inducing ability. *Chem. Eng. Sci.* 66, 55–63. doi:10.1016/j.ces.2010.09.038

Wu, C., Huang, X., Wu, X., Qian, R., and Jiang, P. (2013). Mechanically flexible and multifunctional polymer-based graphene foams for elastic conductors and oil-water separators. *Adv. Mat.* 25, 5658–5662. doi:10.1002/adma.201302406

Wu, J., Hu, R., Zeng, S., Xi, W., Huang, S., Deng, J., et al. (2020). Flexible and robust biomaterial microstructured colored textiles for personal thermoregulation. *ACS Appl. Mat. Interfaces* 12, 19015–19022. doi:10.1021/acsami.0c02300

Yang, J., Gu, D., Lin, K., Zhang, Y., Guo, M., Yuan, L., et al. (2022). Laser additive manufacturing of bio-inspired metallic structures. *Chin. J. Mech. Eng. Addit. Manuf. Front.* 1, 100013. doi:10.1016/j.cjmeam.2022.100013

Yang, S., Leong, K. F., Du, Z., and Chua, C. K. (2001). The design of scaffolds for use in tissue engineering. Part I. Traditional factors. *Tissue Eng.* 7, 679–689. doi:10.1089/107632701753337645

Yeh, S. K., Liu, Y. C., Chu, C. C., Chang, K. C., and Wang, S. F. (2017). Mechanical properties of microcellular and nanocellular thermoplastic polyurethane nanocomposite foams created using supercritical carbon dioxide. *Ind. Eng. Chem. Res.* 56, 8499–8507. doi:10.1021/acs.iecr.7b00942

Yin, H., Zhang, W., Zhu, L., Meng, F., Liu, J., and Wen, G. (2023). Review on lattice structures for energy absorption properties. *Compos. Struct.* 304, 116397. doi:10.1016/j.compstruct.2022.116397

Yu, P., Mi, H. Y., Huang, A., Geng, L. H., Chen, B. Y., Kuang, T. R., et al. (2015). Effect of poly(butylenes succinate) on poly(lactic acid) foaming behavior: Formation of open cell structure. *Ind. Eng. Chem. Res.* 54, 6199–6207. doi:10.1021/acs.iecr.5b00477

Zhai, W., Jiang, J., and Park, C. B. (2022). A review on physical foaming of thermoplastic and vulcanized elastomers. *Polym. Rev. Phila. Pa.* 62, 95–141. doi:10.1080/15583724.2021.1897996

Zhang, R. Z., Chen, J., Huang, M. W., Zhang, J., Luo, G. Q., Wang, B. Z., et al. (2019). Synthesis and compressive response of microcellular foams fabricated from thermally expandable microspheres. *Chin. J. Polym. Sci.* 37, 279–288. doi:10.1007/s10118-019-2187-2

Zhang, S., Shi, X., Miao, Z., Zhang, H., Zhao, X., Wang, K., et al. (2022). 3D-Printed polyurethane tissue-engineering scaffold with hierarchical microcellular foam structure and antibacterial properties. *Adv. Eng. Mat.* 24, 2101134–2101210. doi:10.1002/adem.202101134

Zhang, X., Fan, W., and Liu, T. (2020). Fused deposition modeling 3D printing of polyamide-based composites and its applications. *Compos. Commun.* 21, 100413. doi:10.1016/j.coco.2020.100413

Zhang, X., Wang, J., and Liu, T. (2021). 3D printing of polycaprolactone-based composites with diversely tunable mechanical gradients via multi-material fused deposition modeling. *Compos. Commun.* 23, 100600. doi:10.1016/j.coco.2020.100600

Zhou, C., Yang, K., Wang, K., Pei, X., Dong, Z., Hong, Y., et al. (2016). Combination of fused deposition modeling and gas foaming technique to fabricated hierarchical macro/microporous polymer scaffolds. *Mat. Des.* 109, 415–424. doi:10.1016/j.matdes.2016.07.094

Zhou, J., and Hsieh, Y. L. (2020). Nanocellulose aerogel-based porous coaxial fibers for thermal insulation. *Nano Energy* 68, 104305. doi:10.1016/j.nanoen.2019.104305

Zhu, W., Qu, X., Zhu, J., Ma, X., Patel, S., Liu, J., et al. (2017). Direct 3D bioprinting of prevascularized tissue constructs with complex microarchitecture. *Biomaterials* 124, 106–115. doi:10.1016/j.biomaterials.2017.01.042

Zhu, W., Tringale, K. R., Woller, S. A., You, S., Johnson, S., Shen, H., et al. (2018). Rapid continuous 3D printing of customizable peripheral nerve guidance conduits. *Mat. TodayKidlingt.* 21, 951–959. doi:10.1016/j.mattod.2018.04.001

frontiers | Frontiers in Materials

TYPE Original Research
PUBLISHED 09 December 2022
DOI 10.3389/fmats.2022.1097547

OPEN ACCESS

EDITED BY
Jingjun Wu,
Zhejiang University, China

REVIEWED BY
Xiaozhen Zhang,
Jingdezhen Ceramic Institute, China
Shanwen Tao,
University of Warwick, United Kingdom

*CORRESPONDENCE
Kui Xie,
kxie@fjirsm.ac.cn

SPECIALTY SECTION
This article was submitted to Polymeric and Composite Materials, a section of the journal Frontiers in Materials

RECEIVED 14 November 2022
ACCEPTED 24 November 2022
PUBLISHED 09 December 2022

CITATION
Li X and Xie K (2022), Porous single-crystalline molybdenum nitride enhances electroreduction of nitrogen to ammonia.
Front. Mater. 9:1097547.
doi: 10.3389/fmats.2022.1097547

Porous single-crystalline molybdenum nitride enhances electroreduction of nitrogen to ammonia

Xue Li[1,2] and Kui Xie[2,3]*

[1]College of Chemistry and Materials Science, Fujian Normal University, Fuzhou, China, [2]Key Laboratory of Design and Assembly of Functional Nanostructures, Fujian Institute of Research on the Structure of Matter, Chinese Academy of Sciences, Fuzhou, China, [3]Advanced Energy Science and Technology Guangdong Laboratory, Huizhou, China

The industrial ammonia synthesis reaction has the disadvantage of large energy consumption; thus, the electrochemical reduction method of ammonia synthesis characterized by its clean nature and environmental protectiveness has received extensive attention. Molybdenum nitride is a commonly used electrocatalyst for ammonia synthesis, and its Faraday efficiency is low, which may be due to many internal grain boundaries and few active sites. In this work, we grow microscale porous Mo_2N single crystals and polycrystalline Mo_2N from non-porous MoO_3 single crystals. Porous molybdenum nitride materials facilitate charge transport in grain boundaries due to their single-crystal nature and enhance the catalytic properties of ammonia synthesis reactions. Compared with polycrystalline Mo_2N, the porous Mo_2N single crystal shows better performance, with a high NH_4^+ yield of 272.56 μg h^{-1} mg^{-1} and a Faradaic efficiency of 7.3%. In addition, the porous Mo_2N single crystal exhibits superior long-term stability with little attenuation after 16 h electrolysis reaction. It provides a new method for the catalyst of ammonia synthesis.

KEYWORDS

porous single crystal, molybdenum nitride, electrochemical reactions, ammonia, hydrothermal method

Introduction

Shortage of ammonia (NH_3), which is used as the raw material for chemical fertilizer, chemical pharmaceuticals, and zero-carbon emission fuel, has become an urgent energy problem with the continuous growth of the population. Fixing N_2 in the atmosphere to NH_3 is an important method to realize nitrogen storage and the conversion of Earth's nitrogen cycle (Service, 2014; Brown et al., 2016). Up to now, the Haber–Bosch method ($N_2 + 3H_2 \rightarrow 2NH_3$) has been used to synthesize NH_3 in the industry, which works at high temperatures and pressure with high energy consumption (Van Der Ham et al., 2014). Most raw materials of hydrogen and energy consumption are obtained through the steam reformation of fossil fuels, while a large amount of CO_2 is also produced (Kyriakou et al.,

2020). Therefore, the more economical, environmental, and sustainable method of producing NH_3 is in great demand.

Electrochemical reduction is a prospective method for artificial nitrogen fixation (Amar et al., 2011; Costentin et al., 2013; She et al., 2017; Guo et al., 2018). However, the N_2 reduction reaction (NRR) requires breaking the inert molecular structure of N_2, which requires sufficient energy to break the N≡N bond (~941 kJ mol^{-1}) (Han et al., 2021). Noble metal catalysts (Ru, Au, Ag, and Rh) have shown to have superior NRR activity, but the high cost and rareness limit their commercial applications (Aioub et al., 2017; Bao et al., 2017; Nazemi et al., 2018; Liu et al., 2019; Tao et al., 2019). The search for inexpensive, earth-abundant materials with high activity and excellent stability has recently attracted significant research interest and has become an important pursuit toward ammonia economy. In recent years, transition metal has attracted extensive attention as NRR catalysts because of their high activity, abundant reserves, and low price. It has been reported that molybdenum-based catalysts have been designed and applied to artificial nitrogen fixation (Banerjee et al., 2015; Sun et al., 2017; Wickramasinghe et al., 2017; Yang et al., 2017; Han et al., 2018; Li et al., 2019; Ou et al., 2019). Molybdenum nitride has attracted much attention due to its platinum-like properties. Specifically, Mo_2N is a typical interstitial compound in which the metal atoms express a tight stacking pattern to stabilize the lattice structure, where the top element is mainly a metal atom on the surface. The nearest metal ions with short distances will provide the possibility to form metallic bonds to facilitate electron transport in the connected channels. MoN and Mo_2N nanosheets also have an electrocatalytic activity of N_2 reduction, with the FE of 1.15% and 4.5%, respectively (Ren et al., 2018; Zhang et al., 2018). Although molybdenum-based catalysts have excellent performance, they still suffer from weak FE efficiency. Thus, it is attractive to search for new Mo-based catalysts with enhanced FE performance.

In catalytic and electrocatalytic systems, uniform dispersion of active sites on the surface of porous structures ensures the high activity of porous materials (Zhang et al., 2021; Lu et al., 2022). Single crystals with almost no grain boundary reduce the resistance of charge transmission between grain boundaries. Therefore, porous single crystals with anisotropy and a long-range structural order and structural coherence combined with a large specific surface area provide unsaturated nitrogen coordination on the surface of metal nitride, and its internal structures exhibit regularity and periodicity in three-dimensional space. Due to the porous single-crystal structure, the electrocatalytic properties are also improved (Wu et al., 2019; Zhang et al., 2019; Lin et al., 2020, 2022; Xiao and Xie, 2022). Different from the conventionally used nano-catalyst materials such as nanosheets or nanorods, which are smooth in surface and poor in single crystallinity, porous single crystals have a large amount of nanopores and good crystallinity which increase the active site and improve the stability during the reaction, thus improving the catalytic performance of the catalyst.

In this paper, we prepare the micron-scale porous Mo_2N single crystal (PSC Mo_2N) and polycrystalline Mo_2N (PPC Mo_2N) cubes by the lattice reconstruction strategy and investigate their catalytic performance in the electrocatalytic reduction of N_2 to NH_3. PSC Mo_2N can provide a large surface area for chemical adsorption, and the internal interconnected pores and channels are conducive to the diffusion of ions in the electrolyte. PSC Mo_2N exhibits ultra-high yield of NH_3 and FE, which greatly enhances the catalytic performance of NRR.

Materials and methods

Syntheses of a porous Mo_2N single crystal

The MoO_3-PEG precursor is obtained by the hydrothermal method. MoO_3-PEG is kept at 300°C for 5 h in air and cooled down naturally to obtain MoO_3. PSC Mo_2N is obtained in a tube furnace at 650°C for 10 h at a pressure of 50–200 Torr with 100 sccm NH_3 gas flow rates. Similarly, irregular porous polycrystalline molybdenum nitride (PPC Mo_2N) is obtained by direct treatment of MoO_3 single crystals in a tube furnace at atmospheric pressure with NH_3 gas at 50–200 sccm for 10 h at 650°C. All reagents are used without any purification.

Characterizations

An X-ray diffractometer (XRD, Bruker D8-Advance) is used to characterize the phase composition of synthetic materials and determine the crystal face and crystal orientation. The surface morphologies of MoO_3 and Mo_2N are observed by field emission scanning electron microscopy (FE-SEM, SU8010) with 10 kV accelerating voltage. The Tecnai F30 microscope with 200 kV accelerating voltage is tested for transmission electron microscopy (TEM) and selected area electron diffraction (SAED). TEM (FEI Titan 3G2 60-300) is corrected by the spherical aberration method at 300 kV accelerating voltage, and the atomic information and crystal structure of the material are characterized. The Brunauer–Emmett–Teller (BET) tests are performed by an automatic specific surface and micropore analyzer (Tristar II 3020). X-ray photoelectron spectroscopy (XPS, Escalab 250Xi) tests the binding energy of the crystals. The product NH_4^+ is quantified by cation chromatography (IC 1826 Qingdao, Shunyuhengping).

Preparation of electrodes

The catalyst samples are mixed in ethanol and Nafion solution and sonicated for 30 min to prepare a homogeneous suspension of the catalyst. The prepared suspension is then

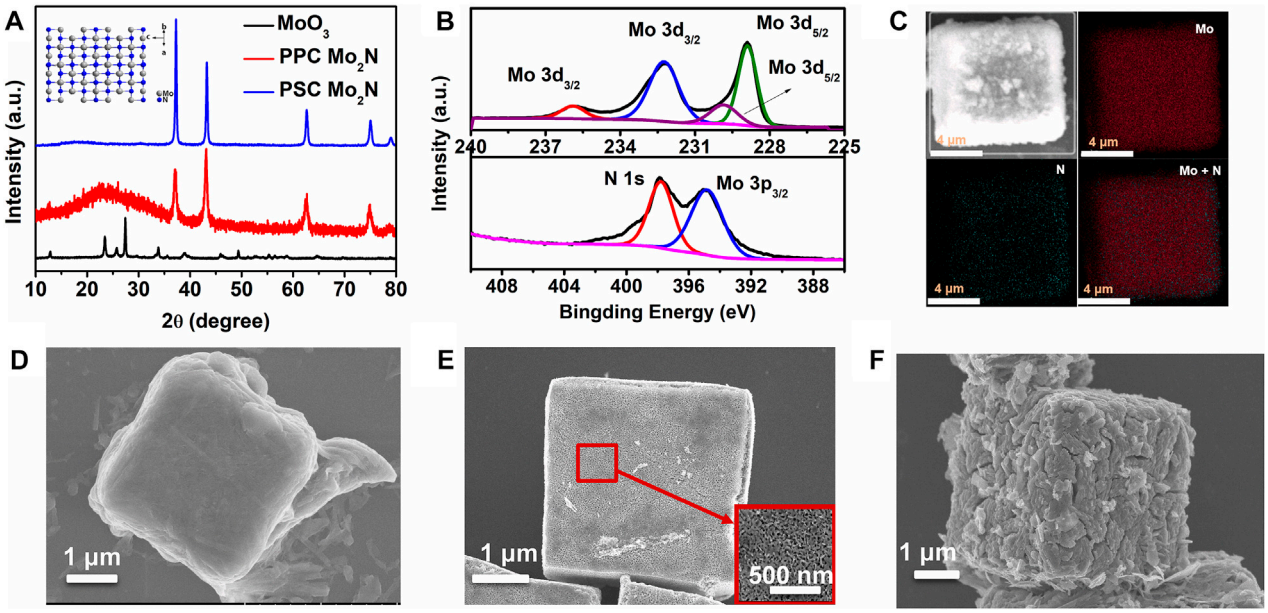

FIGURE 1
(A) XRD patterns of MoO_3 microcubes, Mo_2N porous single crystals, and polycrystalline microcubes. The inset in **(A)** is the crystal structure of Mo_2N. **(B)** Mo_2N of XPS spectra. **(C)** EDX elemental mapping of Mo and N in Mo_2N microcubes. SEM of **(D)** MoO_3, **(E)** PSC Mo_2N, and **(F)** PPC Mo_2N. The inserted image of **(E)** is a partial amplification of the SEM image.

dropped on a piece of carbon paper (CP) to obtain a 5 mg cm^{-2} sample, which is dried naturally at room temperature to acquire the working electrode.

Electrochemical measurements

Electrochemical data are obtained by testing with the three-electrode system (Zahner, Ennium) of the chemical workstation. Electrocatalytic NRR is a typical hydrogen reduction process. The study is performed in a closed H-shaped vessel with the middle section separated by a Nafion 117 membrane. The electrochemical workstation is operated at room temperature with Mo_2N (Mo_2N/CP) as the working electrode, carbon paper as the substrate, a graphite electrode as the counter electrode, and a saturated Ag/AgCl electrode as the reference electrode, as well as 0.1 M HCl solution as the electrolyte. With the help of N_2 and H^+, NH_3 is obtained at the cathode. Two-compartment batteries can avoid NH_3 oxidation in the anode. In particular, the resistance of the Nafion 117 membrane is negligible. The Nafion 117 membrane only transmits H^+, which can limit the diffusion of NH_3 to the anode. The potential is calibrated and converted into a reversible hydrogen electrode (RHE) using the following formulas (Ren et al., 2018).

$$E\,(RHE) = E\,(Ag/AgCl) + 0.059\,pH + 0.197\,V, \quad (1)$$

where E (RHE) is the corrected potential (V) versus RHE, E (Ag/AgCl) is the experimental test potential with Ag/AgCl as the reference electrode, and 0.197 V is the potential at room temperature at the standard electrode for the Ag/AgCl electrode.

We simultaneously collected products under different potential conditions ranging from −0.3 to −0.8 V for 2 h. The concentration of NH_4^+ is tested by cation chromatography. The generation rate of NH_4^+ and the Faradaic efficiency (FE) of the current are calculated by the formula and plotted. Among them, the calculation of the NH_3 generation rate and FE is as follows:

$$\text{Ammonia formation rate}\,(ug\,h^{-1}\,mg^{-1}) = [NH_4^+] \times V \div (m \times t), \quad (2)$$

$$FE\,(\%) = 3 \times F \times [NH_4^+] \times V \div (17 \times Q), \quad (3)$$

where $[NH_4^+]$ is the result of measuring the NH_4^+ concentration, V is the volume of the electrolyte at the cathode, m is the loaded mass of the catalyst, t is the time of potential application, Q is the Coulomb volume through the electrode, and F is the Faraday constant.

Linear sweep voltammetry (LSV) is applied to estimate the catalytic performance and stability of OER at 10 mV s^{-1} in 0.1 M HCl. We measure a three-electrode cell system whose electrochemical impedance spectrum (EIS) is measured between 0.1 Hz and 2 MHz at 0.1 M hydrochloric acid and 5 mV AC potential. The current density curve is obtained from the variation of Mo_2N of NRR with time at various potentials in 0.1 M HCl.

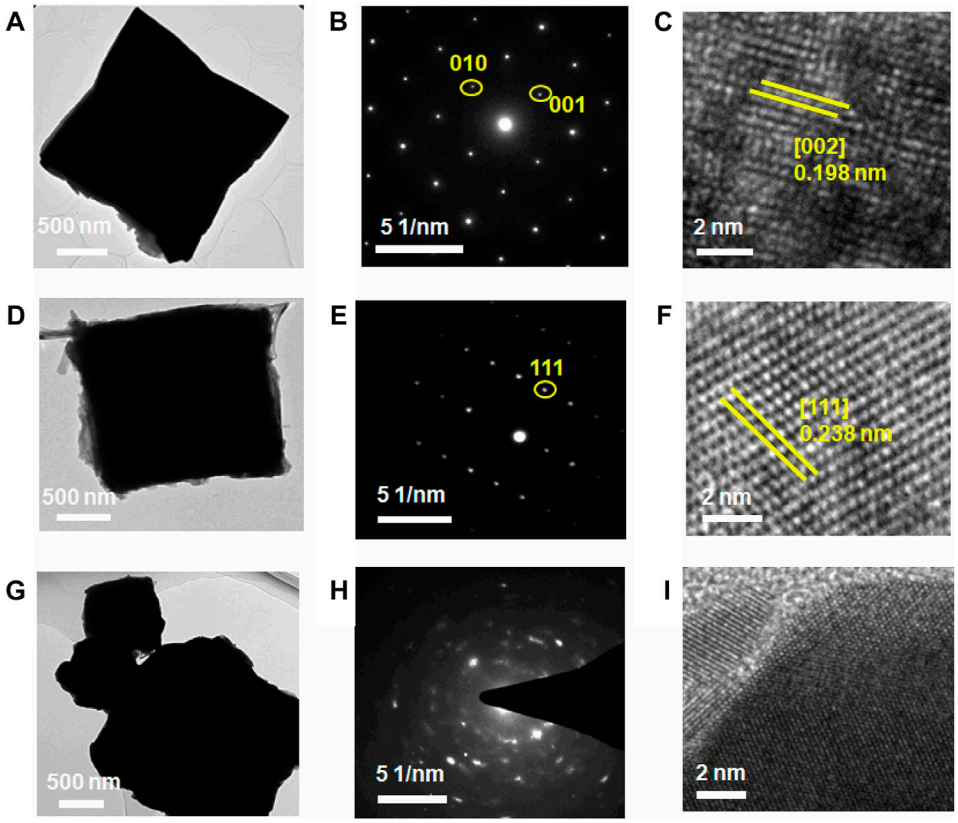

FIGURE 2
TEM image, SAED pattern, and HRTEM image of the material. **(A–C)** MoO_3 single-crystal microcube, **(D–F)** PSC Mo_2N microcube, and **(G–I)** PPC Mo_2N.

Results and discussion

Figure 1A shows the XRD patterns of MoO_3, PSC Mo_2N, and PPC Mo_2N. The XRD patterns of MoO_3 and Mo_2N single crystals conform to the JCPDS standard cards 75-0512 and 75-1150, respectively. The diffraction peaks are sharp and narrow, indicating that molybdenum nitride has excellent crystallinity. From a polycrystalline versus a single crystal perspective, molybdenum nitride single crystals tend to be [111] oriented. The inset in Figure 1A is ball-and-stick model of the crystal structure of Mo_2N. Supplementary Figure S1 illustrates the growth mechanism for obtaining micron-scale metal nitride cubes from metal oxides. When the intrinsic oxygen atoms in the MoO_3 lattice are heated in an ammonia atmosphere, the oxygen atoms gradually leave the intrinsic position in the lattice and slowly disappear. The nitrogen atom in ammonia gradually enters the position before the oxygen atom. Due to the different sizes of oxygen and nitrogen atoms, the lattice configuration also changes, and then, the molybdenum nitride skeleton is gradually formed. By changing the ammonia flow rate and pressure, the molybdenum nitride lattice is reconstructed to form a porous Mo_2N cube.

To explore the relationship between the structure and properties of porous single-crystal molybdenum nitride, we perform XPS tests. The test results are shown in Figure 1B; the results specifically show that the characteristic peaks at 229.8 and 232.3 eV are caused by Mo $3d_{5/2}$ and Mo $3d_{3/2}$ (Ozkan et al., 1997; Afanasiev, 2002; Liu et al., 2013). In addition, the combining energies at 228.9 and 235.9 eV are consistent with $Mo^{\delta+}$ and Mo^{6+}, respectively, which is ascribed to the surface oxidation of Mo_2N (Yoon et al., 2012). The peak at 397.81 eV is the N 1 s of Mo_2N, while the peak value of 394.77 eV corresponds to the shoulder of $Mo3p_{3/2}$ with Mo_2N, indicating the presence of Mo–N bonds (Ozkan et al., 1997; Afanasiev, 2002; Yoon et al., 2012; Liu et al., 2013). To further confirm the presence of chemical elements in Mo_2N, energy dispersive X-ray (EDX) and its mapping are used for further identification (Figure 1C). The results indicate that only two chemical elements (Mo and N) can be detected in the final product Mo_2N, and no other impurity phases are observed. Moreover, the chemical elements Mo and N are uniformly

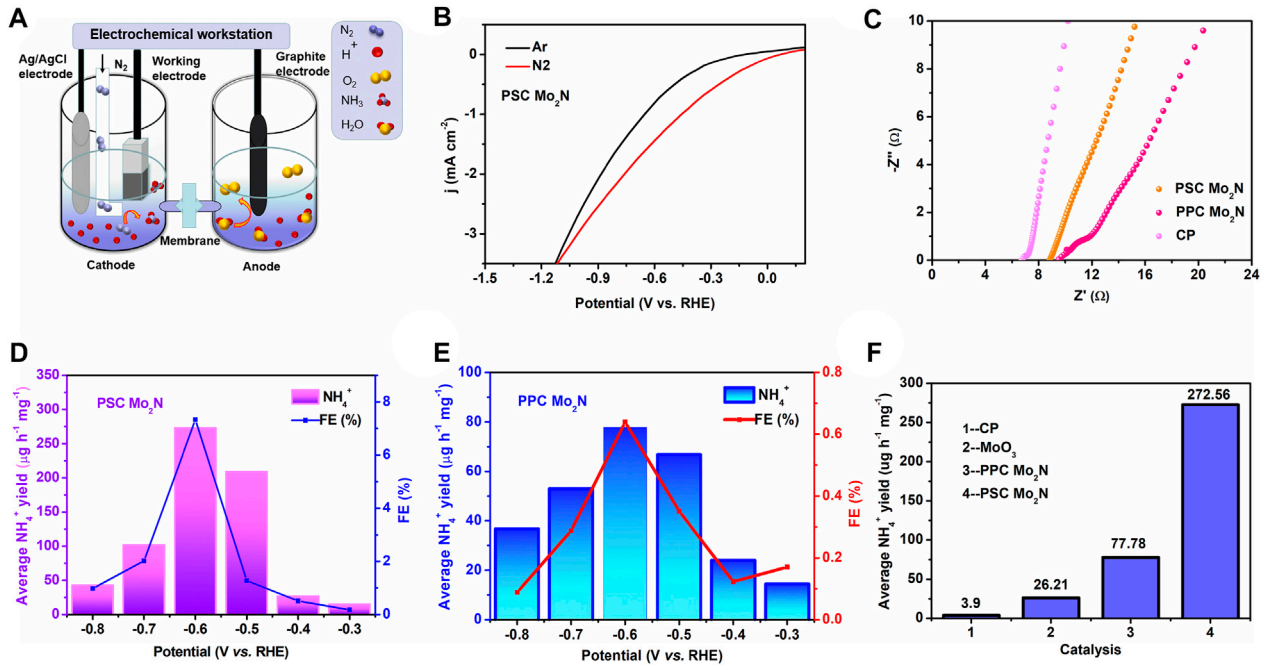

FIGURE 3
(A) Schematic diagram of electrocatalytic NRR. **(B)** LSV curve of PSC Mo_2N electrocatalytic NRR in a saturated electrolyte of N_2 (red line) and Ar (black line). **(C)** Nyquist plots of CP, PSC Mo_2N, and PPC Mo_2N catalysts in 0.1 M HCl solution. The yields of NH_4^+ and FEs at different potentials of **(D)** PSC Mo_2N and **(E)** PPC Mo_2N. **(F)** Yields of NH_4^+ in different catalysts under the same environmental conditions at −0.6 V vs. RHE.

distributed in the sample, which confirms well the complete transformation process of the non-porous MoO_3 single crystal.

We observe the changes in the microscopic morphology of the crystals during the growth and preparation processes by SEM, and Figure 1D shows the MoO_3 cubes of about 3–10 μm obtained after calcination of the precursor MoO_3-PEG. Figures 1E,F display the microcube scanning diagram of PSC Mo_2N and PPC Mo_2N formed by ammoniation of MoO_3, which have the same morphology before and after calcination from the microscopic scale. In addition, Figure 1E reveals the magnified morphology, and it can be seen that the pore channels are uniformly connected roughly around 50 nm, while the polycrystalline surface is in a sintered state with some cracks. Therefore, we speculate that the specific surface area of single crystals should be larger than that of polycrystals. We use a lattice reconstruction strategy to grow porous molybdenum nitride from non-porous molybdenum nitride, whose BET results (Supplementary Figure S2) indicate that the BET-specific surface areas of PSC Mo_2N and PPC Mo_2N are 14.347 and 7.676 $m^2 g^{-1}$, respectively. The larger specific surface area has more active sites, which is consistent with our subsequent test results (PSC Mo_2N > PPC Mo_2N).

For the purpose of obtaining further information about the microstructure and crystal orientation of the synthesized material, TEM and HRTEM are used for characterization and analysis. Figure 2A demonstrates that the precursor MoO_3 has good single crystallinity, where SAED (Figure 2B) corresponds to the (002) plane of MoO_3. HRTEM (Figure 2C) indicates a crystal surface spacing of 0.198 nm that corresponds to the (002) face of MoO_3, which is in agreement with both results. Mo_2N retains the morphology and structure of the precursor, irrespective of it being a single crystal (Figures 1E, 2D) or polycrystalline (Figures 1F, 2G). Figure 2F taken with HRTEM from a single Mo_2N cube (Figure 2I) reveals highly resolved lattice stripes between the crystal planes with a crystalline spacing of 0.238 nm associated with the (111) plane of Mo_2N, which is consistent with SAED (Figure 2E). This further establishes that the sample has a defined crystal orientation. However, in Figures 2H,I, the SAED is tending to a ring-like pattern, and there are no distinct and regular lattice stripes, which suggests that the sample is polycrystalline.

NRR is a prototypical reduction process by hydrogenation. As shown in Figure 3A, N_2 bubbles to the cathode surface, and H^+ can be transferred through the electrolyte of 0.1 M HCl to react with the cathode Mo_2N to form NH_3. At first, we test the electrochemical performance of the sample and the catalytic activity of N_2. The LSV curves for the reduction reaction (NRR) are obtained by saturating with N_2 and Ar in 0.1 M HCl electrolyte (Figure 3B), and it is clear that the current density of N_2 increases slightly compared to Ar in the saturated

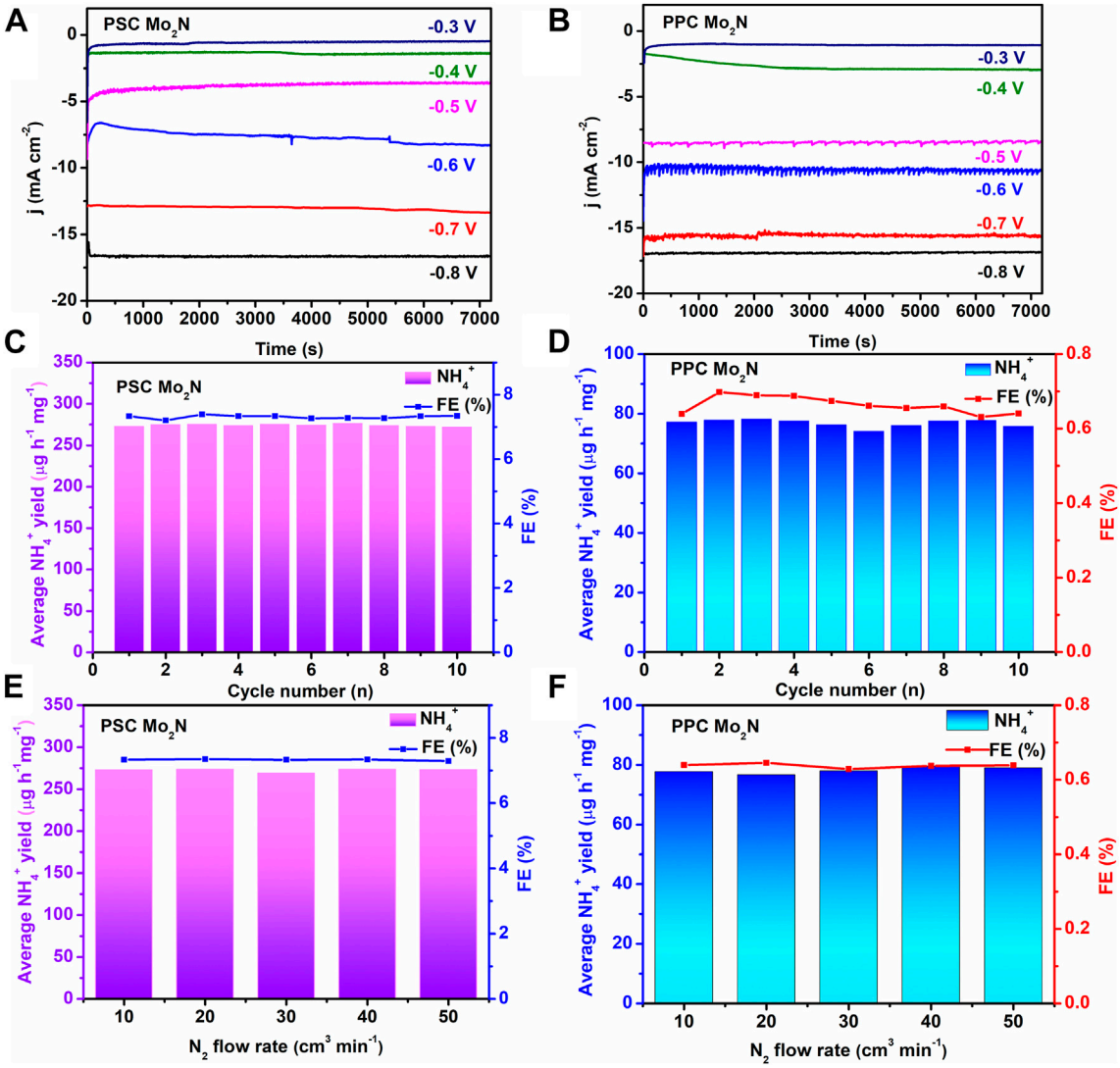

FIGURE 4
Current density curves of **(A)** PSC Mo_2N and **(B)** PPC Mo_2N of NRR with time at different voltages in 0.1 M HCl. The yields of NH_4^+ and FEs, 10 of **(C)** PSC Mo_2N and **(D)** PPC Mo_2N at −0.6 V vs. RHE potential during the cycle test. The yields of NH_4^+ and FEs of **(E)** PSC Mo_2N and **(F)** PPC Mo_2N catalysts at different N_2 flow rates.

electrolyte, which indicates the potential NRR activity of PSC Mo_2N. Apart from that, the AC impedance method is used to verify the electron transfer resistance of molybdenum nitride by fitting the EIS data on the sample to an equivalent circuit. The Nyquist curve (Figure 3C) shows that PSC Mo_2N has a smaller resistance than PPC Mo_2N and therefore has a higher current for the same voltage conditions applied. This indicates that the porous single crystal is conducive to carrier migration, which has better catalytic properties. All these results clearly indicate that the porous Mo_2N single crystals are more effective as electrocatalysts than polycrystals.

In the next step, we collect the products at different voltages at the same time and analyze their contents by cation chromatography. The results are shown in Figures 3D,E, which exhibit the NH_4^+ yields and FEs of PSC Mo_2N and PPC Mo_2N at different voltages. Among them, the catalytic effect of the catalysts is best at −0.6 V, when the NH_4^+ production rate of PPC Mo_2N is 77.78 μg h^{-1} mg^{-1} and the FE reached 0.6%, while the NH_4^+ production rate of PSC Mo_2N reached 272.56 μg h^{-1} mg^{-1} and the FE reached 7.3%. Obviously, PSC Mo_2N implies extremely high catalytic activity compared to PPC Mo_2N. The NH_4^+ yield and FE content increase with the increase in negative voltage; however, the yield of NH_4^+ and FE decreases significantly when it passes −0.6 V vs. RHE. It is possible that the hydrogen evolution reaction (HER) competes fiercely at the Mo_2N electrode to preferentially occupy the active

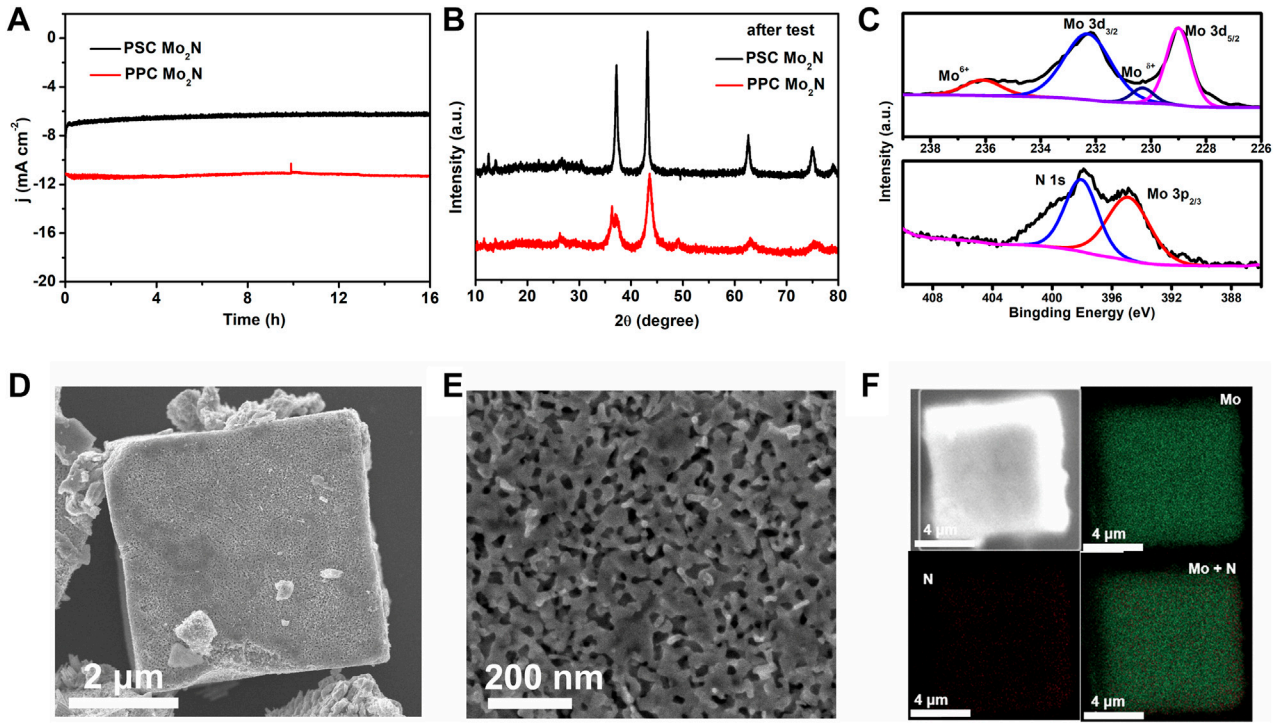

FIGURE 5
(A) Timing ampere curve of PSC Mo_2N and PPC Mo_2N electrolysis for 16 h at a potential of −0.6 V vs. RHE. **(B)** XRD of PSC Mo_2N and PPC Mo_2N after a long-term reaction. **(C)** Mo_2N of the XPS energy spectrum after a long-term reaction. **(D)** SEM images of different magnifications after the reaction. **(E)** Magnified view of SEM of PSC Mo_2N. **(F)** EDX elemental mapping of Mo and N in Mo_2N microcubes.

site with a large amount of free H and limit the effective trapping of N_2, hindering the forward progress of the NRR reaction. Compared with other water-based catalysts, PSC Mo_2N has higher ammonia yield and FE. The specific performance of other catalysts is shown in Supplementary Table S1.

The effect of other impurities in the experiments is excluded by conducting control experiments on the precursor MoO_3 and carbon paper on the results. The results demonstrate that the NRR rate of Mo_2N in Figure 3F is much higher than that of the MoO_3 single crystal (26.21 $\mu g\ h^{-1}\ mg^{-1}$), which implies that N plays an important role in the NRR and excludes the influence of surface oxidation on this reaction. At the same time, the bare CP shows weak NH_4^+ production, which has been subtracted from the starting data to reduce the experimental error. PSC Mo_2N and PPC Mo_2N have similar morphology and dimensions, but they have different specific surface areas, pore size, and lattice arrangement, leading to different ammonia yields of both. This suggests porous single crystals with large specific surface area and lattice continuity can reduce the energy loss of electron transfer between crystals, which results in higher catalytic activity. Therefore, PSC Mo2N exhibits excellent catalytic performance, which is consistent with the experimental results.

Durability is an important credential for assessing NRR response. Figures 4A,B indicate that the relative current density of PSC Mo_2N and PPC Mo_2N catalysts reduced to ammonia at different potentials respectively is stable, which shows the excellent durability of catalysts. Moreover, as the cathodic potential increases, the current density slightly decreases and the HER process is enhanced, inhibiting the NRR reaction, which is also consistent with the decrease of NH_4^+ production and FE. To further evaluate the stability of this catalytic process, we test the samples for 10 cycles at −0.6 V (Figures 4C,D), and the NH_4^+ production rate and FEs have no significant changes, indicating that they have good stability for NRR. In addition, the effect of a different N_2 flow rate on the product is also tested in this electrocatalytic process. As shown in Figures 4E,F, the approximately constant yields of NH_4^+ and FEs demonstrate that the N_2 diffusion rate has no obvious effect on the reaction, which ruled out the effect of the inlet concentration on this reaction. We perform some controlled experiments to verify the reliability of Mo_2N/CP for the electrochemical reduction of N_2 to NH_3. N_2 is led into the electrochemical reaction cell under open-circuit conditions, and saturated-Ar and saturated-N_2 gas flows are introduced separately for 2 h at −0.6 V vs. RHE, respectively. In summary, the influence of the external environment on the reaction during the experiment is excluded, indicating that the obtained NH_3 is derived from Mo_2N/CP.

We test the long-term electrolysis process, as shown in Figure 5A, and the current density electrochemical NRR process hardly changes significantly within 16 h, indicating the excellent performance of the Mo_2N catalyst. We perform a series of characterizations on the tested PSC Mo_2N such as XRD (Figure 5B), XPS (Figure 5C), SEM (Figures 5D,E), EDX (Supplementary Figure S4), and Mapping (Figure 5F). The test results clearly show that the phase composition, valence state, and elemental distribution of the catalyst itself have not changed significantly compared with those before the reaction, indicating that no other impurity phases are generated in the catalyst during the reaction. Further from the microscopic scale, PSC Mo_2N is able to maintain its initial composition and original cubic morphology after electrolysis, which also proves that the catalytic process is reproducibly cyclable and stable.

The aforementioned results and previous literature reports confirm that the possible NRR mechanism of Mo_2N can be described by the Mars–van Krevelen (MvK) process (Supplementary Figure S5) (Abghoui et al., 2016; Yang et al., 2017; Ren et al., 2018; Jin et al., 2019). First, H^+ is adsorbed on the N atoms on the surface of Mo_2N. Second, N vacancies appear on the catalyst face due to the departure of NH_3 molecules. Then, N_2 molecules occupy the vacancies, attracting H^+ to approach. Finally, NH_3 is released from the catalyst surface, and the Mo_2N catalyst returned to its original state. A steady stream of hydrogen ions in the electrolyte promotes the cyclic reaction. In the process of reaction, the porous structure increases the reaction area of the N atom and the active site of the reaction. Single-crystal materials are characterized by lattice continuity, so the migration process of N atoms is not blocked by grain boundaries. Compared with polycrystalline materials, it reduces the reaction kinetic energy of N atom migration, promotes the charge transfer of N atoms at the grain boundary, and accelerates the reaction rate. These results indicate that porous single-crystal molybdenum nitride has fine catalytic activity for the NRR reaction.

Conclusion

In summary, we prepare PSC Mo_2N and PPC Mo_2N. Among them, PSC Mo_2N reduces the charge transfer rate between grain boundaries and improves the rate and stability of the catalytic reaction due to its single-crystal nature. Compared with PPC Mo_2N, PSC Mo_2N exhibits excellent catalytic performance at −0.6 V vs. RHE, resulting in FE and yield of NH_4^+ up to 7.3% and 272.56 $\mu g\, h^{-1}\, mg^{-1}$. In addition, the reaction has superior recyclability and electrochemical durability, which maintains approximately constant yields of NH_3 and FE during 10 cycles and hardly weakens after 16 h long-term electrolysis. This work explores a novel avenue for the reasonable design and advancement of the molybdenum-based porous single crystal as the electrocatalysts of the artificial nitrogen fixation reaction.

Data availability statement

The original contributions presented in the study are included in the article/Supplementary Material; further inquiries can be directed to the corresponding author.

Author contributions

All authors listed have made a substantial, direct, and intellectual contribution to the work and approved it for publication. Investigation, data curation, software, formal analysis, visualization, writing—original draft: XL, Funding acquisition, project operation, writing review and editing: KX.

Funding

This work was supported by the National Key Research and Development Program of China (2021YFA1501500), the Natural Science Foundation of China (91845202), and the Strategic Priority Research Program of Chinese Academy of Sciences (XDB2000000).

Conflict of interest

Author KX was employed by the Advanced Energy Science and Technology Guangdong Laboratory.

The remaining author declares that the research was conducted in the absence of any commercial or financial relationships that could be construed as a potential conflict of interest.

Publisher's note

Supplementary material

The Supplementary Material for this article can be found online at the following link: https://www.frontiersin.org/articles/10.3389/fmats.2022.1097547/full#supplementary-material

References

Abghoui, Y., Garden, A. L., Howalt, J. G., Vegge, T., and Skúlason, E. (2016). Electroreduction of N_2 to ammonia at ambient conditions on mononitrides of Zr, Nb, Cr, and V: A dft guide for experiments. *ACS Catal.* 6, 635–646. doi:10.1021/acscatal.5b01918

Afanasiev, P. (2002). New single source route to the molybdenum nitride Mo_2N. *Inorg. Chem.* 41, 5317–5319. doi:10.1021/ic025564d

Aioub, M., Panikkanvalappil, S. R., and El-Sayed, M. A. (2017). Platinum-Coated gold nanorods: Efficient reactive oxygen scavengers that prevent oxidative damage toward healthy, untreated cells during plasmonic photothermal therapy. *ACS Nano* 11, 579–586. doi:10.1021/acsnano.6b06651

Amar, I. A., Lan, R., Petit, C. T. G., and Tao, S. (2011). Solid-state electrochemical synthesis of ammonia: A review. *J. Solid State Electrochem.* 15, 1845–1860. doi:10.1007/s10008-011-1376-x

Banerjee, A., Yuhas, B. D., Margulies, E. A., Zhang, Y., Shim, Y., Wasielewski, M. R., et al. (2015). Photochemical nitrogen conversion to ammonia in ambient conditions with femos-chalcogels. *J. Am. Chem. Soc.* 137, 2030–2034. doi:10.1021/ja512491v

Bao, D., Zhang, Q., Meng, F. L., Zhong, H. X., Shi, M. M., Zhang, Y., et al. (2017). Electrochemical reduction of N_2 under ambient conditions for artificial N2Fixation and renewable energy storage using N_2/NH_3 cycle. *Adv. Mat.* 29, 1604799. doi:10.1002/adma.201604799

Brown, K. A., Harris, D. F., Wilker, M. B., Rasmussen, A., Khadka, N., Hamby, H., et al. (2016). Light-driven dinitrogen reduction catalyzed by a CdS:nitrogenase MoFe protein biohybrid. *Science* 352, 448–450. doi:10.1126/science.aaf2091

Costentin, C., Robert, M., and Savéant, J. M. (2013). Catalysis of the electrochemical reduction of carbon dioxide. *Chem. Soc. Rev.* 42, 2423–2436. doi:10.1039/c2cs35360a

Guo, C., Ran, J., Vasileff, A., and Qiao, S. Z. (2018). Rational design of electrocatalysts and photo(electro)catalysts for nitrogen reduction to ammonia (NH_3) under ambient conditions. *Energy Environ. Sci.* 11, 45–56. doi:10.1039/c7ee02220d

Han, D., Liu, X., Cai, J., Xie, Y., Niu, S., Wu, Y., et al. (2021). Superior surface electron energy level endows WP_2 nanowire arrays with N2 fixation functions. *J. Energy Chem.* 59, 55–62. doi:10.1016/j.jechem.2020.11.006

Han, J., Ji, X., Ren, X., Cui, G., Li, L., Xie, F., et al. (2018). MoO_3 nanosheets for efficient electrocatalytic N_2 fixation to NH_3. *J. Mat. Chem. A* 6, 12974–12977. doi:10.1039/c8ta03974g

Jin, H., Li, L., Liu, X., Tang, C., Xu, W., Chen, S., et al. (2019). Nitrogen vacancies on 2D layered W_2N_3: A stable and efficient active site for nitrogen reduction reaction. *Adv. Mat.* 31, 1902709. doi:10.1002/adma.201902709

Kyriakou, V., Garagounis, I., Vourros, A., Vasileiou, E., and Stoukides, M. (2020). An electrochemical haber-bosch process. *Joule* 4, 142–158. doi:10.1016/j.joule.2019.10.006

Li, X., Ren, X., Liu, X., Zhao, J., Sun, X., Zhang, Y., et al. (2019). A MoS_2 nanosheet-reduced graphene oxide hybrid: An efficient electrocatalyst for electrocatalytic N_2 reduction to NH_3 under ambient conditions. *J. Mat. Chem. A* 7, 2524–2528. doi:10.1039/c8ta10433f

Lin, G., Li, H., and Xie, K. (2022). Identifying and engineering active sites at the surface of porous single-crystalline oxide monoliths to enhance catalytic activity and stability. *CCS Chem.* 4, 1441–1451. doi:10.31635/ccschem.021.202000740

Lin, G., Li, H., and Xie, K. (2020). Twisted surfaces in porous single crystals to deliver enhanced catalytic activity and stability. *Angew. Chem. Int. Ed.* 59, 16440–16444. doi:10.1002/anie.202006299

Liu, G., Cui, Z., Han, M., Zhang, S., Zhao, C., Chen, C., et al. (2019). Ambient electrosynthesis of ammonia on a core–shell-structured Au@CeO_2 catalyst: Contribution of oxygen vacancies in CeO_2. *Chem. Eur. J.* 25, 5904–5911. doi:10.1002/chem.201806377

Liu, J., Tang, S., Lu, Y., Cai, G., Liang, S., Wang, W., et al. (2013). Synthesis of Mo_2N nanolayer coated MoO_2 hollow nanostructures as high-performance anode materials for lithium-ion batteries. *Energy Environ. Sci.* 6, 2691–2697. doi:10.1039/c3ee41006d

Lu, Z., Zhou, G., Li, B., Xu, Y., Wang, P., Yan, H., et al. (2022). Heterotopic reaction strategy for enhancing selective reduction and synergistic oxidation ability through trapping Cr (VI) into specific reaction site: A stable and self-cleaning ion imprinted CdS/htnw photocatalytic membrane. *Appl. Catal. B Environ.* 301, 120787. doi:10.1016/j.apcatb.2021.120787

Nazemi, M., Panikkanvalappil, S. R., and El-Sayed, M. A. (2018). Enhancing the rate of electrochemical nitrogen reduction reaction for ammonia synthesis under ambient conditions using hollow gold nanocages. *Nano Energy* 49, 316–323. doi:10.1016/j.nanoen.2018.04.039

Ou, P., Zhou, X., Meng, F., Chen, C., Chen, Y., and Song, J. (2019). Single molybdenum center supported on N-doped black phosphorus as an efficient electrocatalyst for nitrogen fixation. *Nanoscale* 11, 13600–13611. doi:10.1039/c9nr02586c

Ozkan, U. S., Zhang, L., and Clark, P. A. (1997). Performance and postreaction characterization of γ-Mo_2N catalysts in simultaneous hydrodesulfurization and hydrodenitrogenation reactions. *J. Catal.* 172, 294–306. doi:10.1006/jcat.1997.1873

Ren, X., Cui, G., Chen, L., Xie, F., Wei, Q., Tian, Z., et al. (2018). Electrochemical N_2 fixation to NH_3 under ambient conditions: Mo2N nanorod as a highly efficient and selective catalyst. *Chem. Commun.* 54, 8474–8477. doi:10.1039/c8cc03627f

Service, R. F. (2014). New recipe produces ammonia from air, water, and sunlight. *Science* 80345, 610. doi:10.1126/science.345.6197.610

She, Z. W., Kibsgaard, J., Dickens, C. F., Chorkendorff, I., Nørskov, J. K., and Jaramillo, T. F. (2017). Combining theory and experiment in electrocatalysis: Insights into materials design. *Science* 80, eaad4998. doi:10.1126/science.aad4998

Sun, S., Li, X., Wang, W., Zhang, L., and Sun, X. (2017). Photocatalytic robust solar energy reduction of dinitrogen to ammonia on ultrathin MoS_2. *Appl. Catal. B Environ.* 200, 323–329. doi:10.1016/j.apcatb.2016.07.025

Tao, H., Choi, C., Ding, L. X., Jiang, Z., Han, Z., Jia, M., et al. (2019). Nitrogen fixation by Ru single-atom electrocatalytic reduction. *Chem* 5, 204–214. doi:10.1016/j.chempr.2018.10.007

Van Der Ham, C. J. M., Koper, M. T. M., and Hetterscheid, D. G. H. (2014). Challenges in reduction of dinitrogen by proton and electron transfer. *Chem. Soc. Rev.* 43, 5183–5191. doi:10.1039/c4cs00085d

Wickramasinghe, L. A., Ogawa, T., Schrock, R. R., and Müller, P. (2017). Reduction of dinitrogen to ammonia catalyzed by molybdenum diamido complexes. *J. Am. Chem. Soc.* 139, 9132–9135. doi:10.1021/jacs.7b04800

Wu, D., Wang, Y., Ma, N., Cao, K., Zhang, W., Chen, J., et al. (2019). Single-crystal-like ZnO mesoporous spheres derived from metal organic framework delivering high electron mobility for enhanced energy conversion and storage performances. *Electrochim. Acta* 305, 474–483. doi:10.1016/j.electacta.2019.03.077

Xiao, Y., and Xie, K. (2022). Active exsolved metal–oxide interfaces in porous single-crystalline ceria monoliths for efficient and durable CH_4/CO_2 reforming. *Angew. Chem. Int. Ed. Engl.* 61, e202113079. doi:10.1002/anie.202113079

Yang, D., Chen, T., and Wang, Z. (2017). Electrochemical reduction of aqueous nitrogen (N2) at a low overpotential on (110)-oriented Mo nanofilm. *J. Mat. Chem. A* 5, 18967–18971. doi:10.1039/c7ta06139k

Yoon, S., Jung, K. N., Jin, C. S., and Shin, K. H. (2012). Synthesis of nitrided MoO_2 and its application as anode materials for lithium-ion batteries. *J. Alloys Compd.* 536, 179–183. doi:10.1016/j.jallcom.2012.04.116

Zhang, F., Xi, S., Lin, G., Hu, X., Lou, X. W., David)and Xie, K. (2019). Metallic porous iron nitride and tantalum nitride single crystals with enhanced electrocatalysis performance. *Adv. Mat.* 31, 1806552. doi:10.1002/adma.201806552

Zhang, L., Ji, X., Ren, X., Luo, Y., Shi, X., Asiri, A. M., et al. (2018). Efficient electrochemical N_2 reduction to NH_3 on Mon nanosheets Array under ambient conditions. *ACS Sustain. Chem. Eng.* 6, 9550–9554. doi:10.1021/acssuschemeng.8b01438

Zhang, M. Di, Yi, J. D., Huang, Y. B., and Cao, R. (2021). Covalent triazine frameworks-derived N, P dual-doped porous carbons for highly efficient electrochemical reduction of CO_2. *Chin. J. Struc Chem.* 40, 1213–1222. doi:10.14102/j.cnki.0254-5861.2011-3118

frontiers | Frontiers in Materials

TYPE Mini Review
PUBLISHED 05 January 2023
DOI 10.3389/fmats.2022.1118943

OPEN ACCESS

EDITED BY
Jianlei Wang,
Chinese Academy of Sciences (CAS), China

REVIEWED BY
Yao Yuan,
Xiamen University of Technology, China
Rongmin Dun,
Structural Ceramics Engineering Research Center (CAS), China

*CORRESPONDENCE
Yuewei Li,
ywli@hqu.edu.cn

SPECIALTY SECTION
This article was submitted to Polymeric and Composite Materials, a section of the journal Frontiers in Materials

RECEIVED 08 December 2022
ACCEPTED 20 December 2022
PUBLISHED 05 January 2023

CITATION
Li Y, Wang W, Wu F and Kankala RK (2023), Vat polymerization-based 3D printing of nanocomposites: A mini review. *Front. Mater.* 9:1118943. doi: 10.3389/fmats.2022.1118943

Vat polymerization-based 3D printing of nanocomposites: A mini review

Yuewei Li[1,2]*, Wanyue Wang[1], Fuhang Wu[1] and Ranjith Kumar Kankala[1,2]

[1]Institute of Biomaterials and Tissue Engineering, Huaqiao University, Xiamen, China, [2]Fujian Provincial Key Laboratory of Biochemical Technology (Huaqiao University), Xiamen, China

Vat polymerization, the earliest and most established 3D printing technology, offers abundant advantages of high-precision fabrication and rapid printing speed, among others. This technology is often applied to fabricated objects with complex and delicate structures, which are of specific interest in numerous fields. However, it suffers from poor mechanical properties of the resultant printed parts due to layer-by-layer manufacturing patterns and the absence of functionality, restricting the broader application of printed objects. Integrating nanomaterials with vat polymerization-based 3D printing endows the creation of products with enhanced properties and unprecedented functional adjunction with flexible designs. Giving a brief description of 3D printing technology, this review illustrates the principles and characteristics of vat polymerization technology. In this mini-review, we emphasize recent advances in nanocomposite fabricated using vat polymerization, predominantly focusing on creating nanocomposites with enhanced mechanical, thermal properties, and electrical conductivity. Finally, we summarize the article with the challenges being faced and future perspectives of nanocomposites fabricated from vat polymerization.

KEYWORDS

vat polymerization, 3D printing, nanocomposites, mechanical properties, thermal properties, conductivity

1 Introduction

3D printing, often referred to as additive manufacturing, is a disruptive manufacturing technology in which replica physical objects with complicated internal structures are fabricated directly from interacted digital models in a layer-by-layer fashion. In recent times, 3D printing has been employed in various fields of research due to the enormous advantages of product-design freedom, simple customization, and the waste minimization of raw materials, including catalysis (Lawson et al., 2021), electronics (Espera et al., 2019), aerospace (Joshi and Sheikh, 2015), and tissue engineering (Distler and Boccaccini, 2020). According to the principle of pattern formation, 3D printing employs diverse technologies, including material extrusion, binder jetting, material jetting, directed energy deposition, sheet lamination, powder bed fusion, and vat photo polymerization (Lee et al., 2017). Each technology has its pros and cons in terms of practical applicability. Nevertheless, choosing a unique technology often considers the manufacturing material, printing speed, resolution, cost, and performance requirements of the final product (Clarissa et al., 2021).

The lack of reliable load-bearing ability and functionality in 3D-printed structural work pieces makes them insufficiently fabricated as functional end-use products. To address this concern, the possibility of tuning the performances by introducing nanomaterials into 3D

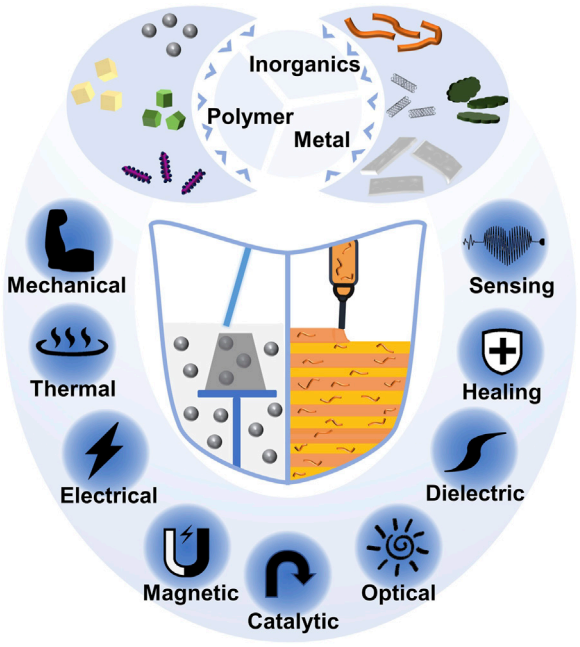

FIGURE 1
Nanomaterials used in 3D printing.

printed constructs furnishes an attractive path for achieving high performance and multi-functional integration (Kankala et al., 2018; Valino et al., 2019). Due to the advancement of nanotechnology, incorporating nanofillers (in the range of 1–100 nm) produces different properties than their micro- and macro-sized counterparts (Roduner, 2006). Nanomaterials have a wide range of application prospects owing to their electrical, magnetic, thermal, optical, sensitive properties, and surface stability (Baig et al., 2021). These unique interactions give rise to the optimal control of polymer performance. Several efforts have been dedicated to developing nanocomposites based on 3D printing by incorporating ceramic, metallic, and/or organic fillers to improve thermal, electrical, mechanical, and other properties to overcome the limitations of traditional single-component materials (Campbell and Ivanova, 2013; Hassan et al., 2019; Wang et al., 2020) (Figure 1).

2 Vat polymerization

Vat polymerization, the most mature and widely used 3D printing technology, offers the advantages of high resolution and printing efficiency. It can be subdivided into stereolithography appearance (SLA), digital light processing (DLP), liquid crystal display, continuous liquid interface production, two-photon 3D printing, and computed axial lithography (Sampson et al., 2021). Vat polymerization is based on photopolymerization, where a photosensitive liquid resin can be utilized as the raw material. As illustrated in Figure 2, three processes are commonly used: The design of a computer-aided model, the development of vat polymerization, and dispensing for practical applications. During the printing process, laser emitters or a projector projects a pattern of light onto a layer of liquid photosensitive resin that hardens in the desired shape. The platform engaged as the printed part moves in the layer-thickness, and the resin is replenished. This procedure is repeated until the successful construction of the final 3D object. The light source and imaging systems differ for different vat polymerization technologies to some extent, while the control and stepping systems remain similar. The photosensitive resin can be cured under light irradiation at a corresponding wavelength. While in places without irradiation, it can be maintained as a liquid. Hence, parts can be easily separated from the liquid resin. It is noteworthy to acknowledge the high precision of light irradiation and the rapid photocuring polymerization of vat polymerization for the quick printing of complex objects.

Photosensitive resin for vat polymerization is typically composed of initiator, oligomer, monomer (active diluent), and additives (Skliutas et al., 2018). The initiators in photosensitive resin are shifted to highly active intermediates under irradiation at specific wavelengths. These trigger cross-linking reactions between oligomers and monomers in the photosensitive resin, transforming it from the original liquid resin into a solid object. The typical raw materials and photocuring mechanisms are chosen depending on the laser wavelength and the printer projector. Acrylate resins, which undergo a free-radical polymerization mechanism, are the most popular photosensitive resin for vat polymerization technologies due to their high photopolymerization curing speed. However, acrylate resins exhibit large volume shrinkage after photopolymerization, resulting in a reduction in printing precision and the deformation of printed objects. To overcome the problem of volume shrinkage, epoxy resin has been incorporated into cationic photopolymerization (Crivello, 1999). However, the photopolymerization induction period for the cationic photosensitive resin remains longer and has a relatively slower

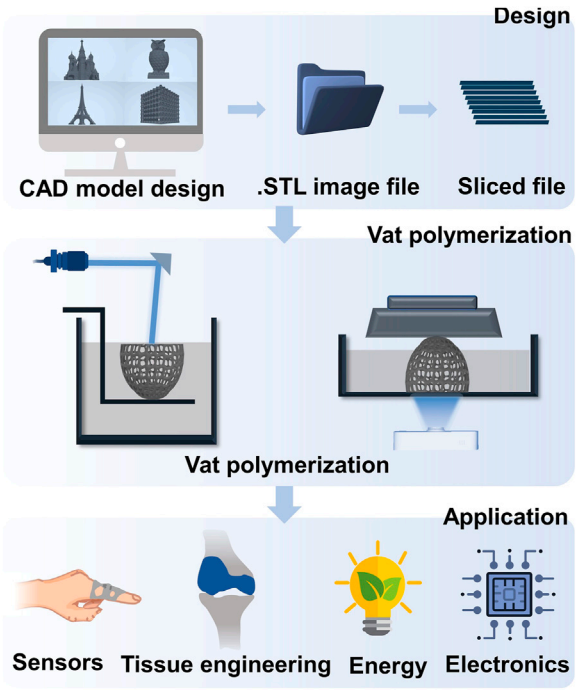

FIGURE 2
Schematic illustration of the vat polymerization process, from design to application.

curing rate. Hence, a hybrid photosensitive resin containing acrylate and epoxy resin is an optimal choice when considering volume shrinkage, curing speed, and cost when the light source matches. Although numerous studies have been devoted to obtaining multiple printed parts by adjusting and designing segments constructed by photosensitive resin polymer backbones (Peng et al., 2020; Zhou et al., 2020; Yiming et al., 2021), currently, vat polymerization products generally suffer from several disadvantages, such as fragility, ease of deformation, poor thermal resistance, and low biocompatibility. However, there is an urgent need for higher-performance products to meet high-end application demands.

3 Nanocomposites from vat polymerization

3.1 Mechanical enhancement

The demand for lightweight, high-strength materials is increasing in various engineering sectors. Polymeric composites, including nanofillers, offer outstanding improvements at relatively lower loadings than micro-sized fillers, helping achieve high-level performance improvements across various advanced applications (Quaresimin et al., 2012). Recently, the mechanical properties of engineered structural components, including structural integrity and durability, produced by vat polymerization have been enhanced by incorporating second-phase nanofillers.

Nanoparticles are widely used to enhance the mechanical properties of vat polymerization polymers because of their low cost and the significant enhancements they deliver, of which, SiO_2 nanoparticles are the most widely used. In an instance, (Weng et al., 2016) and colleagues demonstrated that the absorption and scattering of UV light by SiO_2 nanoparticles were weaker than that of other 1D and 2D materials containing silicon elements (i.e., attapulgite and montmorillonite), which improved the tensile strength and elastic modulus of SiO_2-containing nanocomposites. In another instance, Chiappone and coworkers (Chiappone et al., 2016) introduced the precursor tetraethoxysilane to a photosensitive resin and post-treated samples with acidic vapor to generate SiO_2 nanoparticles *in situ* by the sol-gel reaction of the precursor in the polymer network after DLP printing. The generation of a SiO_2 inorganic phase contributed to significant enhancement of the tensile and compressive strengths, modulus, and surface hardness of the fabricated samples due to the preferential growth of induced nanoparticles on the surface of the samples. Moreover, different surface treatments create diverse nanoparticle interfacial adhesion and dispersion stability, leading to altered mechanical properties of various nanocomposites (Song et al., 2018). Some other 1D nanomaterials, including nano-TiO_2 (Duan et al., 2011), Cu nanopowder (Vidakis et al., 2022), and polyhedral oligomeric silsesquioxane (Li et al., 2019), have been used as reinforcing phases for photosensitive resins. In addition, the specific orientation of reinforcing fillers is believed to supply the creation of composites with design properties (Martin et al., 2015).

Carbon nanotubes (CNTs) are structurally stable, long, thin carbon columns with high aspect ratios. These CNTs often exhibit excellent polymer reinforcement due to their ability to cause the formation of higher-order interphase polymer layers and promote mechanical strength through interfacial stress transfer between nanotubes and polymers (Wong et al., 2003; Spitalsky et al., 2010). Creating CNT composites with photosensitive resins greatly improves the performance of the matrix. Sandoval et al., (2007) demonstrated that the ultimate tensile and fracture stress of SLA epoxy-based resins increased by 17% and 37%, respectively, with the introduction of .05% (w/v) multiwall CNTs (MWCNTs). Introducing MWCNTs would create strong interfacial bonding between the SLA epoxy matrix and buckled MWCNTs. However, the resultant mechanical properties of nanocomposites depended on the arrangement of CNTs in resins (Chavez et al., 2019). In addition, other 1D nanofillers, such as boehmite nanowires (Han et al., 2018), Al_2O_3 nanowires (Han et al., 2017), and cellulose nanocrystals (Kumar et al., 2012), have been incorporated into photosensitive resins for vat polymerization to enhance mechanical properties.

Graphene, a single layer of carbon atoms, consists of a backbone of sp^2 hybrid bonds filled in a honeycomb lattice. 2p orbitals forming the π state bands delocalize over the carbon layer and result in the highly stiff characteristic graphene (Papageorgiou et al., 2017), which is often applied in photosensitive resins (Li et al., 2018). The combination of enhanced strength and flexibility in SLA manufacturing is realized by introducing graphene oxide (GO), which is related to increasing the crystallinity of nanocomposites (Lin et al., 2015). Nanocomposites prepared by the bottom-up vat polymerization exhibit significant anisotropic mechanical properties because graphene nanosheets tend to be arranged more parallel in resins during 3D printing (Markandan and Lai, 2020). The annealing process after the completion of printing also affects the mechanical properties of nanocomposites (Manapat et al., 2017). In addition, Ti_3C_2 MXene, a novel 2D ultrathin nanomaterial, is an excellent candidate for enhancing the tensile strength of photosensitive resins to obtain reliable elastomers (Li et al., 2022a). The dispersion effect of nanofillers in photosensitive resins contributes directly to the strengthening development of 3D printed objects. A uniformly dispersed nanofiller can effectively absorb and dissipate energy, improving the mechanical properties of nanocomposites in terms of fracturing. Agglomerated nanofillers induce the formation of micro flaws, deteriorating the mechanical properties. Therefore, there is an optimum loading level for incorporated nanofillers to increase the mechanical strength of nanocomposites from vat polymerization.

3.2 Thermal enhancement

A growing task in the design and application of advanced devices is heat management. In this context, an expanding demand for high thermal conductivity materials that can dissipate waste heat from the operation processes of devices exists. The preparation of composites by introducing fillers, such as graphene, metal, and inorganic nanomaterials, is a promising strategy for improving the thermal conductivity of photosensitive resins (Lee et al., 2021; Pezzana et al., 2021). Carbon fibers, due to their remarkable thermal conductivity and high aspect ratio, are also widely used to enhance the thermal conductivity of polymers, which is beneficial for forming nanocomposite percolating networks (Hong et al., 2010). In a case, acidified vapor-grown carbon nanofiber (VGCF)-supplemented dual-cure photosensitive resins were prepared by the SLA technology (Li et al., 2022b). The addition of 2% w/w VGCFs increased the thermal conductivity of a composite by 79% compared to control through the transfer of thermal energy by VGCF phonons.

High filler loadings are typically necessary to achieve appropriately enhanced thermal conductivity in polymeric matrices. It has been reported that the 7.4 wt% loading of a polymer with graphene caused nozzle clogging in a fused filament fabrication printer (Wei et al., 2015). For vat polymerization, using liquid resin would avoid the problem of the repeated clogging of nozzles or spraying devices due to the introduced nanofillers. This would create a quantum leap in the thermal conductivity of printed products through the high loading of nanofillers. However, vat polymerization remains a significant challenge due to the processing requirements of photoactivity and viscosity. Yang et al., (2022) prepared a nanocomposite with a high loading (60 wt%) of micro silica, resulting in the improved thermal conductivity of .44 W m^{-1} K^{-1}, with 196.91% compared with the pure matrix. Nanocomposites assembled with high thermal conductivity due to closely arranged phonon transportation pathways in resin matrices could be applied to fabrication injection and vacuum casting molding to extend the service life. In addition, the fabrication of ultralow thermal conductivity thermoelectric materials can be realized by mixing thermoelectric materials, including $Bi_{0.5}Sb_{1.5}Te_3$ (He et al., 2015) and Ag_2Se (Park et al., 2021) materials, with photosensitive resins.

Incorporating nanoparticles also offers the possibility of improving the thermal stability of vat-polymerized printed fabrications. However, it should be noted that the thermal stability of the composite is influenced by the organic modifier, filler content, and structural features of nanocomposites (Leszczyńska et al., 2007). The introduction of nanoparticles can also effectively enhance the thermal resistance of nanocomposites (Chiu and Wu, 2008). Zhang et al., (2015) and colleagues dispersed SiO_2 nanoparticles, which modified the silane coupling agent, into a photosensitive resin by ultrasonic and a planetary ball mill treatment, followed by 3D printing. The glass-transition temperature of the nanocomposites increased from 67.28°C for the pure resin to 80.18°C for the nanocomposites with the addition of .7 wt% SiO_2. Similarly, the addition of a 1D nanomaterial, microcrystalline cellulose, had a formative influence on the thermal properties of the photosensitive resin, which increased the degradation temperature of the nanocomposite, and the β-relaxation of the photosensitive resin tended to move toward higher temperatures (Han et al., 2017).

3.3 Conductivity enhancement

3D printing has been used as an alternative approach for manufacturing conductive composites due to the advantages of reduced cost and eco-friendly features, which are of unique interest in various functional applications, such as electrodes (Ahn et al., 2009; Rymansaib et al., 2016), wearable devices (Hao et al., 2021), and sensors (Leigh et al., 2017). This method balances a low-cost, fast, and versatile production process with the excellent performance of the resultant products.

Metal fillers with good conductivity have been used for conductive materials in vat polymerization. Fantino and coworkers (Fantino et al., 2016) introduced silver nitrate to a photosensitive resin. The silver nitrate was reduced to silver nanoparticles *via* a UV post-curing process after DLP printing to prepare conductive nanocomposites. The direct loading of the filler affected the electrical conductivity of the composites: Increased amounts of silver nitrate increased the silver nanoparticle content in the matrix, thereby promoting the formation of charge movement paths between the nanoparticles, which led to a decline in the electrical resistance of the nanocomposites. However, due to its prohibitive cost and ease of oxidation, the application of metal has been limited.

In comparison, carbon fillers exhibit considerable stability and high conductivity, which makes them easier to obtain and more widely used (Gonzalez et al., 2017; Zhang et al., 2017). Therefore, CNTs are widely used due to their excellent electrical properties arising from the freedom of the movement of unpaired electrons in orbitals perpendicular to the π-π plane within the plane. Mu et al., (2017) and colleagues combined commercial photosensitive resin with MWCNTs to obtain conductive composite structures using a DLP printer. To optimize printability and conductivity, .3 wt% of MWCNTs was added, increasing the nanocomposite conductivity to .027 S m^{-1}. Guo and coworkers (Guo et al., 2020) prepared a DLP-printed conductive nanocomposite with 2 wt% carboxyl CNTs that exhibited an electrical conductivity of .13 S m^{-1}. These shreds of evidence indicated that the composites with high conductivity, high gauge strain sensors, and superior cycling stability could provide stable signal information for human motion monitoring.

The use of graphene is also an effective strategy for increasing the electrical conductivity of photosensitive resins. Since GO has better compatibility with photosensitive resins, GO can be used directly as a filler. It is reduced to graphene during post-processing after printing, and different post-processing processes affect the electrical conductivity of the samples (Chiappone et al., 2017). Nanocomposites post-cured by UV light exhibit a non-linear electrical correspondence due to uneven internal curing, while homogeneous thermally post-cured models show a linear electrical response. In addition, the combination of 1D and 2D nanofillers provides effective conductive pathways in nanocomposites and has been used to produce conductive structures (Han and Cho, 2018).

4 Challenges and outlook

Although numerous designs of vat polymerization-based 3D printed nanocomposites have been prepared, there is still a gap in meeting the demands of industrial applications, and many impediments, from molding craft to product performance, remain unsolved. First, the viscosity of photosensitive resin tends to increase with increased nanofiller content. Meanwhile, the polymer self-diffusion coefficient is reduced (Mu et al., 2009), challenging the leveling properties of photosensitive resin and thus affecting the surface quality of printed products (Gurr et al., 2008). Second, the random scattering of UV light in a photosensitive resin observed in vat polymerization has been attributed to either the aggregation of nanoparticles or the incorporation of overlarge nanofillers (Cho et al., 2005), resulting in reduced UV penetration depth and lateral resolution. Nevertheless, it should be noted that slower speeds and/or higher laser power are required to remedy the degeneration of curing depth and group conversions (Cheah et al., 1999). Third, it is difficult to disperse nanofillers uniformly with high surface energy in photosensitive resins, and weak interfacial interaction usually leads to poor performance of the fabricated parts. At the same time, the density of nanofillers and photosensitive resins usually differs, resulting in a tendency to settle in the resin without forming a stable dispersion. Therefore, the chemical compatibility of nanofillers with photosensitive resins must be considered to improve the stability of the resins, which contain nanofillers, and enhance the performance of printed parts.

Overcoming the current bottleneck in the vat polymerization-based 3D printing of nanocomposites requires a further reduction in the production costs of nanofillers and the improved compatibility of nanofillers and resin matrices. These aspects will undoubtedly result in the excellent performance and competitiveness of fabricated products towards the further development of the main directions. Various new vat-polymerized nanocomposites with outstanding performance, including magnetic, catalytic, and dielectric properties and so on, should be developed to meet new frontiers and evolving technology requirements. The evaluation criteria of vat-polymerized nanomaterials are necessary to establish and improve, favoring the development of new composites and selecting suitable materials for various applications.

Author contributions

YL investigated and processed the data, pointed out the framework of the paper, made a summary and analysis, supported the project and completed the writing of the article. WW and FW participated in proofreading and part of the writing. At the same time, RKK reviewed the paper.

Funding

This work was supported by the National Natural Science Foundation of China (32071323), the Natural Science Foundation of Fujian Province (2021J05054), the Fundamental Research Funds for the Central University (ZQN-1004), and the Scientific Research Funds of Huaqiao University (20BS302).

Conflict of interest

The authors declare that the research was conducted in the absence of any commercial or financial relationships that could be construed as a potential conflict of interest.

Publisher's note

All claims expressed in this article are solely those of the authors and do not necessarily represent those of their affiliated organizations, or those of the publisher, the editors and the reviewers. Any product that may be evaluated in this article, or claim that may be made by its manufacturer, is not guaranteed or endorsed by the publisher.

References

Ahn, B. Y., Duoss, E. B., Motala, M. J., Guo, X., Park, S. I., Xiong, Y., et al. (2009). Omnidirectional printing of flexible, stretchable, and spanning silver microelectrodes. *Science* 323, 1590–1593. doi:10.1126/science.1168375

Baig, N., Kammakakam, I., Falath, W., and Nanomaterials (2021). Nanomaterials: A review of synthesis methods, properties, recent progress, and challenges. *Mat. Adv.* 2, 1821–1871. doi:10.1039/d0ma00807a

Campbell, T. A., and Ivanova, O. S. (2013). 3D printing of multifunctional nanocomposites. *Nano Today* 8, 119–120. doi:10.1016/j.nantod.2012.12.002

Chavez, L. A., Regis, J. E., Delfin, L. C., Rosales, C. A. G., Kim, H., Love, N., et al. (2019). Electrical and mechanical tuning of 3D printed photopolymer–MWCNT nanocomposites through *in situ* dispersion. *J. Mat. Sci.* 136, 47600. doi:10.1002/app.47600

Cheah, C. M., Fuh, J. Y. H., Nee, A. Y. C., and Lu, L. (1999). Mechanical characteristics of fiber-filled photo-polymer used in stereolithography. *Rapid Prototyp. J.* 5, 112–119. doi:10.1108/13552549910278937

Chiappone, A., Fantino, E., Roppolo, I., Lorusso, M., Manfredi, D., Fino, P., et al. (2016). 3D printed PEG-based hybrid nanocomposites obtained by sol-gel technique. *ACS Appl. Mat. Interfaces* 8, 5627–5633. doi:10.1021/acsami.5b12578

Chiappone, A., Roppolo, I., Naretto, E., Fantino, E., Calignano, F., Sangermano, M., et al. (2017). Study of graphene oxide-based 3D printable composites: Effect of the *in situ* reduction. *Compos. Pt. B-Eng.* 124, 9–15. doi:10.1016/j.compositesb.2017.05.049

Chiu, S. H., and Wu, D. C. (2008). Preparation and physical properties of photopolymer/SiO_2 nanocomposite for rapid prototyping system. *J. Appl. Polym. Sci.* 107, 3529–3534. doi:10.1002/app.27535

Cho, J. D., Ju, H. T., and Hong, J. W. (2005). Photocuring kinetics of UV-initiated free-radical photopolymerizations with and without silica nanoparticles. *J. Polym. Sci. Pol. Chem.* 43, 658–670. doi:10.1002/pola.20529

Clarissa, W. H. Y., Chia, C. H., Zakaria, S., and Ycy, Evyan (2021). Recent advancement in 3-D printing: Nanocomposites with added functionality. *Prog. Addit. Manuf.* 7, 325–350. doi:10.1007/s40964-021-00232-z

Crivello, J. V. (1999). UV and electron beam-induced cationic polymerization. *Nucl. Instrum. Methods Phys. Res. Sect. B Beam Interact. Mater. Atoms* 151, 8–21. doi:10.1016/s0168-583x(99)00109-3

Distler, T., and Boccaccini, A. R. (2020). 3D printing of electrically conductive hydrogels for tissue engineering and biosensors–A review. *Acta Biomater.* 101, 1–13. doi:10.1016/j.actbio.2019.08.044

Duan, Y., Zhou, Y., Tang, Y., and Li, D. (2011). Nano-TiO_2-Modified photosensitive resin for RP. *Rapid Prototyp. J.* 17, 247–252. doi:10.1108/13552541111138360

Espera, A. H., Dizon, J. R. C., Chen, Q., and Advincula, R. C. (2019). 3D-Printing and advanced manufacturing for electronics. *Prog. Addit. Manuf.* 4, 245–267. doi:10.1007/s40964-019-00077-7

Fantino, E., Chiappone, A., Roppolo, I., Manfredi, D., Bongiovanni, R., Pirri, C. F., et al. (2016). 3D printing of conductive complex structures with *in situ* generation of silver nanoparticles. *Adv. Mat.* 28, 3712–3717. doi:10.1002/adma.201505109

Gonzalez, G., Chiappone, A., Roppolo, I., Fantino, E., Bertana, V., Perrucci, F., et al. (2017). Development of 3D printable formulations containing CNT with enhanced electrical properties. *Polymer* 109, 246–253. doi:10.1016/j.polymer.2016.12.051

Guo, B., Ji, X., Chen, X., Li, G., Lu, Y., and Bai, J. (2020). A highly stretchable and intrinsically self-healing strain sensor produced by 3D printing. *Virtual Phys. Prototyp.* 15, 520–531. doi:10.1080/17452759.2020.1823570

Gurr, M., Hofmann, D., Ehm, M., Thomann, Y., Kübler, R., and Mülhaupt, R. (2008). Acrylic nanocomposite resins for use in stereolithography and structural light modulation based rapid prototyping and rapid manufacturing technologies. *Adv. Funct. Mat.* 18, 2390–2397. doi:10.1002/adfm.200800344

Han, H., and Cho, S. (2018). Fabrication of conducting polyacrylate resin solution with polyaniline nanofiber and graphene for conductive 3D printing application. *Polymers* 10, 1003. doi:10.3390/polym10091003

Han, Y., Wang, F. K., Wang, H., Jiao, X., and Chen, D. (2018). High-strength boehmite-acrylate composites for 3D printing: Reinforced filler-matrix interactions. *Compos. Sci. Technol.* 154, 104–109. doi:10.1016/j.compscitech.2017.10.026

Han, Y., Yeo, C. C. J., Chen, D., Wang, F., Chong, Y., Li, X., et al. (2017). Nanowire enhanced dimensional accuracy in acrylate resin-based 3D printing. *New J. Chem.* 41, 8407–8412. doi:10.1039/c7nj02145c

Hao, S., Li, T., Yang, X., Song, H., and Ultrastretchable (2021). Ultrastretchable, adhesive, fast self-healable, and three-dimensional printable photoluminescent ionic skin based on hybrid network ionogels. *ACS Appl. Mat. Interfaces* 14, 2029–2037. doi:10.1021/acsami.1c21325

Hassan, M., Dave, K., Chandrawati, R., Dehghani, F., and Gomes, V. G. (2019). 3D printing of biopolymer nanocomposites for tissue engineering: Nanomaterials, processing and structure-function relation. *Eur. Polym.* 12, 1109340.

He, M., Zhao, Y., Wang, B., Xi, Q., Zhou, J., and Liang, Z. (2015). 3D printing fabrication of amorphous thermoelectric materials with ultralow thermal conductivity. *Small* 11, 5889–5894. doi:10.1002/smll.201502153

Hong, J., Park, D. W., and Shim, S. E. (2010). A review on thermal conductivity of polymer composites using carbon-based fillers: Carbon nanotubes and carbon fibers. *Carbon Lett.* 11, 347–356. doi:10.5714/cl.2010.11.4.347

Joshi, S. C., and Sheikh, A. A. (2015). 3D printing in aerospace and its long-term sustainability. *Virtual Phys. Prototyp.* 10, 175–185. doi:10.1080/17452759.2015.1111519

Kankala, R. K., Zhu, K., Sun, X. N., Liu, C. G., Wang, S. B., and andChen, A. Z. (2018). Cardiac tissue engineering on the nanoscale. *ACS Biomater. Sci. Eng.* 4, 800–818. doi:10.1021/acsbiomaterials.7b00913

Kumar, S., Hofmann, M., Steinmann, B., Foster, E. J., and Weder, C. (2012). Reinforcement of stereolithographic resins for rapid prototyping with cellulose nanocrystals. *ACS Appl. Mat. Interfaces* 4, 5399–5407. doi:10.1021/am301321v

Lawson, S., Li, X., Thakkar, H., Rownaghi, A. A., and Rezaei, F. (2021). Recent advances in 3D printing of structured materials for adsorption and catalysis applications. *Chem. Rev.* 121, 6246–6291. doi:10.1021/acs.chemrev.1c00060

Lee, J. Y., An, J., and Chua, C. K. (2017). Fundamentals and applications of 3D printing for novel materials. *Appl. Mat. Today* 7, 120–133. doi:10.1016/j.apmt.2017.02.004

Lee, S., Kim, Y., Park, D., and Kim, J. (2021). The thermal properties of a UV curable acrylate composite prepared by digital light processing 3D printing. *Compos. Commun.* 26, 100796. doi:10.1016/j.coco.2021.100796

Leigh, S. J., Bradley, R. J., Purssell, C. P., Billson, D. R., and Hutchins, D. A. (2017). A simple, low-cost conductive composite material for 3D printing of electronic sensors. *PLoS One* 7, e49365. doi:10.1371/journal.pone.0049365

Leszczyńska, A., Njuguna, J. A. K., Pielichowski, K., and Banerjee, J. R. (2007). Polymer/montmorillonite nanocomposites with improved thermal properties: Part I. Factors influencing thermal stability and mechanisms of thermal stability improvement. *Thermochim. Acta.* 453, 75–96. doi:10.1016/j.tca.2006.11.002

Li, J., Wang, L., Dai, L., Zhong, L., Liu, B., Ren, J., et al. (2018). Synthesis and characterization of reinforced acrylate photosensitive resin by 2-hydroxyethyl methacrylate-functionalized graphene nanosheets for 3D printing. *J. Mat. Sci.* 53, 1874–1886. doi:10.1007/s10853-017-1432-8

Li, Y., Kankala, R. K., Weng, Z., and Wu, L. (2022). Dual-cure vapor-grown carbon nanofiber-supplemented 3D-printed resin: Implications for improved stiffness and thermal resistance. *ACS Appl. Nano Mat.* 5, 9544–9553. doi:10.1021/acsanm.2c01774

Li, Y., Peng, S., Kankala, R. K., Wu, L., Chen, A. Z., and Wang, S. B. (2022). 3D printing of mechanically robust MXene-encapsulated polyurethane elastomer. *Compos. Pt. A-Appl. Sci. Manuf.* 163, 107182. doi:10.1016/j.compositesa.2022.107182

Li, Y., Zhong, J., Wu, L., Weng, Z., Zheng, L., Peng, S., et al. (2019). High performance POSS filled nanocomposites prepared via UV-curing based on 3D stereolithography printing. *Compos. Pt. A-Appl. Sci. Manuf.* 117, 276–286. doi:10.1016/j.compositesa.2018.11.024

Lin, D., Jin, S., Zhang, F., Wang, C., Wang, Y., Zhou, C., et al. (2015). 3D stereolithography printing of graphene oxide reinforced complex architectures. *Nanotechnology* 26, 434003. doi:10.1088/0957-4484/26/43/434003

Manapat, J. Z., Mangadlao, J. D., Tiu, B. D. B., Tritchler, G. C., and Advincula, R. C. (2017). High-strength stereolithographic 3D printed nanocomposites: Graphene oxide metastability. *ACS Appl. Mat. Interfaces* 9, 10085–10093. doi:10.1021/acsami.6b16174

Markandan, K., and Lai, C. Q. (2020). Enhanced mechanical properties of 3D printed graphene-polymer composite lattices at very low graphene concentrations. *Compos. Pt. A-Appl. Sci. Manuf.* 129, 105726. doi:10.1016/j.compositesa.2019.105726

Martin, J. J., Fiore, B. E., and Erb, R. M. (2015). Designing bioinspired composite reinforcement architectures via 3D magnetic printing. *Nat. Commun.* 6, 8641. doi:10.1038/ncomms9641

Mu, M. F., Clarke, N., Composto, R. J., and Winey, K. I. (2009). Polymer diffusion exhibits a minimum with increasing single-walled carbon nanotube concentration. *Macromolecules* 42, 7091–7097. doi:10.1021/ma901122s

Mu, Q., Wang, L., Dunn, C. K., Kuang, X., Duan, F., Zhang, Z., et al. (2017). Digital light processing 3D printing of conductive complex structures. *Addit. Manuf.* 18, 74–83. doi:10.1016/j.addma.2017.08.011

Papageorgiou, D. G., Kinloch, I. A., and andYoung, R. J. (2017). Mechanical properties of graphene and graphene-based nanocomposites. *Prog. Mat. Sci.* 90, 75–127. doi:10.1016/j.pmatsci.2017.07.004

Park, D., Lee, S., and Kim, J. (2021). Enhanced thermoelectric performance of UV-curable silver (I) selenide-based composite for energy harvesting. *Sci. Rep.* 11, 16683–16688. doi:10.1038/s41598-021-96267-x

Peng, S., Li, Y., Wu, L., Zhong, J., Weng, Z., Zheng, L., et al. (2020). 3D printing mechanically robust and transparent polyurethane elastomers for stretchable electronic sensors. *ACS Appl. Mat. Interfaces* 12, 6479–6488. doi:10.1021/acsami.9b20631

Pezzana, L., Riccucci, G., Spriano, S., Battegazzore, D., Sangermano, M., and Chiappone, A. (2021). 3D printing of pdms-like polymer nanocomposites with enhanced thermal conductivity: Boron nitride based photocuring system. *Nanomaterials* 11, 373. doi:10.3390/nano11020373

Quaresimin, M., Salviato, M., and Zappalorto, M. (2012). Strategies for the assessment of nanocomposite mechanical properties. *Compos. Pt. B-Eng.* 43, 2290–2297. doi:10.1016/j.compositesb.2011.12.012

Roduner, E. (2006). Size matters: Why nanomaterials are different. *Chem. Soc. Rev.* 35, 583–592. doi:10.1039/b502142c

Rymansaib, Z., Iravani, P., Emslie, E., Medvidović-Kosanović, M., Sak-Bosnar, M., Verdejo, R., et al. (2016). All-polystyrene 3D-printed electrochemical device with embedded carbon nanofiber-graphite-polystyrene composite conductor. *Electroanalysis* 28, 1517–1523. doi:10.1002/elan.201600017

Sampson, K. L., Deore, B., Go, A., Nayak, M. A., Orth, A., Gallerneault, M., et al. (2021). Multimaterial vat polymerization additive manufacturing. *ACS Appl. Polym. Mat.* 3, 4304–4324. doi:10.1021/acsapm.1c00262

Sandoval, J. H., Soto, K. F., Murr, L. E., and Wicker, R. B. (2007). Nanotailoring photocrosslinkable epoxy resins with multi-walled carbon nanotubes for stereolithography layered manufacturing. *J. Mat. Sci.* 42, 156–165. doi:10.1007/s10853-006-1035-2

Skliutas, E., Kasetaite, S., Jonušauskas, L., Ostrauskaite, J., and Malinauskas, M. (2018). Photosensitive naturally derived resins toward optical 3-D printing. *Opt. Eng.* 57, 1. doi:10.1117/1.oe.57.4.041412

Song, S. Y., Park, M. S., Lee, J. W., and Yun, J. S. (2018). A study on the rheological and mechanical properties of photo-curable ceramic/polymer composites with different silane coupling agents for SLA 3D printing technology. *Nanomaterials* 8, 93. doi:10.3390/nano8020093

Spitalsky, Z., Tasis, D., Papagelis, K., and Galiotis, C. (2010). Carbon nanotube–polymer composites: Chemistry, processing, mechanical and electrical properties. *Prog. Polym. Sci.* 35, 357–401. doi:10.1016/j.progpolymsci.2009.09.003

Valino, A. D., Dizon, J. R. C., JrAH, Espera, Chen, Q., Messman, J., and Advincula, R. C. (2019). Advances in 3D printing of thermoplastic polymer composites and nanocomposites. *Prog. Polym. Sci.* 98, 101162. doi:10.1016/j.progpolymsci.2019.101162

Vidakis, N., Petousis, M., Velidakis, E., Mountakis, N., Tsikritzis, D., Gkagkanatsiou, A., et al. (2022). Investigation of the biocidal performance of multi-functional resin/copper nanocomposites with superior mechanical response in SLA 3D printing. *Biomimetics* 7, 8. doi:10.3390/biomimetics7010008

Wang, J., Mubarak, S., Dhamodharan, D., Divakaran, N., Wu, L., and andZhang, X. (2020). Fabrication of thermoplastic functionally gradient composite parts with anisotropic thermal conductive properties based on multicomponent fused deposition modeling 3D printing. *Compos. Commun.* 19, 142–146. doi:10.1016/j.coco.2020.03.012

Wei, X., Li, D., Jiang, W., Gu, Z., Wang, X., Zhang, Z., et al. (2015). 3D printable graphene composite. *Sci. Rep.* 5, 11181–11187. doi:10.1038/srep11181

Weng, Z., Zhou, Y., Lin, W., Senthil, T., and Wu, L. (2016). Structure-property relationship of nano enhanced stereolithography resin for desktop SLA 3D printer. *Compos Pt A-Appl Sci. Manuf.* 88, 234–242. doi:10.1016/j.compositesa.2016.05.035

Wong, M., Paramsothy, M., Xu, X. J., Ren, Y., Li, S., and Liao, K. (2003). Physical interactions at carbon nanotube-polymer interface. *Polymer* 44, 7757–7764. doi:10.1016/j.polymer.2003.10.011

Yang, Z., Peng, S., Wang, Z., Miao, J. T., Zheng, L., Wu, L., et al. (2022). UV-curable, low-viscosity resin with a high silica filler content for preparing ultrastiff, 3D-printed molds. *ACS Appl. Polym. Mat.* 4, 2636–2647. doi:10.1021/acsapm.1c01920

Yiming, B., Han, Y., Han, Z., Zhang, X., Li, Y., Lian, W., et al. (2021). A mechanically robust and versatile liquid-free ionic conductive elastomer. *Adv. Mat.* 33, 2006111. doi:10.1002/adma.202006111

Zhang, C., Cui, Y., Li, J., and Jiang, D. (2015). Nano-SiO_2-Reinforced ultraviolet-curing materials for three-dimensional printing. *J. Appl. Polym. Sci.* 132, 42307. doi:10.1002/app.42307

Zhang, J., Yang, B., Fu, F., You, F., Dong, X., and Dai, M. (2017). Resistivity and its anisotropy characterization of 3D-printed acrylonitrile butadiene styrene copolymer (ABS)/Carbon black (CB) composites. *Appl. Sci.* 7, 20. doi:10.3390/app7010020

Zhou, Z. X., Li, Y., Zhong, J., Luo, Z., Gong, C. R., Zheng, Y. Q., et al. (2020). High-performance cyanate ester resins with interpenetration networks for 3D printing. *ACS Appl. Mat. Interfaces* 12, 38682–38689. doi:10.1021/acsami.0c10909

frontiers | Frontiers in Materials

TYPE Mini Review
PUBLISHED 26 January 2023
DOI 10.3389/fmats.2023.1129676

OPEN ACCESS

EDITED BY
Jianlei Wang,
Chinese Academy of Sciences (CAS), China

REVIEWED BY
Zhaoqi Niu,
Northwestern Polytechnical University, China
Yuewei Li,
Huaqiao University, China

*CORRESPONDENCE
Qinghui Chen,
chenqh@fjnu.edu.cn
Yonggui Li,
lygwxjd@sina.com
Rui Wang,
wangrui@fjirsm.ac.cn

SPECIALTY SECTION
This article was submitted to Polymeric and Composite Materials, a section of the journal Frontiers in Materials

RECEIVED 22 December 2022
ACCEPTED 17 January 2023
PUBLISHED 26 January 2023

CITATION
Miao Y, Chen Q, Li Y, Zhuo D and Wang R (2023), Tribological properties of carbon nanotube/polymer composites:A mini-review.
Front. Mater. 10:1129676.
doi: 10.3389/fmats.2023.1129676

Tribological properties of carbon nanotube/polymer composites:A mini-review

Ye Miao[1], Qinghui Chen[1]*, Yonggui Li[2]*, Dongxian Zhuo[3,4] and Rui Wang[3,4]*

[1]College of Chemistry and Materials Science, Fujian Normal University, Fuzhou, China, [2]Fujian Key Laboratory of Novel Functional Textile Fibers and Materials, Minjiang University, Fuzhou, China, [3]School of Chemical Engineering and Materials Science, Quanzhou Normal University, Quanzhou, China, [4]Fujian Key Laboratory of New Materials for Light Textile and Chemical Industry, Quanzhou, China

With the development of modern industry, the requirements for mechanical equipment are increasingly stringent, and increasing attention has been paid to reducing wear or lubrication in the movement of mechanical structural parts. Polymers are widely used in the field of mechanical structural parts due to their high processing performance and comprehensive performance. However, the relatively weak mechanical and tribological properties of polymers limit their further application in mechanical equipment lubrication. Incorporation of fillers is a common method to improve the friction properties of polymers. Among various fillers, carbon nanotubes (CNTs) are considered the ideal fillers to significantly improve the tribological properties of polymers. Therefore, this paper reviews the tribological properties of carbon nanotube modified polymer materials. The tribological wear mechanism of polymers and the influence of friction-reducing fillers on the tribological properties of polymers and the related lubrication mechanism explanation are outlined, and the factors influencing the tribological properties of composites by carbon nanotubes and the related lubrication mechanism explanation are analyzed. The presented review will be beneficial for the production of high-performance polymer nanocomposites.

KEYWORDS

carbon nanotube, polymer, composite, tribologcial properties, mechanical properties

Introduction

In recent years, due to the development of society and the growing depletion of the traditional fossil energy, the requirements for energy saving and environmental protection of machinery and equipment have increase. Reducing wear loss and strengthen the lubricating between the mechanical moving parts are the important ways to achieve the energy saving and material loss, and therefore wear-resistant materials, as an essential component in the operation of equipment, have increasingly high requirements for their frictional properties (Lin et al., 2011; Kuang et al., 2022). The use of lubricating oil or the self-lubricating structural parts is a common method to reduce friction and anti-wear (Maruyama et al., 2017; John and Menezes, 2021). However, liquid lubricating materials are susceptible to environmental factors and lose their lubricating effects in the harsh scenarios such as high vacuum, high load and extreme high or low temperature environments (Kian et al., 2019). Therefore, the role of lubricated, wear-resistant solid materials in machinery and equipment is becoming increasingly important.

Polymers are compounds with relative molecular masses of several thousand to several million, with the excellent processing properties and comprehensive performance, widely used in people's clothing, food, housing, transportation, various sectors of the national economy and

cutting-edge technology (Moreno-Navarro et al., 2017; Grancarić et al., 2018; Afolabi et al., 2019; Wang et al., 2022b). Polymers have important applications in wear resistant parts such as bearings. For example, epoxy resins are used in machinery and equipment as bearing materials and friction members due to their high corrosion resistance, low coefficient of friction (COF) and high dimensional stability (Bashandeh et al., 2021), polytetrafluoroethylene (PTFE) is used as oil-free lubricated mechanical parts due to high chemical resistance and low COF (Jang et al., 2007), etc. However, pure polymers are often difficult to use directly as wear-resistant materials (Unal et al., 2010; Kaybal et al., 2021). For the one hand, the intrinsic low thermal conductivity and heat resistance of polymers may lead to the significant changes in their mechanical properties under high temperature conditions, thus reducing their wear resistance and service life. For the other hand, different polymers have different properties and also exhibit different frictional behaviors. For example, PTFE, ultra-high molecular weight polyethylene (UHMWPE) and polyurethane (PU) have excellent self-lubricating properties, but their mechanical properties and heat resistance are relatively poor. Polyimide (PI), poly (ether-ether-ketone) (PEEK) and epoxy resin (EP) have better mechanical and thermal properties, but their COF are relatively high (Maksimkin et al., 2017; Lim et al., 2018; Arif et al., 2020; Cui et al., 2022; Ding et al., 2022). Therefore, these problems limit the universality of polymer applications in the actual mechanical equipment.

Compounding fillers or blending other polymers is the most common and effective way to improve the tribological properties of polymers. PTFE, UHMWPE, Molybdenum disulfide (MoS_2), SiC, carbon fiber, etc. Are used as lubricant materials or reinforcing fillers to improve the friction properties of polymers (Li et al., 2007; Chanda et al., 2019; Salem et al., 2019; Cao et al., 2020). Among them, CNTs are the ideal modifiers for the fabrication of polymer composites with high tribological properties due to their unique structures and excellent properties.

This paper reviews the tribological properties of carbon nanotube modified polymer materials. Firstly, the tribological wear mechanism of polymers, the friction-reducing fillers on the tribological properties of polymers and the related lubrication mechanism explanation are outlined. Then, the factors influencing the tribological properties of carbon nanotube/polymer composites and the related lubrication mechanism explanation are analyzed. Finally, the challenges and prospects of carbon nanotube/polymer composites with high tribological properties are summarized.

Friction and wear behavior and improvement mechanism of the polymers

The wide range of variations in the mechanical properties of polymers and their strong dependence on temperature, deformation rate and the sensitivity of their failure process to environmental conditions make the polymer wear process much more complex compared to metals. Most scholars now classify this complex process into four types: adhesive wear, corrosive wear, abrasive wear and fatigue wear, and the various types of wear can undergo transformation (Lancaster, 1978).

In the relative motion of the friction vice, the surface of the friction couples, although the surface appears flat, the micro-surface is still uneven, which only shows the local contact. At this point, even if a smaller load is applied, the local stress on the actual contact surface is sufficient to cause plastic deformation, so that the oxide film on this part of the surface, etc. is squeezed, and the atoms of the two contact surfaces will be bonded due to bonding interaction. In the subsequent continuation of sliding, the adhesion point is sheared off and transferred to the counterpart surface, which comes off to form abrasive chips, resulting in the loss of material on the surface of the part (Archard, 1953; Belyi et al., 1977; Bijwe et al., 2001; Fukuda and Morita, 2017; Paul and Bhowmik, 2022). Abrasive wear is also caused when hard particles are present within the contact surface. The polymer undergoes a cutting process like planing under the action of abrasive particles, and this process can directly cause material removal and form a chip, which is micro cutting. In contrast, plowing is the extrusion of the polymer by abrasion to the sides, which does not directly cause material removal, but after several deformations can produce shedding and secondary chip formation. The rougher the counterpart surface, the greater the wear rate (WR) of the polymer (Dmitriyeva and Grayevskaya, 1983; Njoku et al., 2021). There may also be fatigue wear on the rough pair surface, when the friction pair slides against each other, the rough peaks of the soft surface are easily deformed, while the soft rough peaks break first under cyclic loading, resulting in a smoother surface. In this way, the contact state is no longer rough peak to rough peak, but the hard surface of the rough peak on the relatively smooth soft surface sliding. When the hard surface rough peak slides on the soft surface, the points on the soft surface are subjected to a cyclic load, which produces shear plastic deformation in the surface layer and accumulates, causing dislocation buildup at a certain depth under the surface, which leads to the formation of cracks or pores. When the crack is formed at a certain depth, according to the stress field analysis, the positive stress on the parallel surface prevents the crack from expanding in the depth direction, so the crack extends in the direction of the parallel surface at a certain depth. When the crack extends to a critical length, the material between the crack and the surface will flake off in the form of flakes of abrasive chips (Atkins et al., 1984; Bogdanovich, 2013; Hussain and Khan, 2022; Zhou et al., 2023). While the corrosive wear of polymers mainly takes place in the form of chemical degradation and oxidation, the high temperature generated at the sliding interface can cause severe degradation or softening of some polymers. In addition to temperature, many factors influence the chemical degradation of polymers, such as the catalytic effect of some oxygen species, the activation energy of polymer degradation and interfacial contact stress (Chen et al., 2014).

Based on the friction and wear behavior of polymers, incorporation of functional fillers to affect the friction process, leading to the improvement of tribological properties of polymer is an effective and viable way. In filler modified polymer composites, the fillers can be classified into reinforcing fillers and lubricating fillers according to their functions.

The lubricant fillers include the familiar PTFE, graphite, MoS_2, etc (Lu and Friedrich, 1995; Qiao et al., 2007; Khare et al., 2015; Zalaznik et al., 2016; Chen et al., 2020; Li et al., 2022b). Gu et al. found that the wear surface of polymethyl methacrylate (PMMA) was uneven with many torn flakes and surface bumps, and the COF curve fluctuated in a wide range, while the wear surface of PTFE/PMMA composites filled with PTFE was relatively smooth with only slight scratches and a smoother COF curve, indicating that the friction process of PMMA-based composites is more stable by filling with PTFE. This is because

the PTFE carbon chain backbone can only accommodate the bulk F atoms in a helical conformation, and the whole macromolecular chain presents a stiff rod-like structure. Due to the strong electrostatic repulsive force of F atoms around the carbon chain and the bulk effect of fluorine atoms, the smooth linear chains without branching side chains are connected by weak van der Waals forces, and the PTFE macromolecule chains are very easy to unwind and slip, and form transfer film and reduce the COF, but the filling of PTFE will make the hardness of the composite material decrease and cause the increase of WR (Gu et al., 2018). Because of the weak van der Waals force between the layers and interlaminar sliding occurs easily, graphite was considered as a typical lubricant filler. Zhang et al. found that the COF of graphite/PTFE composites decreased gradually with the increase of graphite content. During the sliding process, the graphite flakes become thinner and fall off, exposing the surface of the friction substrate, while the peeled graphite micro flakes form a hard transfer film on the surface of the friction substrate, which can effectively reduce the COF (Zhang et al., 2008). The other lubricant fillers such as MoS_2 (Yang et al., 2020), Hexagonal boron nitride (h-BN) (Rao et al., 2021), Zirconium phosphate (ZrP) (Cai et al., 2023), etc. were also reported to improve the tribological properties of polymers by forming the complete transfer film on the surface of the friction substrate, thus reducing the COF of the composite. However, the addition of lubricant fillers adversely affects the WR. The increase of WR can be attributed to the decrease in the hardness of the resultant composite caused by the addition of the lubricant fillers. The wear resistance of the composites depends to some extent on the hardness of the composites, so the decrease in hardness will cause a decrease in the wear resistance of the composites.

Unlike abrasion-reducing fillers, the addition of reinforcing fillers aims to improve the mechanical properties of the composite material such as hardness, strength, impact resistance, creep resistance, etc. (Lustiger et al., 1990; Friedrich et al., 1993; Friedrich et al., 1995). The elastic modulus and tensile strength of the reinforced filler are generally higher than those of the polymer, which in turn leads to filler composite reinforcement (Papon et al., 2012). When the complex is subjected to external stress, the stress is transferred to the filler particles through the resin-filler phase interface, making the filler particles the main stressed phase. The stress transfer mechanism is applicable to both zero-dimensional, one-dimensional and two-dimensional nano-reinforced fillers (Papageorgiou et al., 2020). The improved mechanical properties of polymeric materials increase the load-bearing capacity of polymeric materials, meaning that the material is less prone to plastic deformation and spalling during friction. At the same time, it can maintain the structural integrity of the composite material under high loads (Su et al., 2016). In addition, the excellent mechanical properties significantly inhibit the creation and spread of cracks on the wear surface, thus improving wear resistance (Huang et al., 2013). He et al. found that Perfluoroalkoxy filled with Al_2O_3 particles exhibited ultra-high load-bearing capacity and low COF under sliding conditions (He et al., 2017). Li et al. demonstrated that glass fiber incorporation can substantially improve the mechanical properties of the composites such as tensile strength, tensile modulus, flexural strength, and flexural modulus, and at the same time, the composites exhibit excellent wear resistance (Li et al., 2013). This is due to the strong interfacial bonding between glass fibers and polyether ether ketone, which leads to the interruption of the fiber removal process and causes the accumulation of abrasive particles near the glass fibers, thus avoiding the abrasion of the matrix resin. Nemati et al. studied the effect of graphene on the wear resistance of PTFE was investigated, and the results showed that the addition of graphene effectively improved the wear resistance of the PTFE coating. When graphene was added up to 15 vol%, the friction factor and WR were significantly reduced to 0.1 and 0.65×10^{-9}mm^3/(N-m), respectively (Nemati et al., 2016).

Tribological properties of CNT/polymer composites

Although remarkable achievements have been made in the researches of the friction properties of polymer composites, there are still some technical problems. The addition of the solid lubricating fillers can significantly reduce the friction coefficient of polymer composites, but the friction loss effect is not obvious due to the adverse effects on the hardness, modulus and other properties of polymer composites. With regards to the reinforced fillers, they can significantly improve the mechanical properties of polymer composites, but the large amounts of loadings are often needed to achieve the required friction properties, which may affect other properties of the polymer. Therefore, it is still important to research the new wear-resistant fillers.

CNTs

CNTs are an ideal one-dimensional nanomaterial currently prepared artificially as hollow cylinders enclosed by concentric graphitic surfaces, which exhibit many unique physical properties due to the uniqueness of their own compositional structure (Jun and Gaind, 2015; Zang et al., 2015). CNTs have strong wear resistance and self-lubricating properties, with a wear resistance 100 times higher than that of bearing steel and a COF of 0.06–0.1. CNTs also have excellent Thermal stability and electrical conductivity (He et al., 2018; Cui et al., 2021). CNTs have received a great deal of attention from researchers since their introduction in 1991.

Due to the unique structure and excellent properties, CNTs were introduced to modify polymer for improving the properties of polymer such as mechanical properties, electrical properties, and thermal stability, which have been confirmed by the previous reports (Kotop et al., 2021; Parnian and D'Amore, 2021). Kang et al. prepared CNT/PP composites by melt injection molding method. It was found that the thermal degradation temperature of PP increased by 50°C after filling with CNT, and the thermal conductivity and tensile strength increased with the increase of CNT content (Kang et al., 2010). Liang et al. showed that the flexural modulus of PP increased with increasing CNTs content when filled with CNTs, indicating that CNTs can effectively improve the flexural stiffness of the polymer (Liang et al., 2018). Also, the fracture impact strength of CNT/PP with 4% wt. was increased by 40% compared to pure PP. In addition to this, the addition of CNTs to rubber materials can also reduce the adhesion strength of ice to rubber materials, allowing rubber-based components to work in extreme weather (Valentini et al., 2018). Therefore, the addition of CNTs is an effective method for developing high-performance polymer nanocomposites.

TABLE 1 Tribological properties of polymer nanocomposites based on CNT.

Polymer	Types of CNT	Test conditions	Wear rate	Friction coefficient	References
POM	Pure MWCNT	POD; Steel; Dry; AL: 15, 25, 35 N; SV: 1 m/s; ST: 30 min; Ra: 0.25 μm	−9%	−20%	Goriparthi et al. (2019)
	Acid-treated MWCNT		−19%	−19%	
	Silanized MWCNT		−45%	−27%	
	Carbonylated MWCNT		−28%	−21%	
	Aminated MWCNT		−31%	−22%	
	CNT D: 10nm; L: 2.5 μm	POD; Steel; Dry; AL: 12 N; SV: 1 m/s; ST: 120 min	−70%	N/A	Yousef et al. (2016)
		POD; Steel; Water; AL: 12 N; SV: 1 m/s; ST: 120 min	−60%		
		POD; Steel; Oil; AL: 12 N; SV: 1 m/s; ST: 120 min	−33%		
PTFE	CNT	Dry; AL: 101 kPa	N/A	−25%	Song et al. (2019)
		BOD; Dry; AL: 5 mN,20 mN; SV:4 mm/s; SD: 2mm, 1000 cycles	−31%	-60%	Lim et al. (2018)
PEEK	MWCNT OD: 10–15 nm; L: 0.1–10 μm	BOD R); AISI E52100 stainless-steel ball; Dry; AL: 10 N; SV: 5 Hz; SD: 10,000 cycles	+142%	−67%	Arif et al. (2020)
	CNT D: 10–30 nm; L: 5–30 μm	POD; SiC; Dry; AL:1.5N; SV:300rpm; ST: 5min	−7.32%	−6.71%	Cui et al. (2022)
UHMWPE	Fluorinated MWCNT	POD; Steel; Dry; AL: 32 N; SV: 2.6 m/s; SD: 2355 m	−27%	−95%	Maksimkin et al. (2017)
	MWCNT OD:30–50 nm; ID:5–15 nm; L: 10–20 μm	POD; Titanium alloy; Dry; AL: 60N; SV: 15 mm/s; ST: 24 h	−54%	−21%	Naresh Kumar et al. (2016)
	CNT OD:10–12 nm; L:8–12 μm	BOD; Steel; Dry; AL: 5 N; SV: 0.06 m/s; SD: 460 m	−20%	−36%	Manoj Kumar et al. (2019)
	CNT D:25–26 nm	BOD(R); 440C stainless steel; Dry; AL: 30 N; SV: 0.06 m/s; SD: 68.2 m, 5000 cycles	−63%	+35%	Ali et al. (2017)
		BOD(R); 440C stainless steel; Water; AL: 50 N; SV: 0.06 m/s; SD: 6 k m, 150,000 cycles	−47%	+30%	
	CNT D:50–100 nm; L:10–20 μm	POD; Titanium alloy; Dry; AL: 1 kg; SV: 120 prm; SD: 250 m	−25%	−10%	Deenoi and Dechjarern, (2019)
	CNT D:40–60 nm; L:1–2 μm	BOD; 440C stainless steel; Dry; AL: 7,9,F12,15 N; SV: 0.1 m/s; SD: 5000 cycles	−44%	−38%	Ahmed Baduruthamal et al. (2019)
EP	CNT	POD; Steel disc; 50% relative humidity; AL: 30, 40 N,50N; SV: 200,300,400 rpm	−53%	N/A	Venkatesan et al. (2018)
	CNT L: 10–15 μm; D: 15–20 nm	POD; Steel disc; Dry, Oil-lubricated, and argon; AL: 40 N-120N; SV: 500 rpm; SD: 2.827 km	−18%	−20%	Agrawal et al. (2021)
	MWCNT	POD; 316 L steel discl; Dry; AL: 5 N; SV: 2 Hz; SD: 5 mm	−83%	−31%	Chen et al. (2017)
	Untreated MWCNT	ROD; AL: 10 N; SV: 2.5 m/s; SD: 20000 m	-41%	N/A	Sapiai et al. (2021)
	Silane-treated MWCNT		+23%		
	Acid-treated MWCNT		+9%		
	MWCNT L: 1–10 μm; Number of walls: 3–15	BOD; Bearing steel SAE 52,100 balls, Dry; AL: 2 and 4 N; SV: 0.28 m/s (1000 rpm)	−36%	−78%	Upadhyay and Kumar, (2018)
	poly (urea-formaldehyde) shells assembled with polydopamine-functionalized oxidized CNT	POD; Dry; AL:1 MPa; SV:0.5 m/s; ST: 30min	−99%	−64%	Li et al. (2018)

(Continued on following page)

TABLE 1 (*Continued*) Tribological properties of polymer nanocomposites based on CNT.

Polymer	Types of CNT	Test conditions	Wear rate	Friction coefficient	References
	MWCNTs–alumina	POD; EN8 steel disc; Dry; AL:50N; 100N; 150N; SV:200prm; SD:1250m; ST:30min	−31%	−52%	Saravanan et al. (2019)
	MWCNT-COOH functionalized L: 10–30μm; OD: 20–30 nm; ID:5–10 nm	POD; 100 cr6 steel pin; Dry; AL:20,60,100N; SV:0.1 m/s; SD:1000 m	−87%	−20%	Adarmanabadi et al. (2021)
PP	CNT	POD; Steel disc; Dry; AL: 50 N; SV: 56.5 m/min; ST: 30 min	−12%	−48%	Mertens and Senthilvelan, (2018)
		POD; EN-32 steel; Dry; AL: 10–50 N; SV: 1–5 m/s	−50%	−44%	Ashok Gandhi et al. (2013)
	As-received CNT L: 1.5μm; D: 9.5 nm	BOD(R); steel; Dry; AL: 2 N; SV:0.0128 m/s; SD:200 m	34%	−8%	Ali et al. (2014)
	Purified CNT L: 1.5μm; D: 9.5 nm		−36%	−21%	
TPU	Plasma-treated CNT	Sandpaper; Dry; AL: 0.08N; SV: 7300 rpm	N/A	−55%	Ogawa et al. (2022)
	MWCNT OD:20–30 nm; L:10–30 μm	ROD; Dry; AL: 300N; SV: 0.341 m/s	−52%	−34%	Song et al. (2011)
Polyamide 6	MWCNT L: 20–30μm; OD: 20–30 nm; ID: 10–20 nm	POD; Dry; AL:20–100N; SV:200rpm; SD: 80 mm; ST:3min	−31%	−72%	Chopra et al. (2018)
	CNT	BOR; Dry; GCr15 steel; AL:100–250N	−38%	N/A	Zhang and Deng, (2011)
		BOR; Dry; Quenched medium carbon steel; AL:100–200N; SV: 0.42 m/s; SD: 0.1–0.5 km; ST:0–90min	−30%	−31%	Chang et al. (2013)
	CNT D:50–80 nm, L:5–20 μm	POD; Dry; AL:20–50N; SV: 1 m/s	−33%	−29%	Meng et al. (2009)
		POD; Water; AL:20–50N; SV: 1 m/s	−13%	−93%	
PI	CNT loaded with MoS_2	BOD(R); Stainless-steel ball; Dry; AL:6N; SV:10Hz; SD:10 mm; ST:10min	−31%	−84%	Xin et al. (2018)

Remark, Tribological performances were reported as compared to neat polymer or otherwise stated; D, diameter; OD, outer diameter; ID, inner diameter; L, length; POD, pin-on-disc; BOD, ball-on-disc; BOR, block-on-ring; ROD, ring-on-disc; R, reciprocating mode; AL, applied load; SV, sliding velocity; SD, sliding distance; ST, sliding time.

For the moment, the role of CNTs in wear reduction and wear resistance is also very impressive, mainly as the reinforcement of complexes and additives to lubricating fluids, and the like (Wang et al., 2020; Li et al., 2022a; Wang et al., 2022a). Chen et al. prepared CNTs-reinforced EP composites using oligoaniline assisted dispersion method and investigated their tribological properties (Chen et al., 2017). It was found that the CNTs of the composites had good dispersion, based on which the crystallinity and tribological wear properties of the composites were improved, and the composites had lower WR and COF. Gao et al. showed that significantly lower COF for CNT bio-lubricants compared to dry conditions, showing optimal and durable antifriction characteristics (Gao et al., 2021). It was beneficial to suppressing the removal of multifiber block debris, tensile fracture, and tensile-shear fracture, with the advantages of tribological properties and material removal behavior. CNT improves the wear resistance of polymers more than some other fillers. Remanan et al. added CNT and B_4C to Poly Aryl Ether Ketone. Comparing B_4C, the WR of the composites was reduced by 34% with the addition of CNT (Remanan et al., 2017). Ren et al. added CNT and Mo_2S to EP. at the same 4% content, the WR of the CNT/EP composite was 50% less than that of the Mo_2S/EP composite (Ren et al., 2019). Surya et al. used fibers to reinforce natural rubber materials. CNT and graphite nanofibers reinforced compounds improved the wear resistance simultaneously by 43% and 33% respectively, while SiC and aramid nanofibers improved it by 10% and 8% respectively (Surya et al., 2022). Recent researches on the tribological performance of CNT/polymer nanocomposites were summarized in Table 1.

The reason why CNT improves the frictional properties of polymers is not just a single effect like other conventional fillers, but the result of a synergistic effect of several factors (Figure 1). First of all, due to the special characteristics of the CNT structure, a carbon film is formed regardless of whether the CNT is attached to the polymer matrix or when it falls into the gap of the friction substrate due to wear. This hard and self-lubricating carbon film effectively avoids direct scraping of the friction substrate and reduces the COF and WR (Zhang et al., 2020; Dwivedi et al., 2022). In the next place, when the CNT/polymer composite is subjected to stress, it is transferred to the CNT through the bonding interface, making the CNT the main stressor. Due to the ultra-high aspect ratio and strength of CNT, the strength of the composite is also enhanced, which is less prone to plastic deformation and improves the wear resistance of the polymer (Zare and Rhee, 2020; Duan et al., 2021). Meanwhile, when the composite material produces microcracks due to friction, CNT can effectively inhibit the growth of microcracks, reduce grinding chips, and improve the wear resistance of the material (Bahramnia et al., 2021). The CNT incorporation also improves the thermal conductivity and thermal stability of the composite material, preventing it from softening under the high temperature conditions of frictional heating and failure, which affects wear resistance and service life (Shimizu et al., 2020; Yan et al., 2020).

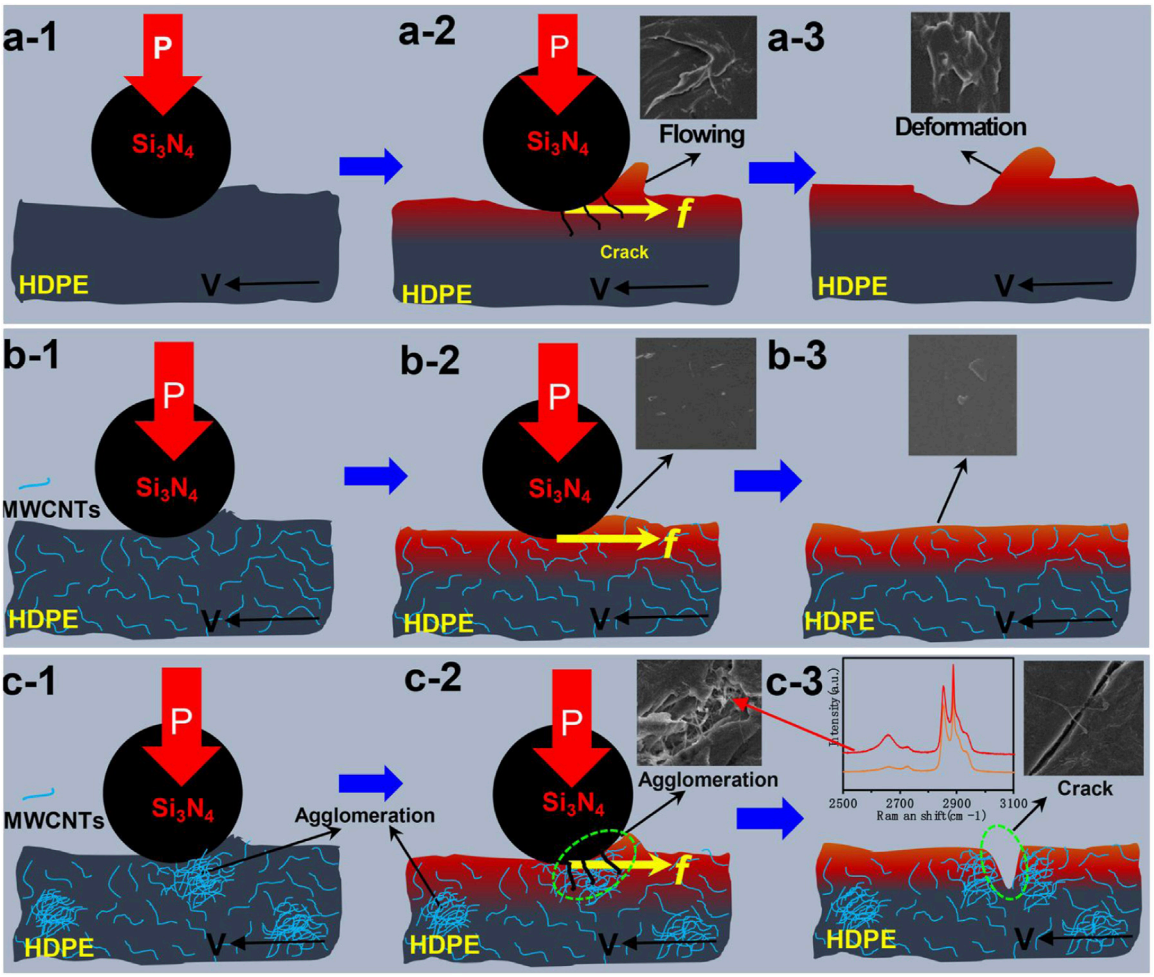

FIGURE 1
Friction reduction models of HDPE (a-1, a-2, a-3), HDPE with moderate 5p [6-xujyhof MWCNTs (b-1, b-2, b-3), and excess MWCNTs (c-1, c-2, c-3) (Wu et al., 2021).

The improvements of the tribological properties of polymer composites by incorporation of CNTs had been confirmed by the previous researches, but in fact, some important factors in CNTs/polymer composites needed to be clarified.

Type of CNTs

CNTs are classified as multi-walled carbon nanotube (MWCNT) and single walled carbon nanotube (SWCNT). Meanwhile, the same type of CNTs have different lengths and diameters. Adrian Cotet et al. compared the effect of SWCNT and MWCNT on the tribological properties of vinyl ester nanocomposites (Cotet et al., 2019). MWCNT decreased the COF of nanocomposites, but the addition of SWCNT increased the COF at high sliding velocities. It was shown that the presence of MWCNT in the fragments contributed to the lubrication effect due to the strong interaction of MWCNT with the polymer matrix, while SWCNT in the fragments played the role of a third body in the sliding motion. Liu et al. introduced two different diameters of MWCNTs to bismaleimide resin, and the significant difference on WR and COF between the resultant MWCNT/bismaleimide composites was observed. Li et al. added CNT to grease to prepare lithium-based grease and investigated the effect of tube diameter and tube length on its frictional properties (Li et al., 2019). The results show that the tube diameter of CNTs has little effect on the friction reduction performance of CNTs, and the COF becomes slightly larger when the tube diameter is larger, and the COF curves all fluctuate not much. However, the length of CNTs has some influence on the friction performance of grease, and the WR is lower when the tube is longer. Due to the strong interaction between CNTs, they are very agglomerated when added to the matrix of polymers, leading to the degradation of composite properties. Therefore, achieving uniform dispersion of CNTs in the matrix resin is the key to prepare high-performance composites. Simultaneously, there are large differences in the properties of the polymer matrix and CNTs, and the regions connecting the transition interact chemically or physically to form interfaces with different properties, and the interface state of CNTs and the matrix has a correlation with the friction properties.

Modification of CNTs

As described above, the interaction between CNTs and polymer matrix is an important factor in the tribological properties of CNTs/polymer composites. Therefore, it can be seen that the modification of CNT has a great influence on the friction properties of the composites. Nowadays, the commonly used modification methods of CNT are covalent bond modification and non-covalent bond modification (Bhattacharyya et al., 2004; Lou et al., 2004; Bahun et al., 2006; Xu et al., 2007; Yan et al., 2011; Zhang et al., 2012; Amirkhani et al., 2020; Atif et al., 2020; Kim et al., 2021). Bhanu et al. explored the changes in the frictional properties of MWCNTs by different functionalizations of MWCNTs, which were prepared into composites with polyformaldehyde (POM), respectively, and found that the WR and COF of 0.5% wt. silylated MWCNTs/POM composites were reduced the most, compared with pure POM, followed by aminated, carbonylated, acid-treated and finally pure MWCNT, which can be attributed to the better dispersion of silylated MWCNTs and stronger interfacial bonding between silylated MWCNTs and POM matrix. However, the excessive modification can greatly destroy the graphite structure of CNTs, leading to the significantly decrease of the intrinsic mechanical properties of CNTs. Therefore, the modified method and the degree of modification needed to be optimized (Goriparthi et al., 2019).

Loading of CNTs

In addition to the type and modification of CNT, the CNT content in the composites also affects the frictional properties of the polymers. Chopra et al. prepared MWCNT/butylene polyterephthalate (PBT) composites with low filler content and investigated their frictional properties using melt compounding method (Chopra et al., 2017). The results showed that the COF of the composites decreased with the increase of carbon nanotube content and the effect of load was not significant. As the carbon nanotube content increased, the wear of the composites was the first to decrease and then to increase. As a matter of fact, the loading of CNTs often relates the dispersion of CNTs in polymer matrix. Severe agglomerates usually observed in the high loading of CNTs/polymer composites fabricated by traditional dispersion technologies, which cause the inefficient improvement of CNTs in the tribological properties of polymer composites. However, Han et al. made a buckypaper (BP) of MWCNT, into EP to improve the frictional properties of BP/EP composites, while solving the dispersion problem of MWCNT with high loading (about 40% wt.). Under the given experimental conditions, BP/EP composites have a lower COF and wear than pure EP. In the case of ozone-modified BP/EP, it has better frictional properties up to four times that of pure EP (Han et al., 2015). Therefore, the method such as pre-building buckypaper may provide a viable way to fabricate the high loading of CNTs/polymer composites with the homogeneous dispersion, which may have unexpected tribological properties.

Comparing with the other fillers, such as PTFE, graphite, UHMWPE, carbon fiber etc., CNTs exhibit some unique features, i) CNTs not only show the self-lubricating effect (low COF), but also strengthen the polymer, indicating the CNTs/polymer composites have low COF and mass loss, and these excellent overall performances make CNTs/polymer composites are more adaptable for mechanical parts (Golchin et al., 2016; Sakka et al., 2017; Chen et al., 2018). ii) CNTs also are other fillers for fabricating functional polymer conposites, for example, the network of CNTs can act as the electrical conductive paths and mass transfer barrier for improving the electrical conductivity, electromagnetic shielding, fire retardance and water-resistance of polymer composites (Kashiwagi et al., 2005; Spitalsky et al., 2010; Xia et al., 2022).

Discussion

According to literature, the incorporation of CNTs can significantly improve the tribological properties of polymer, and the improvement mechanism was researched systematically. However, some problems of the application of CNTs in polymer are still needed to be further clarified. 1) The improvement mechanism of CNTs in the tribological properties of polymer is still not entirely clear, especially in the more complex scenario in terms of wear mechanism and wear-debris formation. The tribological behavior of CNTs/polymer composites is influenced by many factors, and it is difficult to evaluate these factors. Therefore, how to quantity analysis the influences of the factor may help to comprehend the improvement mechanism. 2) The dispersion, appropriate modification and high loading of CNTs are often difficult to achieve. Because of the strong interaction between the nanotubes, CNTs are difficult to achieve the prospective dispersion and the high loadings, leading to the low efficiency of improvements of CNTs in polymer.

Overall, the field of high wear resistant CNTs/polymer composites is still in its infancy. The future development trend of high wear resistant CNTs/polymer composites should focus on refining the theory, optimizing the preparation process (the dispersion and modification of CNTs methods) and achieving the higher loading. Furthermore, the high wear resistant CNTs/polymer composites are rarely in practical applications at present, which means and they have great practical value and broad development prospects.

Conclusion

In order to meet the current manufacturing, the requirements for wear resistance of polymers are increasing, and the design of composite materials with low COF and low WR is of practical importance for energy saving and safety. Filler modification has been the mainstream method to improve the wear resistance of polymers. Since the introduction of CNT, it has been widely used in the research of improving the wear resistance of polymers because of its unique physical properties and advantages. Nowadays, people have gradually overcome the difficulties in the application of CNT and understand its wear resistance mechanism. In the future, starting from the physical and chemical structure of the polymer itself, it will be an important research direction for polymer-based composites to establish the linkage and mechanism between the maintenance of mechanical strength and tribological applications during the service of CNT/polymer, and to provide scientific data and theoretical guidance for the long-term application of polymer lubricant materials.

Author contributions

All authors listed have made a substantial, direct, and intellectual contribution to the work and approved it for publication.

Funding

This research was financially supported by the Open Project Program of Fujian Key Laboratory of Novel Functional Textile Fibers and Materials, Minjiang University, China (No. FKL7FM 2010), National Natural Science Foundation of China (52103356), Fujian Provincial Department of Science and Technology (2020H0045, 2020J01770) and the Bureau of Science and Technology of Quanzhou (2021C009R, 2020C060).

Conflict of interest

The authors declare that the research was conducted in the absence of any commercial or financial relationships that could be construed as a potential conflict of interest.

Publisher's note

All claims expressed in this article are solely those of the authors and do not necessarily represent those of their affiliated organizations, or those of the publisher, the editors and the reviewers. Any product that may be evaluated in this article, or claim that may be made by its manufacturer, is not guaranteed or endorsed by the publisher.

References

Adarmanabadi, S. R., Jafari, M., Farrash, S. M. H., Heidari, M., and Zheng, J. (2021). Effect of nano clay, nano-graphene oxide and carbon nanotubes on the mechanical and tribological properties of crosslinked epoxy nanocomposite. *Plos One* 16, e0259401. doi:10.1371/journal.pone.0259401

Afolabi, L. O., Ariff, Z. M., Megat-Yusoff, P. S. M., Al-Kayiem, H. H., Arogundade, A. I., and Afolabi-Owolabi, O. T. (2019). Red-mud geopolymer composite encapsulated phase change material for thermal comfort in built-sector. *Sol. Energy* 181, 464–474. doi:10.1016/j.solener.2019.02.029

Agrawal, S., Singh, N. K., Upadhyay, R. K., Singh, G., Singh, Y., Singh, S., et al. (2021). Effect of different lubricating environment on the tribological performance of cnt filled glass reinforced polymer composite. *Materials* 14, 2965. doi:10.3390/ma14112965

Ahmed Baduruthamal, Z., Mohammed, A. S., Kumar, A. M., Hussein, M. A., and Al-Aqeeli, N. (2019). Tribological and electrochemical characterization of uhmwpe hybrid nanocomposite coating for biomedical applications. *Materials* 12, 3665. doi:10.3390/ma12223665

Ali, A. B., Abdul Samad, M., and Merah, N. (2017). Uhmwpe hybrid nanocomposites for improved tribological performance under dry and water-lubricated sliding conditions. *Tribol. Lett.* 65, 102–110. doi:10.1007/s11249-017-0884-y

Ali, S. D., Ferda, M., and Harun, M. (2014). Mechanical and tribological performances of polypropylene composites containing multi-walled carbon nanotubes. *Int. J. Surf. Sci. Eng.* 8, 292. doi:10.1504/ijsurfse.2014.065831

Amirkhani, F., Mosadegh, M., Asghari, M., and Parnian, M. J. (2020). The beneficial impacts of functional groups of cnt on structure and gas separation properties of peba mixed matrix membranes. *Polym. Test.* 82, 106285. doi:10.1016/j.polymertesting.2019.106285

Archard, J. F. (1953). Contact and rubbing of flat surfaces. *J. Appl. Phys.* 24, 981–988. doi:10.1063/1.1721448

Arif, M. F., Alhashmi, H., Varadarajan, K. M., Koo, J. H., Hart, A. J., and Kumar, S. (2020). Multifunctional performance of carbon nanotubes and graphene nanoplatelets reinforced peek composites enabled via fff additive manufacturing. *Compos. Part B, Eng.* 184, 107625. doi:10.1016/j.compositesb.2019.107625

Ashok Gandhi, R., Palanikumar, K., Ragunath, B. K., and Paulo Davim, J. (2013). Role of carbon nanotubes (cnts) in improving wear properties of polypropylene (pp) in dry sliding condition. *Mater. Eng.* 48, 52–57. doi:10.1016/j.matdes.2012.08.081

Atif, M., Afzaal, I., Naseer, H., Abrar, M., and Bongiovanni, R. (2020). Review-surface modification of carbon nanotubes: A tool to control electrochemical performance. *Ecs J. Solid State S. C.* 9, 041009. doi:10.1149/2162-8777/ab8929

Atkins, A. G., Omar, M. K., and Lancaster, J. K. (1984). Wear of polymers. *J. Mater. Sci. Lett.* 3, 779–782. doi:10.1007/BF00727971

Bahramnia, H., Semnani, H. M., Habibolahzadeh, A., and Abdoos, H. (2021). Epoxy/polyurethane hybrid nanocomposite coatings reinforced with mwcnts and sio_2 nanoparticles: Processing, mechanical properties and wear behavior. *Surf. Coat. Tech.* 415, 127121. doi:10.1016/j.surfcoat.2021.127121

Bahun, G. J., Wang, C., and Adronov, A. (2006). Solubilizing single-walled carbon nanotubes with pyrene-functionalized block copolymers. *J. Polym. Sci. Part A, Polym. Chem.* 44, 1941–1951. doi:10.1002/pola.21308

Bashandeh, K., Tsigkis, V., Lan, P., and Polycarpou, A. A. (2021). Extreme environment tribological study of advanced bearing polymers for space applications. *Tribol. Int.* 153, 106634. doi:10.1016/j.triboint.2020.106634

Belyi, V. A., Sviridyonok, A. I., Smurugov, V. A., and Nevzorov, V. V. (1977). Adhesive wear of polymers. *J. Lubr. Technol.* 99, 396–400. doi:10.1115/1.3453232

Bhattacharyya, S., Kymakis, E., and Amaratunga, G. A. J. (2004). Photovoltaic properties of dye functionalized single-wall carbon nanotube/conjugated polymer devices. *Chem. Mater* 16, 4819–4823. doi:10.1021/cm0496063

Bijwe, J., Indumathi, J., John Rajesh, J., and Fahim, M. (2001). Friction and wear behavior of polyetherimide composites in various wear modes. *Wear* 249, 715–726. doi:10.1016/S0043-1648(01)00696-2

Bogdanovich, P. N. (2013). Fatigue wear of materials under dynamic contact loading. *J. Frict. Wear+* 34, 349–357. doi:10.3103/S1068366613050036

Cai, T., Zhan, S. P., Yang, T., Jia, D., Cheng, B. X., Tu, J. S., et al. (2023). Molecular dynamics simulation of α-ZrP/uhmwpe blend composites containing compatibilizer and its tribological behavior under seawater lubrication. *J. Appl. Polym. Sci.* 140, e53321. doi:10.1002/app.53321

Cao, X. W., Li, Y. P., and He, G. J. (2020). Fabrication of self-lubricating porous uhmwpe with excellent mechanical properties and friction performance via rotary sintering. *Polymers-Basel* 12, 1335. doi:10.3390/polym12061335

Chanda, A., Sinha, S. K., and Datla, N. V. (2019). Tribological studies of epoxy-carbon nanofiber composites-effect of nanofiber alignment using ac electric field. *Tribol. Int.* 138, 450–462. doi:10.1016/j.triboint.2019.06.014

Chang, Q. X., Wang, K. S., and Zhao, H. J. (2013). The friction and wear properties of short carbon/cnt/pa6 hybrid composites under dry sliding conditions. *Int. J. Polym. Mater.* 62, 540–543. doi:10.1080/00914037.2011.641629

Chen, B. B., Li, X., Jia, Y. H., Xu, L., Liang, H. Y., Li, X. F., et al. (2018). Fabrication of ternary hybrid of carbon nanotubes/graphene oxide/mos2 and its enhancement on the tribological properties of epoxy composite coatings. *Compos. Part A, Appl. Sci. Manuf.* 115, 157–165. doi:10.1016/j.compositesa.2018.09.021

Chen, B., Chen, J., Li, J. Y., Tong, X., Zhao, H. C., and Wang, L. P. (2017). Oligoaniline assisted dispersion of carbon nanotubes in epoxy matrix for achieving the nanocomposites with enhanced mechanical, thermal and tribological properties. *Chin. J. Polym. Sci.* 35, 446–454. doi:10.1007/s10118-017-1911-z

Chen, J. H., Trevarthen, J. A., Deng, T., Bradley, M. S. A., Rahatekar, S. S., and Koziol, K. K. K. (2014). Aligned carbon nanotube reinforced high performance polymer composites with low erosive wear. *Compos. Part A, Appl. Sci. Manuf.* 67, 86–95. doi:10.1016/j.compositesa.2014.08.009

Chen, W., Wang, Z. X., Liu, X., Jia, J. H., and Hua, Y. (2020). Effect of load on the friction and wear characteristics of si3n4-hbn ceramic composites sliding against peek in artificial seawater. *Tribol. Int.* 141, 105902. doi:10.1016/j.triboint.2019.105902

Chopra, S., Batthula, S., Deshmukh, K., and Peshwe, D. (2017). Tribological behaviour of multi-walled carbon nanotubes (mwcnt) filled polybutylene terephthalate (pbt) nanocomposites. *T Indian I Met.* 70, 801–807. doi:10.1007/s12666-017-1055-4

Chopra, S., Deshmukh, K. A., Deshmukh, A. D., and Peshwe, D. R. (2018). Functionalization and melt-compounding of mwcnts in pa-6 for tribological applications. *IOP Conf. Ser. Mater. Sci. Eng.* 346, 012005. doi:10.1088/1757-899X/346/1/012005

Cotet, A., Bastiurea, M., Andrei, G., Cantaragiu, A., and Hadar, A. (2019). Dry sliding friction analysis and wear behavior of carbon nanotubes/vinylester nanocomposites, using pin-on-disc test. *Rev. Chim-Bucharest* 70, 3592–3596. doi:10.37358/RC.19.10.7603

Cui, J., Zhao, J., Wang, S., Wang, Y., and Li, Y. (2021). Effects of carbon nanotubes functionalization on mechanical and tribological properties of nitrile rubber nanocomposites: Molecular dynamics simulations. *Comp. Mater Sci.* 196, 110556. doi:10.1016/j.commatsci.2021.110556

Cui, Y., Li, C., Li, Z. L., Yao, X. J., Hao, W., Xing, S. L., et al. (2022). Deformation-driven processing of cnts/peek composites towards wear and tribology applications. *Coatings (Basel)* 12, 983. doi:10.3390/coatings12070983

Deenoi, S., and Dechjarern, S. (2019). Effect of cryogenic and coating treatments on wear and friction between titanium alloy and uhmwpe for knee implants. *Mater. today Proc.* 17, 1939–1948. doi:10.1016/j.matpr.2019.06.237

Ding, C. J., Xing, Z. Y., Wang, Z. H., Qin, Z. Z., Wang, J., Zhao, X. L., et al. (2022). The comprehensive effect of tensile strength and modulus on abrasive wear performance for polyurethanes. *Tribol. Int.* 169, 107459. doi:10.1016/j.triboint.2022.107459

Dmitriyeva, T. V., and Grayevskaya, L. M. (1983). The processes accompanying metal wear in polymer-containing abrasive media. *Wear* 84, 353–359. doi:10.1016/0043-1648(83)90275-2

Duan, K., Li, L., Wang, F., Liu, S., Hu, Y., and Wang, X. (2021). New insights into interface interactions of cnt-reinforced epoxy nanocomposites. *Compos Sci. Technol.* 204, 108638. doi:10.1016/j.compscitech.2020.108638

Dwivedi, U. K., Singh, S., Shukla, S. C., and Hashmi, S. A. R. (2022). Investigation on tribo-characteristics of calotropis gigantea fiber-reinforced-cnt modified polymer composites. *Polym. Bull. Berl. Ger.* 79, 697–707. doi:10.1007/s00289-020-03532-6

Friedrich, K., Lu, Z., and Häger, A. M. (1993). Overview on polymer composites for friction and wear application. *Theor. Appl. Fract. Mec.* 19, 1–11. doi:10.1016/0167-8442(93)90029-b

Friedrich, K., Lu, Z., and Hager, A. M. (1995). Recent advances in polymer composites' tribology. *Wear* 190, 139–144. doi:10.1016/0043-1648(96)80012-3

Fukuda, K., and Morita, T. (2017). Physical model of adhesive wear in early stage of sliding. *Wear* 376-377, 1528–1533. doi:10.1016/j.wear.2017.01.078

Gao, T., Zhang, Y. B., Li, C. H., Wang, Y., An, Q. L., Liu, B., et al. (2021). Grindability of carbon fiber reinforced polymer using cnt biological lubricant. *Sci. Rep-Uk* 11, 22535. doi:10.1038/s41598-021-02071-y

Golchin, A., Wikner, A., and Emami, N. (2016). An investigation into tribological behaviour of multi-walled carbon nanotube/graphene oxide reinforced uhmwpe in water lubricated contacts. *Tribol. Int.* 95, 156–161. doi:10.1016/j.triboint.2015.11.023

Goriparthi, B. K., Naveen, P. N. E., Ravi Sankar, H., and Ghosh, S. (2019). Effect of functionalization and concentration of carbon nanotubes on mechanical, wear and fatigue behaviours of polyoxymethylene/carbon nanotube nanocomposites. *B Mater Sci.* 42, 98–12. doi:10.1007/s12034-019-1746-z

Grancarić, A. M., Jerković, I., Koncar, V., Cochrane, C., Kelly, F. M., Soulat, D., et al. (2018). Conductive polymers for smart textile applications. *J. Industrial Text.* 48, 612–642. doi:10.1177/1528083717699368

Gu, D. P., Zhang, L. X., Chen, S. W., Song, K. F., and Liu, S. Y. (2018). Significant reduction of the friction and wear of pmma based composite by filling with ptfe. *Polymers-Basel* 10, 966. doi:10.3390/polym10090966

Han, J. H., Zhang, H., Chu, P. F., Imani, A., and Zhang, Z. (2015). Friction and wear of high electrical conductive carbon nanotube buckypaper/epoxy composites. *Compos Sci. Technol.* 114, 1–10. doi:10.1016/j.compscitech.2015.03.012

He, Y., Farokhzadeh, K., and Edrisy, A. (2017). Characterization of thermal, mechanical and tribological properties of fluoropolymer composite coatings. *J. Mater Eng. Perform.* 26, 2520–2534. doi:10.1007/s11665-017-2690-y

He, Y., Luo, H. X., Jin, H. H., Qiu, S., and Li, Q. W. (2018). Thiophene-containing polymer on sorting semiconducting single-walled carbon nanotubes. *Polym. (Guilford)* 159, 59–63. doi:10.1016/j.polymer.2018.11.011

Huang, T., Li, T. S., Xin, Y. S., Liu, P., and Su, C. (2013). Mechanical and tribological properties of hybrid fabric–modified polyetherimide composites. *Wear* 306, 64–72. doi:10.1016/j.wear.2013.06.010

Hussain, M. Z., and Khan, S. (2022). Fabrication and tribological behavior of mno2/epoxy nanocomposites. *High. Perform. Polym.* 34, 742–758. doi:10.1177/09540083221079510

Jang, I., Burris, D. L., Dickrell, P. L., Barry, P. R., Santos, C., Perry, S. S., et al. (2007). Sliding orientation effects on the tribological properties of polytetrafluoroethylene. *J. Appl. Phys.* 102, 123509. doi:10.1063/1.2821743

John, M., and Menezes, P. L. (2021). Self-lubricating materials for extreme condition applications. *Materials* 14, 5588. doi:10.3390/ma14195588

Jun, L., and Gaind, P. P. (2015). Advanced physical chemistry of carbon nanotubes. *Annu. Rev. Phys. Chem.* 66, 331–356. doi:10.1146/annurev-physchem-040214-121535

Kang, C. H., Yoon, K. H., Park, Y., Lee, D., and Jeong, S. (2010). Properties of polypropylene composites containing aluminum/multi-walled carbon nanotubes. *Compos. Part A, Appl. Sci. Manuf.* 41, 919–926. doi:10.1016/j.compositesa.2010.03.011

Kashiwagi, T., Douglas, J. F., Du, F., Winey, K. I., Harris, R. H., and Shields, J. R. (2005). Nanoparticle networks reduce the flammability of polymer nanocomposites. *Nat. Mater* 4, 928–933. doi:10.1038/nmat1502

Kaybal, H. B., Ulus, H., and Avcı, A. (2021). Seawater aged basalt/epoxy composites: Improved bearing performance with halloysite nanotube reinforcement. *Fiber Polym.* 22, 1643–1652. doi:10.1007/s12221-021-0671-0

Khare, N., Limaye, P. K., Soni, N. L., and Patel, R. J. (2015). Friction and wear characteristics of peek and peek composites in water lubricated slow speed sliding. *Tribol. online* 10, 84–90. doi:10.2474/trol.10.84

Kian, B., Pixiang, L., Jacob, L. M., and Andreas, A. P. (2019). Tribological performance of graphene and ptfe solid lubricants for polymer coatings at elevated temperatures. *Tribol. Lett.* 67, 99. doi:10.1007/s11249-019-1212-5

Kim, Y., Kim, Y., Park, J., Han, S. W., and Kim, S. M. (2021). Purification effect of carbon nanotube fibers on their surface modification to develop a high-performance and multifunctional nanocomposite fiber. *Carbon (New York)* 173, 376–383. doi:10.1016/j.carbon.2020.11.026

Kotop, M. A., El-Feky, M. S., Alharbi, Y. R., Abadel, A. A., and Binyahya, A. S. (2021). Engineering properties of geopolymer concrete incorporating hybrid nano-materials. *Ain Shams Eng. J.* 12, 3641–3647. doi:10.1016/j.asej.2021.04.022

Kuang, W. J., Miao, Q., Ding, W. F., and Li, H. N. (2022). A short review on the influence of mechanical machining on tribological and wear behavior of components. *Int. J. Adv. Manuf. Tech.* 120, 1401–1413. doi:10.1007/s00170-022-08895-w

Lancaster, J. K. (1978). Wear mechanisms of metals and polymers. *Trans. IMF* 56, 145–153. doi:10.1080/00202967.1978.11870471

Li, E. Z., Guo, W. L., Wang, H. D., Xu, B. S., and Liu, X. T. (2013). Research on tribological behavior of peek and glass fiber reinforced peek composite. *Phys. Procedia* 50, 453–460. doi:10.1016/j.phpro.2013.11.071

Li, H., Ma, Y., Li, Z., Cui, Y., and Wang, H. (2018). Synthesis of novel multilayer composite microcapsules and their application in self-lubricating polymer composites. *Compos Sci. Technol.* 164, 120–128. doi:10.1016/j.compscitech.2018.05.042

Li, M., Jiang, J., Lu, X., Gao, J., Jiang, D., and Gao, L. (2022a). Natural rubber reinforced with super-hydrophobic multiwalled carbon nanotubes: Obvious improved abrasive resistance and enhanced thermal conductivity. *J. Polym. Eng.* 42, 688–694. doi:10.1515/polyeng-2021-0233

Li, M. X., Deng, X. Q., Guo, P. K., Xu, P., and Tian, H. Y. (2019). Tribological properties and mechanism of carbon nanotubes in grease. *Lubr. Eng.* 44, 120–126. doi:10.3969/j.issn.0254-0150.2019.04.020

Li, W. J., Cui, S. H., and Han, J. M. (2007). Sliding wear resistance of metal-ptfe self-lubricant material. *Hang kong cai liao xue bao* 27, 75–78. doi:10.1016/S1001-6058(07)60030-4

Li, Y., Chen, Y., Guo, Y., Bian, D., and Zhao, Y. (2022b). Tribological behavior of peek/ptfe composites reinforced with carbon fibers and graphite. *Materials* 15, 7078. doi:10.3390/ma15207078

Liang, J. Z., Zou, S. Y., and Du, Q. (2018). Impact and flexural properties of polypropylene composites reinforced with multi-walled carbon nanotubes. *Polym. Test.* 70, 434–440. doi:10.1016/j.polymertesting.2018.07.029

Lim, W. S., Khadem, M., Anle, Y., and Kim, D. E. (2018). Fabrication of polytetrafluoroethylene–carbon nanotube composite coatings for friction and wear reduction. *Polym. Compos.* 39, E710–E722. doi:10.1002/pc.24135

Lin, L., Kim, D., Kim, W., and Jun, S. (2011). Friction and wear characteristics of multi-layer graphene films investigated by atomic force microscopy. *Surf. Coat. Tech.* 205, 4864–4869. doi:10.1016/j.surfcoat.2011.04.092

Lou, X. D., Daussin, R., Cuenot, S., Duwez, A. S., Pagnoulle, C., Detrembleur, C., et al. (2004). Synthesis of pyrene-containing polymers and noncovalent sidewall functionalization of multiwalled carbon nanotubes. *Chem. Mater* 16, 4005–4011. doi:10.1021/cm0492585

Lu, Z. P., and Friedrich, K. (1995). On sliding friction and wear of peek and its composites. *Wear* 181, 624–631. doi:10.1016/0043-1648(95)90178-7

Lustiger, A., Uralil, F. S., and Newaz, G. M. (1990). Processing and structural optimization of peek composites. *Polym. Compos.* 11, 65–75. doi:10.1002/pc.750110109

Maksimkin, A. V., Nematulloev, S. G., Chukov, D. I., Danilov, V. D., and Senatov, F. S. (2017). Bulk oriented uhmwpe/fmwcnt films for tribological applications. *Polymers-Basel* 9, 629. doi:10.3390/polym9110629

Manoj Kumar, R., Rajesh, K., Haldar, S., Gupta, P., Murali, K., Roy, P., et al. (2019). Surface modification of cnt reinforced uhmwpe composite for sustained drug delivery. *J. Drug Deliv. Sci. Tec.* 52, 748–759. doi:10.1016/j.jddst.2019.05.044

Maruyama, T., Saitoh, T., and Yokouchi, A. (2017). Differences in mechanisms for fretting wear reduction between oil and grease lubrication. *Tribol. T* 60, 497–505. doi:10.1080/10402004.2016.1180469

Meng, H., Sui, G. X., Xie, G. Y., and Yang, R. (2009). Friction and wear behavior of carbon nanotubes reinforced polyamide 6 composites under dry sliding and water lubricated condition. *Compos Sci. Technol.* 69, 606–611. doi:10.1016/j.compscitech.2008.12.004

Mertens, A. J., and Senthilvelan, S. (2018). Mechanical and tribological properties of carbon nanotube reinforced polypropylene composites. *Proc. Institution Mech. Eng. Part L, J. Mater. Des. Appl.* 232, 669–680. doi:10.1177/1464420716642620

Moreno-Navarro, F., Sol-Sánchez, M., and Rubio-Gámez, M. C. (2017). Structural analysis of polymer modified bituminous materials in the rehabilitation of light-medium traffic volume roads. *Constr. Build. Mater.* 156, 621–631. doi:10.1016/j.conbuildmat.2017.09.006

Naresh Kumar, N., Yap, S. L., Bt Samsudin, F. N. D., Khan, M. Z., and Pattela Srinivasa, R. S. (2016). Effect of argon plasma treatment on tribological properties of uhmwpe/mwcnt nanocomposites. *Polymers-Basel* 8, 295. doi:10.3390/polym8080295

Nemati, N., Emamy, M., Yau, S., Kim, J. K., and Kim, D. E. (2016). High temperature friction and wear properties of graphene oxide/polytetrafluoroethylene composite coatings deposited on stainless steel. *Rsc Adv.* 6, 5977–5987. doi:10.1039/c5ra23509j

Njoku, C. E., Omotoyinbo, J. A., Alaneme, K. K., and Daramola, M. O. (2021). Physical and abrasive wear behaviour of urena lobata fiber-reinforced polymer composites. *J. Reinf. Plast. Comp.* 40, 341–351. doi:10.1177/0731684420960210

Ogawa, D., Morimune-Moriya, S., and Nakamura, K. (2022). Effective polymerization technique for plasma-treated multiwalled carbon nanotubes to maximize wear resistance of composite polyurethane. *J. Vac. Sci. Technol. B, Nanotechnol. Microelectron.* 40, 022803. doi:10.1116/6.0001390

Papageorgiou, D. G., Li, Z., Liu, M., Kinloch, I. A., and Young, R. J. (2020). Mechanisms of mechanical reinforcement by graphene and carbon nanotubes in polymer nanocomposites. *Nanoscale* 12, 2228–2267. doi:10.1039/c9nr06952f

Papon, A., Montes, H., Lequeux, F., Oberdisse, J., Saalwchter, K., and Guy, L. (2012). Solid particles in an elastomer matrix: Impact of colloid dispersion and polymer mobility modification on the mechanical properties. *Soft Matter* 8, 4090–4496. doi:10.1039/c2sm06885k

Parnian, P., and D'Amore, A. (2021). Fabrication of high-performance cnt reinforced polymer composite for additive manufacturing by phase inversion technique. *Polymers-Basel* 13, 4007. doi:10.3390/polym13224007

Paul, R., and Bhowmik, S. (2022). Adhesive wear behaviour of surface modified bamboo filler reinforced polymer composite under different contact condition. *J. Nat. Fibers* 19, 12208–12223. doi:10.1080/15440478.2022.2054893

Qiao, H., Guo, Q., Tian, A., Pan, G., and Xu, L. (2007). A study on friction and wear characteristics of nanometer al2o3/peek composites under the dry sliding condition. *Tribol. Int.* 40, 105–110. doi:10.1016/j.triboint.2006.02.069

Rao, Y. S., Mohan, N. S., Shetty, N., and Shivamurthy, B. (2021). Effects of solid lubricant fillers on the flexural and shear strength response of carbon fabric-epoxy composites. *Polym. Test.* 96, 107085. doi:10.1016/j.polymertesting.2021.107085

Remanan, M., Kannan, M., Rao, R. S., Bhowmik, S., Varshney, L., Abraham, M., et al. (2017). Microstructure development, wear characteristics and kinetics of thermal decomposition of hybrid nanocomposites based on poly aryl ether ketone, boron carbide and multi walled carbon nanotubes. *J. Inorg. Organomet. P* 27, 1649–1663. doi:10.1007/s10904-017-0626-5

Ren, Z., Yang, Y., Lin, Y., and Guo, Z. (2019). Tribological properties of molybdenum disulfide and helical carbon nanotube modified epoxy resin. *Materials* 12, 903. doi:10.3390/ma12060903

Sakka, M. M., Antar, Z., Elleuch, K., and Feller, J. F. (2017). Tribological response of an epoxy matrix filled with graphite and/or carbon nanotubes. *Friction* 5, 171–182. doi:10.1007/s40544-017-0144-z

Salem, A., Guezmil, M., Bensalah, W., and Mezlini, S. (2019). Tribological behavior of molybdenum disulphide particles-high density polyethylene composite. *Mater Res. Express* 6, 075402. doi:10.1088/2053-1591/ab10d1

Sapiai, N., Jumahat, A., Jawaid, M., and Santulli, C. (2021). Abrasive wear behavior of cnt-filled unidirectional kenaf–epoxy composites. *Processes* 9, 128. doi:10.3390/pr9010128

Saravanan, D., Palanisamy, C., and Raajeshkrishna, C. R. (2019). Tribological performance of multi walled carbon nanotubes-alumina hybrid/epoxy nanocomposites under dry sliding condition. *Mater Res. Express* 6, 105067. doi:10.1088/2053-1591/ab3ada

Shimizu, T., Kishi, R., Kobashi, K., Morimoto, T., Okazaki, T., Yamada, T., et al. (2020). Improved thermal stability of silicone rubber nanocomposites with low filler content, achieved by well-dispersed carbon nanotubes. *Compos. Commun.* 22, 100482. doi:10.1016/j.coco.2020.100482

Song, H., Qi, H., Li, N., and Zhang, X. (2011). Tribological behaviour of carbon nanotubes/polyurethane nanocomposite coatings. *Micro Nano Lett.* 6, 48. doi:10.1049/mnl.2010.0167

Song, J. F., Lei, H., and Zhao, G. (2019). Improved mechanical and tribological properties of polytetrafluoroethylene reinforced by carbon nanotubes: A molecular dynamics study. *Comp. Mater Sci.* 168, 131–136. doi:10.1016/j.commatsci.2019.05.058

Spitalsky, Z., Tasis, D., Papagelis, K., and Galiotis, C. (2010). Carbon nanotube–polymer composites: Chemistry, processing, mechanical and electrical properties. *Prog. Polym. Sci.* 35, 357–401. doi:10.1016/j.progpolymsci.2009.09.003

Su, C., Xue, F., Li, T. S., Xin, Y. S., and Wang, M. M. (2016). Study on the tribological properties of carbon fabric/polyimide composites filled with sic nanoparticles. *J. Macromol. Sci. Phys.* 55, 627–641. doi:10.1080/00222348.2016.1179248

Surya, K. P., Mukhopadhyay, R., Naskar, K., and Bhowmick, A. K. (2022). A comparative study on the effect of different fibrous nanofillers on the properties of natural rubber nanocomposites. *Polym. Compos.* doi:10.1002/pc.27169

Unal, H., Kurtulus, E., Mimaroglu, A., and Aydin, M. (2010). Tribological performance of ptfe bronze filled composites under wide range of application conditions. *J. Reinf. Plast. Comp.* 29, 2184–2191. doi:10.1177/0731684409345617

Upadhyay, R. K., and Kumar, A. (2018). A novel approach to minimize dry sliding friction and wear behavior of epoxy by infusing fullerene c70 and multiwalled carbon nanotubes. *Tribol. Int.* 120, 455–464. doi:10.1016/j.triboint.2018.01.028

Valentini, L., Bittolo Bon, S., Hernández, M., Lopez-Manchado, M. A., and Pugno, N. M. (2018). Nitrile butadiene rubber composites reinforced with reduced graphene oxide and carbon nanotubes show superior mechanical, electrical and icephobic properties. *Compos Sci. Technol.* 166, 109–114. doi:10.1016/j.compscitech.2018.01.050

Venkatesan, M., Palanikumar, K., and Boopathy, S. R. (2018). Experimental investigation and analysis on the wear properties of glass fiber and cnt reinforced hybrid polymer composites. *Sci. Eng. Compos. Mater.* 25, 963–974. doi:10.1515/secm-2017-0068

Wang, H. Y., Zhu, M. L., Chang, L., and Ye, L. (2020). Mechanical reinforcement and wear resistance of aligned carbon nanotube/epoxy nanocomposites from nanoscale investigation. *J. Appl. Polym. Sci.* 137, 49182. doi:10.1002/app.49182

Wang, J. H., Zhuang, W. P., Liang, W. F., Yan, T. T., Li, T., Zhang, L. X., et al. (2022a). Inorganic nanomaterial lubricant additives for base fluids, to improve tribological performance: Recent developments. *Friction* 10, 645–676. doi:10.1007/s40544-021-0511-7

Wang, Y., Borgatta, J., and White, J. C. (2022b). Protecting foods with biopolymer fibres. *Nat. food* 3, 402–403. doi:10.1038/s43016-022-00519-6

Wu, Y., Dong, C., Yuan, C., Bai, X., Zhang, L., and Tian, Y. (2021). Mwcnts filled high-density polyethylene composites to improve tribological performance. *Wear* 477, 203776. doi:10.1016/j.wear.2021.203776

Xia, Z., Wang, R., Qu, B., Wu, Q., Zhuo, D., and Zheng, Y. (2022). Microwave absorbing properties of polyaniline coated buckypaper reinforced epoxy resin composites. *J. Appl. Polym. Sci.* 139, e53154. doi:10.1002/app.53154

Xin, Y. S., Xu, F. L., Wang, M. M., and Li, T. S. (2018). Synergistic effects of carbon nanotube/nano-MoS2 hybrid on tribological performance of polyimide nanocomposite films. *Tribol. Lett.* 66, 25. doi:10.1007/s11249-017-0977-7

Xu, G. D., Zhu, B., Han, Y., and Bo, Z. S. (2007). Covalent functionalization of multi-walled carbon nanotube surfaces by conjugated polyfluorenes. *Polymer* 48, 7510–7515. doi:10.1016/j.polymer.2007.11.012

Yan, Y. F., Meng, Z. J., Xin, X. C., Liu, H., and Yan, F. Y. (2020). Tribological behavior and thermal stability of thermoplastic polyimide/poly (ether ether ketone) blends at elevated temperature. *J. Macromol. Sci. Phys.* 60, 175–189. doi:10.1080/00222348.2020.1841952

Yan, Y. H., Yang, S. B., Cui, J., Jakisch, L., Pötschke, P., and Voit, B. (2011). Synthesis of pyrene-capped polystyrene for dispersion of pristine single-walled carbon nanotubes. *Polym. Int.* 60, 1425–1433. doi:10.1002/pi.3096

Yang, M., Zhang, C. H., Su, G. D., Dong, Y. J., Mekuria, T. D., and Lv, Q. T. (2020). Preparation and wear resistance properties of thermosetting polyimide composites containing solid lubricant fillers. *Mater Chem. Phys.* 241, 122034. doi:10.1016/j.matchemphys.2019.122034

Yousef, S., Visco, A. M., Galtieri, G., and Njuguna, J. (2016). Wear characterizations of polyoxymethylene (pom) reinforced with carbon nanotubes (pom/cnts) using the paraffin oil dispersion technique. *JOM* 68, 288–299. doi:10.1007/s11837-015-1674-3

Zalaznik, M., Novak, S., Huskić, M., and Kalin, M. (2016). Tribological behaviour of a peek polymer containing solid mos 2 lubricants: Tribological behaviour of a peek/mos 2 polymer composite. *Lubr. Sci.* 28, 27–42. doi:10.1002/ls.1299

Zang, X. N., Zhou, Q., Chang, J. Y., Liu, Y. M., and Lin, L. W. (2015). Graphene and carbon nanotube (cnt) in mems/nems applications. *Microelectron. Eng.* 132, 192–206. doi:10.1016/j.mee.2014.10.023

Zare, Y., and Rhee, K. Y. (2020). Analysis of the connecting effectiveness of the interphase zone on the tensile properties of carbon nanotubes (cnt) reinforced nanocomposite. *Polymers-Basel* 12, 896. doi:10.3390/polym12040896

Zhang, A. B., Tang, M., Luan, J. F., and Li, J. Y. (2012). Noncovalent functionalization of multi-walled carbon nanotubes with amphiphilic polymers containing pyrene pendants. *Mater Lett.* 67, 283–285. doi:10.1016/j.matlet.2011.09.103

Zhang, J. G., and Deng, J. (2011). The effect of maleic anhydride grafted styrene-ethylene-butylene-styrene on the friction and wear properties of polyamide6/carbon nanotube composites. *Polym-Plast Technol.* 50, 1533–1536. doi:10.1080/03602559.2011.603778

Zhang, M. J., Chen, B. B., Dong, Z., Wang, S., Li, X., Jia, Y. H., et al. (2020). Enhancement on the tribological properties of poly(phthalazinone ether sulfone ketone) by carbon nanotube-supported graphitic carbon nitride hybrid. *Polym. Compos.* 41, 3768–3777. doi:10.1002/pc.25674

Zhang, X. T., Liao, G. X., Jin, Q., Feng, X. B., and Jian, X. G. (2008). On dry sliding friction and wear behavior of ppesk filled with ptfe and graphite. *Tribol. Int.* 41, 195–201. doi:10.1016/j.triboint.2007.08.003

Zhou, S. F., Yan, J., Chen, J. L., Yan, H. M., Zhang, Y., Huang, J., et al. (2023). Polydopamine/polyethyleneimine co-crosslinked graphene oxide for the enhanced tribological performance of epoxy resin coatings. *J. Mater Sci. Technol.* 136, 13–20. doi:10.1016/j.jmst.2022.07.019

frontiers | Frontiers in Materials

TYPE Original Research
PUBLISHED 03 April 2023
DOI 10.3389/fmats.2023.1096475

OPEN ACCESS

EDITED BY
Yadong Wu,
Harbin Institute of Technology, China

REVIEWED BY
Yanhu Zhan,
Liaocheng University, China
Tifeng Jiao,
Yanshan University, China

*CORRESPONDENCE
Guo-Lin Gao,
gaoguol@hit.edu.cn
Zaixing Jiang,
jiangzaixing@hit.edu.cn

SPECIALTY SECTION
This article was submitted to Polymeric and Composite Materials, a section of the journal Frontiers in Materials

RECEIVED 12 November 2022
ACCEPTED 15 March 2023
PUBLISHED 03 April 2023

CITATION
Li Y, Zheng W, Zhang J, Xu L, Li B, Dong J, Gao G-L and Jiang Z (2023), 3D printed thermo-responsive electroconductive hydrogel and its application for motion sensor.
Front. Mater. 10:1096475.
doi: 10.3389/fmats.2023.1096475

3D printed thermo-responsive electroconductive hydrogel and its application for motion sensor

Yangyang Li, Wenhui Zheng, Jichi Zhang, Lijuan Xu, Bing Li, Jidong Dong, Guo-Lin Gao* and Zaixing Jiang*

MIIT Key Laboratory of Critical Materials Technology for New Energy Conversion and Storage, School of Chemistry and Chemical Engineering, Harbin Institute of Technology, Harbin, China

Stimulus-responsive hydrogels with excellent conductivity have been widely used in electrical, electrochemical, biomedical, and other fields. It is still a challenge to prepare gels with high conductivity. In this paper, poly (N-isopropyl acrylamide) is 3D printed by changing the rheological properties of the printing solution with clay. By forming phytic acid cross-linked polyaniline conductive polymer network *in situ* on the poly (N-isopropyl acrylamide) matrix, 3D printing of thermally responsive conductive hybrid hydrogels was realized. The interpenetrating polymer network structure provides an electron transport path for hydrogels. The hydrogels have high porosity, strong interaction, high electrical conductivity, high thermal response sensitivity, and significant mechanical enhancement. The results show that the swelling and mechanical properties of the gel are influenced by soaking in different concentrations. The application scenario of the hydrogel was confirmed by a temperature-sensitive switch and finger motion detection.

KEYWORDS

3D printing, bodily motion sensors, conductive hydrogels, double network, PNIPAM

Introduction

Stimulus-response gels are functional hydrogels that respond to external signals, such as temperature, (Li et al., 2011), PH, (Li et al., 2014), electric field, (Yang et al., 2011; Annabi et al., 2014), magnetic force, (Zhai et al., 2013), and so on. 3D printing of functional gels can be used in a wide range of applications. Traditional response gels tend to respond to only one source. The multi-response and multi-function intelligent gel materials have a wider range of application scenarios, such as intelligent sensors, intelligent robots, flexible wearables, and other fields. Thermosensitive conductive gel is a kind of conductive gel that is sensitive to temperature. He can feel the stimulation of temperature changes in the outside world and translate it into electrical signals. This can be widely used in smart clothing, real-time monitoring, and other fields.

In recent years, flexible sensors have been widely paid attention to and used in electronic skin (Gao et al., 2019), soft robots (Treml et al., 2018), artificial intelligence (Fernandes et al., 2019), health monitoring (Wu et al., 2020), and other fields. Flexible sensors need excellent mechanical properties, high sensitivity, good stability and repeatability. Conductive hydrogels have good flexibility and biocompatibility, which make them a rational flexible sensor material. Traditional hydrogels are generally non-conductive. The prepared conductive hydrogels usually introduce a second component into the collective of traditional hydrogels to conduct electricity. Such as conductive filler, conductive polymer, etc., Pan et al. (2012) introduced a conductive polymer network into the

traditional NIPAM gel collective to prepare polyaniline and polypyrrole, which realized the conductive characteristics of the temperature-sensitive gel. Qin et al. (2022) introduced LiCl into polyacrylamide/hydroxypropyl methylcellulose (PAM/HPMC) composite hydrogel, A method for the rapid synthesis of N, N-dimethyl acrylamide-Paam/Ca hydrogels (MBAA-PAAM/Ca gels) sensors using a "one-pot method" has been reported by Bai et al. (2021) PAAM hydrogel has the characteristics of low raw material cost, uniform polymerization, good transparency, and non-toxic. Bai et al. (2020) report on a new transparent and highly ionic conductivity hydrogel that regulates the crosslinking interaction of hydrogel networks by introducing biomineral calcium ions into the pam Sodium carboxymethylcellulose (CMC) crosslinking network. The hydrogel integrates high strength, high tensile, and self-adhesive skin sensor-like properties.

3D printed hydrogels have been extensively studied in recent years Boere et al. (2015) present a new bio ink for 3D printing, capable of forming large, highly defined constructs. Abbadessa et al. (2016) design a hydrogel system based on methacrylate chondroitin sulfate (CSMA) and a thermo-sensitive poly [N-(2-hydroxypropyl) methacrylamide-mono/dilactate]-polyethylene glycol triblock copolymer (M15P10) as a suitable material for additive manufacturing of scaffolds. Because polymers are by far the most utilized class of materials for 3D printing additive manufacturing, Ligon et al. (2017) focus on polymer processing and the development of polymers and advanced polymer systems specifically for AM. Polymer designs that meet the rheological requirements for direct ink writing are outlined and successful examples are summarized, which include the development of polymer micelles, co-assembled hydrogels, supramolecular cross-linked systems, polymer liquids with microcrystalline domains, and hydrogels with dynamic covalent cross-links Li et al. (2019) SiO nanoparticles are loaded into alginate-gelatin composite hydrogels and chemically crosslinked with CaCl solution Roopavath et al. (2019). Cristovao et al. (2019) combine chemical and UV laser polymeric cross-linkage to control the mechanical properties of 3D-printed hydrogel blends. Without imitating dynamic movements, there are limitations on the extent to which the proper implementation of the tissue's own functions can be achieved.

In this paper, the conductive polymer hydrogel was introduced into the preprinted thermosensitive hydrogel poly (N-isopropyl acrylamide) (PNIPAM), and the conductive smart gel sensitive to temperature change was developed. Phytic acid molecules can protonate nitrogen groups on the PANI molecular chain, and a single phytic acid molecule can react with multiple PANI molecular chains. In this way, a conductive gel network can be *in-situ* polymerized inside the printed PNIPAM gel. The effect of two gel networks can greatly improve the mechanical properties of the gel. The inner porous and loose morphology provides a way for water molecules to flow. The hybrid gels we obtained have excellent temperature sensitivity and electrical conductivity.

Results and discussion

Smart gels have broad applications. Traditional smart hydrogels are generally electrically non-conductive. Few relevant types of research focus on the preparation of conductive gels through 3D printing. In this paper, a 3D printable thermo-sensitive conductive gel was prepared by *in-situ* polymerization, and the target shape of the thermo-sensitive gel matrix was prepared by 3D printing. The thermo-sensitive gel matrix was immersed in a mixture of water and ethanol containing aniline monomer. The initiator and phytic acid promote the polymerization of aniline monomer.

The aniline monomer was *in-situ* polymerized within the molecular chain of Poly (N-Isopropyl acrylamide) (PNIPAM) by the action of initiator and phytic acid to form a conductive polyaniline network. Phytic acid is a kind of natural substance that exists widely in plants and has abundant yield. Phytic acid reacts with the Pani chain by protonating the nitrogen group. A single phytic acid molecule can react with multiple polyaniline molecular chains simultaneously to form a conductive network. As shown in Figure 1, the aqueous solution of NIPam is thin and not suitable for direct extrusion printing. The rheological modifier lapnito XLG, a 10 nm nm sheet, is distributed directly in water to increase the viscosity of the water. The clay-thickened NIPAM solution can be extruded directly. Nipam gel after 3D printing has certain temperature sensitivity. When the phase transition temperature was higher than 35°C, the molecular chain of NIPAM was curled and the gel volume shrank. The shrunk gel is then immersed in a mixture of water and ethanol containing aniline monomers. Under the condition of the lower phase transition temperature, the molecular chain of NIPAM stretched and the gel volume swelled. In the process of swelling, the gel sucked the surrounding mixed solution into the gel network, during which the aniline monomer was dispersed within the molecular network of Nipam. Phytic acid molecules are linked by inducing the protonation of nitrogen groups on aniline. In this process, a single phytic acid molecule reacts with multiple nitrogen groups to form a polyaniline network. The polyaniline network provides a transmission path for electron transport and forms an *in-situ* polymerized gel conducting network on the NIPAM molecular chain.

Figure 1A shows the real pictures of the gel in each process. The initial PNIPAM was a transparent gel after being printed and cured. The aniline monomer is absorbed inside the gel after being soaked in an aniline water/ethanol solution. The gel is light yellow. In the last step, the sample was transferred to phytic acid solution, and the aniline monomer was *in-situ* polymerized within the PNIPAM gel network to form a polyaniline network. The whole sample was brown, and a few parts were green. The chemical structure of the PNIPAM/PANI hybrid gel was analyzed by Fourier transform infrared spectroscopy (FTIR). Figure 1B shows the FTIR spectra of PANIPAM, the gel after swelling of aniline absorption monomer, and the hybrid gel after *in-situ* polymerization of aniline monomer (PNIPAM/PANI). In the spectrum of PNIPAM, the two characteristic absorption peaks of PNIPAM are 1,540 cm^{-1} and 1,654 cm^{-1}, respectively. They are attributed to the bending vibration of the N-H bond and the stretching vibration of C=O, respectively. After the swelling and absorption of the aniline monomer, the absorption vibration peak of the benzene ring appeared at 1,480 cm^{-1}. After *in-situ* polymerization, a quinone ring at 1,570 cm^{-1} was formed. All characteristic absorption peaks of PNIPAM and PANI could be found in the whole synthesis process. That proved the formation of the PNIPAM/PANI hybrid gel.

10.3389/fmats.2023.1096475

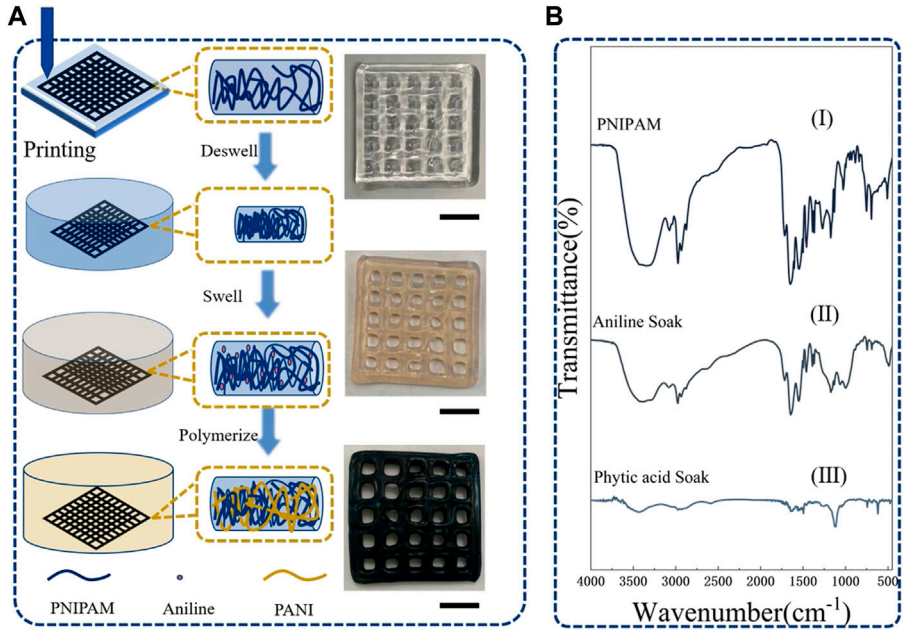

FIGURE 1
(A) The preparation process of hybrid gel, **(B)** FTIR spectra of different stages of gel, the ruler is 1 cm.

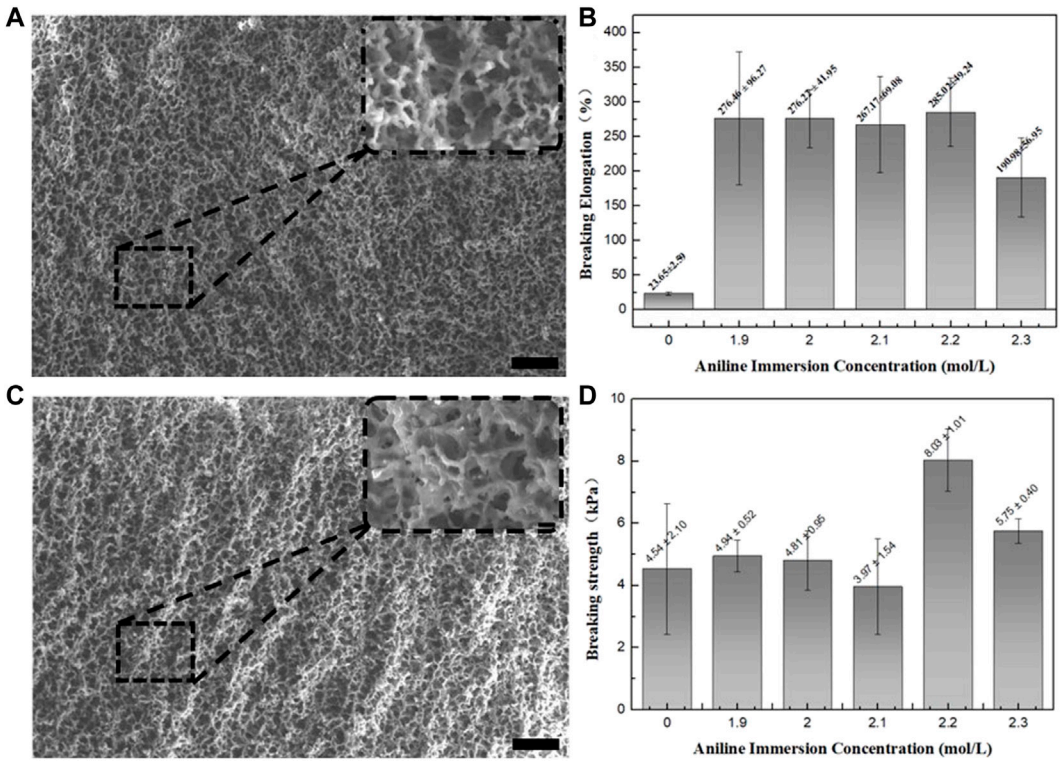

FIGURE 2
(A) SEM image of 1.9 mol/L sample, **(B)** Elongation at break. **(C)** SEM image of 2.3 mol/L sample. **(D)** Tensile fracture strength.

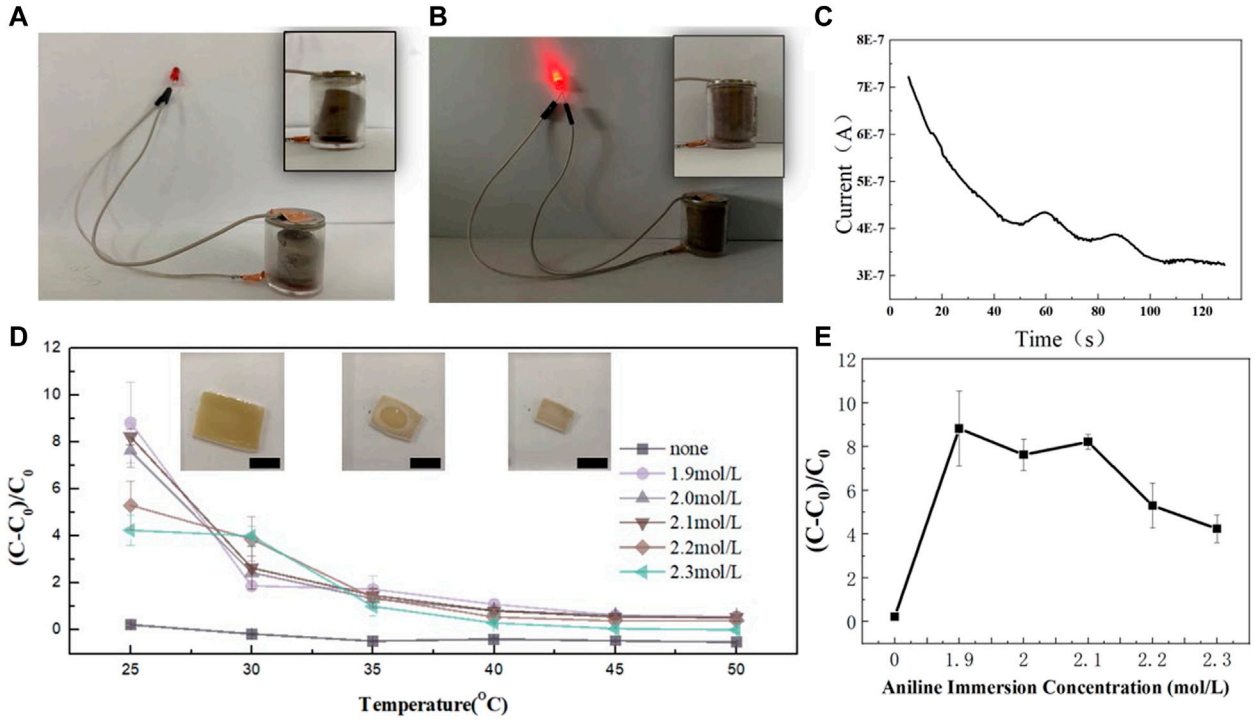

FIGURE 3
(A) Gel circuit diagram at 50°C. **(B)** Gel circuit diagram at 20°C. **(C)** i-t curve of hybrid gel at 50°C. **(D)** The swelling behavior to temperature. **(E)** The swelling behavior to the concentration of aniline.

In this paper, the author prepared hybrid gels under different conditions by changing the concentration of aniline. The possibility of regulating the mechanical properties of hybrid gels by changing aniline concentration was explored. The concentration of aniline monomer was 1.9 mol/L, 2.0 mol/L, 2.1 mol/L, 2.2 mol/L, and 2.3 mol/L, respectively. The microstructure and morphology of the hybrid gel were studied by scanning electron microscopy (SEM). Figures 2A, C show the SEM image of the hybrid gel samples at 1.9 mol/L and 2.3 mol/L. The gel samples were freeze-dried, and the fracture surface was tested. As can be seen in the figure, the hybrid gel presents a porous structure inside. Pore size is evenly distributed, ranging from a few microns to more than 10 microns in size. The pores show a hierarchical porous structure. This special morphology provides a nanoscale transmission channel. Water molecules are transported freely through the channels. The aniline molecules could follow the mixed solution into the gel network, during the swelling process. After aggregation, a PANI network was formed on the PNIPAM network. It can be seen by comparing Figures 2A, C the overall structure of the gel network is similar, with little difference in pore diameter. Similarly, the same result can be obtained by comparing other samples (Supplementary Figure S2). The results showed that the microstructure of the polymer network skeleton was not affected by the change of aniline concentration.

Mechanical properties are an important indicator of hydrogels as sensors. Hydrogels have general mechanical strength because of their porous and loose structure. Figure 2B shows the comparison of elongation at the break of different samples. The graph shows that there has been a steep increase in elongation at the break of the hybrid gel. The elongation at break of PANIM was only 23.65% ± 2.59%, and the tensile fracture strength was 4.54 ± 2.10 kpa. The hybrid gel formed by different concentrations of aniline immersion has a significant increase in elongation at break. The elongation at break of sample 1.9 mol/L, 2.0 mol/L, 2.1 mol/L, 2.2 mol/L and 2.3 mol/L reached 276.46% ± 96.27%, 276.22% ± 41.95%, 267.17% ± 69.08%, 285.02% ± 49.24%, 190.98% ± 56.95%, respectively. Compared with the PNIPAM, the elongation at break was increased by 10 times after hybridization. One reason why elongation have increased is that the introduction of the PANI network formed two networks inside the gel. The PANI polymer network dispersed the external forces to some extent during the stretching process. It is also worth noting that the concentration of aniline does not have a great effect on the elongation at break of the hybrid gel. Figure 2D is the comparison of tensile fracture strength of different samples. The fracture strength of samples 1.9 mol/L, 2.0 mol/L, 2.1 mol/L, 2.2 mol/L and 2.3 mol/L was 4.94 ± 0.52 kPa, 4.81 ± 0.95 kPa, 3.97 ± 1.54 kPa, 8.03 ± 1.01 kPa, 5.75 ± 0.40 kPa, respectively. Compared with the PNIPAM gel, the fracture strength of the hybrid gel was almost the same. When the gel was stretched to an extreme position, the PNIPAM polymer chain still played a major role. The introduction of PANI network did not enhance the fracture strength of the gel. Compared with PNIPAM gel, hybrid gel significantly enhanced the elasticity of the gel due to PANI. In the meantime, the change of aniline concentration has little effect on the mechanical properties of the final hybrid gel.

10.3389/fmats.2023.1096475

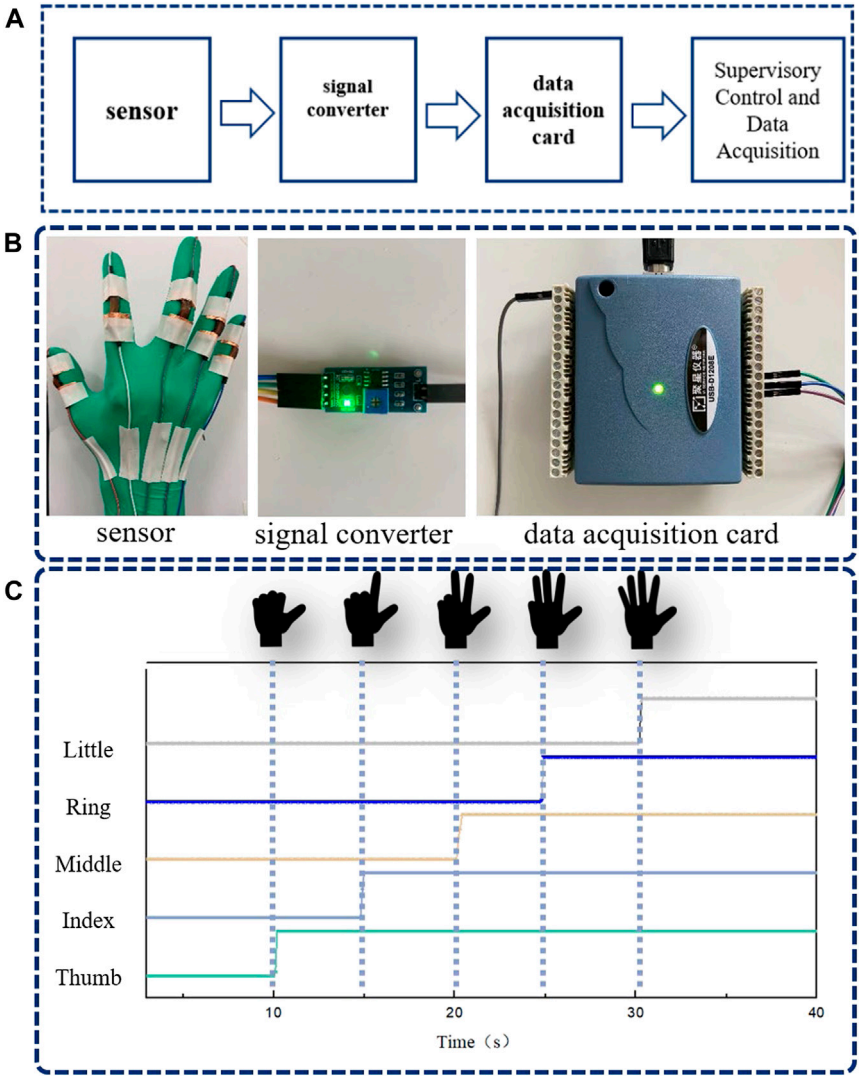

FIGURE 4
(A) Signal transmission flow of sensing device. **(B)** The physical image of the sensor device. **(C)** Signal display of different gestures.

Water absorption swelling is an important characteristic of hydrogels. PNIPAM gel is very sensitive to temperature change. As shown in Figure 3D, PANIPAM gel demonstrates rapid water-loss shrinkage and size smaller with the temperature increases. Figure 3D (I–III) recorded the process of the gel's shrinkage in 50°C water. Figure 3D shows the curve of gel swelling from 25°C to 50°C water. Compared with PANIPAM, the temperature sensitivity of PANIPAM/PANI is significantly enhanced. In addition, the volume shrinkage of all hybrid gels is basically completed near lower critical solution temperature (LCST) (35°C). In a water temperature higher than 40°C, the volume change tends to be stable. Figure 3E shows the swelling capacity of the different samples at room temperature. The PNIPAM/PANI has a higher swelling capacity than the PNIPAM. What can be clearly seen in this figure is the steady decline of swelling capacity with the increase of soaking concentration. However, the downward trend is not very obvious.

Due to the *in-situ* polymerization of pani molecular chain within the gel network of Anupam, the conductive pani molecular chain shifted following the shrinking process of pnipam molecular chain after the temperature increased, and the electrical conductivity also changed. Figure 3C shows the hybrid gel pasted on the outer wall of the beaker. An electrochemical workstation was used to test the i-t curve of the hybrid gel after 50°C hot water was added to the beaker. After hot water is added to the beaker, the hybrid gel attached to the beaker wall feels the temperature rise, and the volume of the hybrid gel changes, the pani molecular chain that carries electricity changes, causing the resistance value to increase and the current to decrease. This experiment confirms the thermosensitive conductivity of hybrid gels and provides the application scenario of hybrid gels as thermosensitive sensors.

The hybrid gels themselves have temperature-sensitive and conductive properties. Figures 3A, B show the application scenario of hybrid gel as a temperature-sensitive sensor. As shown in Figure 3A, a hybrid gel of a specific size and shape is placed in a sealed cylindrical container. At normal temperature, the upper part of the hybrid gel is in contact with the negative electrode

of the button battery. The lower part is connected with the light-emitting diode through copper tape. The whole form conductive circuit. When the gel is heated, the gel dehydrating volume shrinks. The top of the gel loses contact with the button battery. The whole circuit is disconnected (Figure 3B). The hybrid gel acts as a switch throughout the circuit. When the temperature is lower than LCST, the gel is in a swelling state. The circuit closes and the diode lights up. When the temperature is higher than LCST, the gel de-solubilization and volume becomes smaller. The circuit is on, the diode is off. Due to the excellent thermal response sensitivity of the hybrid gel, the whole state switch is very fast. Figure 3C shows the loop current change curve of PNIPAM/PANI during the process of shrinking. PNIPAM/PANI gel is attached to the outer wall of the beaker. An electrochemical workstation was used to monitor the current curve in the gel in. At 0 s, 50°C water was added into the beaker. Then, the gel loses water. Over time, the current in the gel decreases. This experiment confirmed the thermosensitive conductivity of the gel. The application prospect of thermosensitive gel as a thermosensitive sensor is provided.

The proposed sensor has been confirmed to have the potential to monitor human motions. For a practical application, a smart glove for real-time motion detection was assembled, as shown in Figure 4. The smart glove was composed of five strain sensors, a signal converter, and a data acquisition card. The data acquisition card was connected to Supervisory Control and Data Acquisition (SCDA). The sensors were mounted onto the finger joints of a rubber glove by tape to detect the signal of each finger, as shown in Figure 4. The entire circuit can be roughly divided into four parts: Sensor, signal converter, data acquisition card, supervisory control, and data acquisition (SCDA), as shown in Figures 4A, B. Ten current leads were led out from five sensors and all connected to the SCDA eventually through a data acquisition card. After the computer received the data, it drew data graphs in real-time through SCDA. The response of each finger was distinct and independent, as shown in Figure 4C.

Conclusion

In conclusion, we successfully prepared PNIPAM gel through 3D printing. In addition, the conductive polymer network PANI was *in-situ* polymerized on the PNIPAM matrix by phytic acid. The inter-permeable binary polymer network made the hybrid hydrogel show unique characteristics. Hybrid gels have excellent tensile properties, sensitive temperature sensitivity, and electrical conductivity. The application scenario of our gel as a temperature-sensitive sensor was demonstrated by a simple two-stage tube circuit. The effect of aniline concentration on swelling and mechanical properties of hybrid gel was investigated. We have designed a device for real-time hand monitoring. This device can monitor palm movement in real time according to the signals transmitted by the sensor made of gel. This work may have a wide range of applications in stimulus-response electronics, flexible electronics, artificial intelligence wearables, etc.

Experimental section

The ink formula contained n-isopropyl acrylamide (NIPAM), diphenyl (2,4, 6-trimethyl benzoyl) phosphine oxide (TPO) as UV initiator, and Laponite XLG nanosheet as a rheological modification. Dissolve the platinum XLG in 10 mL deionized water and stir with other reagents. All chemicals were purchased from Sigma-Aldrich. Food bot food 3D printer extrusion printing molding. A 365 nm UV light source was used for photocuring molding The printed NIPAM gel was soaked in deionized water for 48 h to remove the unreacted impurities. NIPAM gel was soaked in 60°C hot water to shrink, and then the shrunk gel sample was soaked in an aniline water/ethanol mixture for 24 h to fully expand, the volume ratio of water to ethanol was 1:1. NIPAM gel, fully swollen by aniline solution, was transferred to 13 wt% phytic acid solution to form a polyaniline network *in situ*.

Data availability statement

The original contributions presented in the study are included in the article/Supplementary Material, further inquiries can be directed to the corresponding authors.

Author contributions

YL: Conceptualization, methodology, writing—original draft preparation WZ: Methodology, software, JZ: Methodology, software, LX: Methodology, software, BL: Validation, formal analysis, JD: Methodology, G-LG: Writing—review and editing, supervision ZJ: Writing—review and editing, supervision.

Funding

The authors acknowledge financial support from the National Program for Support of Top-Notch Young Professionals, the National Natural Science Foundation of China (No. 51773049), and China Aerospace Science and Technology. Corporation-Harbin Institute of Technology Joint Center for Technology Innovation Fund (HIT15-1A01), China Postdoctoral Science Foundation (Nos. 201003420 and 20090460067), Cultivation plan of major scientific research projects of HIT (XNXWQQ5740001619), Heilongjiang Touyan Innovation Team Program.

Conflict of interest

The authors declare that the research was conducted in the absence of any commercial or financial relationships that could be construed as a potential conflict of interest.

The handling editor (YU) declared a shared affiliation with authors (YL, JZ, LX, BL, JD, G-LG, and ZJ) at the time of the review.

Publisher's note

All claims expressed in this article are solely those of the authors and do not necessarily represent those of

their affiliated organizations, or those of the publisher, the editors and the reviewers. Any product that may be evaluated in this article, or claim that may be made by its manufacturer, is not guaranteed or endorsed by the publisher.

Supplementary material

The Supplementary Material for this article can be found online at: https://www.frontiersin.org/articles/10.3389/fmats.2023.1096475/full#supplementary-material

References

Abbadessa, A., Blokzijl, M. M., Mouser, V. H., Marica, P., Malda, J., Hennink, W. E., et al. (2016). A thermo-responsive and photo-polymerizable chondroitin sulfate-based hydrogel for 3D printing applications. *Carbohydr. Polym.* 149, 163–174. doi:10.1016/j.carbpol.2016.04.080

Annabi, N., Tamayol, A., Uquillas, J. A., Akbari, M., Bertassoni, L. E., Cha, C., et al. *Adv. Mater.* 2014, 25th anniversary article: Rational design and applications of hydrogels in regenerative medicine, 26, 85–124. doi:10.1002/adma.201303233

Bai, J., Wang, R., Ju, M., Zhou, J., Zhang, L., and Jiao, T. (2020). Facile preparation and high performance of wearable strain sensors based on ionically cross-linked composite hydrogels. *Sci. China Mater.* 64, 942–952. doi:10.1007/s40843-020-1507-0

Bai, J., Wang, R., Wang, X., Liu, S., Wang, X., Ma, J., et al. (2021). Biomineral calcium-ion-mediated conductive hydrogels with high stretchability and self-adhesiveness for sensitive iontronic sensors. *Cell. Rep. Phys. Sci.* 2, 100623. doi:10.1016/j.xcrp.2021.100623

Boere, K. W. M., Blokzijl, M. M., Visser, J., Linssen, J. E. A., Malda, J., Hennink, W. E., et al. (2015). Biofabrication of reinforced 3D-scaffolds using two-component hydrogels. *J. Mater Chem. B* 3, 9067–9078. doi:10.1039/c5tb01645b

Cristovao, A. F., Sousa, D., Silvestre, F., Ropio, I., Gaspar, A., Henriques, C., et al. (2019). Customized tracheal design using 3D printing of a polymer hydrogel: Influence of UV laser cross-linking on mechanical properties. *3d Print. Med.* 5, 12. doi:10.1186/s41205-019-0049-8

Fernandes, D. F., Majidi, C., and Tavakoli, M. (2019). Digitally printed stretchable electronics: A review. *J. Mater. Chem. C* 7, 14035–14068. doi:10.1039/c9tc04246f

Gao, W., Ota, H., Kiriya, D., Takei, K., and Javey, A. (2019). Flexible electronics toward wearable sensing. *Accounts Chem. Res.* 52, 523–533. doi:10.1021/acs.accounts.8b00500

Li, D., Zhang, X. Y., Yao, J. F., Simon, G. P., and Wang, H. T. (2011). Stimuli-responsive polymer hydrogels as a new class of draw agent for forward osmosis desalination. *Chem. Commun.* 47, 1710. doi:10.1039/c0cc04701e

Li, L., Lin, Q., Tang, M., Duncan, A. J. E., and Ke, C. (2019). Advanced polymer designs for direct-ink-write 3D printing. *Chemistry-A Eur. J.* 25, 10768–10781. doi:10.1002/chem.201900975

Li, P. J., Yuan, S. S., Tang, Q. W., and He, B. L. (2014). Robust conducting gel electrolytes for efficient quasi-solid-state dye-sensitized solar cells. *Electrochimica Acta* 137, 57–64. doi:10.1016/j.electacta.2014.04.093

Ligon, S. C., Liska, R., Stampfl, J., Gurr, M., and Muelhaupt, R. (2017). Polymers for 3D printing and customized additive manufacturing. *Chem. Rev.* 117, 10212–10290. doi:10.1021/acs.chemrev.7b00074

Pan, L., Yu, G., Zhai, D., Lee, H. R., Zhao, W., Liu, N., et al. (2012). Hierarchical nanostructured conducting polymer hydrogel with high electrochemical activity. *Proc. Natl. Acad. Sci. U. S. A.* 109, 9287–9292. doi:10.1073/pnas.1202636109

Qin, Z., Liu, S., Bai, J., Yin, J., Li, N., and Jiao, T. (2022). Ionic conductive hydroxypropyl methyl cellulose reinforced hydrogels with extreme stretchability, self-adhesion and anti-freezing ability for highly sensitive skin-like sensors. *Int. J. Biol. Macromol.* 220, 90–96. doi:10.1016/j.ijbiomac.2022.08.055

Roopavath, U. K., Soni, R., Mahanta, U., Deshpande, A. S., and Rath, S. N. (2019). 3D printable SiO_2 nanoparticle ink for patient specific bone regeneration. *RSC Adv.* 9, 23832–23842. doi:10.1039/c9ra03641e

Treml, B. E., McKenzie, R. N., Buskohl, P., Wang, D., Kuhn, M., Tan, L.-S., et al. (2018). Autonomous motility of polymer films. *Adv. Mater.* 30, 1705616. doi:10.1002/adma.201705616

Wu, J., Wu, Z., Wei, Y., Ding, H., Huang, W., Gui, X., et al. (2020). Ultrasensitive and stretchable temperature sensors based on thermally stable and self-healing organohydrogels. *ACS Appl. Mater Interfaces* 12, 19069–19079. doi:10.1021/acsami.0c04359

Yang, X. W., Qiu, L., Cheng, C., Wu, Y. Z., Ma, Z. F., and Li, D. (2011). Ordered gelation of chemically converted graphene for next-generation electroconductive hydrogel films. *Angew. Chemie-International Ed.* 50, 7325–7328. doi:10.1002/anie.201100723

Zhai, D. Y., Liu, B. R., Shi, Y., Pan, L. J., Wang, Y. Q., Li, W. B., et al. (2013). Highly sensitive glucose sensor based on Pt nanoparticle/polyaniline hydrogel heterostructures. *ACS Nano* 7, 3540–3546. doi:10.1021/nn400482d

frontiers | Frontiers in Materials

TYPE Original Research
PUBLISHED 06 April 2023
DOI 10.3389/fmats.2023.1177093

OPEN ACCESS

EDITED BY
Jingjun Wu,
Zhejiang University, China

REVIEWED BY
Xiaozhen Zhang,
Jingdezhen Ceramic Institute, China
Guoxiong Wang,
Dalian Institute of Chemical Physics (CAS), China

*CORRESPONDENCE
Xiangang Luo,
lxg@ioe.ac.cn
Kui Xie,
kxie@fjirsm.ac.cn

SPECIALTY SECTION
This article was submitted to Polymeric and Composite Materials, a section of the journal Frontiers in Materials

RECEIVED 01 March 2023
ACCEPTED 22 March 2023
PUBLISHED 06 April 2023

CITATION
Liu K, Cheng F, Luo Y, Liu L, Wang C, Xie K and Luo X (2023), Porous single crystalline-like titanium dioxide monolith with enhanced photoelectrochemical performance. *Front. Mater.* 10:1177093. doi: 10.3389/fmats.2023.1177093

Porous single crystalline-like titanium dioxide monolith with enhanced photoelectrochemical performance

Kaipeng Liu[1,2,3], Fangyuan Cheng[3], Yunfei Luo[1,3], Ling Liu[1,3], Changtao Wang[1,3], Kui Xie[4]* and Xiangang Luo[1,3]*

[1]State Key Laboratory of Optical Technologies on Nano-Fabrication and Micro-Engineering, Institute of Optics and Electronics, Chinese Academy of Sciences, Chengdu, China, [2]School of Optoelectronic Science and Engineering, University of Electronic Science and Technology of China, Chengdu, China, [3]School of Optoelectronics, University of Chinese Academy of Sciences, Beijing, China, [4]Key Laboratory of Design and Assembly of Functional Nanostructures, Fujian Institute of Research on the Structure of Matter, Chinese Academy of Sciences, Fuzhou, China

Macro-sized porous single crystalline-like (PSC-like) TiO_2 is endowed with unique structural advantages due to its structural consistency and porosity in a large area, which would significantly enhance its photoelectrochemical function. However, there are significant technical challenges in the growth of porous single crystalline-like monoliths. The consistency of structure dominates the structure so that the grain boundary is reduced to the minimum, which is in contradiction with the three-dimensional percolation structure. Here we report a lattice reconstruction strategy based on solid-solid transformation to grow porous single crystal-like anatase TiO_2 dominated by (200) and (101) facets at 2 cm scale. In comparison with the traditional definition of porous single crystal, it has two different lattice orientations, but still has good photoelectrochemical properties. The band gap engineering introduces Ti^{3+} gap into the lattice to generate Ti_nO_{2n-1} with Magneli phase, limiting the created active structure to the lattice with two-dimensional surface, which would open a new avenue to create highly active surfaces to capture photons and transport electrons stably. The PSC-like Ti_nO_{2n-1} provides enhanced exciton lifetime (3–5 ns) as a photocatalytic catalyst and shows significant visible light absorption. The independent PSC-like Ti_nO_{2n-1} delivers high photocurrent of 1.8–5.5 mA · cm^{-2} at room temperature and does not decay for 10 h.

KEYWORDS

porous crystal, titanium dioxide, magneli phase, photoelectricity, catalysis

1 Introduction

The surface of transition metal oxides is usually used to carry the reaction of electron transfer and proton coupling, which is very important for the solar energy conversion process (Schrauben et al., 2012; Guo et al., 2019). Among photocatalysts, Ti-based semiconductor materials provide the high photocatalytic activity and play a key role in photocatalysis and solar energy conversion (Zhao et al., 2019; Chen et al., 2020). As an n-type photoanode, the band gap of titanium dioxide is about 3.2eV, and its energy conversion efficiency is often limited by the effective absorption of visible light and the rapid recombination of electrons and holes. In the process of modification of traditional

nano-photocatalytic materials, nitrogen doping with unsaturated coordination structure is widely used to change the catalytic properties of materials (Bie et al., 2019; Meng et al., 2019; Xu et al., 2020). However, the metal-nitrogen group with immeasurable nitrogen coordination has structural disturbance in its catalytic activity, which is frequently accompanied by poor stability and dependability.

Anatase titanium dioxide is one of the transition metal oxide photocatalysts discussed in recent years because of its high photocatalytic activity due to its structural characteristics. As a typical traditional photocatalyst, its conduction band composed of valence electrons and empty orbitals is well understood. The Ti^{4+} and bridging O^{2-} ions are staggered along the [101] axis, providing convenience for electronic structure adjustment (Li et al., 2006; Guo et al., 2016). Generally, titanium dioxide semiconductor with a broadband gap of ~3.2eV is exposed to sunlight as the light collection device, and its absorption of visible light is limited, and the collection rate of light source at near-infrared wavelength is extremely low. Affected by its electronic structure, the conduction band of TiO_2 receives the electrons excited from the valence band, and forms a high-energy and easily mobile electron-hole pair with the valence band structure with holes. Electron-hole pairs are usually used as medium to participate in the chemical reaction on the catalyst surface and reassemble to release heat and light energy. In addition, the electron-hole pair would also be dissociated again and transferred to the active site of the catalyst in the form of free electrons to form surface groups (Kou et al., 2017; Chen and Ardo, 2018). In this process, the band gap adjustment strategy and the sufficient reaction sites provided by the high specific surface are the keys to determine the photocatalytic performance (Li et al., 2022).

Different from the strategy of doping impurities into titanium dioxide lattice to form point defects, the Ti_nO_{2n-1} with Magneli phase effectively enhances the absorption of visible light through the self-doping of Ti^{3+}. The doping strategy with point defects is to achieve effective absorption of visible light by reducing the conduction band or increasing the valence band (Yu et al., 2013; Faraji et al., 2019). However, traditional black titanium dioxide prepared by hydrogenation often forms core-shell nanoparticles covered by Ti^{3+} disordered phase on the surface. The crystal structure that cannot be accurately confirmed and too many grain boundaries will greatly hinder the rapid transport of electrons. Here we adjust the electronic structure of the material to achieve enhanced absorption of visible and infrared light by introducing Ti^{3+} gap into PSC-like Ti_nO_{2n-1} crystal to produce local defect structure (Cheng et al., 2019).

Titanium dioxide is usually used as the photoanode in the photochemical cell, and the direct catalytic splitting of water under light irradiation and external bias is one of the most active topics (Qian et al., 2019; Zhang et al., 2019; Bie et al., 2022). Generally, photogenic holes on the surface of titanium dioxide photoanode would activate water in the electrolyte to generate surface OH, while the electrons are transferred to the opposite electrode to reduce protons to hydrogen (Liu et al., 2019; Ros et al., 2020). The generation of OH is the key to the realization of photocatalytic water, which would provide opportunities for the participation of highly active hydroxyl radicals in heterogeneous catalysis, and shows great potential in basic and applied research (Shin et al., 2022).

In this work, the lattice reconstruction strategy based on the phase transformation is used to fabricate the PSC-like Ti_nO_{2n-1} monoliths at 2 cm scale (Jin et al., 2020; Xiao and Xie, 2022). PSC-like Ti_nO_{2n-1} monoliths has a high monocrystal-like property, and its dominant lattice structure maintains a high consistency with bulk single crystal. Its surface well-defined structure with clear and long-range order at atomic scale significantly reduces the scattering effect of electrons/holes caused by the interface between traditional grains, which will significantly enhance the functionality of charge separation and transmission required to inhibit charge recombination. Moreover, the PSC-like Ti_nO_{2n-1} monoliths possess a large specific surface area, which makes them suitable as photoanodes in photoelectrochemical cells. This provides ample reaction sites for photocatalytic reactions and facilitates the collection of electrons/holes, resulting in ultra-high photocurrent and water decomposition performance.

2 Materials and methods

2.1 Crystal growth

The growth of precursor $KTiOPO_4$ (KTP) single crystal is achieved by the topseed crystal method with molybdate as the cosolvent (Jacco et al., 1984). KTP single crystal with (110) faces is directionally cut and polished to 10 mm × 10 mm × 0.5 mm for growth of PSC-like anatase TiO_2. The KTP single crystal is introduced into the vacuum tube furnace that can accurately control the pressure and temperature, and 100–200 sccm H_2/Ar gas flow is introduced to control the pressure to stabilize to 67–333 mbar. KTP is maintained at 600°C–950°C for 10–30 h in a strong reducing atmosphere to generate PSC-like anatase Ti_nO_{2n-1} monoliths of Magneli phase.

2.2 Characterizations

We detect the formation of the phase and determined the orientation of the crystal plane on the X-ray diffractometer (XRD, Mniflex 600). Then the porous morphology of the crystal material is observed by field emission scanning electron microscopy (FE-SEM, SU8010). TEM samples are prepared by using FIB (ZeissAuriga), selected area electron diffraction (SAED) tests are carried out at 200 kV accelerating voltage. The crystal structure is characterized on spherical aberration corrected high resolution transmission electron microscope (Cs-HRTEM) (FEITitan3G2 60–300) at 300 kV accelerating voltage. X-ray photoelectron spectroscopy (XPS, Escalab 250Xi) determines the chemical state of Ti in Ti_nO_{2n-1}. The electron paramagnetic resonance (EPR) spectrums are obtained on JES TE200 (JEOL) to evaluate the signals of Ti^{3+} and oxygen vacancies. The performance test of photoelectric decomposition water is carried out in 1M NaOH solution at 25°C.

2.3 Photoelectrochemical measurement

In the photoelectrochemical test, we use the three-electrode test method. The electrochemical workstation (IM6, Zahner) is

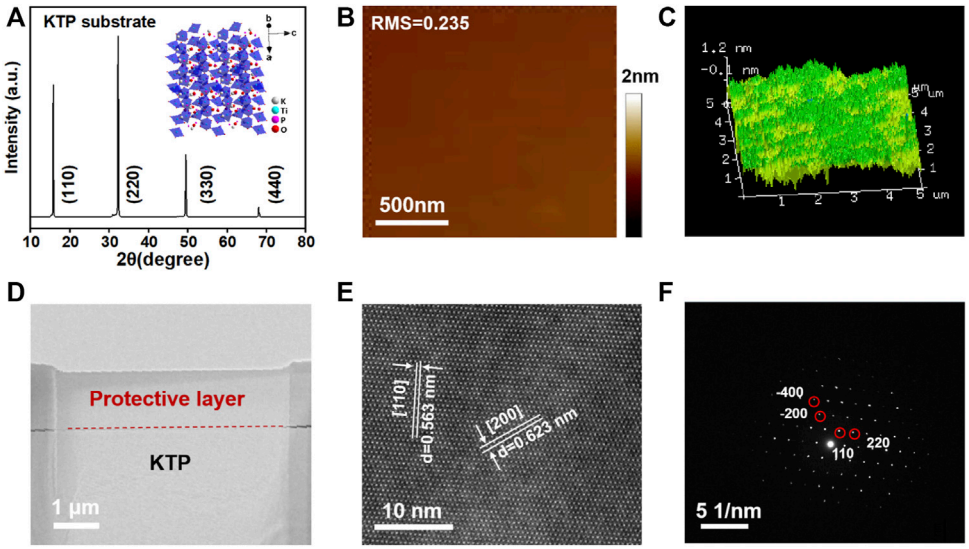

FIGURE 1
(A) XRD pattern of (110) KTP single crystal, the inset is crystal structure of KTP and lattice channel of K/P removal along (110) facet. **(B)** Surface roughness. **(C)** Surface 3D AFM image of KTP substrate. **(D)** TEM image of KTP slice. **(E)** Spherical aberration corrected Scanning Transmission Electron Microscope (Cs-HRTEM) image of the KTP view towards [110] plane. **(F)** SAED pattern of KTP.

equipped with a two-chamber photocatalyst cell with Pt and saturated calomel electrode as the counter electrode and reference electrode, respectively. In addition, PSC-like Ti_nO_{2n-1} monoliths are used as the working electrode, which is separated by an anion exchange membrane (Nafion 212). The photoelectric decomposition of water is tested in 1M sodium hydroxide solution at 25°C. The Nernst equation is that to convert all potentials to RHE reference scale:

$$E_{RHE} = E_{Hg/Hg_2Cl_2} + 0.0591 \times PH + 0.244$$

3 Results and discussion

The growth of porous single crystalline-like TiO_2 is a dynamic equilibrium process between heat and force. We grow and treat (110) KTP (10 mm × 10 mm × 0.5 mm) to grow PSC-like anatase TiO_2 monoliths with the identical dimension in a reducing atmosphere at 600–950°C and 67–333 mbar. It is well known that titanium dioxide is a typical photoelectric semiconductor with different crystal configurations such as rutile and anatase. The growth process of PSC-like rutile TiO_2 often requires higher operating temperatures to drive the phase transition, which remains technically difficult. There is a strong dependence between the formation of PCS-like $TinO_{2n-1}$ crystal rate and the crystal quality of KTP precursor. In the process of solid-solid phase transformation, the growth process of recrystallization is more sensitive to the surface roughness of the parent crystal. In Figure 1A, the sharp characteristic peak in the XRD pattern indicates that KTP with (110) facets has high single crystal quality. In inset image, the K and P atom escape channels along the KTP (110) facet are not completely unobstructed, which is one of the reasons for the appearance of competitive crystal planes in addition to the dominant crystal planes during the PSC-like TiO_2 monolith growth process. As shown in Supplementary Figure S1, the Raman spectroscopy and SEM picture indicate the smooth uniform structure in KTP. We polish the KTP substrate to maintain its surface roughness below 0.24 nm as shown in Figure 1B; Figure 1C shows the flatness of KTP at the three-dimensional nanometer scale under the atomic force microscope. We used focused ion beam (FIB) to prepare the sample of Transmission Electron Microscope (TEM), that is (110) KTP slice with ~50 nm thickness as shown in Figure 1D, which coupled with Cs-HRTEM to observe the lattice structure of mother crystal KTP in the field, as shown in Figure 1E. The uniform distribution of K, Ti, P, and O elements in the form of regular periodic arrays re-certified the surface well-defined structure of the single crystal to accommodate the order of solid-solid phase transformation to Ti-O coordination structure. The lattice spacing of 0.563 nm and 0.623 nm are certified as [110] and [200] facets of KTP, respectively, which is consistent with the structure of the selected area electron diffraction pattern (SAED), as shown in **Figure 1F** (Sorokina and Voronkova, 2007). Breaking the KTP single crystal structure as the starting step of the lattice reconstruction process, the long range ordered crystal structure of the single crystal is the key to the formation of the porous single crystalline TiO_2 nucleus. In order to accelerate the growth of porous single crystalline-like monolith, the mother phase should be single crystalline state to enable stable solid-solid transformation (Li and Xie, 2023).

Porous single crystal monoliths have the unique advantage in the construction of well-defined structures at surface interfaces by combining the consistency of the structure with the porous structure. Porous single crystalline-like monoliths retain a porous skeleton and the grain boundary region is minimized to ensure a high single crystal rate. In Supplementary Figure S2, The PSC-like

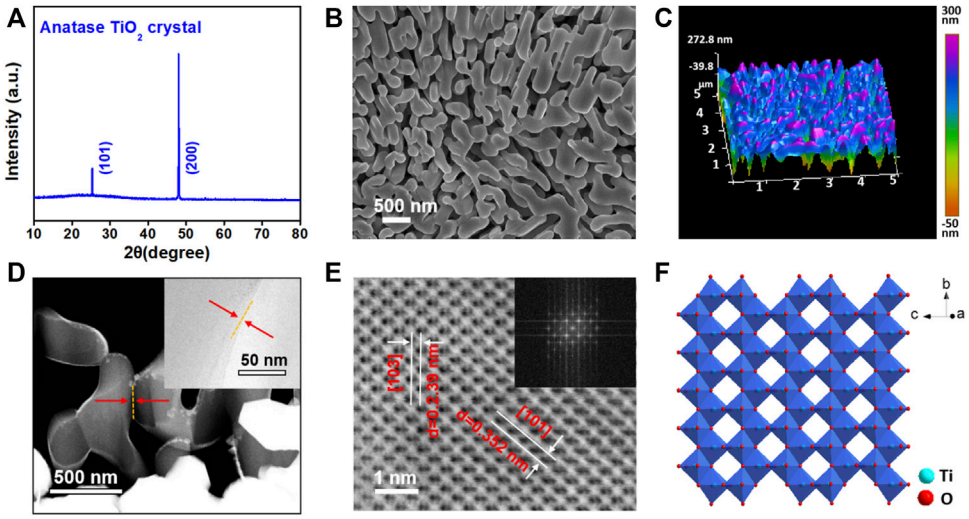

FIGURE 2
(A) XRD pattern of PSC-like anatase TiO_2. **(B)** The SEM image of PSC-like anatase TiO_2 monolith. **(C)** Surface 3D AFM image of TiO_2 with porous structure. **(D)** STEM image of the PSC-like TiO_2, the inset image is TEM at the corresponding interface. **(E)** Cs-HRTEM image of PSC-like $Ti_{38}O_{75}$ viewed towards [-1−31] axis. **(F)** The illustration is the structure of anatase TiO_2.

anatase TiO_2 is grown on the solid-solid phase transformation, and adjusted the single crystal rate by adjusting the annealing process to reduce the longitudinal temperature gradient. The higher the annealing rate, the faster the transverse and longitudinal surface stress changes, which means a lower single crystal rate. Figure 2A shows the XRD pattern of PSC-like anatase TiO_2 dominated by (200) facet. The characteristic peaks of low exponent observed at 25.28° are consistent with the orientation [101] of anatase TiO_2, indicating competitive growth between crystal facets, which is due to a high lattice mismatch of ~23.58% between (110) KTP and (200) TiO_2 (Jiang et al., 2011). Figure 2B and Figure 2C show the microstructure of PSC-TiO_2 growing along the (110) KTP, which with pore size of ~150 nm. The crystal scale of PSC-like TiO_2 remains unchanged relative to KTP, while the directional removal of K/P as the target atom results in the reduction of the overall atomic density to form pores. We further confirmed the TiO_2 transformation using EDS and elemental mapping, as shown in Supplementary Figure S3. Figure 2D shows the STEM image of PSC TiO_2 monolith, confirming the 3D interconnected channel structure at ~100–200 nm. It is noteworthy that the annealing process is one of the methods to adjust the dislocation density in PSC-like TiO_2 monolith. The very small areas in PSC-like TiO_2 monolith evolves from sub-grain boundary to grain boundary during the recrystallization process. Figure 2E shows the Cs-HRTEM image of the skeleton in PSC-like TiO_2 framework. The introduction of a small amount Ti^{3+} causes the random dislocations in PSC $Ti_{38}O_{75}$ monolith, while a periodic dislocation such as Ti_9O_{17} is shown in Supplementary Figure S4 with a large number of Ti^{3+} gaps. The chemical formula of Ti_nO_{2n-1} is determined by the oxidation of graphite in a vacuum system. The SAED image of Fourier transform shown in the Figure 2F confirms that it is also a typical tetragonal single-crystalline structure.

The peaks of Raman spectroscopy at 145, 197, 395, and 515 cm^{-1} are observed in Figure 3A, although slight Raman shift is observed, they are still consistent with the crystal structure of anatase phase (Es-Souni et al., 2008). We use X-ray photoelectron spectroscopy (XPS) to study the evolution of the Ti chemical state in the surface of PSC-like TiO_2 under an Ar atmosphere. The surface Ti is mainly +4 in $Ti_{38}O_{75}$ as shown in Figure 3B, indicating that there is sufficient oxidation state in the lattice. The EPR spectrum in Figure 3C confirms the coexistence of Ti^{3+} and a small amount of oxygen vacancy on the surface of PSC $Ti_{38}O_{75}$ monolith, the signal index increases when the n valve are reduced to 9. The loss of oxygen means that the n value decreases in Ti_nO_{2n-1}, resulting in more Ti^{4+} being reduced to Ti^{3+} gap. Which would adjust the electronic and band gap structure of TiO_2 to expand the visible-infrared light absorption, as shown in Figure 3D. The presence of the high concentration of Ti^{3+} interstitials in PSC-like Ti_9O_{17} monolith with the magneli phase actually transforms it into a black electronic conductor. The transient absorption spectrum of PSC-like Ti_nO_{2n-1} (n = 9 and 38) are further studied under the excitation wavelength of 523 nm. As shown in Figure 3E and Figure 3F, the ultra-long exciton lifetime (~4.7 ns) in PSC-like Ti_nO_{2n-1} (n = 9 and 38) monoliths is verified, which the lifetime is ~5 times that of polycrystalline materials. This result indicates that the inhibition of structural coherence on charge recombination is significantly enhanced.

The precise adjustment of the electronic structure of TiO_2 can achieve the maximum photocurrent response of light collection and increase the specific surface area of porous structure to enhance the photocatalytic performance. Here we use a three-electrode setup to study the photocurrent performance of PSC-like TiO_2, as Figure 4A shown. In Figure 4B, we further used Linear Scanning Voltammetry to test the photocurrent-potential curve of PSC-like Ti_nO_{2n-1} (n = 9 and 38) photoelectrode in 1M NaOH electrolyte solution. Under 10 times air mass (AM) 1.5G illumination of simulated sunlight, the photocurrent generated by PSC-like Ti_9O_{17} photoanode could be as high as 5.5 $mA \cdot cm^{-2}$ at an external bias voltage of 1.6V. In addition, the initial potential of the PSC-like Ti_9O_{17} electrode for water decomposition is ~0.1 V in a 0.5M Na_2SO_4 electrolyte solution under illumination intensity of 10 AM 1.5 G. In Supplementary

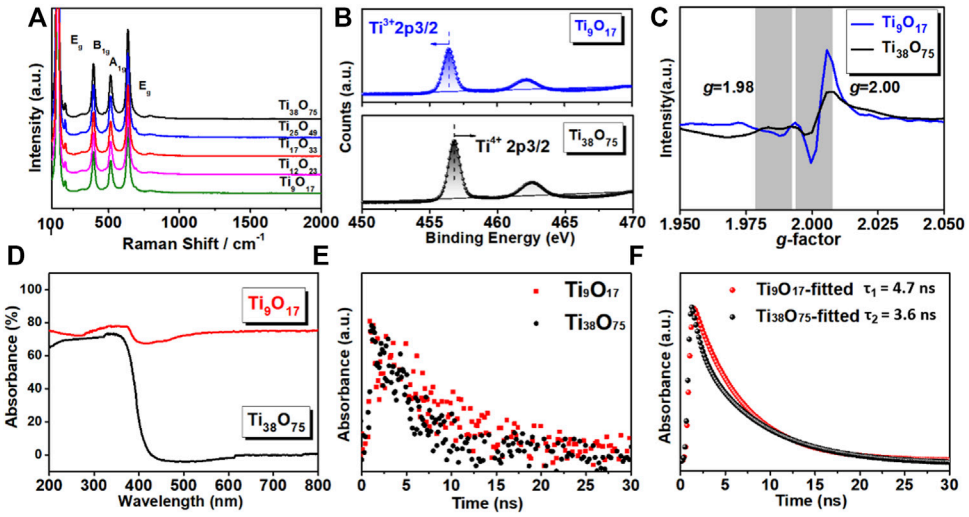

FIGURE 3
(A) Raman scattering spectra of PSC-like Ti_nO_{2n-1}. **(B)** XPS spectra of PSC-like Ti_nO_{2n-1} (n = 9 and 38). **(C)** EPR spectra of Ti_9O_{17} and $Ti_{38}O_{75}$. **(D)** Ultraviolet-visible absorbance spectra. **(E and F)** Decay profiles and fitting curve of femtosecond transient absorption spectra.

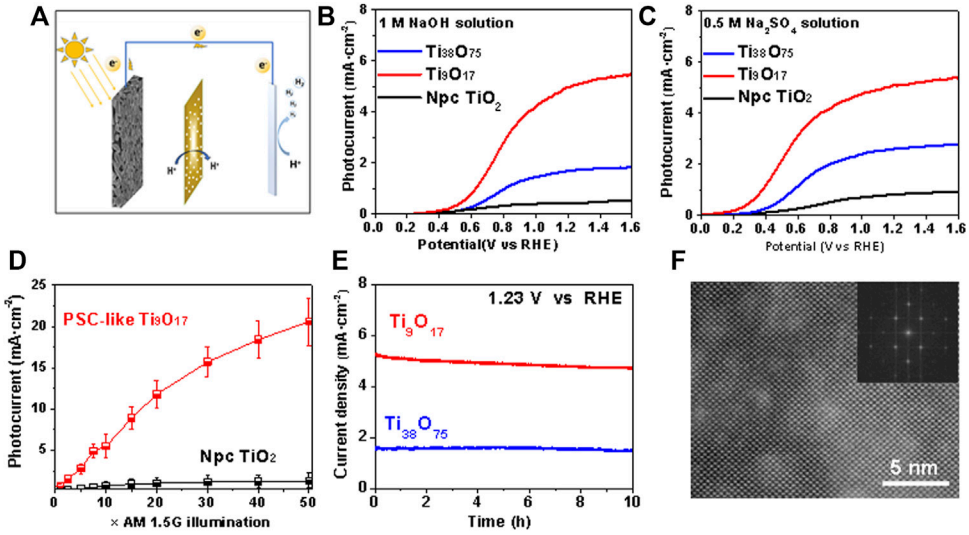

FIGURE 4
(A) The schematic diagram of photoelectrocatalysis cell. **(B** and **C)** Linear Scanning Voltammetry (LSV) curve of three electrode system using the P-SC Ti_nO_{2n-1} photoanodes for water oxidation in the 1 M NaOH and 0.5M $NaSO_4$, respectively. (Ti_nO_{2n-1} as working electrode, Pt as counter electrode, Hg/Hg_2Cl_2 as reference electrode) **(D)** The photocurrent with enhanced light intensity up to 50×AM1.5 G sunlight using PSC-like Ti_9O_{17} and non-porous polycrystalline (Npc) TiO_2 electrodes. The external bias voltage is 1.23V. **(E)** Photocurrent durability test of the PSC-like Ti_9O_{17} and $Ti_{38}O_{75}$ at 1.23V. **(F)** The crystal structure of Ti_9O_{17} after stability test.

Figure S6, the dark current density is generally lower than 0.5 mA cm^{-2}, which can be attributed to the synergy between the structural characteristics of PSC-like monolith and electronic transport. The current density is 5 times higher than that of the PSC-like $Ti_{38}O_{75}$ electrode and ~8 times higher than that of the Non-porous polycrystal (Npc-TiO_2) electrode. Which performance is well above that of nano-catalytic materials, demonstrating the superior activity and structural advantages of PSC-like Ti_9O_{17} crystals in photoanode.

The photocurrent of PSC-like Ti_9O_{17} increases linearly with the irradiation intensity, which photocurrent is as high as ~ 20 mA cm^{-2} under the illumination intensity of 50 AM 1.5 G and the external bias voltage of 1.23 V. In addition, Npc-TiO_2 is uniformly loaded on conductive glass of SnO_2 doped with fluorine (FTO) as a photoanode system, which shows a saturated photocurrent density of ~0.8 mA · cm^{-2} under the illumination intensity of 20 AM 1.5 G at 1.23V, indicating that its high-density grain boundary structure limits the conversion of energy. We further evaluated the durability of the

PSC-like Ti_9O_{17} photoelectrode by chronoamperometric measurement, as shown in Figure 4E, even after 10 h of operation, the photocurrent almost did not decay. It is noteworthy that the catalyst after operation still maintains uniform porous skeleton and well-defined lattice structure, as shown in Supplementary Figure S6 and Figure 4F, thus verifying the structural stability of PSC-like TiO_2 as photoelectrode in the catalytic oxidation of water. In the Cs-HRTEM image of Figure 4E, the presence of residual electrolyte on the catalyst surface causes slight distortion in lattice clarity, but it would be ignored. The synergistic effect of porous microstructure, structural coherence and transport characteristics regulated by band gap engineering significantly enhanced the photocatalytic activity, resulting in an extremely high photoelectrochemical water oxidation performance.

4 Conclusion

In this work, we have grown PSC-like TiO_2 monoliths dominated by (200) facets based on a lattice reconstruction strategy *via* solid-solid phase transformation, which has extremely high single-crystallinity and minimized grain boundary area while maintaining long-range ordered lattice structure and three-dimensional infiltration channels. It has two different lattice orientations, which is different with the porous single crystal, but still has good photoelectrochemical properties. We further introduce Ti^{3+} into the lattice by bandgap engineering to obtain a series of Ti_nO_{2n-1} monolith with the Magneli phase, and tune the electronic structure to narrow the bandgap and enhance the absorption of visible light. We evaluated the PSC-like TiO_2 as a photocathode for water oxidation at 25 °C in a three electrode system and obtained a high current with no obvious attenuation after 10 h of continuous operation. We have demonstrated that the synergistic effect of long-range ordered lattice structure and porous framework can effectively enhance photocatalytic activity and structural stability, providing a new avenue for the design of novel optoelectronic materials and the tuning of surface photoreactivity.

Data availability statement

The original contributions presented in the study are included in the article/Supplementary Material, further inquiries can be directed to the corresponding authors.

Author contributions

KL wrote and revised the manuscript. FC performed the Crystal growth. YL, LL, and CW contributed to the results analysis. KX edited the manuscript. XL supervised the whole project.

Funding

This work was supported by the National Key Research and Development Program of China (2021YFA1501500), the Natural Science Foundation of Fujian Province (2020J05082, 2020J01113), Strategic Priority Research Program of Chinese Academy of Sciences (XDB2000000), Sichuan Science and Technology Program (2019JDJQ0011, 2020ZDZX0018, and 2022YFG0001), Youth Innovation Promotion Association, Chinese Academy of Sciences (2020371, 2023393), and West Light Foundation of the Chinese Academy of Sciences.

Conflict of interest

The authors declare that the research was conducted in the absence of any commercial or financial relationships that could be construed as a potential conflict of interest.

Publisher's note

Supplementary material

The Supplementary Material for this article can be found online at: https://www.frontiersin.org/articles/10.3389/fmats.2023.1177093/full#supplementary-material

References

Bie, C., Wang, L., and Yu, J. (2022). Challenges for photocatalytic overall water splitting. *Chem* 8, 1567–1574. doi:10.1016/j.chempr.2022.04.013

Bie, C., Zhu, B., Xu, F., Zhang, L., and Yu, J. (2019). *In situ* grown monolayer N-doped graphene on CdS hollow spheres with seamless contact for photocatalytic CO_2 reduction. *Adv. Mater.* 31, 1902868–1902876. doi:10.1002/adma.201902868

Chen, D., Cheng, Y., Zhou, N., Chen, P., Wang, Y., Li, K., et al. (2020). Photocatalytic degradation of organic pollutants using TiO2-based photocatalysts: A review. *J. Clean. Prod.* 268, 121725. doi:10.1016/j.jclepro.2020.121725

Chen, H. Y., and Ardo, S. (2018). Direct observation of sequential oxidations of a titania-bound molecular proxy catalyst generated through illumination of molecular sensitizers. *Nat. Chem.* 10, 17–23. doi:10.1038/NCHEM.2892

Cheng, F., Lin, G., Hu, X., Xi, S., and Xie, K. (2019). Porous single-crystalline titanium dioxide at 2 cm scale delivering enhanced photoelectrochemical performance. *Nat. Commun.* 10, 3618–3619. doi:10.1038/s41467-019-11623-w

Es-Souni, M., Kartopu, G., Habouti, S., Piorra, A., Es-Souni, M., Solterbeck, C. H., et al. (2008). Processing and thin film formation of TiO_2-Pt nanocomposites. *Phys. Status Solidi Appl. Mater. Sci.* 205, 305–310. doi:10.1002/pssa.200723181

Faraji, M., Yousefi, M., Yousefzadeh, S., Zirak, M., Naseri, N., Jeon, T. H., et al. (2019). Two-dimensional materials in semiconductor photoelectrocatalytic systems for water splitting. *Energy Environ. Sci.* 12, 59–95. doi:10.1039/c8ee00886h

Guo, Q., Zhou, C., Ma, Z., Ren, Z., Fan, H., and Yang, X. (2016). Elementary photocatalytic chemistry on TiO_2 surfaces. *Chem. Soc. Rev.* 45, 3701–3730. doi:10.1039/c5cs00448a

Guo, Q., Zhou, C., Ma, Z., and Yang, X. (2019). Fundamentals of TiO_2 photocatalysis: Concepts, mechanisms, and challenges. *Adv. Mater.* 31, 1901997–1902026. doi:10.1002/adma.201901997

Jacco, J. C., Loiacono, G. M., Jaso, M., Mizell, G., and Greenberg, B. (1984). Flux growth and properties of $KTiOPO_4$. *J. Cryst. Growth* 70, 484–488. doi:10.1016/0022-0248(84)90306-3

Jiang, H. B., Cuan, Q., Wen, C. Z., Xing, J., Wu, D., Gong, X.-Q., et al. (2011). Anatase TiO_2 crystals with exposed high-index facets. *Angew. Chem.* 123, 3848–3852. doi:10.1002/ange.201007771

Jin, L., Cheng, F., Li, H., and Xie, K. (2020). Porous tantalum nitride single crystal at two-centimeter scale with enhanced photoelectrochemical performance. *Angew. Chem. - Int. Ed.* 59, 8891–8895. doi:10.1002/anie.202001204

Kou, J., Lu, C., Wang, J., Chen, Y., Xu, Z., and Varma, R. S. (2017). Selectivity enhancement in heterogeneous photocatalytic transformations. *Chem. Rev.* 117, 1445–1514. doi:10.1021/acs.chemrev.6b00396

Li, B., Zhao, J., Onda, K., Jordan, K. D., Yang, J., and Petek, H. (2006). Ultrafast interfacial proton-coupled electron transfer. *Science* 311, 1436–1440. doi:10.1126/science.1122190

Li, W. T., and Xie, K. (2023). Porous single crystals at the macroscale: From growth to application. *Acc. Chem. Res.* 56, 374–384. doi:10.1021/acs.accounts.2c00777

Li, Z., Wang, S., Wu, J., and Zhou, W. (2022). Recent progress in defective TiO_2 photocatalysts for energy and environmental applications. *Renew. Sustain. Energy Rev.* 156, 111980. doi:10.1016/j.rser.2021.111980

Liu, N., Xu, M., Yang, Y., Zhang, S., Zhang, J., Wang, W., et al. (2019). Auδ--Ov-Ti^{3+} interfacial site: Catalytic active center toward low-temperature water gas shift reaction. *ACS Catal.* 9, 2707–2717. doi:10.1021/acscatal.8b04913

Meng, A., Zhang, L., Cheng, B., and Yu, J. (2019). Dual cocatalysts in TiO_2 photocatalysis. *Adv. Mater.* 31, 1807660–1807731. doi:10.1002/adma.201807660

Qian, R., Zong, H., Schneider, J., Zhou, G., Zhao, T., Li, Y., et al. (2019). Charge carrier trapping, recombination and transfer during TiO_2 photocatalysis: An overview. *Catal. Today* 335, 78–90. doi:10.1016/j.cattod.2018.10.053

Ros, C., Andreu, T., and Morante, J. R. (2020). Photoelectrochemical water splitting: A road from stable metal oxides to protected thin film solar cells. *J. Mater. Chem. A* 8, 10625–10669. doi:10.1039/d0ta02755c

Schrauben, J. N., Hayoun, R., Valdez, C. N., Braten, M., Fridley, L., and Mayer, J. M. (2012). Titanium and zinc oxide nanoparticles are proton-coupled electron transfer agents. *Science* 336, 1298–1301. doi:10.1126/science.1220234

Shin, H. J., Sohn, S. D., Kim, Y., Jung, S., Kang, J. S., Han, H., et al. (2022). C60 adsorbed on TiO_2 drives dark generation of hydroxyl radicals. *ACS Catal.* 12, 5990–5996. doi:10.1021/acscatal.2c00755

Sorokina, N. I., and Voronkova, V. I. (2007). Structure and properties of crystals in the potassium titanyl phosphate family: A review. *Crystallogr. Rep.* 52, 80–93. doi:10.1134/S1063774507010099

Xiao, Y., and Xie, K. (2022). Active exsolved metal–oxide interfaces in porous single-crystalline ceria monoliths for efficient and durable CH_4/CO_2 reforming. *Angew. Chem. - Int. Ed.* 61, e202113079. doi:10.1002/anie.202113079

Xu, F., Meng, K., Cheng, B., Wang, S., Xu, J., and Yu, J. (2020). Unique S-scheme heterojunctions in self-assembled $TiO_2/CsPbBr_3$ hybrids for CO_2 photoreduction. *Nat. Commun.* 11, 4613–4619. doi:10.1038/s41467-020-18350-7

Yu, X., Kim, B., and Kim, Y. K. (2013). Highly enhanced photoactivity of anatase TiO_2 nanocrystals by controlled hydrogenation-induced surface defects. *ACS Catal.* 3, 2479–2486. doi:10.1021/cs4005776

Zhang, Y. C., Afzal, N., Pan, L., Zhang, X., and Zou, J. J. (2019). Structure-activity relationship of defective metal-based photocatalysts for water splitting: Experimental and theoretical perspectives. *Adv. Sci.* 6, 1900053. doi:10.1002/advs.201900053

Zhao, Y., Zhao, Y., Shi, R., Wang, B., Waterhouse, G. I. N., Wu, L. Z., et al. (2019). Tuning oxygen vacancies in ultrathin TiO 2 nanosheets to boost photocatalytic nitrogen fixation up to 700 nm. *Adv. Mater.* 31, 1806482–1806489. doi:10.1002/adma.201806482

frontiers | Frontiers in Materials

TYPE Original Research
PUBLISHED 28 April 2023
DOI 10.3389/fmats.2023.1183816

OPEN ACCESS

EDITED BY
Jianlei Wang,
Chinese Academy of Sciences (CAS), China

REVIEWED BY
Enrique Cuan-Urquizo,
Monterrey Institute of Technology and Higher Education (ITESM), Mexico
Nidhin Divakaran,
Central Institute of Plastics Engineering and Technology, India

*CORRESPONDENCE
Min-Soo Kang,
Kang10101@sunmoon.ac.kr

RECEIVED 10 March 2023
ACCEPTED 18 April 2023
PUBLISHED 28 April 2023

CITATION
Lee G-W, Kim T-H, Yun J-H, Kim N-J, Ahn K-H and Kang M-S (2023), Strength of Onyx-based composite 3D printing materials according to fiber reinforcement.
Front. Mater. 10:1183816.
doi: 10.3389/fmats.2023.1183816

Strength of Onyx-based composite 3D printing materials according to fiber reinforcement

Gyu-Wol Lee[1], Tae-Hyun Kim[1], Jong-Hwan Yun[2], Nam-Joo Kim[3], Ki-Hwan Ahn[1] and Min-Soo Kang[1]*

[1]Division of Smart Automotive Engineering, Sun Moon University, Asan-si, Republic of Korea, [2]Regional Innovation Platform Project of Kongju National University, Cheonan-si, Republic of Korea, [3]JinSung Boltech Corporation, Asan-si, Republic of Korea

This study evaluates the mechanical strength of 3D-printed objects of composite material. The composite material considered in this study comprises onyx as the base material with glass fiber and carbon fiber as the internal reinforcements. 3D printing using composite materials generally involves laminating fiber reinforcements in the form of layers within the printed part. To analyze the effect of such reinforcements on the printed parts, specimens were prepared by varying the number of layers and arrangement conditions of the reinforcement. The analysis shows that the tensile strength of the composite increases with the number of reinforcement layers due to the effect of the fibers on the longitudinal direction and a larger bonding area between the internal Onyx and the fibers. Furthermore, higher tensile strength is observed when the reinforcements are laminated at regular intervals than when they are arranged in the center. This study serves as a database for 3D printing fiber-reinforced composites aiding future research in comparing and optimizing their strength according to the 3D printing conditions.

KEYWORDS

composite, 3D printing, Onyx, carbon fiber, glass fiber

1 Introduction

Three-dimensional (3D) printing is an additive manufacturing method that receives 3D modeling data, melts various materials, and stacks them to create a 3D structure, in contrast to the cutting process used in conventional manufacturing (Cheng et al., 2020; Yan et al., 2021; Sun and Wu, 2022). In 3D printing, innovative techniques are used to customize shapes and textures by fabricating objects into precise 3D shapes. It generally proceeds quickly from the design stage to prototype production and testing and is extremely economical (Le Tohic et al., 2018; Eisenberg et al., 2013). Additive manufacturing in 3D printing includes several methods, including selective laser sintering (SLS) (Fina et al., 2017; Shirazi et al., 2015; Awad et al., 2020), stereolithography (SLA) (Martín-Montal et al., 2021; Wang et al., 2016; Manapat et al., 2017), polyjet (Tee et al., 2020; Kabandana et al., 2022), and fused deposition modeling (FDM) (Kollamaram et al., 2018; Montero et al., 2001; Rahim et al., 2019). In the SLS method, powder-type materials are temporarily melted with a laser and then fused together into the desired shape. In the SLA method, the laser beams of a specific wavelength are reflected off a mirror to harden the liquid resin. In the polyjet method, a photocurable liquid resin is sprayed through a nozzle, which is solidified c using a UV light source. Thus, 3D printing includes various types of additive manufacturing methods, each with its own characteristics as well as advantages and disadvantages.

FDM is the most widely used additive method. In this method, a filament-type thermoplastic material is melted in a nozzle and stacked up from the bottom while the melted material is solidified in the required part. The size and detail of the layer are determined by the speed and force with which the material is melted and extruded through the nozzle.

Recently, have investigated the use of FDM for printing composite materials. In addition, composite material 3D printing has garnered worldwide attention owing to the promising research in this field. Various studies have scrutinized the different types and structures of composite materials and conducted comparative analyses of tensile strength according to filling patterns, isotropic fiber (Mei et al., 2019; Kriz and Stinchcomb, 1979) and concentric fiber method (Araya-Calvo et al., 2018; Morales U et al., 2021). Research has also been extended to comparing the thermal conductivity and elasticity of composite materials with applications in a wide range of industries and experiments. Typically, even a small amount of reinforcement (fiber) added to the main material (filament) results in composite parts with enhanced mechanical properties and specific strength superior to that of steel. Current 3D composite printing uses onyx with reinforcement layers. Onyx has been measured to be 1.4 times stronger and stiffer than ABS, has a flexural strength of 81 MPa and a flexural stiffness of 2.9 Gpa. Additionally, it has high tensile strength and heat resistance, is easy to print, and is robust in assembly (Bárnik et al., 2019). Furthermore, it combines well with continuous filament fabrication (CFF)-based (Galati et al., 2021; Parmiggiani et al., 2021) fiber materials such as carbon fiber (CF) (Newcomb, 2016) and glass fiber (GF) (El-Tayeb and Gadelrab, 1996). However, owing to its vulnerability to moisture absorption the filament requires careful management (Moreno-Núñez et al., 2023). Onyx is used in most composite material 3D printers as it has good bonding strength with various fiber reinforcements, such as CF, GF, and Kevlar (Morales M A et al., 2021; Tian et al., 2021). Among them, CF is extremely light and does not deform easily, its strength is comparable to aluminum, which is a popular 3D printing material, and possesses excellent heat resistance and impact resistance. In addition, its mechanical properties are superior to those of GF composite materials and it is an ultra-lightweight alternative to next-generation metals. CF is 6 times stronger and approximately 18 times harder than onyx fibers. GF is most often used in fiber-reinforced plastics, has excellent heat-insulating properties, does not rust, and is easy to process. GF composite materials are less expensive than other composite materials, have excellent durability, have no electrical conductivity, and have excellent resistance to impact damage. GF is 2.5 times stronger and 7 times harder than onyx. Therefore, it is used as a general-purpose material that complements the mechanical properties of onyx-based composite materials. However, CF and GF are approximately 13 and 8 times more expensive than onyx, respectively.

Therefore, to print efficiently, the printing process must be optimized while maintaining the mechanical strength of the printed parts. Such optimization requires a database on the effects of various thicknesses and arrangement positions of CF and GF layers inside onyx on the properties of the printed part. Therefore, in this study, the mechanical strength characteristics of composite printed parts were analyzed according to the type and arrangement of reinforcements. Onyx was selected as the base material, CF and GF were selected as reinforcements, and the mechanical behavior was studied according to the change in thickness and position of the CF and GF layers.

2 Materials and methods

2.1 Test specimen

The tensile test standard used in this study was performed by citing the international test standard ISO 527-4, which defines test conditions for isotropic and orthotropic fiber-reinforced plastic composites. ISO 527-4 presents a standardized size for tensile testing of specimens (Pisanu et al., 2021). According to the above standard, the size of the test specimen was set as shown in Figure 1A. 3D modeling was performed to obtain a test specimen 150 mm long, 10 mm wide, and 2.5 mm thick, and the gauge length was set to 50 mm. The conditions that were set for composite material 3D printing are as follows. The composite material for 3D printing was set to 30% of the internal filling density in a grid-type pattern to proceed with the evaluation under conditions similar to the grid pattern of 30% of the PLA material. The onyx thickness of the upper shell and lower surface of the specimen was set to the recommended level of 4-layer to achieve superior finish quality and waterproofing. The side layer of the specimen was set to the recommended level of 2-layer for surface finish and waterproofing to ensure that the reinforcement could be arranged well within the onyx. CF and GF were used as fiber reinforcements inside the composite material. They were selected owing to their inexpensiveness, strength, and bonding strength when combined with onyx. The selected fiber reinforcement was laminated in the form of a plane inside the onyx through the 3D printing process to form a layer.

2.2 Layer arrangement

Table 1 shows the physical properties of the materials used in this study. The setting is shown in Figure 1, with the internal reinforcement arrangement based on the center of the specimen. As shown in Figures 1B–E, the output was set to be arranged from 1-layer to 4-layer according to the location of the center of each layer. Consequently, the reinforcement thickness becomes thicker with an increase in the number of reinforcement layers. To analyze the effective arrangement position of the fiber reinforcement instead of merely adjusting the center of the specimen, the tensile strength was compared and analyzed by setting the arrangement differently based on the location of the center under conditions that enable symmetry. Furthermore, the stacking arrangement of the internal reinforcement was varied; in one iteration, it was positioned at one-third the height of the upper shell from the centerline, as shown in Figure 1F. In another iteration, it was positioned at two-thirds the height of the upper shell from the centerline, as shown in Figure 1G. In all the experiments, the reinforcement was layered using the isotropic fiber method.

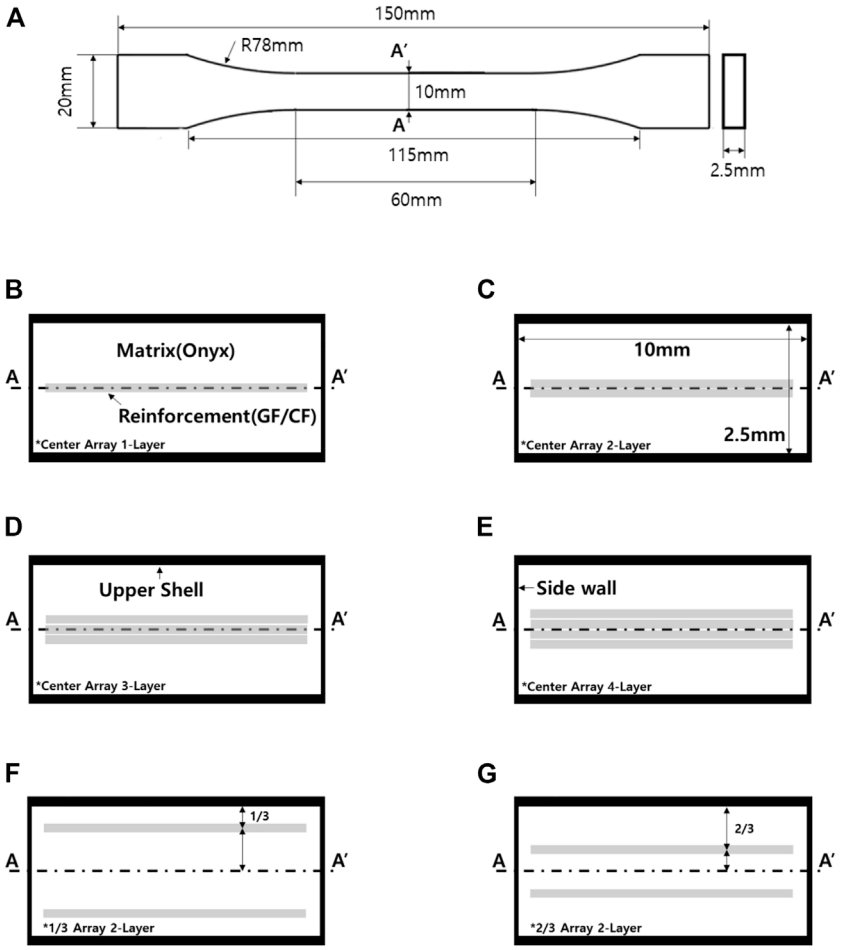

FIGURE 1
Composite specimen geometry and cross section. **(A)** Tensile test specimen shape, **(B)** 1-layer reinforcement, **(C)** 2-layer reinforcement, **(D)** 3-layer reinforcement, **(E)** 4-layer reinforcement, **(F)** 1/3 Arrangement of reinforcement, **(G)** 2/3 Arrangement of reinforcement.

TABLE 1 Material properties.

Properties	Onyx	Glass fiber (GF)	Carbon fiber (CF)
Tensile strength (MPa)	30	590	800
Elastic modulus (GPa)	1.4	21	60
Poisson's ratio	0.35	0.22	0.33
Density (g/cm^3)	1.2	1.5	1.2

2.3 3D printing conditions

The 3D printer used in this study was the mark-two by Markforged to print the composite material. The tensile test was performed by applying a tensile force at a tensile speed of 2 mm/min through a grip of 17.5 mm, according to the test standard. Each specimen was printed seven times, and the average value was calculated and compared, excluding the maximum and minimum values that differed the most from the average value. Finally, the specimen most similar to the average value was selected and analyzed.

3 Results and discussion

In this study, the mechanical strength of onyx-based composites printed using a 3D printing process was investigated. The composite material specimens comprising a matrix of onyx and reinforcement layers of GF and CF were fabricated using a 3D printing process and subsequently analyzed. The results of the tensile tests on the various specimens are shown in Figure 2. As the shape of the specimen, after the tensile test, was similar, regardless of the reinforcements, only the results of the specimens reinforced with CF are presented here. After the tensile test, the cross-sections of all the specimens formed within their gauge length exhibited a similar tendency. Therefore, the results of the tensile test are valid.

Figure 3 shows the tensile test results according to the thickness of the GF and CF reinforcements inside the composite material. The composite material of onyx mixed with 1-layer GF experienced a tensile force of 1308.7 N. In the specimen with a 4-layer GF arrangement, the tensile force was found to be 2867.3 N. In the specimen of onyx mixed with CF, the tensile force was 1271.1 N and 3797.0 N for 1-layer and 4-layer CF, respectively. In other words, the tensile force increases as the reinforcement layer inside onyx

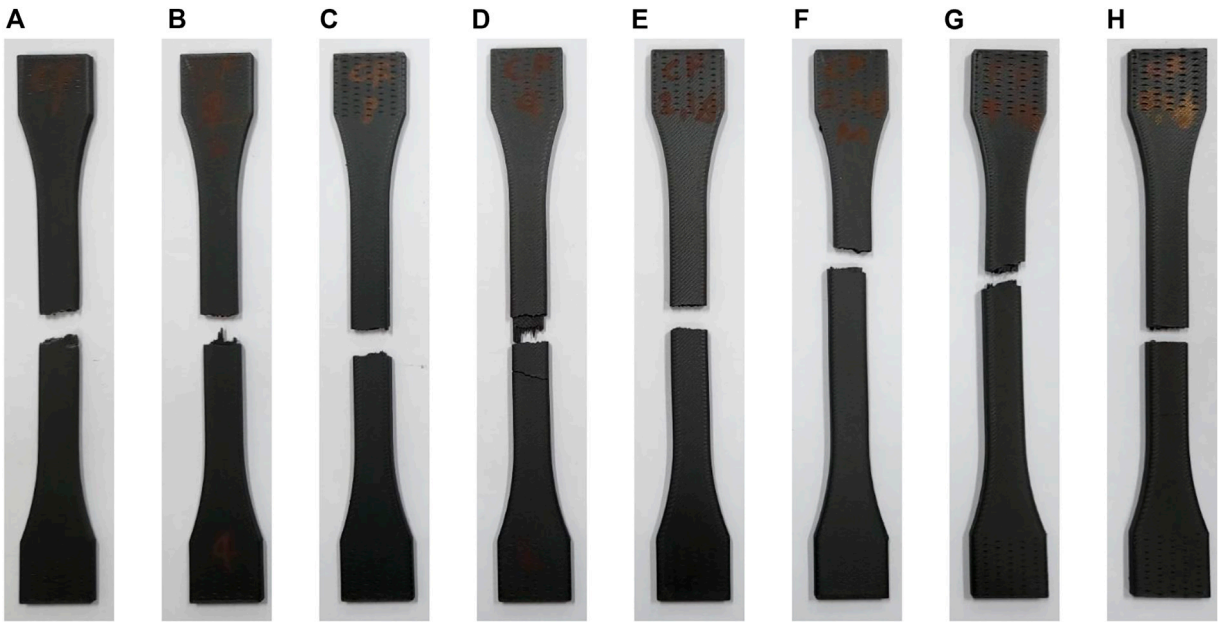

FIGURE 2
Shape after tensile test of composite material specimen using carbon fiber as reinforcement **(A)** 1-layer reinforcement, **(B)** 2-layer reinforcement, **(C)** 3-layer reinforcement, **(D)** 4-layer reinforcement, **(E)** 1/3 Arrangement of 2-layer reinforcement, **(F)** 2/3 Arrangement of 2-layer reinforcement, **(G)** 1/3 Arrangement of 4-layer reinforcement, **(H)** 2/3 Arrangement of 4-layer reinforcement.

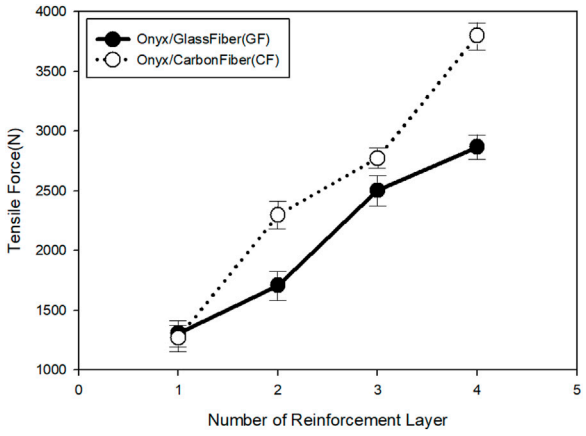

FIGURE 3
Tensile force according to the type of reinforcement and number of layers.

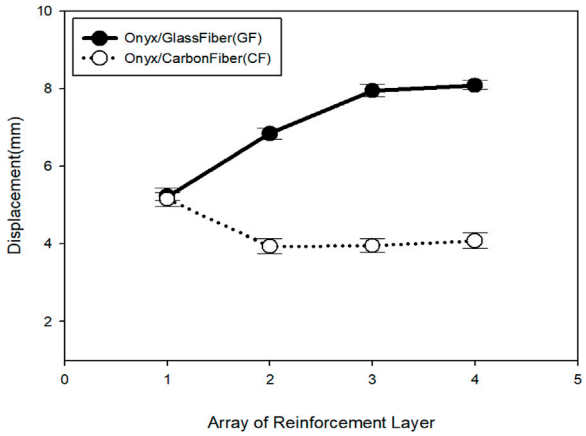

FIGURE 4
Specimen displacement according to the type of reinforcement and number of layers.

becomes thicker. In addition, the composite materials with a 1-layer reinforcement of either CF or GF did not experience significantly different tensile forces. However, as the thickness of the reinforcement increased, CF-reinforced onyx exhibited a considerably higher tensile strength. As shown in Table 1, the larger increase in tensile strength can be attributed to the elastic modulus and tensile strength of CF, which are higher than those of GF. In general, the change in elastic properties of composite materials appears to depend on the volume fraction of the matrix material and the fiber material (Zhou et al., 2017; Makarian and Santhanam, 2020; Yun et al., 2022a; Yun et al., 2022b; Yun et al., 2022c). As the volume fraction increases, i.e., as the thickness of the reinforcement inside the composite material increases, the strength of the composite material increases. Therefore, high-strength components can be printed by increasing the ratio of the reinforcement inside the composite material.

Figure 4 shows the displacement of the specimen according to the tensile test. In the onyx/GF composite material specimen, when

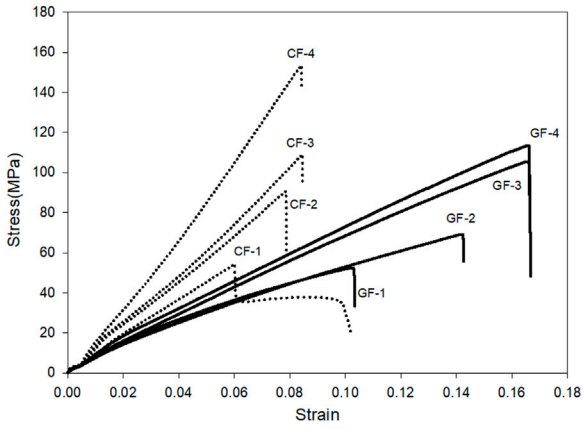

FIGURE 5
Stress-Strain curve depending on the number of reinforcement layers.

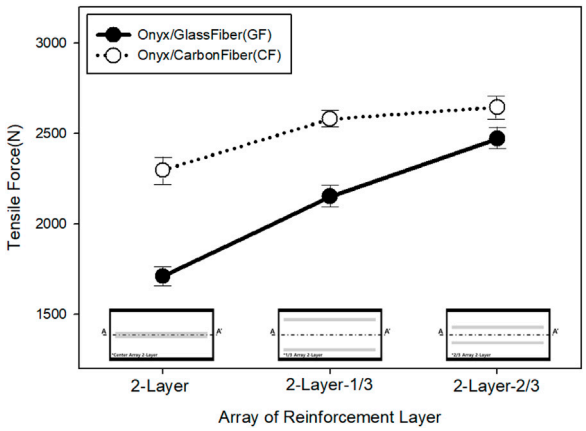

FIGURE 6
Tensile force according to the position of 2-layer reinforcement.

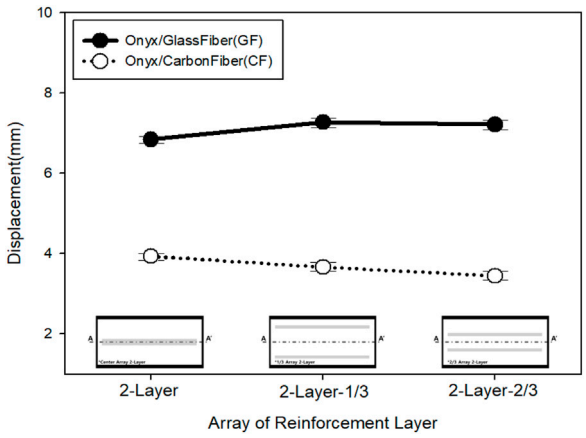

FIGURE 7
Specimen displacement according to the position of 2-layer reinforcement.

the reinforcement GF was included in 1 layer, the gauge length increased by 5.2 mm compared to 50 mm in the specimen without reinforcement. The specimen containing 4-layer GF exhibited a displacement increase of 8.1 mm. In the onyx/CF composite material specimen containing 1-layer CF, the displacement increased by 5.2 mm compared to 50 mm in the specimen without reinforcement but increased by only 4.1 mm in the specimen containing 4-layer CF. No significant difference in displacements was observed after 2-layer CF. This can be attributed to the difference in physical properties of elastic modulus and tensile strength between CF and GF. As the modulus of elasticity is the ratio of the strain to tensile strength, the strain experienced by CF is less because the elastic modulus and tensile strength of CF are higher than those of GF. Therefore, as the number of fiber reinforcement layers inside the composite material increases, the volume fraction of the reinforcement increases, thereby strengthening its effect. Consequently, the composite stiffness increases and its flexibility decreases with increasing CF content.

Figure 5 shows the stress-strain curve according to the number of reinforcement layers. In the onyx/GF specimens, the tensile strength increased as the GF layer became thicker. As shown in Figure 3, the tensile stress applied at the cross-section of the specimen increases as the tensile force of the composite material increases. From Figure 4 and Figure 5, higher specimen displacements correspond to higher strains. In contrast, as the thickness of CF increased in the Onyx/CF specimen, the tensile strength increased, but the strain increased only marginally. The reason for this is related to the Poisson's ratio and strain of the CF. As the number of CF layers increases, the influence of the CF increases. In general, materials with high strain can be printed using onyx/GF composites but the increase in tensile strength is limited. Conversely, materials with high tensile strength can be manufactured by 3D printing using onyx/CF composites; however, the strain rate is limited.

Tests were conducted on various arrangements of the reinforcement to analyze their effect on the properties of the specimen. Interestingly, the 2-layer reinforcement could be arranged symmetrically based on the center of the cross-section of the tensile test specimen. Consequently, the specimen was printed by stacking the reinforcement at one-third the height of the upper shell from its outer boundary. Another specimen was printed by laminating the reinforcement at two-thirds the height of the upper shell from its outer boundary. Figure 6 shows the tensile force according to the arrangement of the 2-layer reinforcement. The lowest and highest tensile forces were measured when the reinforcement was concentrated at the center and when it was arranged at two-thirds the height of the upper shell from its outer boundary, respectively. In the onyx/GF composite specimen, tensile forces of 1709 N, 2150 N, and 2470 N were measured when the reinforcement was concentrated in the center, layered at one-third height, and at two-thirds the height, respectively. The corresponding tensile forces for the onyx/CF composite specimen were 2296 N, 2579 N, and 2644 N, respectively. This increase in tensile strength can be attributed to

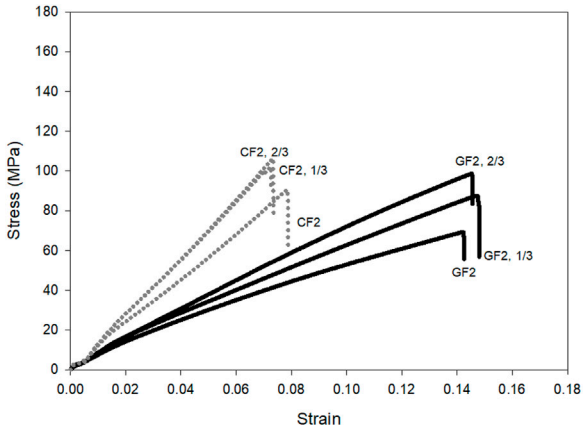

FIGURE 8
Stress-Strain curve depending on the position of 2-layer reinforcement.

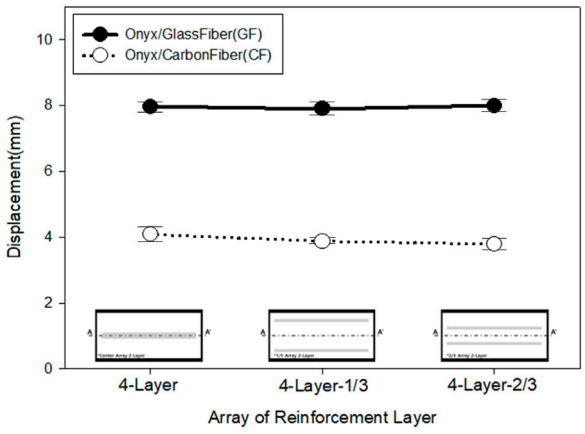

FIGURE 10
Specimen displacement according to the position of 4-layer reinforcement.

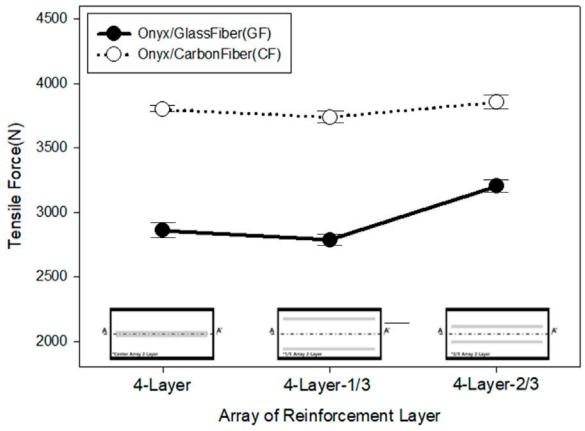

FIGURE 9
Tensile force according to the position of 4-layer reinforcement.

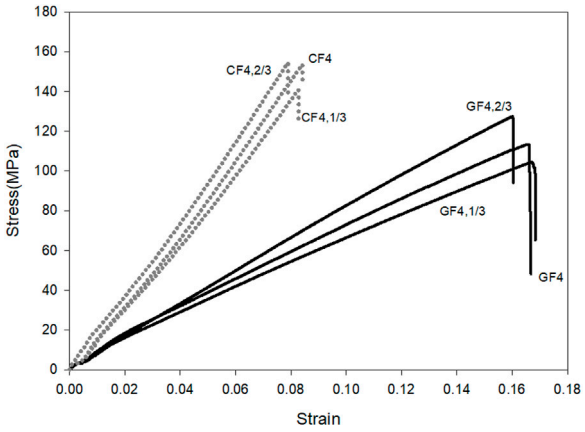

FIGURE 11
Stress-Strain curve according to the position of 4-layer reinforcement.

the increase in the area where the GF and CF reinforcement layers are in contact with onyx, resulting in a larger tensile force. In general, the main variables of tensile force and tensile strength in composite materials are the bonding force and bonding area between the matrix and reinforcement (Joseph et al., 1996; Zhang et al., 2011). Therefore, the effect of the reinforcement is optimal only when it is mixed with the matrix at an appropriate interval. The results of analyzing the extent of displacement according to the tensile test, shown in Figure 7, are as follows. In the onyx/GF composite specimen, a displacement of 6.8 mm occurred when the reinforcement was arranged in the center. When the GF layer was arranged at one-third or two-third heights, the displacement increased by 0.4 mm–7.2 mm. The onyx/CF composite specimens showed a 0.5 mm decrease in displacement from 3.9 mm to 3.4 mm. This difference in displacement can be attributed to the difference in the Poisson's ratio and elongation of CF fiber. The stress-strain curves of onyx-based composites from the tensile test were compared, as shown in Figure 8. The comparison shows that arranging the reinforcement near the surface of the specimen improves its tensile strength, confirming that the elongation of the composite material is affected by the physical properties of the reinforcement.

In addition, the tensile test results of the 4-layer laminated composite material specimens were compared and analyzed. From Figure 9, the 4-layer reinforcement experiences the highest tensile force. In the onyx/GF 4-layer tensile test specimen, tensile forces of 2860 N, 2787 N, and 3204 N were measured when the reinforcement was concentrated in the center, layered at one-third height, and at two-thirds the height, respectively. The corresponding tensile forces for the 4-layer onyx/CF tensile test specimens were 3797 N, 3739 N, and 3854 N, respectively. Figure 10 shows the results of measuring specimen displacement according to the tensile test; the 4-layer composite material specimens do not exhibit significant differences in displacement. In other words, composite material 3D printing

output containing four layers of reinforcement or more is greatly influenced by the reinforcement, confirming that displacement is governed by the physical properties of the fiber. Analyses of the stress-strain curves according to the tensile test are shown in Figure 11. In the onyx/GF composite tensile test specimens, changes in tensile strength were observed according to the arrangement. When the GF reinforcement is arranged outside the composite material, higher tensile strength is exhibited. However, in the onyx/CF specimens, the position and arrangement of the reinforcement did not have a significant effect when four layers of CF were laminated. This indicates that the effect of the reinforcement is strengthened as the volume fraction of the reinforcement inside onyx and the number of laminated layers increase, independent of location and arrangement. Therefore, when printing a composite material part using 3D printing, the volume fraction or specific gravity of the reinforcement must be increased to increase the tensile strength and tensile force. For a given quantity of reinforcement, arranging it close to the outer wall of the composite gives the best results in terms of strength.

4 Conclusion

In this study, the mechanical strength of 3D-printed onyx-based composites was evaluated. The composite comprised a matrix of onyx reinforced with laminated layers of either GF or CF. The evaluation was performed according to the specifications in ISO 527-4, which stipulates an internal filling of 30%. The number of reinforcement layers, formed using either GF or CF, was set from 1 to 4 in consideration of the output conditions of the composite material specimen. Furthermore, the 2-layer and 4-layer reinforcements were symmetrically set inside onyx to compare and analyze the mechanical strength according to the arrangement of the reinforcements. To analyze the effect of internal stiffeners in composite 3D printed parts based on previous studies, we set up different layers of internal stiffeners (Cofaru et al., 2021; Ojha et al., 2022; Ramezani Dana et al., 2022) While the specimens with 1-layer GF and CF exhibited no significant difference in tensile force, it increased as the number of GF or CF layers increased up to 4. The reinforcement effect of CF exceeded that of GF as the number of layers increased. The displacement exhibited by the composite material specimens increased as the number of layers increased in the GF-reinforced specimens. However, in the CF-reinforced specimens, the displacement decreased. This discrepancy can be attributed to the characteristics of the fiber reinforcement used inside onyx; as the number of fiber reinforcement layers increases, the effect of the fiber strengthens. In addition, arranging the reinforcement in the center results in the most optimal combination of physical properties in the final product. Furthermore, layering the matrix and reinforcement sequentially results in the highest values of tensile strength. The results of our study show that the arrangement and thickness of reinforcement layers are crucial factors in obtaining the desired physical properties in 3D-printed composites. Therefore, a database that summarizes the various combinations of arrangement and thickness and their effects will considerably aid the optimization of composite material 3D printing.

Data availability statement

The raw data supporting the conclusion of this article will be made available by the authors, without undue reservation.

Author contributions

Formal analysis, Investigation, G-WL; Resources, Data curation, T-HK; Conceptualization, J-HY; Writing—original draft, N-JK; Writing—review and editing, K-HA; Writing—original draft preparation, supervision, M-SK. All authors have read and agreed to the published version of the manuscript.

Funding

This research was supported by "Regional Innovation Strategy (RIS)" through the National Research Foundation of Korea (NRF) funded by the Ministry of Education (MOE): (2021RIS-004) This work was supported by National Research Foundation of Korea (NRF) grants funded by the Korean government (MSIT): NRF 2022R1G1A1004962.

Acknowledgments

This is a short text to acknowledge the contributions of specific colleagues, institutions, or agencies that aided the efforts of the authors.

Conflict of interest

Author N-JK was employed by JinSung Boltech Corporation.

The remaining authors declare that the research was conducted in the absence of any commercial or financial relationships that could be construed as a potential conflict of interest.

Publisher's note

References

Araya-Calvo, M., López-Gómez, I., Chamberlain-Simon, N., León-Salazar, J. L., Guillén-Girón, T., Corrales-Cordero, J. S., et al. (2018). Evaluation of compressive and flexural properties of continuous fiber fabrication additive manufacturing technology. *Addit. Manuf.* 22, 157–164. doi:10.1016/j.addma.2018.05.007

Awad, A., Fina, F., Goyanes, A., Gaisford, S., and Basit, A. W. (2020). 3D printing: Principles and pharmaceutical applications of selective laser sintering. *Int. J. Pharm.* 586, 119594. doi:10.1016/j.ijpharm.2020.119594

Bárnik, F., Vaško, M., Handrik, M., Dorčiak, F., and Majko, J. (2019). Comparing mechanical properties of composites structures on Onyx base with different density and shape of fill. *Transp. Res. Procedia* 40, 616–622. doi:10.1016/j.trpro.2019.07.088

Cheng, Y., Shi, X., Jiang, X., Wang, X., and Qin, H. (2020). Printability of a cellulose derivative for extrusion-based 3D printing: The application on a biodegradable support material. *Front. Mater.* 7, 86. doi:10.3389/fmats.2020.00086

Cofaru, N. F., Pascu, A., Oleksik, M., and Petruse, R. (2021). Tensile properties of 3D-printed continuous-fiber-reinforced plastics. *Mater. Plast.* 58 (4), 271–282. doi:10.37358/mp.21.4.5552

Eisenberg, M., Hsi, S., and Oh, H. (2013). Machines and minds: The new cognitive science, and the potential evolution of children's intuitions about thinking. *Int. J. Child-Computer Interact.* 14, 1–4. doi:10.1016/j.ijcci.2017.06.001

El-Tayeb, N. S., and Gadelrab, R. M. (1996). Friction and wear properties of E-glass fiber reinforced epoxy composites under different sliding contact conditions. *Wear* 192 (1-2), 112–117. doi:10.1016/0043-1648(95)06770-1

Fina, F., Goyanes, A., Gaisford, S., and Basit, A. W. (2017). Selective laser sintering (SLS) 3D printing of medicines. *Int. J. Pharm.* 529 (1-2), 285–293. doi:10.1016/j.ijpharm.2017.06.082

Galati, M., Viccica, M., and Minetola, P. (2021). A finite element approach for the prediction of the mechanical behaviour of layered composites produced by Continuous Filament Fabrication (CFF). *Polym. Test.* 98, 107181. doi:10.1016/j.polymertesting.2021.107181

Joseph, K., Varghese, S., Kalaprasad, G., Thomas, S., Prasannakumari, L., Koshy, P., et al. (1996). Influence of interfacial adhesion on the mechanical properties and fracture behaviour of short sisal fibre reinforced polymer composites. *Eur. Polym. J.* 32 (10), 1243–1250. doi:10.1016/s0014-3057(96)00051-1

Kabandana, G. K. M., Zhang, T., and Chen, C. (2022). Emerging 3D printing technologies and methodologies for microfluidic development. *Anal. Methods* 14, 2885–2906. doi:10.1039/d2ay00798c

Kollamaram, G., Croker, D. M., Walker, G. M., Goyanes, A., Basit, A. W., and Gaisford, S. (2018). Low temperature fused deposition modeling (FDM) 3D printing of thermolabile drugs. *Int. J. Pharm.* 545 (1-2), 144–152. doi:10.1016/j.ijpharm.2018.04.055

Kriz, R. D., and Stinchcomb, W. W. (1979). Elastic moduli of transversely isotropic graphite fibers and their composites. *Exp. Mech.* 19 (2), 41–49. doi:10.1007/bf02324524

Le Tohic, C., O'Sullivan, J. J., Drapala, K. P., Chartrin, V., Chan, T., Morrison, A. P., et al. (2018). Effect of 3D printing on the structure and textural properties of processed cheese. *J. Food Eng.* 220, 56–64. doi:10.1016/j.jfoodeng.2017.02.003

Makarian, K., and Santhanam, S. (2020). Micromechanical modeling of thermo-mechanical properties of high volume fraction particle-reinforced refractory composites using 3D Finite Element analysis. *Ceram. Int.* 46 (4), 4381–4393. doi:10.1016/j.ceramint.2019.10.162

Manapat, J. Z., Chen, Q., Ye, P., and Advincula, R. C. (2017). 3D printing of polymer nanocomposites via stereolithography. *Macromol. Mater. Eng.* 302 (9), 1600553. doi:10.1002/mame.201600553

Martín-Montal, J., Pernas-Sánchez, J., and Varas, D. (2021). Experimental characterization framework for SLA additive manufacturing materials. *Polymers* 13 (7), 1147. doi:10.3390/polym13071147

Mei, H., Ali, Z., Yan, Y., Ali, I., and Cheng, L. (2019). Influence of mixed isotropic fiber angles and hot press on the mechanical properties of 3D printed composites. *Addit. Manuf.* 27, 150–158. doi:10.1016/j.addma.2019.03.008

Montero, M., Roundy, S., Odell, D., Ahn, S. H., and Wright, P. K. (2001). Material characterization of fused deposition modeling (FDM) ABS by designed experiments. *Soc. Manuf. Eng.* 10 (13552540210441166), 1–21.

Morales, M. A., Atencio Martinez, C. L., Maranon, A., Hernandez, C., Michaud, V., and Porras, A. (2021). Development and characterization of rice husk and recycled polypropylene composite filaments for 3D printing. *Polymers* 13 (7), 1067. doi:10.3390/polym13071067

Morales, U., Esnaola, A., Iragi, M., Aretxabaleta, L., and Aurrekoetxea, J. (2021). The effect of cross-section geometry on crushing behaviour of 3D printed continuous carbon fibre reinforced polyamide profiles. *Compos. Struct.* 274, 114337. doi:10.1016/j.compstruct.2021.114337

Moreno-Núñez, B. A., Abarca-Vidal, C. G., Treviño-Quintanilla, C. D., Sánchez-Santana, U., Cuan-Urquizo, E., and Uribe-Lam, E. (2023). Experimental analysis of fiber reinforcement rings' effect on tensile and flexural properties of onyx™–kevlar® composites manufactured by continuous fiber reinforcement. *Polymers* 15 (5), 1252. doi:10.3390/polym15051252

Newcomb, B. A. (2016). Processing, structure, and properties of carbon fibers. *Compos. Part A Appl. Sci. Manuf.* 91, 262–282. doi:10.1016/j.compositesa.2016.10.018

Ojha, K. K., Gugliani, G., and Francis, V. (2022). "Tensile properties and failure behaviour of continuous kevlar fibre reinforced composites fabricated by additive manufacturing process," in *Advances in materials and processing technologies*, 1–15. doi:10.1080/2374068x.2022.2106655

Parmiggiani, A., Prato, M., and Pizzorni, M. (2021). Effect of the fiber orientation on the tensile and flexural behavior of continuous carbon fiber composites made via fused filament fabrication. *Int. J. Adv. Manuf. Technol.* 114 (7), 2085–2101. doi:10.1007/s00170-021-06997-5

Pisanu, L., Santiago, L. C., Barbosa, J. D. V., Beal, V. E., and Nascimento, M. L. F. (2021). Effect of the process parameters on the adhesive strength of dissimilar polymers obtained by multicomponent injection molding. *Polymers* 13 (7), 1039. doi:10.3390/polym13071039

Rahim, T. N. A. T., Abdullah, A. M., and Md Akil, H. (2019). Recent developments in fused deposition modeling-based 3D printing of polymers and their composites. *Polym. Rev.* 59 (4), 589–624. doi:10.1080/15583724.2019.1597883

Ramezani Dana, H., El Mansori, M., Barrat, M., and Seck, C. A. (2022). Tensile behavior of additively manufactured carbon fiber reinforced polyamide-6 composites. *Polymer-Plastics Technol. Mater.* 61 (6), 624–641. doi:10.1080/25740881.2021.2005094

Shirazi, S. F. S., Gharehkhani, S., Mehrali, M., Yarmand, H., Metselaar, H. S. C., Kadri, N. A., et al. (2015). A review on powder-based additive manufacturing for tissue engineering: Selective laser sintering and inkjet 3D printing. *Sci. Technol. Adv. Mater.* 16 (3), 033502. doi:10.1088/1468-6996/16/3/033502

Sun, B., and Wu, L. (2022). Research progress of 3D printing combined with thermoplastic foaming. *Front. Mater.* 9, 1083931. doi:10.3389/fmats.2022.1083931

Tee, Y. L., Peng, C., Pille, P., Leary, M., and Tran, P. (2020). PolyJet 3D printing of composite materials: Experimental and modelling approach. *Jom* 72 (3), 1105–1117. doi:10.1007/s11837-020-04014-w

Tian, J., Zhang, R., Yang, J., Chou, W., Xue, P., and Ding, Y. (2021). Additive manufacturing of wood flour/PHA composites using micro-screw extrusion: Effect of device and process parameters on performance. *Polymers* 13 (7), 1107. doi:10.3390/polym13071107

Wang, J., Goyanes, A., Gaisford, S., and Basit, A. W. (2016). Stereolithographic (SLA) 3D printing of oral modified-release dosage forms. *Int. J. Pharm.* 503 (1-2), 207–212. doi:10.1016/j.ijpharm.2016.03.016

Yan, X., Bethers, B., Chen, H., Xiao, S., Lin, S., Tran, B., et al. (2021). Recent advancements in biomimetic 3d printing materials with enhanced mechanical properties. *Front. Mater.* 8, 518886. doi:10.3389/fmats.2021.518886

Yun, J. H., Jeon, Y. J., and Kang, M. S. (2022b). Analysis of elastic properties of polypropylene composite materials with ultra-high molecular weight polyethylene spherical reinforcement. *Materials* 15 (16), 5602. doi:10.3390/ma15165602

Yun, J. H., Jeon, Y. J., and Kang, M. S. (2022a). Numerical investigation of the elastic properties of polypropylene/ultra high molecular weight polyethylene fiber inside a composite material based on its aspect ratio and volume fraction. *Polymers* 14 (22), 4851. doi:10.3390/polym14224851

Yun, J. H., Jeon, Y. J., and Kang, M. S. (2022c). Prediction of elastic properties using micromechanics of polypropylene composites mixed with ultrahigh-molecular-weight polyethylene fibers. *Molecules* 27 (18), 5752. doi:10.3390/molecules27185752

Zhang, Y., Luo, R., Zhang, J., and Xiang, Q. (2011). The reinforcing mechanism of carbon fiber in composite adhesive for bonding carbon/carbon composites. *J. Mater. Process. Technol.* 211 (2), 167–173. doi:10.1016/j.jmatprotec.2010.08.028

Zhou, L., Cui, C., Zhang, P. F., and Ma, Z. Y. (2017). Finite element and experimental analysis of machinability during machining of high-volume fraction SiCp/Al composites. *Int. J. Adv. Manuf. Technol.* 91 (5), 1935–1944. doi:10.1007/s00170-016-9933-1

frontiers | Frontiers in Materials

TYPE Original Research
PUBLISHED 26 May 2023
DOI 10.3389/fmats.2023.1202281

OPEN ACCESS

EDITED BY
Jingjun Wu,
Zhejiang University, China

REVIEWED BY
Luhao Yuan,
Nanjing University of Aeronautics and Astronautics, China
Rafael Comesaña,
University of Vigo, Spain
Yuewei Li,
Huaqiao University, China
Lin Fenglong,
Xiamen Institute of Rare Earth Materials, China

*CORRESPONDENCE
C. Belei,
carlos.beleifeliciano@student.tugraz.at
S. T. Amancio-Filho,
sergio.amancio@tugraz.at

RECEIVED 07 April 2023
ACCEPTED 12 May 2023
PUBLISHED 26 May 2023

CITATION
Belei C, Effertz PS, Meier B and Amancio-Filho ST (2023), Additive manufacturing of metal-polymer hybrid parts: the influence of as-printed LPBF surface roughness on the joint strength. *Front. Mater.* 10:1202281. doi: 10.3389/fmats.2023.1202281

Additive manufacturing of metal-polymer hybrid parts: the influence of as-printed LPBF surface roughness on the joint strength

C. Belei[1]*, P. S. Effertz[1], B. Meier[2] and S. T. Amancio-Filho[1]*

[1]Institute of Material Science, Joining and Forming—BMK Endowed Professorship for Aviation, Graz University of Technology, Graz, Austria, [2]Joanneum Research—Materials, Graz, Austria

As-printed Laser-Powder Bed Fusion (LPBF) surfaces can provide anchoring spots for the infiltration of polymer printed by Fused Filament Fabrication (FFF), enhancing metal-polymer joint strength. This work evaluates the influence of the as-printed LPBF surface roughness and FFF parameters on the strength of Ti-6Al-4V/PA-CF joints produced by this process combination. A three-point bending testing method based on ISO 14679:1997 was deployed, whereby the energy dissipated by the joint interface was measured. Roughness was varied by 3D-printing the substrate with different inclination angles; Height and printing speed of the coating layer (the polymer layer in direct contact with the metal) were also varied. Data was interpreted using a combination between Decision Tree and Gradient Boosting Regression, ultimately suggesting that printing speed is the prominent parameter followed by inclination angle for joint strength. Additionally, the combined effect of low printing speed and inclination angle resulted in the highest energy absorption at the interface (>200 J).

KEYWORDS

additive manufacturing, fused-filament fabrication, laser powder bed fusion, metal-polymer hybrid joining, three-point bending

1 Introduction

The Additive Manufacturing (AM) of polymers and metals—both extensively explored by researchers and industries nowadays—have mostly developed in separate ways. While both groups of AM processes share advantages (e.g., the production of complex near-net shape parts with low material waste (Ngo et al., 2018)), the processes themselves differ considerably, being this a natural consequence of the inherent discrepancies in terms of chemical composition, atomic arrangement and therefore processing requirements and material properties. On the one hand, metal AM normally requires a high energy density to melt the feedstock material due to their relatively high melting temperature ranges (Liu et al., 2018). On the other hand, polymer AM does not require the same levels of energy density. Thus, it can be performed by controlling the solidification (or consolidation when printing temperature is above glass transition temperature) of feedstock material that is liquefied beforehand (instead of melting/softening it locally, which is the case in metal AM).

Combining polymer and metal AM into a single process would allow for the production of fully additively-manufactured metal-polymer hybrid parts, enabling a greater designing freedom regarding not only part geometry, but also local and global properties. Such a

combination is however an extremely challenging task, for the reasons mentioned earlier. Although processes such as SLS are capable of 3D-printing both metals and polymers (Papazoglou et al., 2022; Liu et al., 2007), merging those capabilities into a single print job to produce a metal-polymer hybrid joint is not trivial. A likely difficulty with this approach would be the handling of different powders, which would require a machine with separate powder dispensers and recoaters (Mehrpouya et al., 2022). One could also argue that SLS is not the most effective AM technique for neither metals nor polymers, since better alternatives are available, such as powder bed fusion and fused filament fabrication, respectively. Therefore, the production of metal and polymer parts could also be accomplished by separate AM processes, with the subsequent joining being done by a third, non-AM process, such as adhesive bonding, mechanical fastening or friction-based techniques (Amancio-Filho and Blaga, 2018; Lambiase et al., 2021; Carvalho and Amancio-Filho, 2022).

Such an alternative, however, can be further optimized by reducing manufacturing steps, specifically the third one (i.e., metal-polymer joining). The use of Fused Filament Fabrication principles to 3D-print polymer/composite parts directly onto metallic substrates (thus skipping a later joining step) has been recently gaining momentum in the scientific community. A description of this approach (which in the present manuscript will be referred to as "AddJoining" (Filho and Falck, 2018)) is presented in Figures 1A. It has been proven feasible for a number of metal-polymer combinations, including AA2024-T3/CF-PA6 (R. Falck et al., 2018), AA2024-T3/ABS (Rielson et al., 2019), AA6082-T6/PLA (Bechtel et al., 2020), AA5052/PLA (Alhmoudi et al., 2022), AA6082-T6/PETG (Bechtel et al., 2022), AA5754/PP (Hertle et al., 2020), Ti-4Al-4V/PA-CF (Belei et al., 2022a), SS 316L/PLA and PET (Chueh et al., 2020), AlSi10Mg/PLA (Englert et al., 2022) and PC (Oliveira et al., 2023), among others.

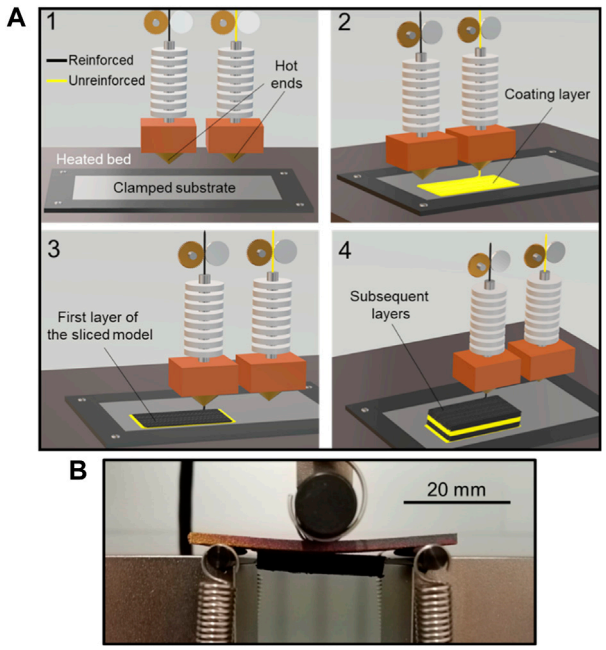

FIGURE 1
(A) Schematics of the AddJoining approach based on a three-axis 3D-printer and a generic material combination. (1) A flat substrate is clamped onto a heated bed, while a dual extrusion system is loaded with unreinforced and reinforced filaments; (2) a layer of unreinforced polymer is deposited in direct contact with the substrate ("coating layer"); (3) the first layer of the sliced model is deposited over the coating layer; (4) the subsequent layers of the model are 3D-printed following FFF principles. Adapted from (Belei et al., 2022a) with permission; **(B)** Three-pointing bending test of a Ti-6Al-4V/PA-CF hybrid joint.

The latter study of this list, by Chueh et al. (2020), explored for the first time the use of Laser-Powder Bed Fusion (LPBF) SS 316L parts as substrates for the AddJoining. In that study, the authors proposed the use of specially-designed surfaces with well-defined cavities in the millimeter scale, onto which the polymer model (PLA and PET) would be subsequently 3D-printed. Those cavities ensured that a satisfactory anchoring between metal and polymer would be achieved, enhancing the joint strength both under shear and tensile loading. This was realized using a custom-made, multi-material 3D setup, which integrated the LPBF and FFF stages into a single print job. In the near future, alternatives such as the one introduced by (Chueh et al., 2020) may be proven feasible in the large scale production of metal-polymer hybrid parts by AM. Later on, Englert et al. (2022) and Oliveira et al. (2023) reproduced a similar idea, with a different substrate material (AlSi10Mg) and increased variety of surface designs and sub-milimetric micro-anchoring features (e.g., gecko-like micro-pillars), achieving satisfactory results in terms of quasi-static mechanical strength.

Based on those particular studies, it would be worth considering that, before anything else, as-printed LPBF parts tend to already have a relatively high surface roughness (Yadollahi et al., 2017; Koutiri et al., 2018; Skalon et al., 2020; Lizzul et al., 2021; Pérez-Ruiz et al., 2022; Simson and Subbu, 2022), being this feature most likely a positive trait for the AddJoining approach. Studies in the past resorted to a number of different strategies to make metallic surfaces more susceptible to metal-polymer interlocking, such as sandblasting (Falck et al., 2019; Hertle et al., 2020; Belei et al., 2022a) and CNC machining (Alhmoudi et al., 2022). Theoretically, those strategies would not be necessary for as-printed LPBF substrates, since their inherently rough surfaces may already provide enough anchoring sites for metal-polymer interlocking. If this is indeed the case, one could save time and energy by forgoing both surface finishing steps and also the implementation of special surface features for improved mechanical interlocking (such as the ones in (Chueh et al., 2020; Englert et al., 2022)), since those in particular could be rendered redundant.

Normally, the bond strength in these cases is evaluated using single lap-shear tests. This is a well-known and widely used approach (Falck et al., 2018; Falck et al., 2019; Bechtel et al., 2022; Belei et al., 2022a; Oliveira et al., 2023) that can be used as a powerful benchmarking tool to evaluate the performance of joints produced under different circumstances. Additionally, this test also provides information regarding the behavior of the joint when exposed to a mix between fracture modes I and II. As such, however, it does not necessarily provide a complete picture of the interfacial strength, which can be assessed using other loading conditions as well (Genty et al., 2017). An alternative is the three-point bending test based on ISO 14679:1997 (Roche et al., 1982; Genty et al., 2017; Birro et al., 2021; Belei et al., 2022a), which consists of measuring the force necessary to bend a metallic substrate

until the detachment of an adhesive block that was previously adhered to it. Based on the force x displacement curve, the energy absorbed by the adhesive/composite part during the test can also be calculated. An example of such a test being performed is shown in Figures 1B. In comparison to the single-lap shear, this test offers the advantage that the fracture mode can be mostly considered mode I, as opposed to a mix of I/II (Genty et al., 2017). Since it assesses the joint strength from a different perspective, one cannot expect that satisfactory results in lap shear tests would readily be translated into a high performance under bending and *vice versa*, as proven by (Belei et al., 2022a). In that situation, optimized conditions required about 4 kN to fail on shear tests, but only around 5% of this value for the interface detachment during three-point bending. Finally, another advantage of the three-point bending test is that it requires smaller specimens, which saves time and material resources, thus allowing for a more efficient strength assessment.

Utilizing the three-point bending test as an evaluation tool, the objective of the present study is to explore the relationship between as-printed LPBF surface roughness and joint strength on metal-polymer hybrid parts manufactured by the AddJoining approach. In the present case, a combination of LPBF Ti-6Al-4V, polyamide 6/66 and a short carbon reinforced polyamide-based polymer was used. In order to evaluate different joining scenarios, surface roughness was varied by 3D-printing the substrate with several different inclination angles, which resulted in different roughness levels on the downskin surface (DS). Additionally, process parameters for the AddJoining approach were also varied, namely, the printing speed of the "coating layer" (i.e., the first polymer layer in direct contact with the metal substrate) and also its height. The present study concluded that not only as-printed LPBF surfaces enabled satisfactory levels of metal-polymer interlocking, but also that the rougher those surfaces were, the higher the ensuing joint strength tended to be.

2 Materials and methods

2.1 Materials

2.1.1 Metallic powder

Commercially available Ti-6Al-4V (Grade 5) powder was used to 3D-print the metallic substrates by LPBF (see Section 2.2.1). Its chemical composition (virgin) consisted of the following: 6.13 wt.% Al, 3.90 wt.% V, 0.16 wt.% O, 0.0281 wt.% N, 0.01 wt.% C, 0.07 wt.% Fe, 1.1 ppm Ar, 21 ppm H and balance of Ti (Meier et al., 2022a; Meier et al., 2022b). Particle size distribution and sphericity were measured in accordance with ISO 13322-2 by Dynamic Image Analysis carried out with a Retsch CAMSIZER XT optical particle analyzer (Germany). Particle size distribution were measured as follows: D10 = 18.8 µm; D50 = 33.6 µm; D90 = 48.7 µm. Sphericity: W/H = 0.89; bh13 = 0.94.

2.1.2 Polymer/composite filaments

For the manufacturing of each specimen, two different thermoplastic materials were used: one for the coating layer only and another for the subsequent layers. The coating layer material consisted of Polyamide 6/66, supplied in a filament form (ø 2.85 mm) by Ultimaker (Netherlands). Glass transition temperature (T_g), melting onset (T_{onset}) and melting peak (T_m) were measured by (Belei et al., 2022a) at 50°C, 167°C and 190°C, respectively. Melt mass flow rate (MFR) of 6.2 g/10 min was measured by the supplier based on ISO 1133, at 250°C and with a load of 1.2 kg (Ultimaker Nylon TDS, 2023).

As for the subsequent layers, a commercial-grade polyamide reinforced with short carbon fibers was used, also in filament form (ø 2.85 mm), being supplied by BASF (Netherlands). Fiber volume fraction was 6.5% ± 0.2%, while fiber length and diameter 136.2 ± 83.0 µm and 5.6 ± 1.0 µm, respectively. T_g, T_{onset}, and T_m were measured by (Belei et al., 2022a) at 67°C, 203°C and 237°C, respectively. MFR at 275°C and 5 kg was measured by the supplier based on ISO 1133, registering a value of 51.9 g/10 min (Ultrafuse® PAHT CF15, 2023).

2.2 Manufacturing

2.2.1 Laser-Powder Bed Fusion

Ti-6Al-4V plates (see dimensions in Figures 2A) were 3D-printed by Laser Powder Bed Fusion using an EOS 280 printer (Germany) equipped with a 400 W laser (wavelength of 1,064 nm). Process parameters were kept constant, with a laser power of 280 W, a scan speed of 1,200 mm/s, a hatching distance of 140 µm and a layer thickness of 30 µm. The inclination angle θ in relation to the platform was varied between 40° and 90° in multiples of ten, for a total of six different θ values. No support structures were used. After the process, the 3D-printed substrates were stress relieved for 2 h at 650°C (heating and cooling rates of 30 K/min and 5 K/min, respectively). Parameters for both the process and the stress relieving were obtained based on (Meier et al., 2022a).

2.2.2 AddJoining

The 3D-printing of the polymer part on the metallic substrate (AddJoining) was carried out in an Ultimaker S5 FFF printer (Netherlands). Before proceeding with the AddJoining stage, the substrates were cleaned with an ultrasonic bath for 15 min using water, then rinsed with acetone.

The substrates were then fixed to the print bed using a sample holder originally designed to produce single-lap joints (Belei et al., 2022a), with the schematics presented in Figure 3. The DS of the substrate was positioned facing upwards, being therefore the surface on which the polymer was deposited. Masking tapes (3M Scotch Tape, United States) were applied on both substrate extremities to increase its stability during the polymer deposition.

The polymer part 3D-printed on the metallic substrate consisted of a 25 × 5 × 4 mm block, positioned on the center of the substrate as showed in Figure 2B. This block was printed in two stages. First, one layer of the unreinforced polyamide 6/66 was deposited directly onto the metallic substrate (coating layer). In this stage, process parameters (printing speed v and layer height h, see Table 1), as well as the substrate inclination angle θ (Figure 2A) were varied based on a 3^k full-factorial design of experiments; however, since θ had six levels (instead of three levels, which as the case for the other two factors), the experimental matrix tallied 54 unique conditions. Three replicas per condition were produced.

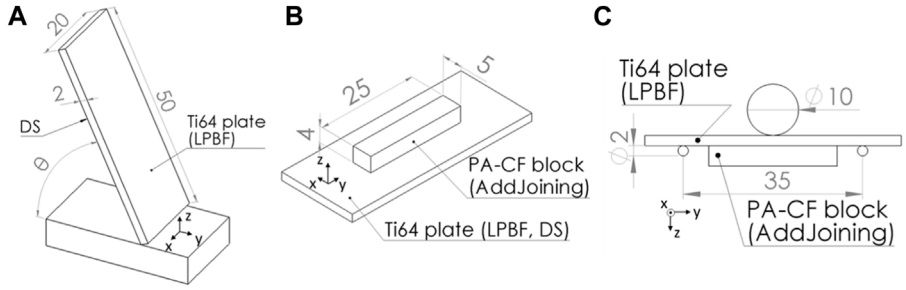

FIGURE 2
(A) Schematics of the Ti-6Al-4V substrates printed by L-PBF. Z denotes the build direction; **(B)** Schematics of the PA-CF block 3D-printed on L-PBF substrates using the AddJoining approach. Z denotes the build direction; **(C)** Schematics of the three-point bending test, based on ISO 14679:1997. Ti64 denotes Ti-6Al-4V. Dimensions in mm.

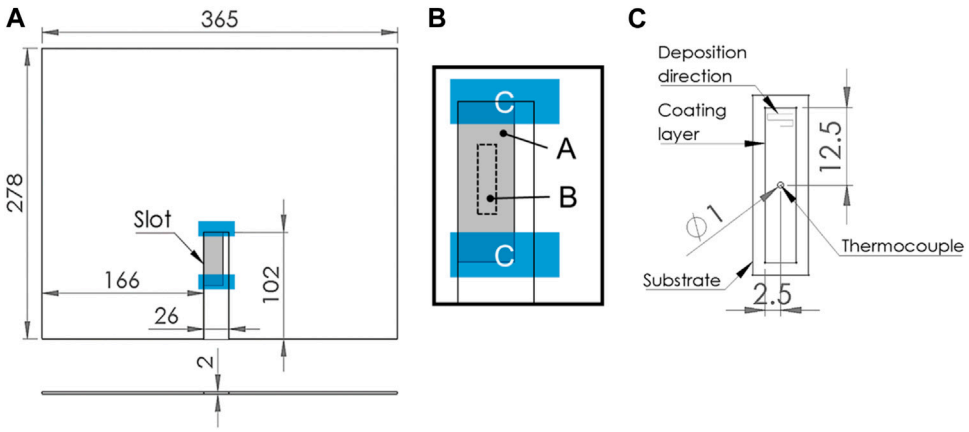

FIGURE 3
(A) Adapted printing platform implemented for the AddJoining experiments; **(B)** Close-up on the substrate placement. A represents the substrate, B the area where the PA-CF block was printed and C strips of masking tape for improved stability; **(C)** Schematics of the thermocouple placement (top view). Dimensions in mm.

TABLE 1 Process parameters for the AddJoining approach.

Parameter	Values	
	Coating layer	*Composite part*
Printing speed (***v***) [mm/s]	5, 35, 65	30
Layer height (***h***) [mm]	0.10, 0.25, 0.40	0.20
Extrusion temperature [°C]	280 °C	280 °C
Printing bed temperature [°C]	140	120
Nozzle diameter [mm]	0.40	0.60
Road width [mm]	0.40	0.40
Air gap [mm]	0.40	0.40
Layer orientation (relative to substrate length)	90°	30°/-30°

Next, following the deposition of the coating layer, subsequent layers of the PA-CF block ("composite part") were printed with the reinforced polyamide, using constant process parameters for every condition (Table 1). Those parameters were obtained based on a previous optimization study (Belei et al., 2022b).

Finally, for some pre-determined conditions (v = 5, 35 and 65 mm/s; h = 0.4 mm; θ = 90°), the temperature at the metal-polymer interface during the coating layer deposition was recorded using a type K thermocouple inserted from underneath the substrate through a hole drilled on it (Figure 3C). The acquisition rate was 300 Hz. Specimens used during temperature measurements were not mechanically tested afterwards.

The pre-determined conditions mentioned earlier were selected as such in order to enable a direct comparison with the temperature measurements reported by (Belei et al., 2022a). By that time, the authors kept h constant at 0.4 mm since this was the value that resulted in the highest joint strength (via single-lap shear tests). Additionally, the inclination angle θ (variable absent in (Belei et al., 2022a)) was kept at 90° for the present study, since this was the value resulting in the closest surface roughness (see Section 3.1) in comparison to (Belei et al., 2022a).

2.3 Three-point bending test

Joints were tested with an adapted three-point bending test based on the ISO 14679:1997, with a setup presented in Figures 2C. The test was performed on a Shimadzu AGS-X (Japan), equipped with a loading cell of 5 kN, carried out with a traverse speed of 0.5 mm/min. Force and displacement were registered at a frequency of 100 Hz. Other than the Force x Displacement curve, the force at which the block detached from the substrate (critical force, F_c) was also recorded. The critical force F_c was identified on the Force x Displacement curve as the earliest point at which the derivative of the Force with respect to the Displacement assumed negative values. This represented a loss in stiffness of the system as a result of the block detachment (Roche et al., 1982; Sauvage et al., 2017; Birro et al., 2021; Belei et al., 2022b). However, as latter explained in Section 2.3, this stiffness loss was not always sharp enough to result in negative force derivatives; in those cases, F_c was defined by the point at which the force derivative assumed the lowest value.

Additionally, the three-point bending test was also conducted in substrates without blocks, as a means to evaluate the force at yield, as well as the slope of the Force x Displacement curve at the elastic region excluding the influence of the PA-CF block. Those measurements used the same experimental setup as mentioned earlier. The slope of the elastic region was calculating using points between 400 N and 500 N. The force at yield was inferred adopting the 0.2% offset method, commonly applied to determine the yield stress of metals based on uniaxial tensile tests (Ang et al., 2016; Benito et al., 2016; Hasemann et al., 2019). In the present case, the use of force (as in "force at yield") instead of strength was chosen, as it facilitates a direct comparison with subsequent F_c values from metal-polymer specimens.

2.3.1 Assessment of the absorbed energy during three-point bending test

In this work, the effectiveness of a parameter combination on the joint strength was evaluated using an energy approach based on the work from Birro et al. (2021). This approach consisted in the following steps: (i) the total resilience of the substrate-block system up to the detachment (W_{total}) is calculated based on the integral of the Force x Displacement curve, (ii) the resilience expected for the substrate without the block (W_{metal}) is calculated and then (iii) subtracted from W_{total}. The result is the resilience of the composite block (including the coating layer), which is represented by $W_{composite}$. The sequence is summarized by Figure 4. With this approach, it is possible to mitigate the influence of possible differences in substrate stiffness across different parameter combinations, which would affect a direct comparison using only F_c.

For step (i), the area below the Force x Displacement curve for substrate-block hybrid joints was approximated by subdividing it into individual rectangles up to the displacement at F_c, see Figure 4A. The area from rectangles below 10 N were discarded. The total area (W_{total}) was equal to the sum of the areas of each rectangle. The width of the rectangles was equal to one displacement step, or 8.3×10^{-5} mm.

For step (ii), an approach similar to step (i) was implemented, this time using Force x Displacement curves from standalone, substrate-only specimens. Three different curves for each θ value where averaged, point by point, resulting in six individual curves. Then, for each hybrid joint condition, the area below the substrate-only curve (W_{metal}) was calculated up to F_c (Figure 4B), with the corresponding substrate-only curve being selected depending on θ. Similar to step (i), the area from rectangles below 10 N were discarded. Finally, for step (iii) W_{metal} was subtracted from W_{total} to obtain a $W_{composite}$ (Figure 4C).

2.4 Surface roughness measurements

For each θ value, the DS of three distinct LPBF specimens (prior to AddJoining) had their average area surface roughness (S_a) measured using a Keyence VHX-6000 digital microscope (Germany). This resulted in a unique S_a average and standard deviation for each θ value. For the roughness measurements, an area of 5 mm × 5 mm was scanned, using a magnification of 100x. A Gaussian filter was applied on the initial results, using S = 25 μm and L = 2 μm.

2.5 Prediction modelling using Decision Tree Regression and ensemble methods

2.5.1 Decision Tree Regression

The Decision Tree Regression (DTR) algorithm generates, based on the input data set, a single decision tree which will predict a specific outcome dependent on various input parameters. In this case, generating a model means training a model with a certain training data set. Depending on the desired response, python builds a regression or classification decision tree following the, slightly changed, CART-algorithm (Classification And Regression Tree). With this algorithm, only binary trees can be built, meaning that at each node there are only two possible ways to go.

2.5.1.1 Decision Tree Regression—Mathematical formulation

Given training vectors $x \in R^n, i = 1, \ldots, l$ and a label vector $y \in R^n$, a decision tree recursively partitions the feature space such that the samples with the same labels or similar target values are grouped together. Assuming the data at a particular node m can be

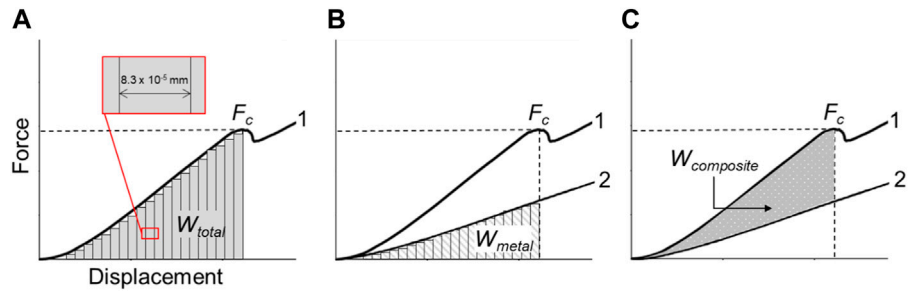

FIGURE 4
Summary of the sequence used for the calculation of W_{total}, based on (Birro et al., 2021). Step **(A)** integral of Force x Displacement curve for hybrid specimen (1) calculated up to F_c (W_{total}); Step **(B)** integral of average curve for standalone substrates (2) calculated up to F_c (W_{metal}); Step **(C)** W_{metal} is subtracted from W_{total}, resulting in $W_{composite}$, visualized as the area between curves 1 and 2.

represented by Q_m with samples N_m, thus each candidate split $\theta = (j, t_m)$ partitions the data into subsets $Q_m^{left}(\theta)$ and $Q_m^{right}(\theta)$, where:

$$Q_m^{left}(\theta) = \left\{(x, y) \middle| x_j \le t_m\right\} \quad (1)$$

$$Q_m^{right}(\theta) = Q_m \Big/ Q_m^{left} \quad (2)$$

Subsequently, the impurity function or loss function $H()$ is used to assess the quality of the candidate split, according to:

$$G(Q_m, \theta) = \frac{N_m^{left}}{N_m} H\left(Q_m^{left}(\theta)\right) + \frac{N_m^{right}}{N_m} H\left(Q_m^{right}(\theta)\right) \quad (3)$$

to which appropriate parameters should be selected to minimize the impurity, i.e.,:

$$\theta^* = \text{argmin}_\theta G(Q_m, \theta) \quad (4)$$

In regression, since the label (target or response) is a continuous value, Mean Squared Error (MSE) was employed as the criteria to minimize the loss function $H(Q_m)$ for node m, as for determining locations for future splits. Thus,

$$H(Q_m) = \frac{1}{N_m} \sum_{y \in Q_m} (y - \bar{y}_m)^2 \quad (5)$$

Where $\bar{y}_m$ represents the mean of all elements in the label vector,

$$\bar{y}_m = \frac{1}{N_m} \sum_{y \in Q_m} y \quad (6)$$

This procedure is repeated until a certain number of splits is reached (i.e., maximum depth) or the number of samples in a node is 1 ($N_m = 1$) (Breiman et al., 1984).

2.5.1.2 DTR statistical indicators

A coefficient of determination of 0.99 and 0.70 was obtained for the training and test set, respectively, with MSE at 244.49. The discrepancy in R^2 between training and testing, with testing being significantly lower, implies the model clearly shows high variance, hence overfitting. Ultimately, DTR is not well suited to generalize for unseen data.

2.5.2 Ensemble methods

An ensemble is an approach that combines multiple algorithms into a single predictive model able to decrease bias and variance, and increase predictive ability. A single decision tree will rarely generalize well to data it was not trained on, as is the case described herein, due to the fact that "pure" decision trees display low bias and high variance. To overcome this, several decision trees can be combined to obtain accurate predictions, since averaging the result of many trees will reduce variance while maintain bias.

This work brings together not only application of "pure" DTR, but also a comparison with ensemble methods based on Decision Tree theory (Breiman et al., 1984), from which the best model was selected and scrutinized for the purposes of AddJoining performance optimization. Table 2 summarizes relevant statistical indicators obtained for the generated ensemble models. Even though each ensemble's hyperparameters were optimized, a considerable amount of overfitting was observed for Random Forest, Extra Trees, Bagging and AdaBoost. Nonetheless, for all the aforementioned, MSE was reduced in comparison with DTR, which indicates the ensemble approach was effective in curtail bias. Contrastingly, Gradient Boosting Regression (GBR) exhibits very satisfactory R^2 and MSE values, that alludes to adequate bias-variance trade-off. This evidence will be made clear when validating the model in Sub-Section 3.2.2. for unseen, randomly selected data points (parameter combinations).

Since GBR proved to be the most reliable model, for the sake of completion, a more in-depth review over the mathematical details of this algorithm is provided in the upcoming sub-section.

2.5.2.1 Gradient Boosting Regression—Mathematical formulation

Gradient boosting Regression (GBR) is one of the variants of regression ensemble methods where multiple weak models are combined to achieve better overall performance. GBR is one of the most popular algorithms to handle tabular datasets, with the ability to find any nonlinear relationship between your model target and features and has great usability that can deal with missing values, outliers, and high cardinality categorical values on your features without any special treatment (Friedman, 2001).

The formulation of the GBR algorithm can be described according to the following pseudo-code (Friedman, 2001; Hastie et al., 2009).

TABLE 2 Statistical evaluation of the studied regression ensemble models.

Statistical indicator	*Random forest*	Extra trees	Bagging	AdaBoost	Gradient boosting
R^2-Training Set	0.97	1.00	0.97	0.96	0.99
R^2-Test Set	0.68	0.68	0.78	0.51	0.86
MSE	145.58	141.44	158.53	160.47	114.11

1. Create an initial constant value prediction F_0, in which,

$$F_0(x) = \text{argmin}_\gamma \sum_{i=1}^{n} L(y_i, \gamma) \tag{7}$$

where L the squared loss function given by,

$$L = (y_i - \gamma)^2 \tag{8}$$

Since the objective is to find the value γ that minimizes $\sum_{i=1}^{n} L$, one has to take the first order derivative, such that,

$$\frac{\partial}{\partial \gamma} \sum_{i=1}^{n} L = 0 \tag{9}$$

Performing the calculation yields that $\gamma = \bar{y}$. Thus the mean of y is used as initial prediction,

$$F_0(x) = \bar{y} \tag{10}$$

2. Iteratively, from $m = 1$ to M:

i. Calculate the pseudo-residuals r_{im} by taking a derivative of the loss function with respect to the previous prediction F_{m-1}, i.e.,:

$$r_{im} = -\left[\frac{\partial L(y_i, F(x_i))}{\partial F(x_i)}\right]_{F(x)=F_{m-1}(x)} \text{for } i = 1, \ldots, n \tag{11}$$

The negative gradient is convenient to access the direction and magnitude in which the loss function can be minimized.

ii. Fit a base learner (or weak learner, e.g., tree) against the pseudo-residuals r_{im}, and create terminal node disjoint regions $R_{1m}, \ldots, R_{J_m m}$, where J_m is the number of leaves.

iii. Compute γ_m by solving the following equation:

$$\gamma_{jm} = \text{argmin}_\gamma \sum_{x_i \in R_{jm}} L(y_i, F_{m-1}(x_i) + \gamma) \text{ for } i = 1, \ldots, J_m \tag{12}$$

thus,

$$\frac{\partial}{\partial \gamma} \sum_{x_i \in R_{jm}} L(y_i, F_{m-1}(x_i) + \gamma) = 0 \tag{13}$$

By computing Eq. (13), it can be concluded that the optimal γ_{jm} that minimizes the loss function is the average of the residuals r_{im} in the terminal node R_{jm}, thus,

$$\gamma = \frac{1}{n_j} \sum_{x_i \in R_{jm}} r_{im} \tag{14}$$

where n_j is the umber of samples in the terminal node j.

iv. Update the model:

$$F_m(x) = F_{m-1}(x) + \nu \sum_{j=1}^{J_m} \gamma_{jm} 1\left(x \in R_{jm}\right) \tag{15}$$

2.5.3 Training, test and hyperparameter tuning

The Machine Learning (ML) endeavors realized herein, where performed using python programming language, with proper use of the relevant API's (e.g., sklearn, numpy, pandas, *etc.*). To train a model that can adequately fit the data, but also generalizes well for "unseen" observations, a suitable train/test split must be specified. For this problem, due to the low amount of data available, a sensitivity analysis was conducted, from which a train/test split of 75% and 25% was considered, respectively, and partitioned in 6-fold-cross-validation. Additionally, the hyperparameters of each algorithm were tuned, using automated using "GridSearchCV" technique. This method creates a grid of hyperparameters of interest and their considered values, subsequently fitting models to every single combination of these parameters (Raschka and Mirjalili, 2019). An optimized set of parameters, regarding specific criterion (e.g., the lowest MSE or the highest R^2), was displayed and evaluated.

2.6 Microstructural characterization

Optical and Scanning Electron Microscopy (OM and SEM, respectively) were deployed during the present study. For OM, a Zeiss AX10 Observer Z1m optical microscope (Germany) in bright field mode was utilized; for SEM, a Tescan Mira-3 scanning microscope (Czech Republic), utilizing both secondary electron (SE) and backscattered electron (BSE) detectors. For fracture surfaces, specimens containing residual polymer where carbon sputtered prior to the SEM analysis, which was carried out with an acceleration voltage of 5 kV, a chamber pressure of 10^{-1} Pa and a work distance of 50 mm.

3 Results and discussion

3.1 Substrate characterization

The three-point bending test as proposed by Roche et al. (1982) is highly dependent on the substrate properties. For one, the detachment force is a result not only of the adhesive strength (which ultimately is the object of study of the test), but also of the substrate stiffness (Sauvage et al., 2017). Moreover, the test is conducted ideally within the elastic domain, meaning that the force at yield should be higher than the F_c range. Finally, besides the

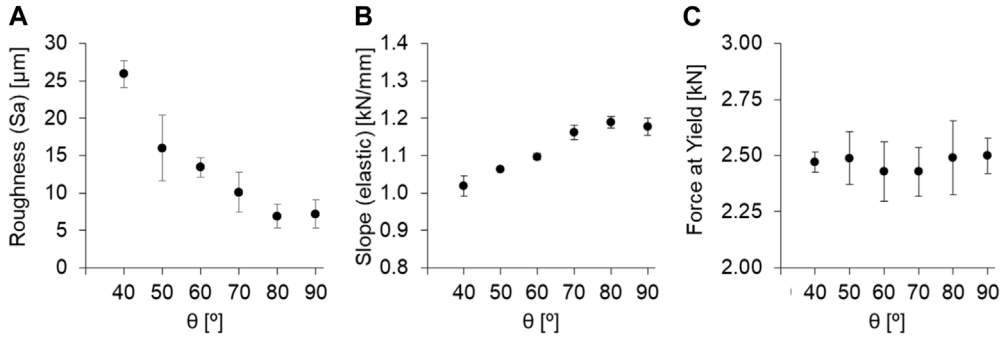

FIGURE 5
Results of the L-PBF Ti-6Al-4V substrate characterization with respect to the inclination angle θ. **(A)** Areal surface roughness, **(B)** slope of the Force x Displacement curve in the elastic region, **(C)** Force at yield.

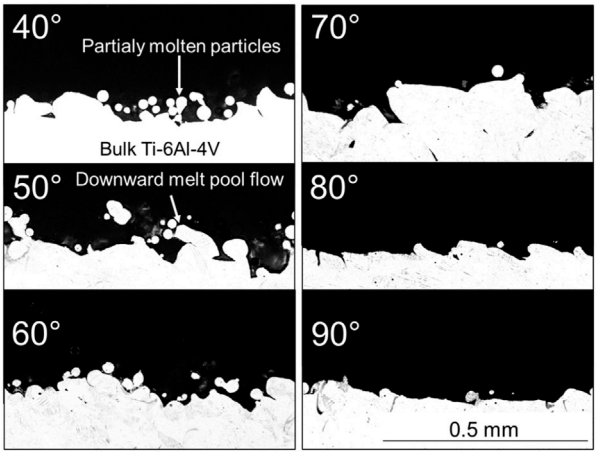

FIGURE 6
OM images of the DS from L-PBF Ti-6Al-4V specimens 3D-printed with different inclination angles.

remarks related to mechanical properties of the substrates, their surface roughness also plays a role on the test outcome, since it is closely related to the effectiveness of micromechanical anchoring between metal and adhesive (in this case 3D-printed polymer) (Leeden and Frens, 2002; Zhang and Huang, 2021; Schmidt and Chen, 2022). Therefore, in order to obtain a better understanding of the substrate role on subsequent three-point bending tests, substrates from different θ values were evaluated both mechanically and in terms of roughness (see Section 2.3 and 2.4), with Figure 5 summarizing the results.

These results reveal two different aspects that will later be relevant for the mechanical testing of hybrid joints. Firstly, it can be observed that the surface roughness is highly dependent on θ, with lower θ values resulting in rougher surfaces (Figure 5A). According to the literature (Covarrubias and Eshraghi, 2018; Ni et al., 2018; Melia et al., 2020; Skalon et al., 2020; Hofele et al., 2021), this can be attributed to the presence of partially molten particles, which during the LPBF process acted as a partial support for the melt pool at contour regions, remaining attached to the DS subsequently. As θ decreases, a greater melt pool area rests over loose particles, which leads to a higher quantity of such particles getting fused to the DS surface, effectively increasing its roughness. The melt pool can also flow downwards, causing protuberances to which surrounding powder can adhere as well (Charles et al., 2021; Feng et al., 2021). These effects can be visualized in Figure 6. Nonetheless, it is important to emphasize that, in this case, rough substrates result in more anchoring sites around which the polymer can flow during the AddJoining process, as previously discussed on Section 1. Consequently, θ may play a role on the hybrid joint strength; this remark will be discussed in further detail in the upcoming sections.

Secondly, the analysis of the mechanical properties as a function of θ revealed a slight increase in stiffness (represented by the slope of the Force x Displacement curve in the elastic domain, Figure 5B) towards higher θ values. Although this trend could not be considered substantial (the difference between $\theta = 40^{\circ}$ and $\theta = 90^{\circ}$ was 16%), the result shows that a proper assessment of the joint strength across different processing conditions must compensate for the differences in stiffness as a function of θ, which is the case for the energy based approach (see Section 2.3.1), which factors out the portion of the resilience attributed to the metallic substrate, i.e., proportional to its stiffness (Sauvage et al., 2017). Lastly, the Force at Yield was relatively constant across different θ values, with an average hovering around 2.5 kN (Figure 5C). Later, this result will show that, during the three-point bending test, the PA-CF block detachment always occurred at a force F_c insufficient to cause plastic deformation on the substrate.

3.2 Hybrid joints characterization

3.2.1 General aspects of the three-point bending test

Two types of Force x Displacement curves could be identified. The criterion to differentiate both types was whether the derivative of the Force with respect to the Displacement ever assumed negative values; if so, that would represent a relatively sharp loss in stiffness as a result of the detachment of the polymer block. On the other hand, if that derivative never assumed negative values, that would mean

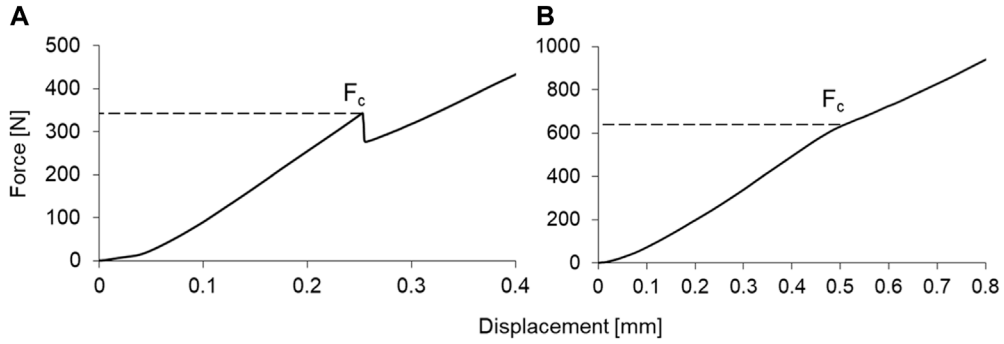

FIGURE 7
Representative Force x Displacement curves resulting from three-point bending tests. **(A)** Sharp transition; **(B)** Smooth transition. Process parameters: v = 5 mm/s, h = 0.25 mm, θ = 90° **(A)** and 60° **(B)**.

TABLE 3 Summary of the average process parameter values and responses for each curve type.

Curve type	n	θ [°]	v [mm/s]	h [mm]	F_c [N]	$W_{composite}$ [J]
Sharp	85	73 ± 15	17 ± 15	0.27 ± 0.13	462 ± 256	42 ± 41
Smooth	84	55 ± 13	22 ± 15	0.22 ± 0.11	458 ± 338	42 ± 58

that the loss in stiffness was smoother, being therefore harder to infer, from the curve, the moment at which the polymer block detached from the substrate. For the following discussion, the former case will be termed "sharp curve" and the latter "smooth curve". A visual representation of those two types of curves can be seen in Figure 7.

The emergence of either type of curve, however, did not seem to be due to any special circumstance or combination of parameter. Table 3 summarizes the average values from parameters and responses for each curve type. Other than a slight tendency of having sharp curves on conditions with lower v, sharp curves also tended to appear in conditions with higher θ, that is, when the surface roughness was lower (see Figure 5A). In terms of responses (F_c and $W_{composite}$), no noticeable differences could be observed with respect to the average results. In either case, there was a high standard deviation on both responses, showing that a given curve could be sharp or smooth within a wide range of outcomes, i.e., both stronger and weaker joints could yield either type of curve. Furthermore, the frequency of occurrence from both curve types is virtually equal.

Those results suggest that the occurrence of a given curve type is mostly random. Other authors also suggested that a stepwise stiffness reduction might be a consequence of defects present at the interface, resulting in a more gradual crack propagation at the metal-polymer interface (Birro et al., 2021; Belei et al., 2022a). In the present case, the interface is highly irregular, containing not only defects such as entrapped air bubbles (as covered in Section 3.2.3), but also protuberances of irregular shapes and sizes (see Figure 6). Those may have affected the shape of the curve unpredictably.

However, it is also important to point out that the substrate thickness may have also played a role on this matter. A stepwise crack propagation on a thinner substrate would most likely reveal a curve with a distinct peak (F_c) followed by a gradual descent with several smaller peaks until the curve reached the substrate baseline. This was evidenced by (Belei et al., 2022a), which used rolled Ti-6Al-4V substrates with a thickness of 0.5 mm. On the other hand, since the substrates used on the present study were substantially thicker (2 mm), the substrate baseline was higher; thus, the visual features expected from a stepwise propagation curve were blended with the substrate baseline itself, resulting in a single smooth curve. Nevertheless, the use of thicker substrates in this case was justified, since they required a higher force to deform plastically. This ensured that the three-point testing of hybrid joints would be carried out entirely on the elastic domain, meaning that any deviation from the expected linear-elastic behavior could only stem from the presence of the PA-CF block, and not from any plastic strain on the substrate itself.

Lastly, it is important to emphasize that, despite the high scatter observed in the average responses across all conditions, the results of the statistical analysis revealed that process parameters did have a significant influence on both F_c and $W_{composite}$, see Table 4. By performing Analysis of Variance (ANOVA) using an α of 0.05, both θ and v were found to have a statistically significant effect, as indicated by their very low p-values and F above F-crit both with respect to F_c and $W_{composite}$. These findings suggest that despite the variability in the data, there are clear associations between the response variable and these parameters, which will be further discussed in the upcoming sections.

3.2.2 Prediction model

Valuable information can be drawn from the GBR model concerning the influence of parameters in the bending

TABLE 4 ANOVA summary (α = 0.05) describing the statistical significance of each process parameter on both F_c and $W_{composite}$.

	Levels	Critical F (F-crit)	F_c		$W_{composite}$	
			F	*p*-value	F	*p*-value
Inclination angle (θ)	6	2.27	10.20	1.63E-08	7.52	2.23E-06
Printing speed (v)	3	3.05	105.35	2.89E-30	76.54	2.79E-24
Layer height (h)	3	3.05	0.89	0.41	0.58	0.56

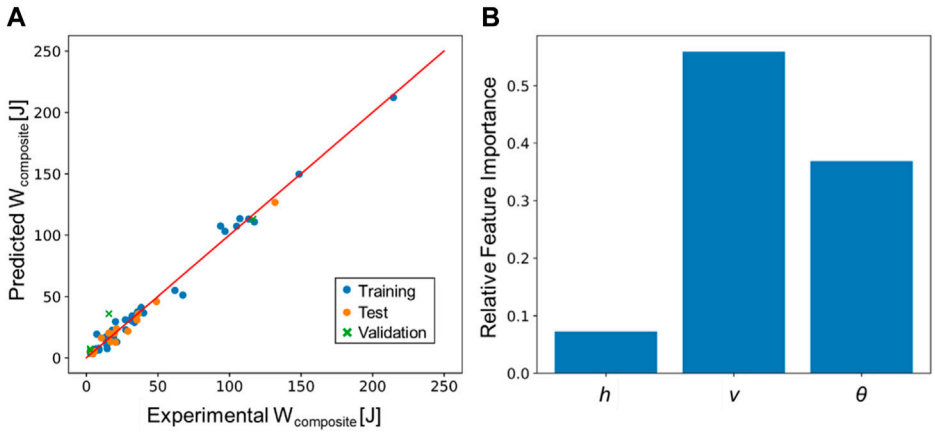

FIGURE 8
(A) Predicted vs. Experimental $W_{composite}$ plot; **(B)** Relative feature importance based on the GBR model.

performance of AddJoined components. In terms of performance, the model achieved a coefficient of determination (R^2) of 0.997 and 0.860 for the training and test sets, respectively, as already described in Table 2. Figure 8A provides visual intuition to those statistical indicators, highlighting the adequacy of GBR, as predicted $W_{composite}$ values matched the actual experimental values. This hold true for both training and tests sets. Moreover, a validation set, consisting of five experiments each with distinct parameter sets, was used for the *post hoc* evaluation of the GBR model, revealing a satisfactory predicting ability.

In terms of feature importance (Figure 8B), the printing speed v was considered the most influent parameter on the response $W_{composite}$, followed by the inclination angle θ and layer height h, respectively. This corroborates the results from the ANOVA presented earlier, but were the opposite of what has been observed in (Belei et al., 2022a). In that study, using F_c as a response, h was considered statistically significant while v was not. However, even in that case, a tendency indicating the average F_c being inversely proportional to v could be noticed. Moreover, according to the present findings, such a tendency appeared to be boosted by the substrate roughness, which in turn was dependent on θ. This can be concluded by comparing the resulting contour plots for different θ values, see Figure 9. As θ decreased, the response ($W_{composite}$) progressively increased towards the left-hand side of the plot, i.e., low v values. Moreover, it is also possible to see an increase towards low h values, although less prominently. Ultimately, this culminated in the global peak at θ = 40°, v = 5 mm/s and h = 0.10 mm (lower left-hand corner), where $W_{composite}$ surpassed 200 J. Further discussion on this topic is addressed on Section 3.2.3.

The high relative importance of v was most likely a product of the temperature evolution at the metal-polymer interface, which was a function of v itself (see Figure 10). As reported by (Belei et al., 2022a), the speed at which the coating layer is printed affects the temperature of the substrate both ahead and after the deposition. Slower prints cause a greater heat build-up effect (also reported by (Belei et al., 2022b), which in turn can (i) decrease the viscosity of the deposited polymer (Bechtel et al., 2020; Brostow et al., 2020; Calafel et al., 2020), allowing for a greater penetration into surface cavities and (ii) improve the wettability by providing enough energy to trigger a Cassie-Wenzel state transition (Ishino et al., 2004; Bormashenko, 2015; Su et al., 2016; Wang et al., 2016), which will be further discussed in Section 3.2.3. In either case, a stronger bond between metal and polymer would be achieved.

Based on Figure 10, it can be observed that at v = 5 mm/s, the temperature of the measured region was already above T_{onset} for around 15 s before the deposition, staying above that level for an extra 30 s interval afterwards. This comes in stark contrast with faster prints, where the temperature is raised above T_{onset} almost instantaneously before the deposition and then falling off much sooner. Although this was also observed by (Belei et al., 2022a), the present findings showed temperature peaks up to 30°C higher in

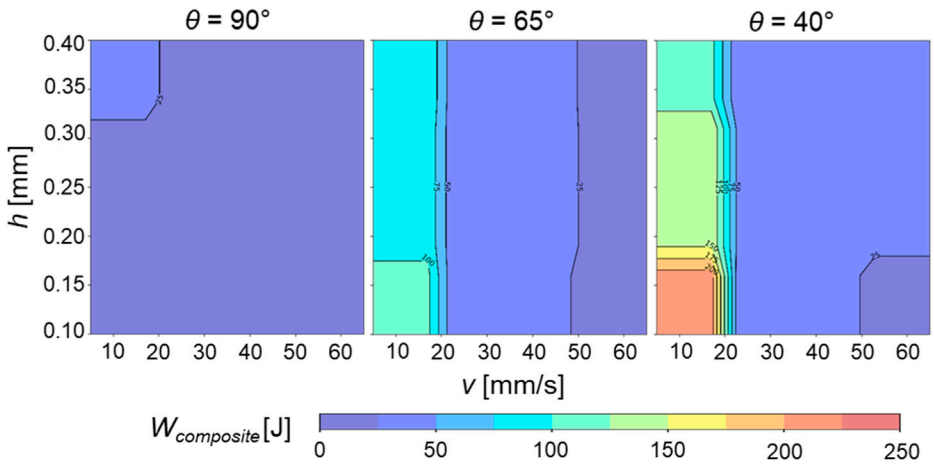

FIGURE 9
Contour plots for layer height h and printing speed v at different inclination angle θ levels, adopting $W_{composite}$ as a response.

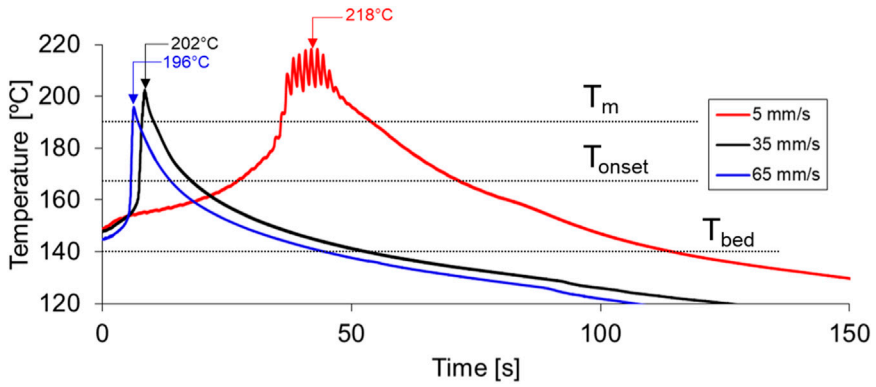

FIGURE 10
Temperature evolution during the coating layer deposition with different printing speeds. Layer height and inclination angles kept constant at 0.4 mm and 90°, respectively. Moment at which the nozzle passes over the thermocouple is indicated by an arrow. T_m, T_{onset} and T_{bed} denote Melting peak, melting onset and bed temperature, respectively.

comparison, most likely as a result of the difference in the width of the coating layer (14 mm and 5 mm, respectively). This is in accordance with (Belei et al., 2022b), which discussed that the shorter are the successive nozzle paths, the more prominent the heat build-up effect will be. Ultimately, these conclusions suggest that, for the AddJoining approach on larger models, it is advisable to subdivide the coating layer in several narrow strips as a means to locally increase temperature and consequently adhesion. This strategy may substitute a further increase in T_{bed}, which is less energy efficient and also potentially harmful to the substrate (Moreira, 2020; Belei et al., 2022a).

3.2.3 Microstructural features and fractography analysis

During the AddJoining process, polymer from the coating layer was able to infiltrate irregularities present on the as-printed LPBF surfaces. This occurred regardless of roughness (i.e., θ), meaning that even cavities present on the roughest DS surfaces could potentially be infiltrated by the unreinforced polymer. However, Figure 11 shows that not every cavity could be fully infiltrated, since some of those contained air pockets that were subsequently entrapped by the coating layer. This phenomenon has been also observed with sandblasted surfaces with much lower surface roughness (Belei et al., 2022a). This was most likely a result of the polymer freezing while the metal-polymer interface was still at a transitional state between Cassie–Baxter (wetting prevented by entrapped air, metastable) and Wenzel (full wetting, stable) regimes, as mentioned earlier. Nevertheless, despite the occasional presence of air pockets at the interface, the joint strength could be considered satisfactory depending on the parameter combination, as discussed in Section 3.2.2.

Under peeling, the intricate contact between substrate and coating layer led to a number of different fracture micromechanisms at the joint interface. Those affected both

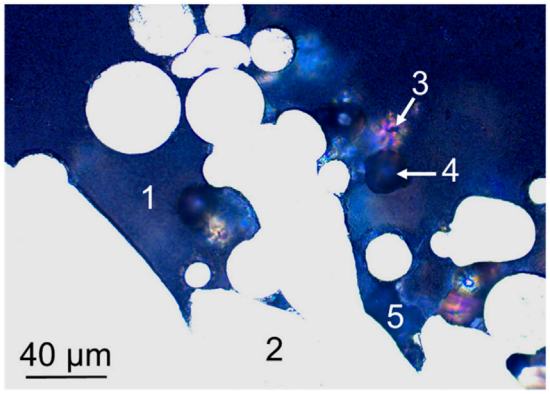

FIGURE 11
OM image showing the metal-polymer interface of a specimen produced with v = 5 mm/s, h = 0.25 mm and θ = 40°. (1) Coating layer; (2) substrate; (3) particle below the cross-sectional plane visible through the translucent polymer; (4) particle detached during metallography; (5) air pocket.

polymer and metal. For one, particles embedded in the coating layer deformed plastically and eventually failed, detaching themselves from the metallic substrate while remaining embedded in the polymer. An evidence for this can be seen in Figure 12, where a region previously occupied by a particle (or a group thereof) presented dimples; these features are a result of micro void coalescence, being normally observed on LPBF Ti-6Al-4V parts that experienced ductile fracture under tensile stress (Hooreweder and Sas, 2012; Cao et al., 2017; Gorsse et al., 2017). The extent of the individual dimpled regions depended on the prior contact area with the metallic substrate, with a diameter ranging from a few to tens of micrometers (Figures 12A, B, respectively). A similar observation was made by Englert et al. (2022), although in a milimetric scale; in their study, surface structures (i.e., pins) designed to enhance metal-polymer anchoring partially fractured as a result of shear stresses.

Based on those observations, it can be reasonably assumed that the presence of partially-molten particles on as-printed L-PBF substrates contributed positively to the metal-polymer joint strength, as the breakage of those particles provided the joint with an additional energy dissipation mechanism (Kim et al., 2010; Libanori et al., 2016). Evidence of particles ripped off from the metallic substrate was found regardless of θ (see Figures 13A, B), being therefore a general tendency of the AddJoining process on as-printed LPBF substrates. The difference between θ values, however, was the amount of particles on the detached polymer after testing. Figures 13C, D show a comparison between detached coating layers from 90° to 40° substrates, respectively, whereby a much greater amount of detached particles could be observed on 40°. Such a difference can be attributed to the increasing presence of partially-molten particles on the DS as the inclination angle θ decreases, as discussed in Section 3.1. It also explains the increase in $W_{composite}$ as θ decreases, as detected by the aforementioned prediction model (see Figure 9).

A closer look at the embedded particles reveals not only the opposite fracture surfaces in relation to the ones presented in Figure 12, but also the situation of those particles with respect to the surrounding polymer as of the moment of their fracture. While fully enveloped particles expectedly broke off from the substrate (Figure 14A), particles that were only partially surrounded by polymer also presented signs of breakage (Figure 14B). This suggests that in spite of the occasional presence of air entrapment preventing a full embedding, those particles still contributed somehow to the overall joint strength. However, the fractured areas in those cases were found to be relatively small in comparison to the fully enveloped particles. This means that the presence of a neighboring air pocket most likely avoided particle breakage in situations where there was a larger contact area between partially-molten particle and substrate, hindering the effectiveness of the micromechanical interlocking.

In most cases, however, the fracture of metallic particles did not occur; instead, the coating layer itself failed (see Figure 15), resulting in cavities and occasionally lacerations from ductile drawing (Greenhalgh, 2009). Cavities in the detached coating layer were a direct consequence of particles being pulled out from it (comparable to what is normally observed on fiber pullout in fiber-reinforced composites (Belei et al., 2022b). Similar cavities have been also reported in a previous study reproducing similar circumstances

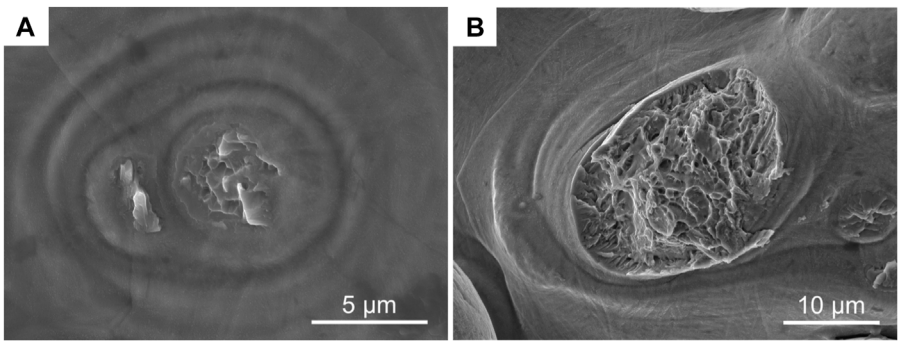

FIGURE 12
SE-SEM images from DS of L-PBF substrates after three-point bending test. Fracture surfaces resulting from the removal of **(A)** loosely-attached particle (θ = 90°) and **(B)** particle with a larger contact area (θ = 40°). Global crack propagation direction from top to bottom. Other process parameters: v = 5 mm/s, h = 0.40 mm.

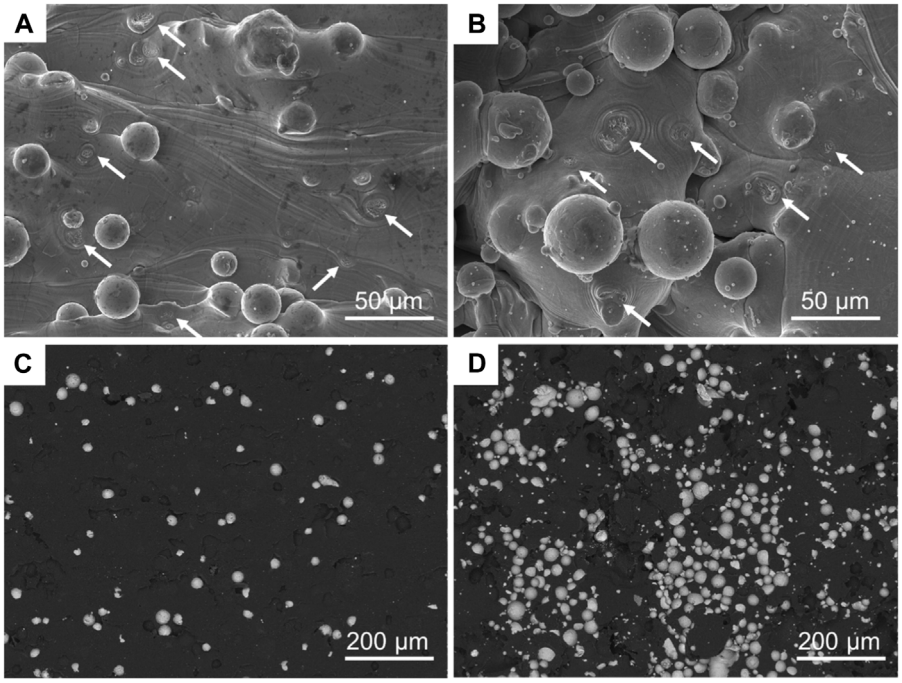

FIGURE 13
(A) and **(B)** SE-SEM images of metallic substrates after testing, with θ = 90° and 40°, respectively; white arrows indicate fractured areas previously occupied by particles. **(C)** and **(D)** BSE-SEM images of coating layers detached from substrates with θ = 90° and 40°, respectively; metallic particles are represented by brighter areas, while dark areas represent the surrounding polymer. For each picture, the global crack propagation occurred from top to bottom. Other process parameters: v = 5 mm/s and h = 0.40 mm.

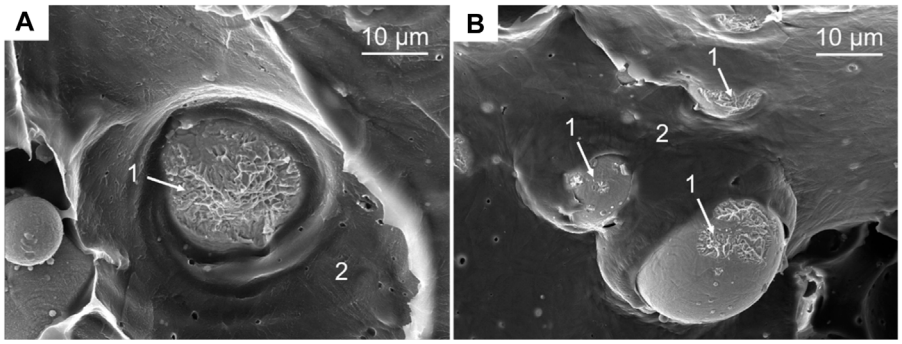

FIGURE 14
SE-SEM images of Ti-6Al-4V particles embedded in the coating layer after its detachment from the L-PBF substrate upon mechanical testing. **(A)** Particle totally surrounded by polymer; **(B)** partially surrounded particles. 1 indicates the respective facture surfaces for each individual particle; 2 represents the surrounding polymer. Process parameters: θ = 40°, v = 5 mm/s, h = 0.10 mm.

(Schmidt and Chen, 2022). Around such cavities, a damage zone comprised of plastically-deformed polymer was present (Figure 15-2), which has been identified elsewhere as well (Seo et al., 2021). The presence of those features is another indication that the interface failed under peeling loading. In this scenario, the presence of lacerations (see Figure 15-3) would also be expected, as previously observed for the AddJoining approach using sandblasted Ti-6Al-4V substrates (Belei et al., 2022a).

While lacerations resulting from ductile drawing were somewhat discernable on the detached coating layer (as seen in Figure 15-3), they could be better observed as a part of polymer leftovers found on the metallic substrate after testing, see Figure 16. However, polymer residue on the substrate was not present on all conditions, being instead limited to specimens with low h values. In those cases, polymer residue was found surrounded by partially-molten particles, which previously

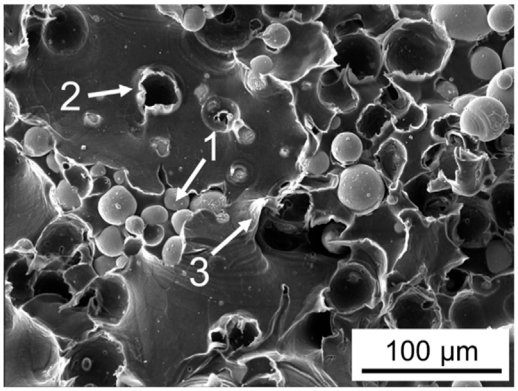

FIGURE 15
SE - SEM images of the as-tested coating layer surface. Partially-molten Ti-6Al-4V particles are indicated by 1; cavities resulting from the particle pullout are indicated by 2; lacerations as a result of ductile drawing are indicated by 3. Process parameters: θ = 40°, v = 5 mm/s, h = 0.40 mm.

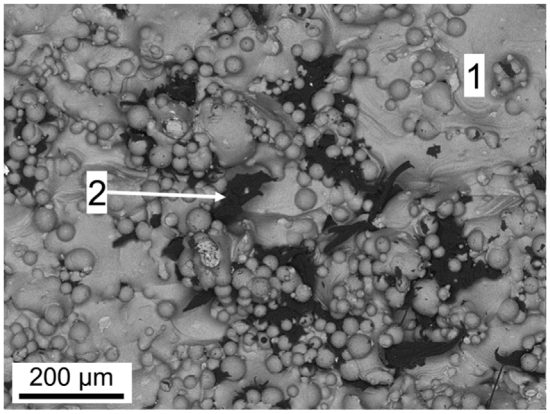

FIGURE 16
BSE-SEM images of metal substrate (1) after three-point bending test. Polymer leftovers trapped by partially molten particles is indicated by 2. Process parameters: θ = 40°, v = 5 mm/s, h = 0.10 mm.

constituted deep, intricate cavities where molten polymer could penetrate during AddJoining. The exact same tendency was also observed on rolled, sandblasted substrates (Belei et al., 2022a), where low h values also led to polymer residue on the metallic substrate. In the referred study, it was suggested that the coating layer—acting as a ductile interphase between metal and composite—was able to store energy via plastic deformation as the test progressed. Thus, decreasing h reduced the amount of ductile interphase material and consequently the amount of storable energy as well. Eventually, this resulted in two different outcomes: (i) at low enough h values (h = 0.10 mm), the coating layer torn apart before the onset of metal-polymer delamination; or (ii) for higher h values (h = 0.25 mm and above), detaching the polymer from the metal required less energy than tearing the coating layer, which led to the former occurring before the latter.

A fundamental difference between the present study and (Belei et al., 2022a) is, however, the surface roughness of the respective substrates. The sandblasted pre-treatment on rolled substrates (the strategy utilized in the referred study) resulted in a considerably lower areal surface roughness (S_a = 1.4 µm), therefore providing the deposited polymer with less anchoring sites. The referred study suggested that the outcome (ii) (i.e., coating layer detachment without failure) could cease to occur by increasing the metal-polymer interfacial strength, which in turn could be done, for example, by increasing the substrate roughness. However, according to the present findings, substrate roughness did not seem to matter: under peeling stresses, thinner coating layers were more prone to failure than thicker ones, regardless of the substrate roughness.

In terms of the "global" hybrid joint strength, however, a conclusion on this subject is not as straightforward. On the one hand, the previous study with sandblasted substrates (Belei et al., 2022a) suggested that h was indeed a statistically-significant parameter, with a positive effect on the response (in that case F_c). On the other hand, the present findings show that the influence of h had a negative effect on the response ($W_{composite}$), although only observable at low v and θ values. However, the apparent contradiction may stem from a multitude of factors, being a direct comparison difficult due the different experimental approaches. For one, the referred study only evaluated the effect of h using a constant printing speed of v = 35 mm/s and at a surface roughness level that could not be achieved by any θ value. There may exist an interaction of higher order between h, v and θ, perhaps only identifiable beyond the hereby evaluated ranges, which could potentially explain the observed contradiction.

4 Conclusion

Based on the results collected during the present work, the following conclusions can be drawn.

- Fully additively-manufactured metal-polymer hybrid specimens, consisted of a LPBF Ti-6Al-4V/PA-CF material combination, were successfully produced using the FFF-based "AddJoining" approach. The LPBF specimens were 3D-printed with several inclination angles, resulting in different levels of surface roughness. The polymer was printed using a two-step approach, whereby a "coating layer" of unreinforced PA was firstly deposited, with subsequent reinforced PA layers 3D-printed on it.
- A standardized three-point bending test, originally designed to test the strength adhesives on solid substrates, was successfully adapted for the 3D-printed hybrid specimens. The main output of this test was the force at which the polymer detaches from the metallic substrate (F_c), which later can be converted into the energy absorbed at the interface up to the detachment (hereby termed $W_{composite}$, measured in J). Average $W_{composite}$ results showed a strong dependence of the process parameters, ranging between 4.9 J (weak joint) and 214.5 J (strong joint).
- A ML approach based on a Decision Tree Regression algorithm was applied to determine the influence of process

parameters (i.e., coating layer height and printing speed, as well as the inclination angle with which the LPBF substrates were printed) on the responses from the three-point bending test. The model achieved a coefficient of determination (R^2) of 0.997 and 0.860 for the training and test sets, respectively, which were considered satisfactory. Thereby it was possible to conclude that printing speed and inclination angle (i.e., substrate roughness) were, in order, the most relevant parameters dictating the hybrid joint strength, with the coating layer height exhibiting only a minor influence.

- Slower coating layer printing speeds were related to an increased temperature at the metal-polymer interface, which theoretically decreases the polymer viscosity while increasing wettability. On the same note, rougher substrates offered more cavities into which the molten polymer could penetrate. Those acted as anchoring sites, thereby increasing the joint strength.
- After three-point bending tests, partially-molten particles resulting from the LPBF process either suffered ductile fracture or were pulled out of the coating layer. Either mechanism is thought to have contributed to the energy dissipation capabilities of the metal-polymer interface. Additionally, the coating layer itself exhibited signs of ductile deformation, as evidenced by numerous lacerations found on the fracture surfaces. Leftovers of polymer on the metal surface were not prevalent, being limited mostly to conditions with low coating layer height.

Data availability statement

The original contributions presented in the study are included in the article/Supplementary Material, further inquiries can be directed to the corresponding authors.

Author contributions

CB performed experimental work, data analysis and wrote this manuscript. PE provided the prediction modelling and data analysis, as well as reviewed the manuscript. BM provided the LPBF substrates and powder data, discussed the LPBF-related contents and reviewed the manuscript. STA-F provided the funding, infrastructure, supervised the experimental work and reviewed the manuscript.

Funding

The work was supported by the Austrian Research Promotion Agency (FFG) ["TAKEOFF" PILOT, grant number 852796, 2018] and the BMK—The Austrian Ministry for Climate Action, Environment, Energy, Mobility, Innovation and Technology.

Acknowledgments

The authors would like to acknowledge the Open Access Funding by the Graz University of Technology.

Conflict of interest

The authors declare that the research was conducted in the absence of any commercial or financial relationships that could be construed as a potential conflict of interest.

Publisher's note

Supplementary material

The Supplementary Material for this article can be found online at: https://www.frontiersin.org/articles/10.3389/fmats.2023.1202281/full#supplementary-material

References

Alhmoudi, A., Sheikh-Ahmad, J., Almaskari, F., and Bojanampati, S. 2022. "Joining of polymer-metal hybrid structures by fused deposition modelling." In 2022 Advances in Science and Engineering Technology International Conferences (ASET), 1–5. doi:10.1109/ASET53988.2022.9734841

Amancio-Filho, S., and Blaga, L. A. (2018). *Joining of polymer-metal hybrid structures: Principles and applications*. doi:10.1002/9781119429807

Ang, H. Q., Abbott, T. B., Zhu, S., Gu, C., and Easton, M. A. (2016). Proof stress measurement of die-cast magnesium alloys. *Mater. Des.* 112, 402–409. doi:10.1016/j.matdes.2016.09.088

Bechtel, S., Meisberger, M., Klein, S., Tobias, H., Quirin, S., and Herrmann, H.-G. (2020). Estimation of the adhesion interface performance in aluminum-PLA joints by thermographic monitoring of the material extrusion process. *Materials* 13 (15), 3371. doi:10.3390/ma13153371

Bechtel, S., Schweitzer, R., Frey, M., Busch, R., and Herrmann, H.-G. (2022). Material extrusion of structural polymer–aluminum joints—examining shear strength, wetting, polymer melt rheology and aging. *Materials* 15 (9), 3120. doi:10.3390/ma15093120

Belei, C., Jana, J., and Sergio, T. A.-F. (2022b). Fused-filament fabrication of short carbon fiber-reinforced polyamide: Parameter optimization for improved performance under uniaxial tensile loading. *Polymers* 14 (7), 1292. doi:10.3390/polym14071292

Belei, C., Pommer, R., and Amancio-Filho, S. T. (2022a). Optimization of additive manufacturing for the production of short carbon fiber-reinforced polyamide/Ti-6Al-4V hybrid parts. *Mater. Des.* 219, 110776. doi:10.1016/j.matdes.2022.110776

Benito, J. A., Cobo, R., Lei, W., Calvo, J., and Cabrera, J. M. (2016). Stress–strain response and microstructural evolution of a FeMnCAl TWIP steel during tension–compression tests. *Mater. Sci. Eng. A* 655, 310–320. doi:10.1016/j.msea.2016.01.004

Birro, T. V., Aufray, M., Paroissien, E., and Lachaud, F. (2021). Assessment of interface failure behaviour for brittle adhesive using the three-point bending test. *Int. J. Adhesion Adhesives* 110, 102891. doi:10.1016/j.ijadhadh.2021.102891

Bormashenko, E. (2015). Progress in understanding wetting transitions on rough surfaces. Adv. Colloid Interface Sci. *Reinhard Mill. Honorary Issue* 222, 92–103. doi:10.1016/j.cis.2014.02.009

Breiman, L., Friedman, J., Stone, C. J., and Olshen, R. A. (1984). *Classification and regression trees*. Taylor and Francis.

Brostow, W., Gonçalez, V., Perez, J. M., and Shipley, S. C. (2020). Wetting angles of molten polymers on thermoelectric solid metal surfaces. *J. Adhesion Sci. Technol.* 34 (11), 1–9. doi:10.1080/01694243.2019.1701893

Calafel, I., Aguirresarobe, R. H., Peñas, M. I., Santamaria, A., Tierno, M., Conde, J. I., et al. (2020). Searching for rheological conditions for FFF 3D printing with PVC based flexible compounds. *Materials* 13 (1), 178. doi:10.3390/ma13010178

Cao, S., Chen, Z., Lim, C. V. S., Yang, K., Jia, Q., Jarvis, T., et al. (2017). Defect, microstructure, and mechanical property of Ti-6Al-4V alloy fabricated by high-power selective laser melting. *JOM* 69 (12), 2684–2692. doi:10.1007/s11837-017-2581-6

Carvalho, W. S., and Amancio-Filho, S. T. (2022). On the feasibility of joining additively-manufactured 316L stainless steel and poly-ether-ether-ketone by ultrasonic energy. *Addit. Manuf. Lett.* 3, 100098. doi:10.1016/j.addlet.2022.100098

Charles, A., Ahmed, E., Paggi, U., Thijs, L., Hagenmeyer, V., and Scholz, S. (2021). Down-facing surfaces in laser powder bed fusion of Ti6Al4V: Effect of dross formation on dimensional accuracy and surface texture. *Addit. Manuf.* 46, 102148. doi:10.1016/j.addma.2021.102148

Chueh, Y.-H., Wei, C., Zhang, X., and Lin, L. (2020). Integrated laser-based powder bed fusion and fused filament fabrication for three-dimensional printing of hybrid metal/polymer objects. *Addit. Manuf.* 31, 100928. doi:10.1016/j.addma.2019.100928

Covarrubias, E. E., and Eshraghi., M. (2018). Effect of build angle on surface properties of nickel superalloys processed by selective laser melting. *JOM* 70 (3), 336–342. doi:10.1007/s11837-017-2706-y

Englert, L., Heuer, A., Engelskirchen, M. K., Frölich, F., Dietrich, S., Liebig, W. V., et al. (2022). Hybrid material additive manufacturing: Interlocking interfaces for fused filament fabrication on laser powder bed fusion substrates. *Virtual Phys. Prototyp.* 17 (3), 508–527. doi:10.1080/17452759.2022.2048228

Falck, R., Goushegir, S. M., dos Santos, J. F., and Amancio-Filho, S. T. (2018). AddJoining: A novel additive manufacturing approach for layered metal-polymer hybrid structures. *Mater. Lett.* 217, 211–214. doi:10.1016/j.matlet.2018.01.021

Falck, R., Jorge, F., and Sergio, T. A.-F. (2019). Microstructure and mechanical performance of additively manufactured aluminum 2024-T3/acrylonitrile butadiene styrene hybrid joints using an AddJoining technique. *Materials* 12 (6), 864. doi:10.3390/ma12060864

Feng, S., Kamat, A. M., Sabooni, S., and Pei, Y. (2021). Experimental and numerical investigation of the origin of surface roughness in laser powder bed fused overhang regions. *Virtual Phys. Prototyp.* 16, S66–S84. doi:10.1080/17452759.2021.1896970

Filho, S., and Falck, R. (2018). *Method for producing a layered component*. Germany DE102016121267A1. filed November 7, 2016, and issued May 9, 2018. Available at: https://patents.google.com/patent/DE102016121267A1/en.

Friedman, J. H. (2001). Greedy function approximation: A gradient boosting machine. *Ann. Statistics* 29 (5), 1189–1232. doi:10.1214/aos/1013203451

Genty, S., Sauvage, J.-B., Philippe, T., and Aufray, M. (2017). Experimental and statistical study of three adherence tests for an epoxy-amine/aluminum alloy system: Pull-off, single lap joint and three-point bending tests. *Int. J. Adhesion Adhesives* 79, 50–58. doi:10.1016/j.ijadhadh.2017.09.004

Gorsse, S., Hutchinson, C., Goune, M., and Banerjee, R. (2017). Additive manufacturing of metals: A brief review of the characteristic microstructures and properties of steels, Ti-6Al-4V and high-entropy alloys. *Sci. Technol. Adv. Mater.* 18, 584–610. doi:10.1080/14686996.2017.1361305

Greenhalgh, E. (2009). *Failure analysis and fractography of polymer composites*. 1–595.

Hasemann, G., Müller, C., Grüner, D., Wessel, E., and Krüger, M. (2019). Room temperature plastic deformability in V-rich V–Si–B alloys. *Acta Mater.* 175, 140–147. doi:10.1016/j.actamat.2019.06.007

Hastie, T., Tibshirani, R., and Friedman, J. (2009). *Springer series in statistics*. New York, NY: Springer. doi:10.1007/978-0-387-84858-7The elements of statistical learning

Hertle, S., Tobias, K., Wörz, A., and Drummer, D. (2020). Production of polymer-metal hybrids using extrusion-based additive manufacturing and electrochemically treated aluminum. *Addit. Manuf.* 33, 101135. doi:10.1016/j.addma.2020.101135

Hofele, M., Roth, A., Schanz, J., Harrison, D. K., De Silva, A. K. M., and Riegel, H. (2021). Laser polishing of laser powder bed fusion AlSi10Mg parts—influence of initial surface roughness on achievable surface quality. *Mater. Sci. Appl.* 12, 15–41. doi:10.4236/msa.2021.121002

Hooreweder, B. V., Moens, D., Boonen, R., Kruth, J., and Sas, P. 2012. Analysis of fracture toughness and crack propagation of Ti6Al4V produced by selective laser melting. *Adv. Eng. Mater.* 14 (1–2), 92–97. doi:10.1002/adem.201100233

Ishino, C., Ko, O., and Quéré, D. (2004). Wetting transitions on rough surfaces. *Europhys. Lett.* 68, 419–425. doi:10.1209/epl/i2004-10206-6

Kim, W.-S., Yun, I. H., Jung, H. T., Il-Han, Y., Jung-Ju, L., and Hee-Tae, J. 2010. "Evaluation of mechanical interlock effect on adhesion strength of polymer–metal interfaces using micro-patterned surface topography." *Int. J. Adhesion Adhesives* 30 (6): 408–417. doi:10.1016/j.ijadhadh.2010.05.004

Koutiri, I., Pessard, E., Peyre, P., Amlou, O., and De Terris, T. (2018). Influence of SLM process parameters on the surface finish, porosity rate and fatigue behavior of as-built inconel 625 parts. *J. Mater. Process. Technol.* 255, 536–546. doi:10.1016/j.jmatprotec.2017.12.043

Lambiase, F., Silvia Ilaria, S., Lee, C.-J., Ko, D.-C., and Liu, F. (2021). A state-of-the-art review on advanced joining processes for metal-composite and metal-polymer hybrid structures. *Materials* 14 (8), 1890. doi:10.3390/ma14081890

Leeden, M., and Frens, G. (2002). Surface properties of plastic materials in relation to their adhering performance. *Adv. Eng. Mater.* 4, 280–289. doi:10.1002/1527-2648(20020503)4:5<280:AID-ADEM280>3.0.CO;2-Z

Libanori, R., Carnelli, D., Rothfuchs, N., Binelli, M. R., Zanini, M., Nicoleau, L., et al. (2016). Composites reinforced via mechanical interlocking of surface-roughened microplatelets within ductile and brittle matrices. *Bioinspiration Biomimetics* 11 (3), 036004. doi:10.1088/1748-3190/11/3/036004

Liu, J. H., Shi, Y. S., Lu, Z. L., Xu, Y., Chen, K. H., and Huang, S. H. (2007). Manufacturing metal parts via indirect SLS of composite elemental powders. *Mater. Sci. Eng. A* 444 (1), 146–152. doi:10.1016/j.msea.2006.08.070

Liu, Z. Y., Li, C., Fang, X. Y., and Guo, Y. B. (2018). Energy consumption in additive manufacturing of metal parts. Procedia Manuf. *46th SME North Am. Manuf. Res. Conf. NAMRC* 26, 834–845. doi:10.1016/j.promfg.2018.07.104

Lizzul, L., Sorgato, M., Bertolini, R., Ghiotti, A., and Bruschi, S. (2021)., 102. Surface finish of additively manufactured Ti6Al4V workpieces after ball end millingProcedia CIRP, *18th CIRP Conf. Model. Mach. Operations (CMMO)* Ljubljana, Slovenia, 228–233. doi:10.1016/j.procir.2021.09.039

Mehrpouya, M., Tuma, D., Vaneker, T., Afrasiabi, M., Bambach, M., and Gibson, I. (2022). Multimaterial powder bed fusion techniques. *Rapid Prototyp. J.* 28 (11), 1–19. doi:10.1108/RPJ-01-2022-0014

Meier, B., Godja, N., Warchomicka, F., Belei, C., Schäfer, S., Schindel, A., et al. (2022a). Influences of surface, heat treatment, and print orientation on the anisotropy of the mechanical properties and the impact strength of Ti 6Al 4V processed by laser powder bed fusion. *J. Manuf. Mater. Process.* 6 (4), 87. doi:10.3390/jmmp6040087

Meier, B., Warchomicka, F., Petrusa, J., Paul, A., Wosik, J., Kaindl, R., et al. (2022b). Influence of powder production process and properties on material properties of Ti6Al4V manufactured by L-PBF. *Int. J. Adv. Manuf. Technol.* 123, 1577–1588. doi:10.1007/s00170-022-10250-y

Melia, M. A., Jesse, G. D., Koepke, J. R., Saiz, D. J., Jared, B. H., and Schindelholz, E. J. (2020). How build angle and post-processing impact roughness and corrosion of additively manufactured 316L stainless steel. *Npj Mater. Degrad.* 4 (1), 1–11. doi:10.1038/s41529-020-00126-5

Moreira, M. F. R. (2020). A new additive manufacturing technique for layered metal-composite hybrid structures. *Thesis, Tech. Univ. Hambg.* doi:10.15480/882.2961.4

Ngo, T. D., Kashani, A., Imbalzano, G., Nguyen, K. T. Q., and Hui, D. (2018). Additive manufacturing (3D printing): A review of materials, methods, applications and challenges. *Compos. Part B Eng.* 143, 172–196. doi:10.1016/j.compositesb.2018.02.012

Ni, C., Shi, Y., and Jia, L. (2018). Effects of inclination angle on surface roughness and corrosion properties of selective laser melted 316L stainless steel. *Mater. Res. Express* 6 (3), 036505. doi:10.1088/2053-1591/aaf2d3

Oliveira, G. H. M., Belei, C., de Carvalho, W. S., Canto, L. B., and Amancio-Filho, S. T. (2023). On the fully additive manufacturing of PC/AlSi10Mg hybrid structures. *Mater. Lett.* 330, 133378. doi:10.1016/j.matlet.2022.133378

Papazoglou, E. L., Karkalos, N. E., Karmiris-Obratański, P., and Markopoulos, A. P. (2022). On the modeling and simulation of slm and SLS for metal and polymer powders: A review. *Archives Comput. Methods Eng.* 29 (2), 941–973. doi:10.1007/s11831-021-09601-x

Pérez-Ruiz, J. D., Marin, F., Martínez, S., Lamikiz, A., Urbikain, G., and Norberto López de Lacalle, L. (2022). Stiffening near-net-shape functional parts of inconel 718 LPBF considering material anisotropy and subsequent machining issues. *Mech. Syst. Signal Process.* 168, 108675. doi:10.1016/j.ymssp.2021.108675

Raschka, S., and Mirjalili, V. (2019). *Python machine learning: Machine learning and deep learning with Python, scikit-learn, and TensorFlow 2*. Birmingham, United Kingdom: Packt Publishing Ltd.

Roche, A. A., Behme, A. K., and Solomon, J. S. (1982). A three-point flexure test configuration for improved sensitivity to metal/adhesive interfacial phenomena. *Int. J. Adhesion Adhesives* 2 (4), 249–254. doi:10.1016/0143-7496(82)90032-X

Sauvage, J.-B., Aufray, M., Jeandrau, J.-P., Chalandon, P., Poquillon, D., and Nardin, M. (2017). Using the 3-point bending method to study failure initiation in epoxide-aluminum joints. *Int. J. Adhesion Adhesives* 75, 181–189. doi:10.1016/j.ijadhadh.2017.03.011

Schmidt, K. T. A., and Chen, Z. W. (2022). Effect of surface morphology of Ti6Al4V alloy parts manufactured by electron beam powder bed fusion on bonding strength of adhesive joints. *Addit. Manuf. Lett.* 3, 100059. doi:10.1016/j.addlet.2022.100059

Seo, J. S., Ho, T. J., and Han, T. H. (2021). Peeling mechanism of interlocked interface between etched acrylonitrile-butadiene-styrene and electroplated metal layer. *Surfaces Interfaces* 26, 101337. doi:10.1016/j.surfin.2021.101337

Simson, D., and Subbu, S. K. (2022). Effect of process parameters on surface integrity of LPBF Ti6Al4V." *Procedia CIRP. 6th CIRP Conf. Surf. Integr.* 108, 716–721. doi:10.1016/j.procir.2022.03.111

Skalon, M., Meier, B., Gruberbauer, A., de Traglia Amancio-Filho, S., and Sommitsch, C. (2020). Stability of a melt pool during 3D-printing of an unsupported steel component and its influence on roughness. *Materials* 13 (3), 808. doi:10.3390/ma13030808

Su, J., Charmchi, M., and Sun, H. (2016). A study of drop-microstructured surface interactions during dropwise condensation with quartz crystal microbalance. *Sci. Rep.* 6, 35132. doi:10.1038/srep35132

Ultimaker Nylon TDS." 2023. Accessed April 27, 2023. Available at: https://support.makerbot.com/s/article/1667410781976.

Ultrafuse® PAHT CF15." 2023. Accessed April 27, 2023. Available at: https://forward-am.com/material-portfolio/ultrafuse-filaments-for-fused-filaments-fabrication-fff/reinforced-filaments/ultrafuse-paht-cf15/.

Wang, Z., Elimelech, M., and Lin, S. (2016). Environmental applications of interfacial materials with special wettability. *Environ. Sci. Technol.* 50, 2132–2150. doi:10.1021/acs.est.5b04351

Yadollahi, A., Shamsaei, N., Thompson, S. M., Elwany, A., and Bian, L. (2017). Effects of building orientation and heat treatment on fatigue behavior of selective laser melted 17-4 PH stainless steel. Int. J. Fatigue, *Fatigue Fract. Behav. Addit. Manuf. Parts* 94, 218–235. doi:10.1016/j.ijfatigue.2016.03.014

Zhang, D., and Huang, Y. (2021). Influence of surface roughness and bondline thickness on the bonding performance of epoxy adhesive joints on mild steel substrates. *Prog. Org. Coatings* 153, 106135. doi:10.1016/j.porgcoat.2021.106135

Frontiers in Materials

Investigates the discovery and design of materials for future application

A multidisciplinary journal that explores the breadth of materials science, engineering and mechanics - from carbon-based materials to smart materials.

Discover the latest Research Topics

See more →

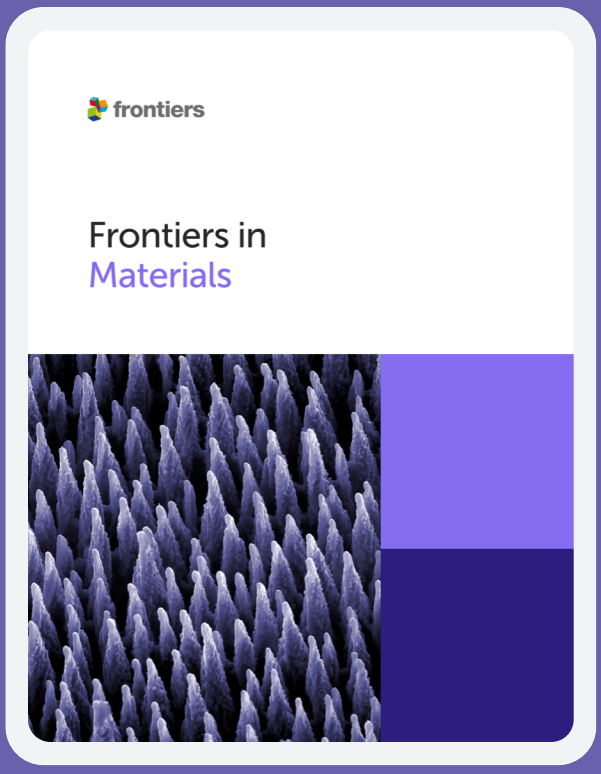

Frontiers

Avenue du Tribunal-Fédéral 34
1005 Lausanne, Switzerland
frontiersin.org

Contact us

+41 (0)21 510 17 00
frontiersin.org/about/contact